Corrosion of Bipolar Plates in PEM Fuel Cells

By

Seyed Ali Azimifar

A thesis submitted to the University of Birmingham for the degree of DOCTOR OF PHILOSOPHY

School of Metallurgy and Materials
College of Engineering and Physical Science
University of Birmingham
October 2015

UNIVERSITY OF
BIRMINGHAM

University of Birmingham Research Archive

e-theses repository

This unpublished thesis/dissertation is copyright of the author and/or third parties. The intellectual property rights of the author or third parties in respect of this work are as defined by The Copyright Designs and Patents Act 1988 or as modified by any successor legislation.

Any use made of information contained in this thesis/dissertation must be in accordance with that legislation and must be properly acknowledged. Further distribution or reproduction in any format is prohibited without the permission of the copyright holder.

Abstract

Laboratory and synchrotron X-ray fluorescence (XRF) have been used to investigate the microscopic and macroscopic distribution of metallic contaminants in membrane electrode assemblies (MEAs) which were used in proton exchange membrane fuel cell (PEM FC) stacks. The laboratory XRF results were consistent with the synchrotron XRF results. Higher levels of contaminants observed for the areas near to the coolant outlet than the areas near to the coolant inlet. The cathode side of MEAs showed higher levels of contamination than the anode side of the MEAs. Fe was the main contaminant, and there were also significant levels of Ni. Levels of Cu and Cr were significantly lower.

Synchrotron XRF maps of the MEA cross sections generally showed higher levels of contaminants on the cathode side compared with the anode side. Fe was mainly observed in the cathode side microporous layers, whereas Ni, Cr and Cu were mostly accumulated in the cathode side or in the membrane. Synchrotron XRF maps of MEA plan views showed a crack-like distribution for Fe and Pt which were similar to cracks in the microporous layer of the MEAs.

A novel electrochemical cell that simulated galvanic and crevice corrosion, temperature cycles for a PEM fuel cell, and pressure across the stacks was designed and used to discriminate between the corrosion behaviour of candidate coatings for bipolar plates.

Dedicated to my grandmothers, my grandfathers and my family.

Acknowledgment

The author is grateful for funding provided by the Technology Strategy Board under programme number BH064B in support of this work and that of project partners, on which this study relied for provision of materials and components.

I am grateful for all people help me during my PhD. I would like to express my special thanks to my supervisor Professor Alison J. Davenport for her great supervision of my PhD for writing synchrotron beamtime proposals, useful criticisms and especially for her insightful comments about presenting results and writing reports for the TSB project, first year report, second year presentation and this thesis.

I am particularly grateful for fast and precious comments on this thesis, good advices, kindness and all supports, especially for data analysis of XRF measurements given by my co-supervisor, Professor Trevor Rayment who improved the quality of my PhD with his ingenuity and broad knowledge.

I would like to express my special appreciation to my supervisors for making it possible to use synchrotron based facilities for my PhD and their supports for organizing, analyzing and presenting data.

I would like to thank all people from Intelligent Energy (IE), Johnson Matthey Fuel Cells (JMFC) and National Physical Laboratory (NPL) who was involved in the TSB project. I would like to express my special thanks to Dr. Gareth Hinds (NPL) for supports during designing of galvanic crevice cell, Dr. Rachel O'Malley (JMFC) for preparation of cross section samples, and Dr. Oliver Curnick (IE) for running stacks in IE. I would like to thank Dr. Jonathan Sharman, Dr. Graham Hards (JM), Dr. Paul Adcock, Dr. Simon Foster

Mr. Simon Armour, Dr. Arman Danelyan, Dr. Xiao Li, and Dr. Emma Farndon (IE) and all other people help in the TSB project.

I am grateful to Dr. Jackie Deans (University of Birmingham School of Chemistry) Dr. Colin Slater and Paul Jones (Bruker UK limited), Dr. Tina Geraki and Dr. Fred Mosselmans (Diamond Light Source) for collaborations and assistance.

I want to thank my friends and colleagues in the corrosion group whom I have great time and memories with them: Dr. Joshua Hammons, Dr. Mehdi Monir, Wayne, Dr Gavin Meredith, Haval, Steven, Andy, Dr. Mi Na (April), Liya, Fei, Georgia, Sarah and Dr. Majid Ghahari.

...and many thanks to my family for their emotional supports.

Table of Contents

Abbreviations

AAS	Atomic Absorption Spectroscopy
FC	Fuel Cell
EDS	Energy Dispersive Spectroscopy
GDL	Gas Diffusion Layer
ICR	Interfacial Contact Resistance
ICP	Inductively-Coupled Plasma
IE	Intelligent Energy
JMFC	Johnson Matthey Fuel Cells
MPL	Microporous Layer
PTFE	Polytetrafluoroethylene
GDM	Gas diffusion media
MEA	Membrane Electrode Assembly
PEM	Polymer Electrolyte / Proton Exchange Membrane
RVC	Reticulated Vitreous Carbon
SCE	Saturated Calomel Electrode
SEM	Scanning Electron Microscopy
XPS	X-ray Photoelectron Spectroscopy
XRF	X-ray Fluorescence
ZRA	Zero Resistance Ammeter

1 Introduction

1.1 PEM Fuel cells

Figure 1-1 illustrates the fundamental operation of a proton exchange membrane fuel cell (PEMFC). PEMFC directly convert chemical energy of hydrogen to electrical energy.

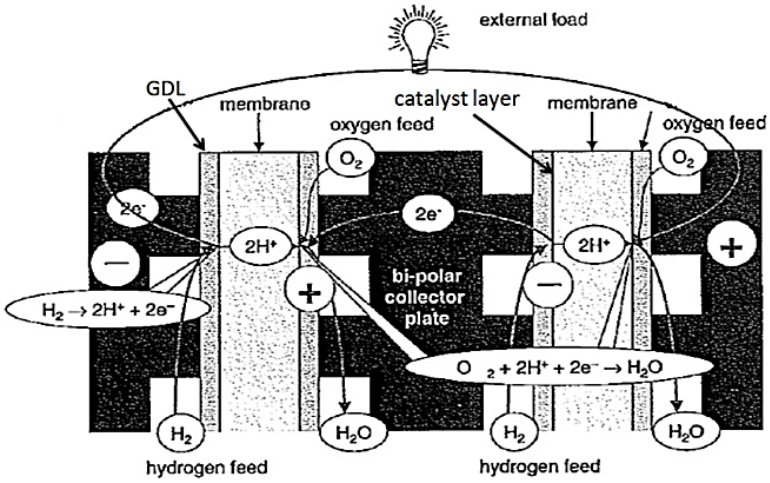

Figure 1-1. Schematic diagram showing how a PEM fuel cell work in a 2 cell stack [1].

The membrane is an electrolyte which conducts H^+ but prevents oxygen and hydrogen mixing. The gases diffuse through the gas diffusion layers (GDL), and between the GDL and the membrane there is a catalyst layer. The GDL, membrane and catalyst layer together are called the membrane electrode assembly (MEA). Oxygen flows in one side of membrane (cathode side) and hydrogen flows in the other side (anode side). Oxygen and hydrogen reach the catalyst surface through the GDL. In the side where hydrogen flows, Reaction 1 takes place on the catalyst surface:

$$H_2 \rightarrow 2H^+ + 2e^- \quad (1)$$

Protons move through the electrolyte to the oxygen side of the cell and the electrons go through the GDL, bipolar plate, and the external circuit and return to in the oxygen flow

side. In the oxygen flow side at the platinum surface, H^+ ions and electrons from Reaction 1 react with oxygen to form water:

$$½\ O_2 + 2H^+ + 2e^- \rightarrow H_2O \quad (2)$$

$$H_2 + ½\ O_2 \rightarrow H_2O + \text{heat} + \text{electrical current} \quad (3)$$

The overall products are an electrical current, heat and water (Reaction 3) [1, 2].

In fuel cell stacks made from multiple cells, electrons move from one cell to the neighbouring cell through a PEMFC component called a bipolar plate (BP) (see Figure 1-1), which is also called flow field plate [3].

1.2 Fuel cell advantages and technical barriers

Public and private investments in hydrogen and fuel cells have dramatically increased since the 1990s to improve energy security, reduce greenhouse gas emissions, and provide sustainable “green” energy for the future [4].

Fuel cells are energy convertors with very promising properties. They have much higher efficiency than internal combustion engines and conventional power plants. Fuel cells which use hydrogen have zero emission. Fuel cells are quiet and therefore attractive for both backup and portable power. In addition, they can be used for a variety of applications because their size can be modified from microwatts to megawatts [5].

Low durability and high prices are the biggest problems facing the practical application of Proton Exchange Membrane Fuel Cells (PEMFCs). Additionally, the performance of fuel cells must be at the same level or better than that of rival technologies [2, 6]. Because some components of fuel cell stacks such as the catalyst and membrane are expensive, they have high prices. High-performance catalysts which allow lower precious material loading and corrosion resistant bipolar plates are needed to make the price of PEMFC stacks competitive.

Fuel cells have no moving parts and long durability may be expected for PEMFC stacks. However, the fuel cell durability can not satisfy the lifetime requirements for important applications such as transportation. Component degradation mechanisms are not fully understood in PEMFC stacks and significant research and development is needed to improve the fuel cell durability [5-7].

1.3 Bipolar plate corrosion issues and thesis scope

The corrosion of bipolar plates and its effects decrease the durability of PEMFCs [8, 9]. The current focuses of research and development for bipolar plates according to the U.S. Department of Energy (DOE) are: decreasing volume and weight, developing and evaluating new coatings and materials to decrease corrosion and cost, identifying degradation mechanisms, and developing strategies for mitigating degradation to improve durability. Table 1-1 shows some of the U.S. DOE testing protocols, 2011 status and 2020 targets for bipolar plates [6].

Table 1-1. U.S. DOE 2011 status and 2020 targets for bipolar plates

Characteristic	Notes	2011 Status	2020 Target
Corrosion in anode	pH 3, 80 °C, 0.1 ppm HF, de-aerated with Ar purge potentiodynamic measurement (- 0.4 to 0.6 V vs. Ag/AgCl reference electrode at a scan rate of 0.1 mVs^{-1})	<1 $\mu A/cm^2$	<1 $\mu A/cm^2$
Corrosion in cathode	pH 3, 0.1ppm HF, 80 °C, aerated solution, potentiostatic test at +0.6V (vs. Ag/AgCl) for >24 h	<1 $\mu A/cm^2$	<1 $\mu A/cm^2$
Areal specific resistance	ICR measurements (before and after potentiostatic test) measured with 138 N/cm^2	0.03 Ω-cm^2	0.01 Ω-cm^2
Cost	Costs of mass production	5-10 $/kW	3 $/kW

Stainless steels are attractive alloys as bipolar plates for PEMFCs; however, they are subject to corrosion [9-11]. Corrosion of bipolar plates increases the interfacial contact resistance (ICR) between the bipolar plates and the gas diffusion layer (GDL) [12-16] and contaminates both the catalyst and the membrane [17-20].

This PhD was part of a UK Technology Strategy Board (TSB) project on component development for improved membrane electrode assembly (MEA) and stack stability carried out in collaboration with Johnson Matthey Fuel Cells Ltd. (lead), Intelligent Energy Ltd., National Physical Laboratory (NPL), Technical Fiber Products Ltd., Mersen Ltd., Loughborough University, and University of Birmingham. This PhD involved the characterization of components of fuel cells that have operated for extended periods as well as the design and development of novel methods/instruments to simulate the corrosion of bipolar plates in PEM fuel cells.

X-Ray Fluorescence (XRF) has been used in the past to measure MEA contamination [15, 20-24]. However, none of the work published thus far has looked at the distribution of metal ions within the MEA. To our knowledge, synchrotron XRF with high resolution has not been used to study MEA contamination following the operation of a fuel cell stack for long time periods.

Electrochemical methods are frequently used to assess the corrosion resistance of bipolar plates [9, 24]. A small number of publications have focused on the galvanic corrosion of bipolar plates in PEM fuel cells and have shown galvanic corrosion can be an important corrosion mechanism for degradation in PEM fuel cells [25, 26]. However, these studies did not take into account all the requirements for simulating PEM fuel cell conditions in ex situ corrosion tests [27].

This thesis focuses on the corrosion of bipolar plates in PEMFCs. Post-mortem analysis of MEAs using laboratory XRF and synchrotron XRF was carried out to determine the distribution of contamination in MEAs used in stacks following long duration tests. Additionally, in this PhD, a novel electrochemical cell (galvanic crevice cell) is used to simulate more representative conditions in PEMFCs. The galvanic-crevice corrosion current between MEAs and metallic samples can be directly measured using this electrochemical cell.

In parallel with the design and development of the galvanic crevice cell in this PhD, NPL carried out in situ measurements in operating PEM fuel cells. NPL's results confirmed that the correct corrosion mechanisms and environmental conditions were simulated in the galvanic crevice cell. In a recently published paper [27], NPL scientists suggested that ex situ tests which are currently used in the U.S. DOE for measuring the corrosion rate of flow field plates should be changed in light of their in situ measurements [27].

1.4 Pourbaix diagrams

Pourbaix diagrams show the role of potential and pH on thermodynamically stable phases of a metal. For this, the well-known Nernst equation [28, 29] is used to graphically show possible reactions in potential-pH diagrams. Reactions that only involve the generation or consumption of electrons are only dependent on potential and they are shown by horizontal lines in Pourbaix diagrams. Reactions that are influenced only by pH are shown by vertical lines. When both pH and potential affect the reaction, it is shown by an angled line.

These diagrams show the range of pH and potential where the metal corrodes, the possible compound of corrosion products and the ranges of potential and pH where the metal

is protected from corrosion. Figure 1-2 shows a Pourbaix diagram for Fe. The dotted lines (labelled “a” and “b”) in Figure 1-2 show the area of stability for water (Figure 1-3) [29, 30].

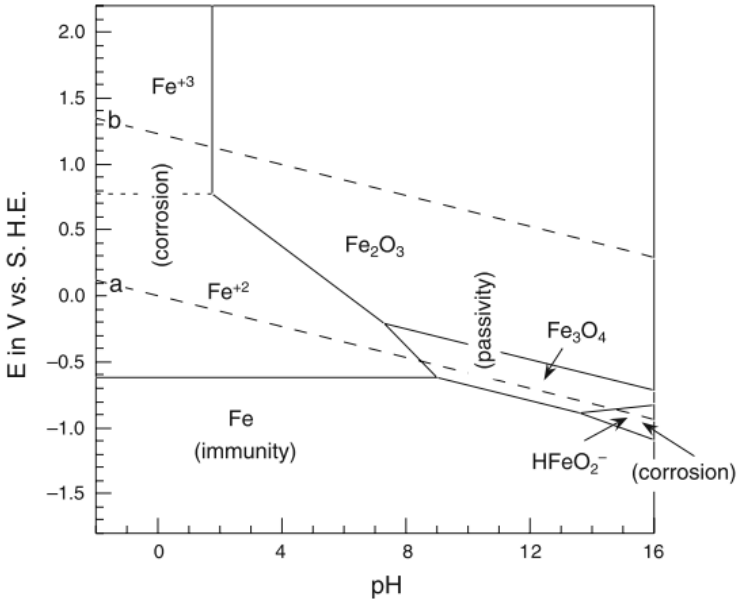

Figure 1-2. Pourbaix diagram for Fe-water system at 25 ºC [30].

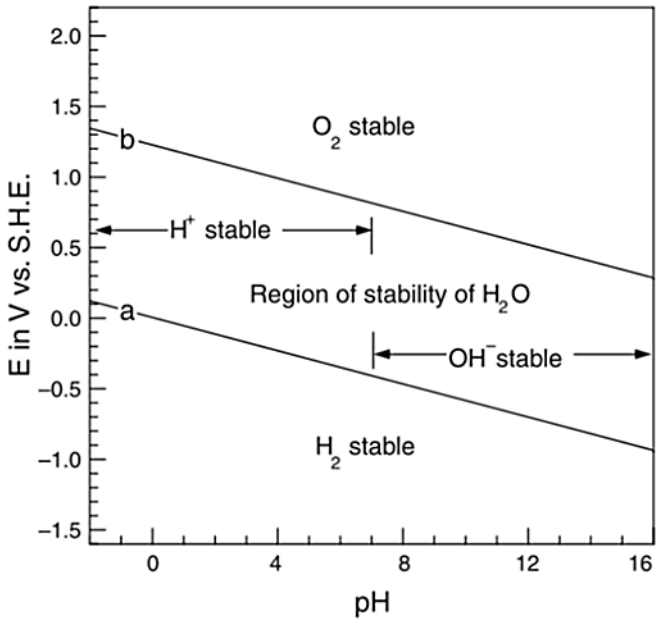

Figure 1-3. Pourbaix diagram for water at 25 ºC [30].

It can be seen in Figure 1-4 that an increase in temperature affects the Pourbaix diagrams. This is because the Nernst equation is functions of temperature and also the concentration of products and reactants of a reaction can be affected by temperature variations [30].

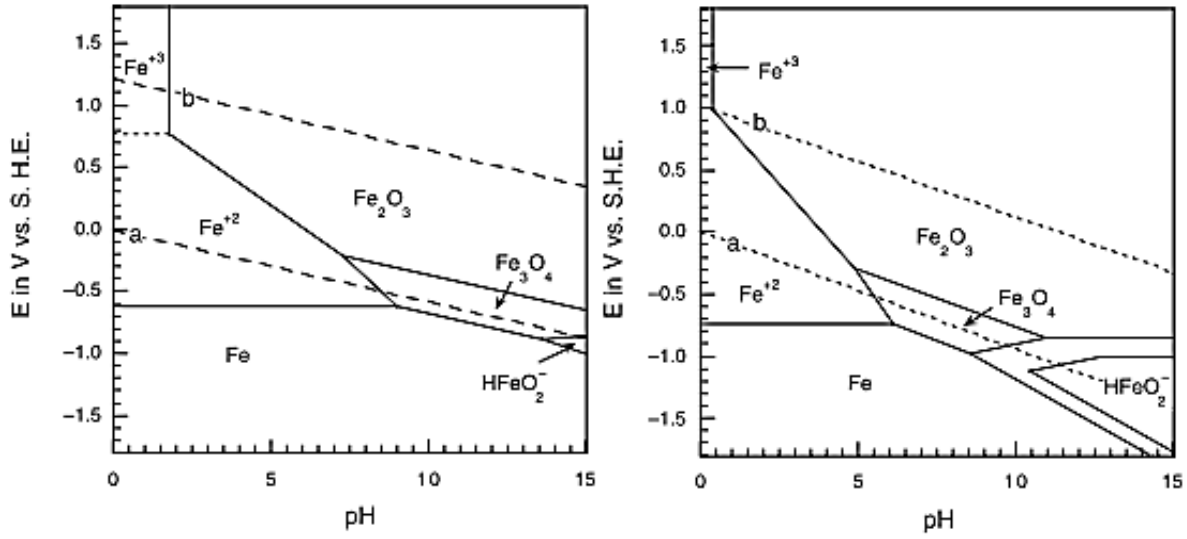

Figure 1-4. Pourbaix diagram for Fe-water system at 25 ºC (left) and 200 ºC (right) [30].

1.5 Polarization

Thermodynamics information such as Pourbaix diagrams only shows the tendency of a metal-electrolyte system to corrode and does not give any information about corrosion rates [30, 31].

The corrosion process involves electrochemical reactions which consume electrons in cathode or generate electrons in anode. This causes a flow of charge (electrons) which is a current. The current can be divided by surface area, known as current density, to remove the surface area effect. For a metal in equilibrium with its ions, anodic current density (i_a) and cathodic current density (i_c) are equal and are called the exchange current density (i_0). The corrosion rate corresponds to the current density. The corrosion current depends on electrode

potential. Therefore it is important to understand the relationship between electrode potentials and corrosion currents [29-31]. The degree of polarization is known as overpotential or overvoltage and is given by Equation 4 [30, 31]:

$$\eta = E - E_o \quad (4)$$

Where η is overpotential, E is the electrode potential when the net current is not zero, E_o is the electrode potential when the net current is zero and the electrode is in equilibrium with solution. Polarization can be activation, concentration or ohmic polarization. The total polarization of an electrode is:

$$\eta_{total} = \eta_{activation} + \eta_{concentration} + \eta_{resistance} \quad (5)$$

Activation polarization ($\eta_{activation}$) is the overvoltage that is needed to overcome the activation energy of the reaction. Concentration polarization ($\eta_{concentration}$) is a polarization due to concentration of products or reactants near the electrode/solution interface. IR drops or ohmic polarization ($\eta_{resistance}$) is a polarization caused by resistance along the current path in the electrochemical cell according to Ohm's Law (V=IR). This resistance could be the resistance of any film on the electrode or the resistance of the solution (ionic resistance), etc. Significant IR drops are common in solutions where the current is transported by the movement of anions and cations.

When electrode potential becomes more positive it is called anodic polarization and when it becomes more negative it is called cathodic polarization (see Figure 1-5) [28, 30-32].

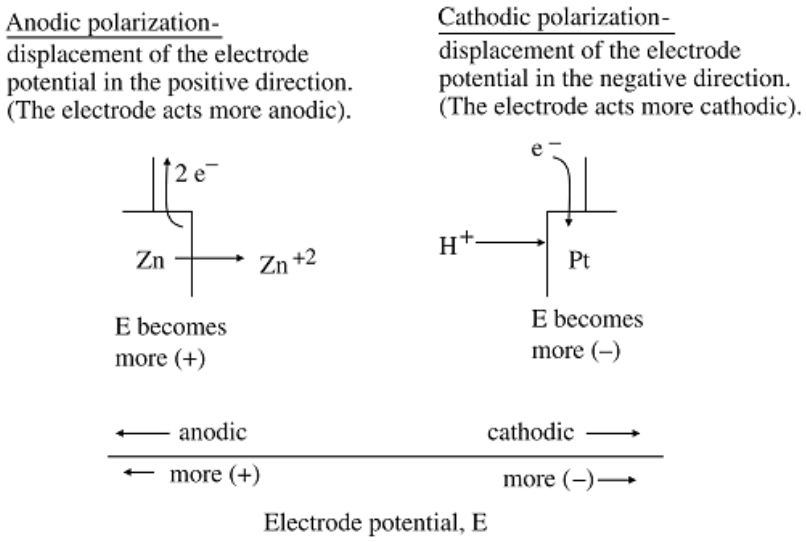

Figure 1-5. Anodic and cathodic polarization [30].

For an overpotential of $\eta=(E-Eo)$ caused by activation polarization it can be shown [31] that:

$$i_a=i_0 \exp(\frac{\alpha(E-Eo)zF}{RT}) \quad (6)$$

$$i_c=i_0 \exp(\frac{(1-\alpha)(E-Eo)zF}{RT}) \quad (7)$$

And the net current density ($i_{meas}= i_a - i_c$) is:

$$i_{meas}=i_0 \left[\exp\left(\frac{-\alpha(E-Eo)nF}{RT}\right) - \exp(\frac{(1-\alpha)(E-Eo)nF}{RT})\right] \quad (8)$$

Where i_a is anodic current density, n is the number of electrons, i_0 is exchange current density and i_c cathodic current density, and α is a dimensionless parameter usually about 0.5. Equation 8 is the well-known Butler-Volmer equation [30].

Because the cathodic current is negative, the $\log|i|$ vs. electrode potential is used for plotting the Butler–Volmer equation as illustrated in Figure 1-6. Polarization curves are a plot of $\log|i|$ vs. electrode potential. At potentials away from the equilibrium the effect of one of the half-cell's currents becomes insignificant and $\log|i|$ vs. overpotential becomes linear [30], it can be shown that for anodic reaction [31]:

$$\eta_a = \beta_a \log i_a - \beta_a \log i_0 \quad \beta_a = \frac{2.303RT}{\alpha zF} \tag{9}$$

And for cathodic reaction:

$$\eta_c = \beta_c \log i_c - \beta_c \log i_0 \quad \beta_c = \frac{2.303RT}{(1-\alpha)zF} \tag{10}$$

These equations are known as the Tafel equation and β_c and β_a (dE/d log|i|) are known as the Tafel slope. Exchange current density (i_o) can be measured by extrapolating anodic and cathodic Tafel lines [30, 31].

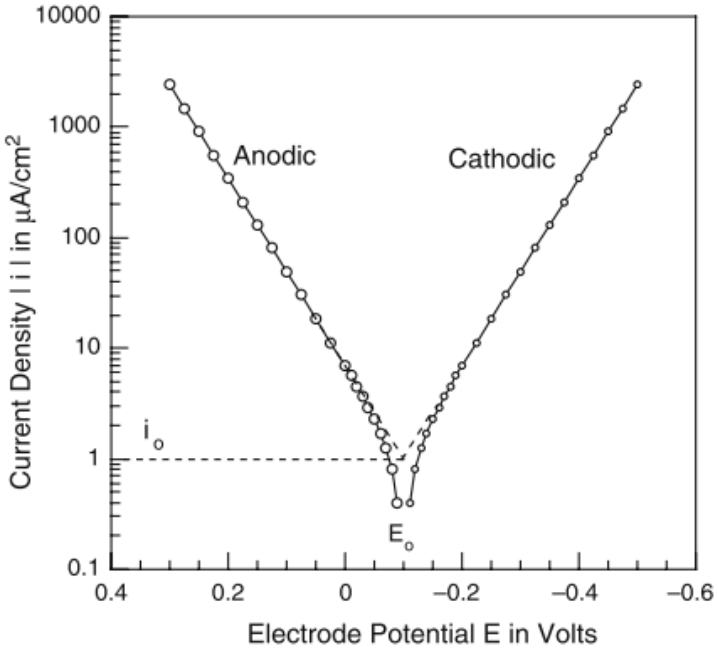

Figure 1-6. Plot of log|i| vs. electrode potential (the Butler–Volmer equation) for β_a = +0.100 V/decade, and β_c = –0.100 V/decade. i_o = 1 μ A/cm is measured by extrapolating anodic and cathodic Tafel lines [30].

1.6 Polarization experiment

Figure 1-7 shows the three-electrode cell for polarization measurements. The working electrode (WE) is the metal under examination. The reference electrode (RE) provides a constant and reproducible potential in the electrolyte. The counter (auxiliary) electrode (CE) is usually Pt which carries the electrons produced in the circuit, either from or to the WE [31-33]. The polarization experiment can be done by controlling the potential and measuring

the current (potentiostatically) or by controlling the current and measuring the resulting potential (galvanostatically) [32].

The instrument that performs the polarization experiments is known as potentiostat. The potentiostat controls the potential difference between the WE and the RE to the set values by supplying the needed current between the WE and the CE. The potential between the RE and the WE is measured using a high-resistance voltmeter. The current flow between the WE and the CE is measured using a low-resistance ammeter [31-33].

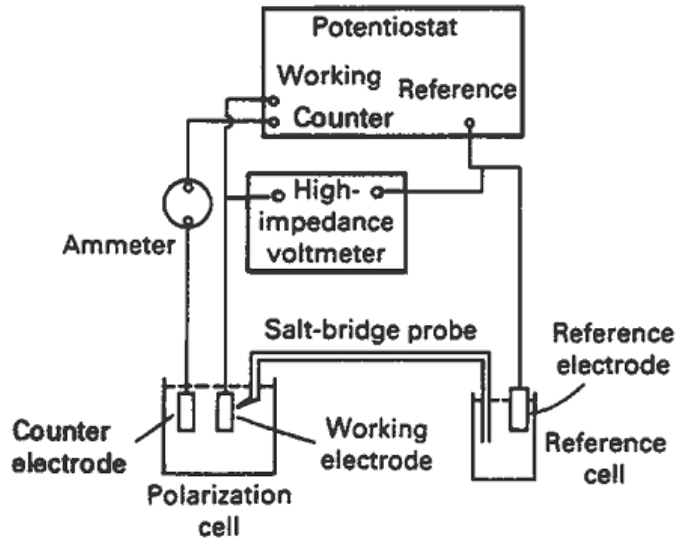

Figure 1-7. Three-electrode cell set up for polarization measurements [32].

1.7 Polarization of metals with passive layer

It is possible for a metal to react with its environment and form a protective layer on its surface which decreases the corrosion rate and protects the underlying metal for a range of potentials. Figure 1-8 shows an anodic polarization curve for a metal which shows passivation behaviour. This curve shows three regions: the active, passive and transpassive regions.

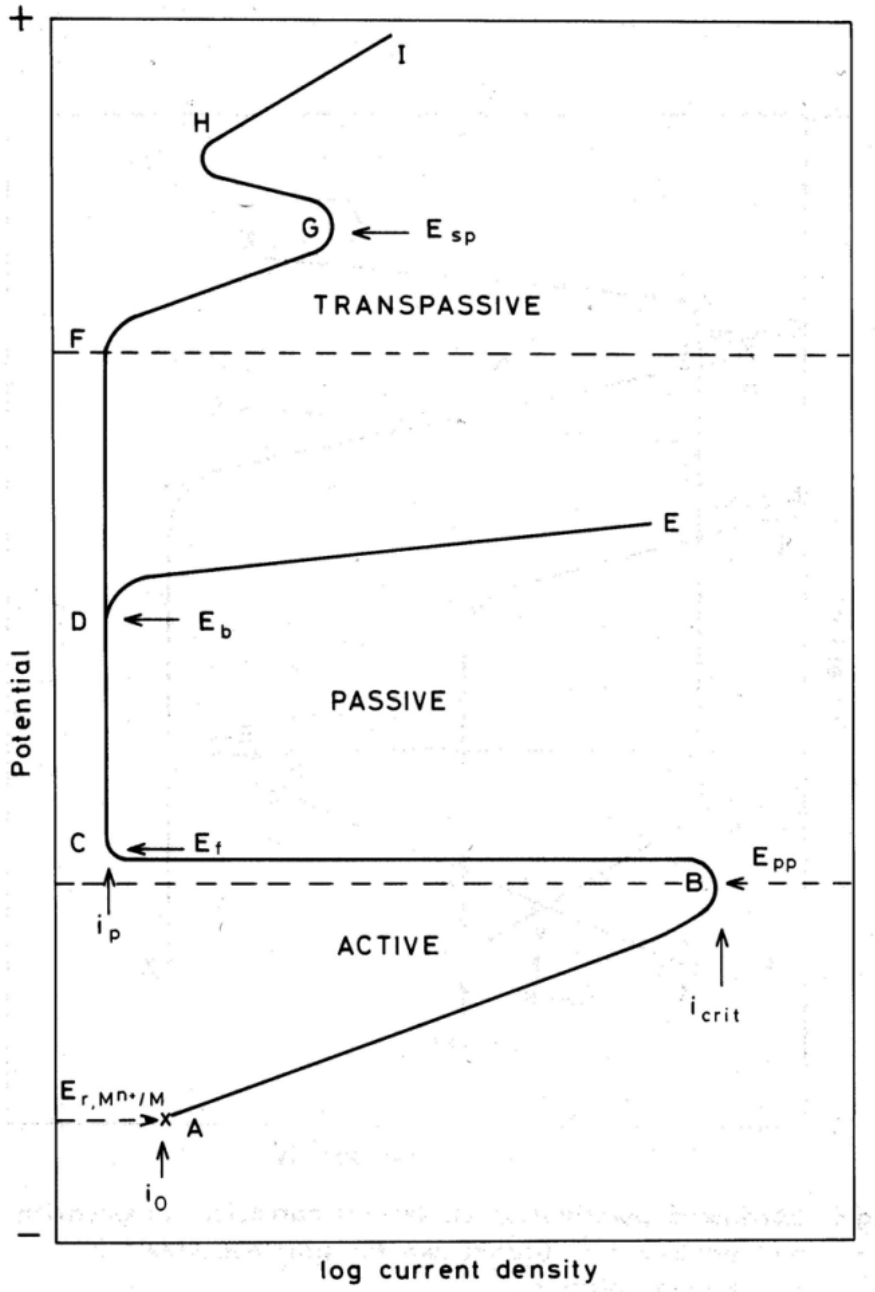

Figure 1-8. Polarization for a metal with active-passive transition [33].

It can be seen in Figure 1-8 that in the active region, when potential increases corrosion rate increases from the exchange current density (i_0) with the reversible potential (E_r) to the peak with the critical current density (i_{crit}) and the critical (primary) passivation potential (E_{pp}).

When the potential is E_{pp} (Figure 1-8) a further increase in the potential causes a sudden decrease in the current. This is due to the formation of a thin protective oxide film on the surface of the metal. The passive film begins to form near B (Figure 1-8) with E_{pp} potential and at the Flade potential (E_f) the oxide film covers the entire surface.

It can be seen in Figure 1-8 that after the Flade potential (E_f), the current is independent of an increase in potential for a range of potential. In this region, known as the passive region, the corrosion process is slow and generates a low current which is called passive current density (i_p). The high value of the i_{crit} shows the low tendency of a metal for passivation in an environment. The high value of i_p shows low protectiveness of a passive film in an environment.

The current again starts to increase by increasing potential in the transpassive region as shown in Figure 1-8. Depending on the anions which are present in the solution and the stability of the oxide films, the reason for an increase in current density in the transpassive region can be pitting, the dissolution of the passive layer, or the evolution of O_2 by the breakdown of H_2O in the solution [30, 33].

If pitting corrosion and the dissolution of the passive layer do not take place, the potential may increase to values which are high enough for the evolution of oxygen according to Reaction 11 (see Figure 1-9):

$$2H_2O \rightarrow O_2 + 4H^+ + 4e^- \qquad (11)$$

If this happens, the increase in current is not because of corrosion of the metal.

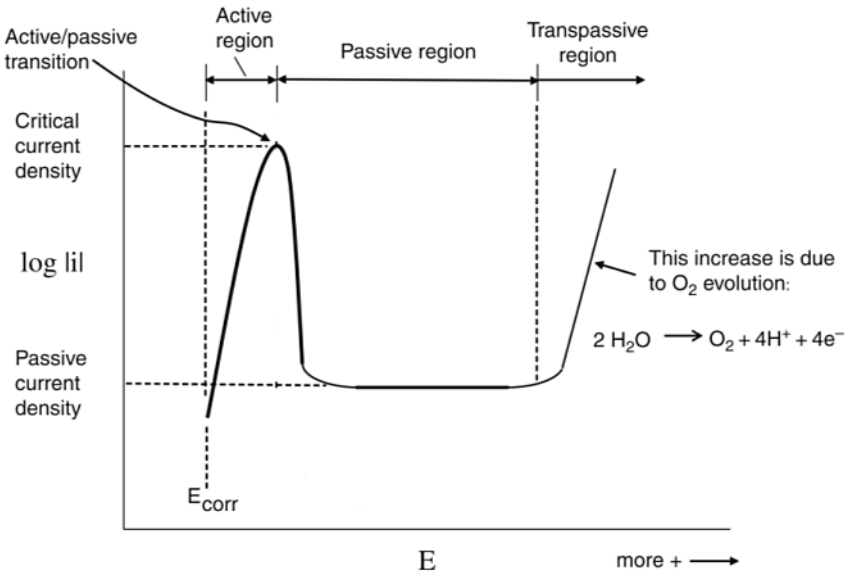

Figure 1-9. Anodic polarization of a metal with passivation. The potential reaches values which are sufficient for the evolution of oxygen. The increase in current is not because of corrosion of the metal.

Pitting corrosion and the dissolution of the passive layer may occur in potentials lower than the potential which is required for the evolution of oxygen [30]. It can be seen in Figure 1-10 and the DE line in Figure 1-8 that pitting in the presence of Cl^- ions may cause an increase in the current in the passive region. Pitting corrosion will be explained in Section 1.9.

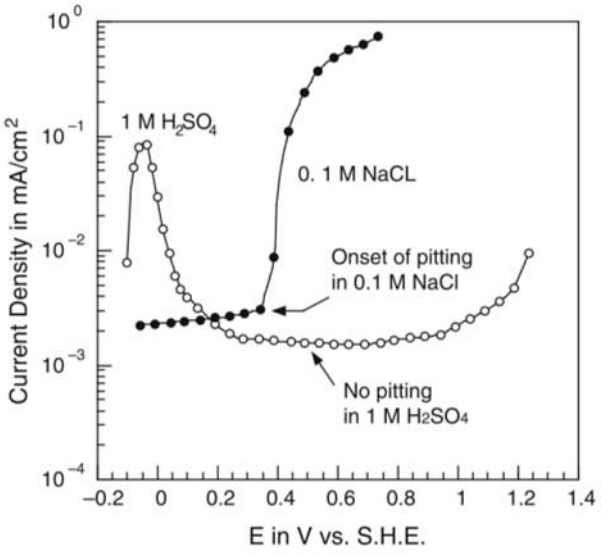

Figure 1-10. Anodic polarization for 18Cr-8Ni SS in two different solutions: 0.1 M NaCl or 1 M H_2SO_4. Pitting is only observed in the presence of chloride [30].

If pitting corrosion does not happen, the increase in anodic potential may lead to an increase in current density because of the dissolution of the passive film [30] (FG in Figure 1-8) [33], For example, Cr_2O_3 may be dissolved to form soluble ions (CrO_4^{2-}) [30]. The secondary passivation may cause a decrease in the corrosion rate as shown by the GH line in Figure 1-8. A further increase in anodic potential leads to the evolution of O_2 (Reaction 11) as shown by the HI line in Figure 1-8 [33].

Figure 1-11 shows the correlation between anodic polarization regions i.e. corrosion (active), passive and transpassive and Pourbaix diagram regions for Cr in pH 6.

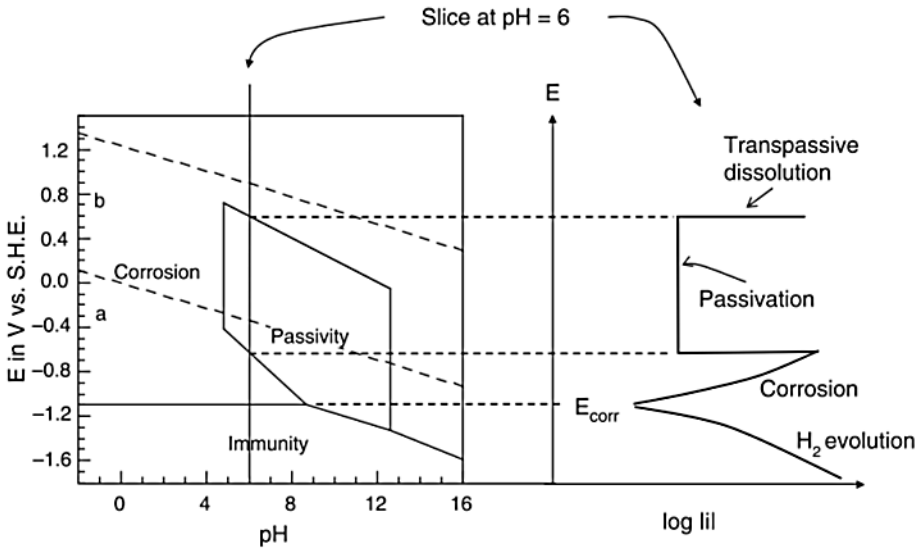

Figure 1-11. Correlation between the polarization curve and Pourbaix diagram for Cr at pH 6.

The pH of the solution can change the shape of polarization curves as can be seen in Figure 1-12. Both i_{crit} and E_{pp} are increased by decreasing pH [30].

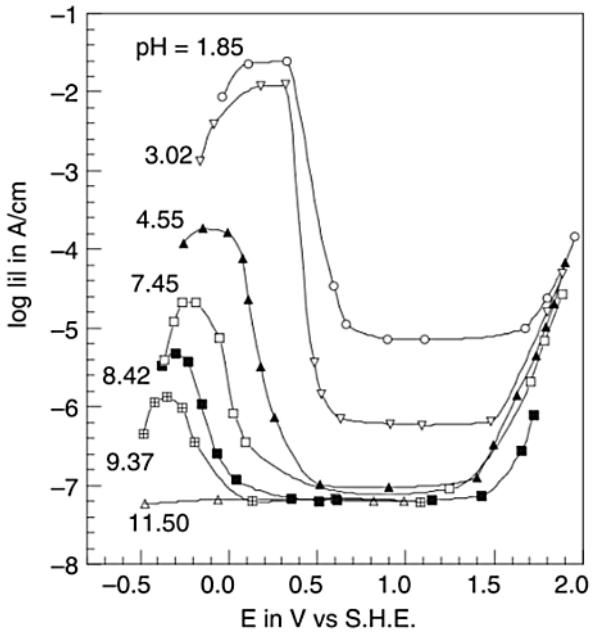

Figure 1-12. Polarization curves for Fe in phosphate solution with different pH [30].

Solutions with a higher acidity than the acidity of the aqueous phase in PEMFC have frequently been used in ex situ tests of bipolar plates. The result of these tests may not be consistent with long-term corrosion of bipolar plates in PEMFC. This will be discussed in more detail in section 2.5.1.

1.8 Evans diagrams

Combining plots of log|i| vs. potential for the cathodic and anodic reactions yields mixed potential diagrams also known as Evans diagrams. Figure 1-13 shows an example of an Evans diagram for the corrosion of a metal (M) in an acidic solution (dotted lines). In mixed potential plots, where the anodic diagram crosses the cathodic diagram, the anodic reaction rate is equal to the cathodic reaction rate. The potential at this point is called the corrosion potential (E_{corr}) and the current density at this point is corrosion current density (i_{corr}) [30, 31, 33].

Figure 1-13 also shows an idealized experimental polarization curve (solid lines); in experiments only the difference between the oxidation and reduction current is measureable ($i_{meas}= i_a - i_c$). E_{corr} and i_{corr} can be found by extrapolating anodic and cathodic Tafel lines [31, 33].

The mixed potential theory can be used to determine i_{corr} and E_{corr} in complex corrosion systems where several cathodic or anodic reactions are possible [28, 30, 31].

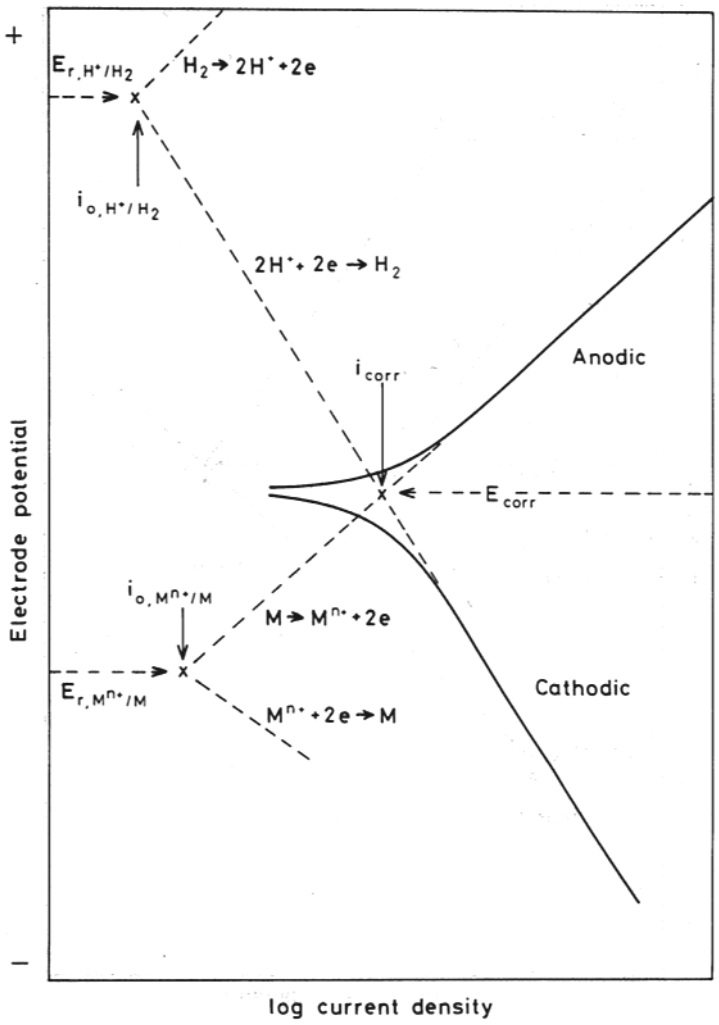

Figure 1-13. An example of an Evans diagram for the corrosion of a metal (M) in an acidic solution (dotted lines) and an idealized experimental polarization curve (solid lines) [33].

1.9 Localised corrosion of stainless steel

Localised corrosion is one of the important corrosion mechanisms for metallic bipolar plates in PEM fuel cells. Post-mortem investigation of 304 SS bipolar plate used in a single cell for 1000 h showed crevice corrosion and pitting corrosion on both anode side and cathode side of the bipolar plates [26].

1.9.1 Pitting corrosion

A pit initiates at sites at the surface such as grain boundaries and inclusions (particularly MnS inclusions); a pit also may initiate because of passive film breakdown [34-36]. After initiation, a pit starts growing with continuous dissolution of metal. At the beginning, the pit is metastable and then it may become stable which implies continuing growth of the pit, the metastable and stable stages of pitting can be investigated using polarization curves as shown in Figure 1-14 for a stainless steel. When the potential is in the metastable pitting range (Figure 1-14) the current shows peaks as can be seen in Figure 1-14 (right) and Figure 1-15 [37, 38].

These peaks or current transients indicate nano-scale or micro-scale pitting on the surface of stainless steel following by repassivation and are called metastable pits or unstable pits [35, 38]. The number of metastable pits, their growth period, and their height (levels of current) increase with increasing potential (Figure 1-14). Above a critical potential known as pitting potential (E_p), a pit undergoes continuous growth and is called a stable pit (Figure 1-14) [38].

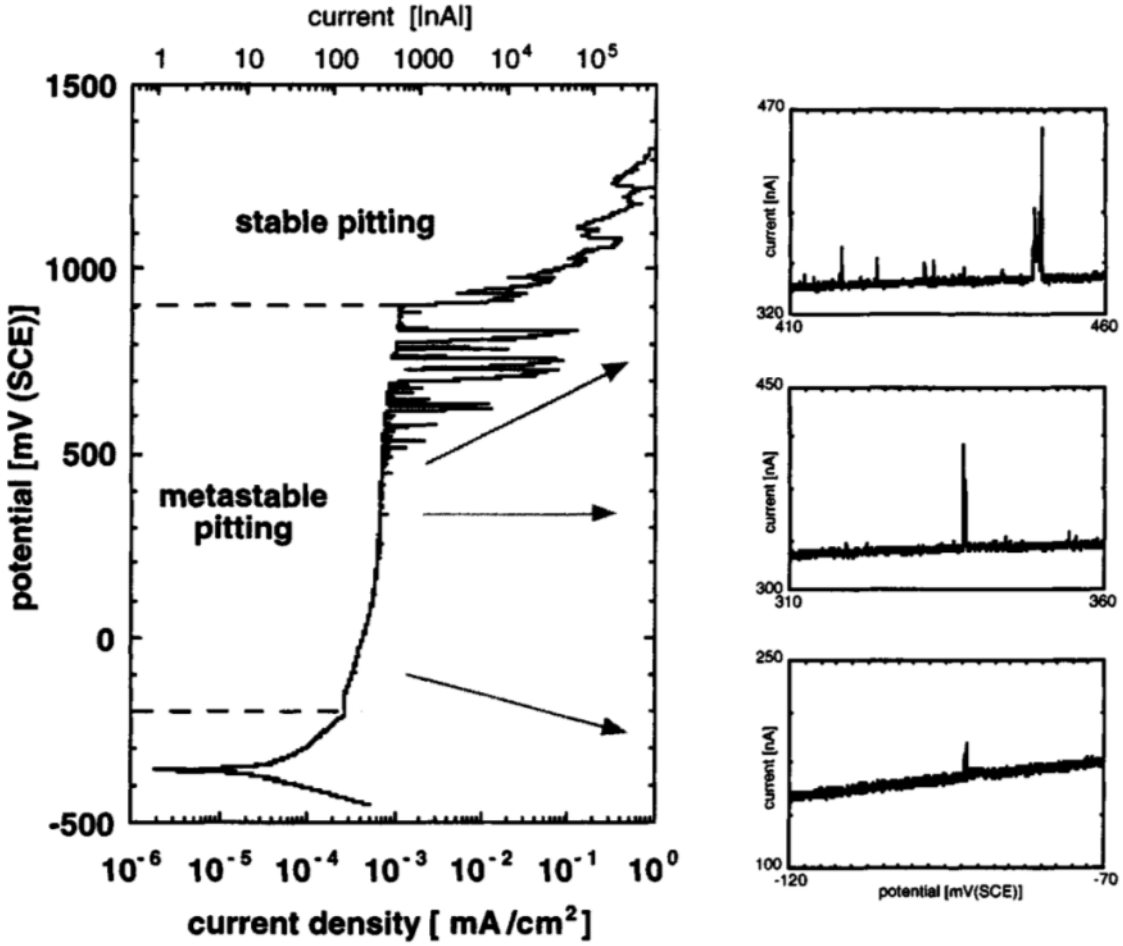

Figure 1-14. Potential-current curve of metastable and stable pitting for stainless steel with passive film in a solution containing chloride ions [38].

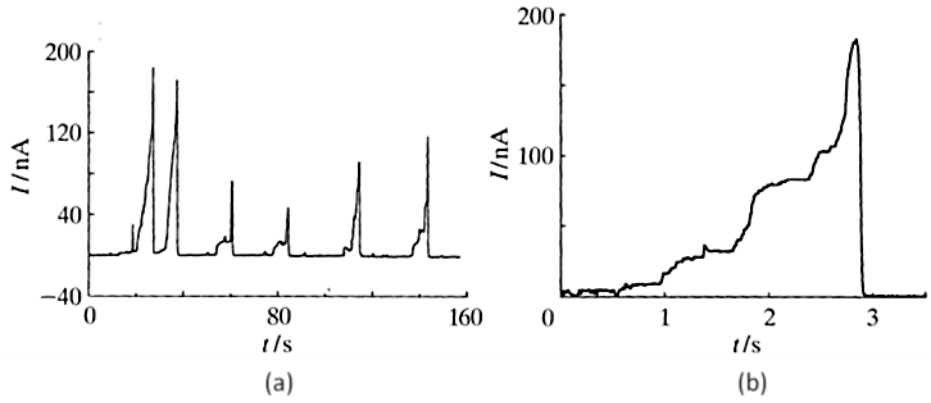

Figure 1-15. Current-time curves for (a) group of metastable pits (b) a metastable pit in an expanded axis [37].

The pitting potential (E_p) decreases with increasing temperature and chloride concentration [38]. It can be seen in Figure 1-16 that in a pit, the pH and chloride concentration are controlled by the concentration of metal ions through hydrolysis and electromigration to balance the charge of H^+ and cations, respectively [30, 35].

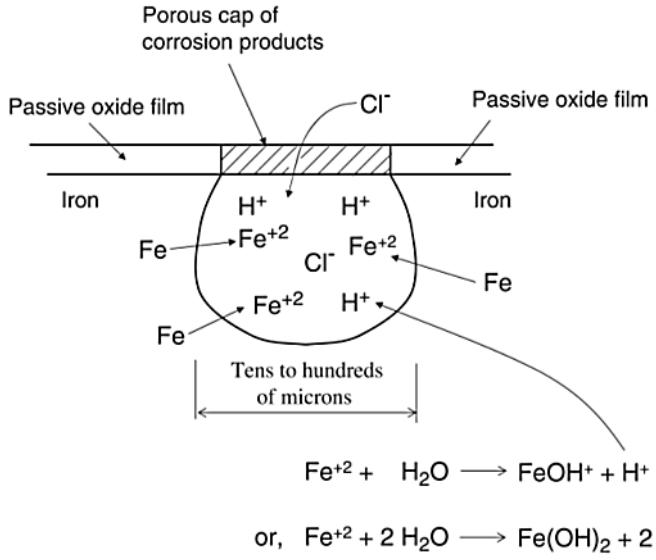

Figure 1-16. Pitting corrosion of Fe. Hydrolysis of Fe^{2+} ions inside a pit increases the acidity [30].

For pit growth, the concentration of metal ions should remain high enough inside the pit. The stable pits are usually covered by passive film or salt film which keeps the chloride concentration and metal concentration high enough inside of the pit [35, 39, 40] (see Figure 1-16). Metastable pits are usually covered by a passive film at the commencement and when the passive film ruptures metallic ions flow outside the pit then the pit walls repassivate and the pit stops growing [34, 35, 40].Therefore the passive film properties such as thickness can affect the growth and stability of pits [39, 41] and number of active pits [40].

Surface preparation affects the properties of the passive film on stainless steel, Isaacs et al.[40] have shown that the number of active pits depend on the surface preparation of 304 stainless steel such as electropolishing or oxidizing at high temperature. In Isaacs et al. [40]

study, electropolished and abraded stainless steel showed better pitting resistance than stainless steels oxidized at high temperature. A mechanically stronger passive film increases the number of active pits and decreases the rate of their death by keeping high concentration of metallic ions and chloride ions inside the pit [39, 42].

Gorse and Baroux [34] investigated metastable pitting of 430 type stainless steels with MnS inclusions and free of MnS inclusion using potentiostatic measurements. They found that the metastable pit current transient for stainless steel with and without MnS inclusions are different regardless of potential conditions as shown in Figure 1-17 [34, 36]. For stainless steels containing MnS, the inclusion dissolves and the pit grows so that the current increases and then because of rupture of the passive film or salt film over the pit, metallic ions inside the pit flows outside the pit and the concentration of metallic ions and chloride ions decreases inside the pit, consequently the pit walls quickly repassivate which causes a sharp current drop as can be seen in Figure 1-17 (a). For stainless steels without MnS, because of passive film breakdown in an area, stainless steel exposes to the solution without a protecting layer and a fast dissolution occurs at the beginning then the current decreases slowly because of passive film healing as shown in Figure 1-17 (b).

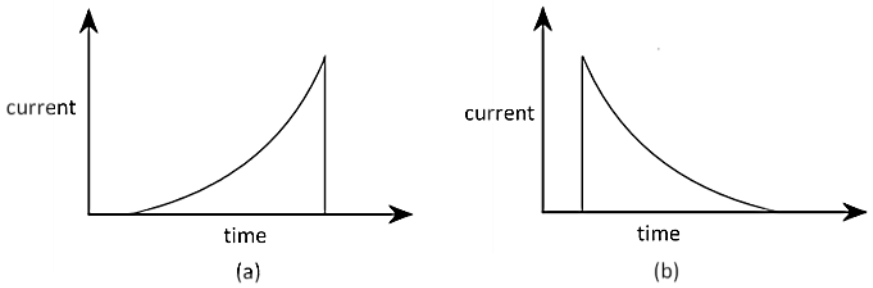

Figure 1-17. Current transient of metastable pits (a) stainless steel with MnS and (b) stainless steel free of MnS [34, 36].

Potential transient during metastable pitting is shown in Figure 1-18. The numbers in Figure 1-18 show stages of metastable pitting: at the beginning of metastable pitting (stage

1), the pit nucleates for example because of passive film breakdown and the potential starts to decrease, during (stage 2) the pit grows and the potential continues to decrease, at (stage 3) the pit stops growing and the potential stops decreasing and during (stage 4), the pit repassivates [36, 41, 43].

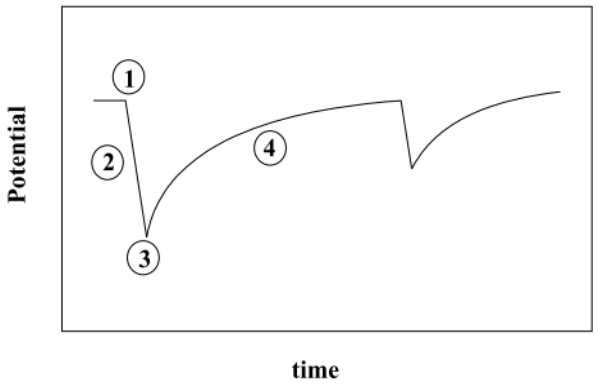

Figure 1-18. Stages of potential transient during metastable pitting [36]. Numbers show different stages of metastable pitting.

1.9.2 Crevice corrosion

Stack water is contaminated by corrosive ions from membrane degradation [8, 25, 44-47] and cations from corrosion of bipolar plates [23, 48]. There is flow of fuel and air in a PEM fuel cell which causes flow of the water in the cell; however, it is possible that water (electrolyte) remains in the shielded areas such as the crevice formed between GDLs and bipolar plates. If the electrolyte does not move or flow for a while in a crevice, the concentration of metallic ions from corrosion of the metal in the crevice increases. Therefore, in the crevice, similar to pitting corrosion, pH from hydrolysis of these metallic ions decreases and also the concentration of halide ions (with negative charges) such as chloride for balancing charge of these positive metallic ions increases (see Figure 1-19). This type of corrosion is known as crevice corrosion [49, 50]. Metallic bipolar plates which were

used in a laboratory single cell for 1000 h showed pitting corrosion on where bipolar plate was in contact with GDL [26].

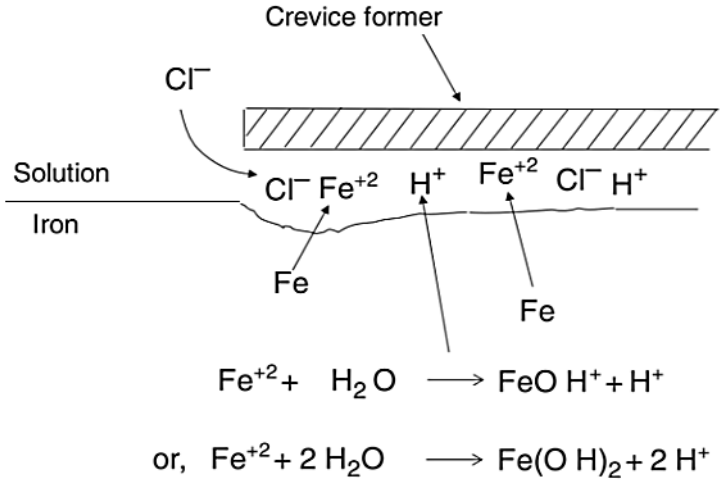

Figure 1-19. Crevice corrosion of Fe [30].

1.10 Galvanic corrosion

If an electrically conductive metal for example a bipolar plate is coupled to another electrically conductive material with a nobler potential such as a GDL and is exposed to an electrolyte such as the electrolyte of a PEM FC which contains corrosive ions [25], a galvanic current flows from metal (anode) to the nobler material (cathode). This causes an increase in the corrosion rate of the anode (bipolar plate) compared with the condition in which the metal and the nobler material are not connected. In the described condition, corrosion of the anode is known as galvanic corrosion. The ratio of the cathode surface area to anode surface area in galvanic corrosion is very important, increasing the ratio of the cathode surface area to the anode surface area increases corrosion of the anode [49, 50].

1.11 Effect of temperature on corrosion

During operation, the temperature inside a PEMFC is usually between 60 °C to 80 °C [1]. Depending on the situation, increasing the temperature may increase or decrease corrosion. The corrosion rate may increase with increasing temperature because the rate of electrochemical reactions and diffusion of ions in the electrolyte increase with increasing temperature. However, increasing temperature may decrease the humidity or may evaporate the electrolyte which may decrease the corrosion rate or stop it [51].

However, the inside of a PEMFC is always humid (> 90% [52]), and for such an environment, increasing temperature increases corrosion rates [9]. Therefore elevated temperature should be considered as an important factor when PEMFC environment is simulated for corrosion tests [53].

2 Literature review

2.1 Bipolar plates

Figure 2-1 shows a PEM fuel cell stack and its bipolar plates. Bipolar plates have flow field channels which are used to distribute reactants and eject produced water/vapour (Figure 2-1 (b) and (c)).

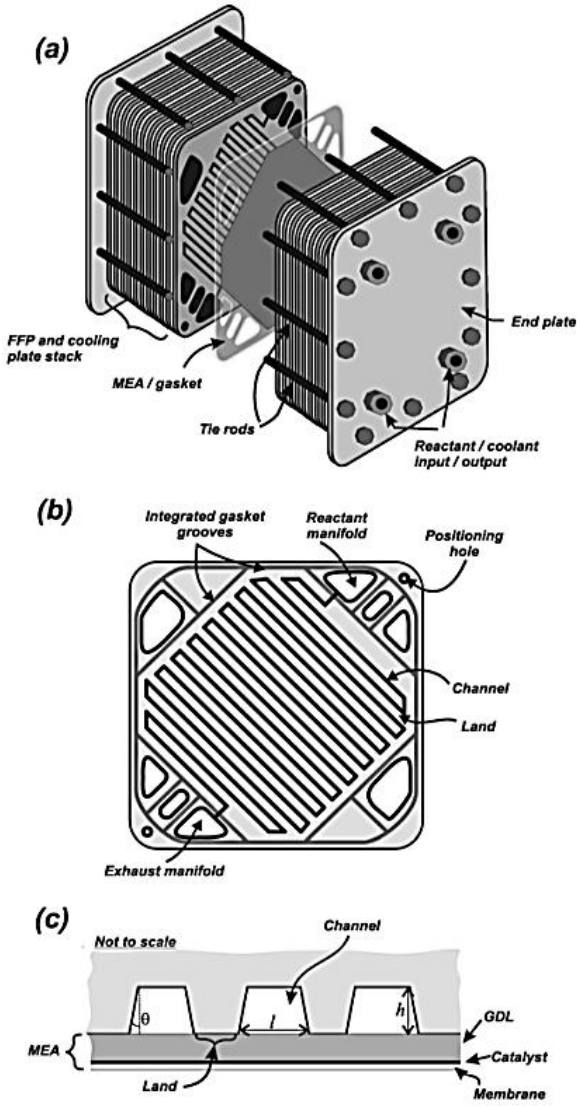

Figure 2-1. (a) a Fuel cell stack, (b) a bipolar plate, (c) cross section of flow-field channels and MEA [3].

Functions of the bipolar plates are removing heat, supplying mechanical strength to stacks, helping to make sealing with gaskets, and distributing and separating oxygen and hydrogen. Bipolar plates should have good electrical conductivity with low interfacial contact resistance (ICR) with the GDL to decrease ohmic losses and be thermally conductive to keep the stack temperature at acceptable levels. They also should be gas impermeable to prevent mixing of oxygen and hydrogen, easy to produce and not expensive. In addition, because the fuel cell environment is a very corrosive environment bipolar plates materials or coating should be corrosion resistant [1, 3].

Metallic bipolar plates are relatively inexpensive, very good thermal and electrical conductors, recyclable, mechanically reliable, impermeable to gas and they can be relatively easily produced in thin plates and potentially are therefore able to satisfy requirements of bipolar plates in PEM fuel cells [1, 3, 54]. However, most of the common metals are susceptible to corrosion in the PEM fuel cell environment and their corrosion can lead to deterioration of stack performance [1, 3].

2.2 The main details of the components which the ions can travel into and affect i.e. GDL properties, catalysts and membranes

Figure 2-2 schematically shows the different layers in a PEM fuel cell and their typical length scales for recently designed PEMFCs. The functions of these layers include the distribution of hydrogen and oxygen, the removal of the products of electrochemical reactions, and the provision of electrical and ionic connections [55].

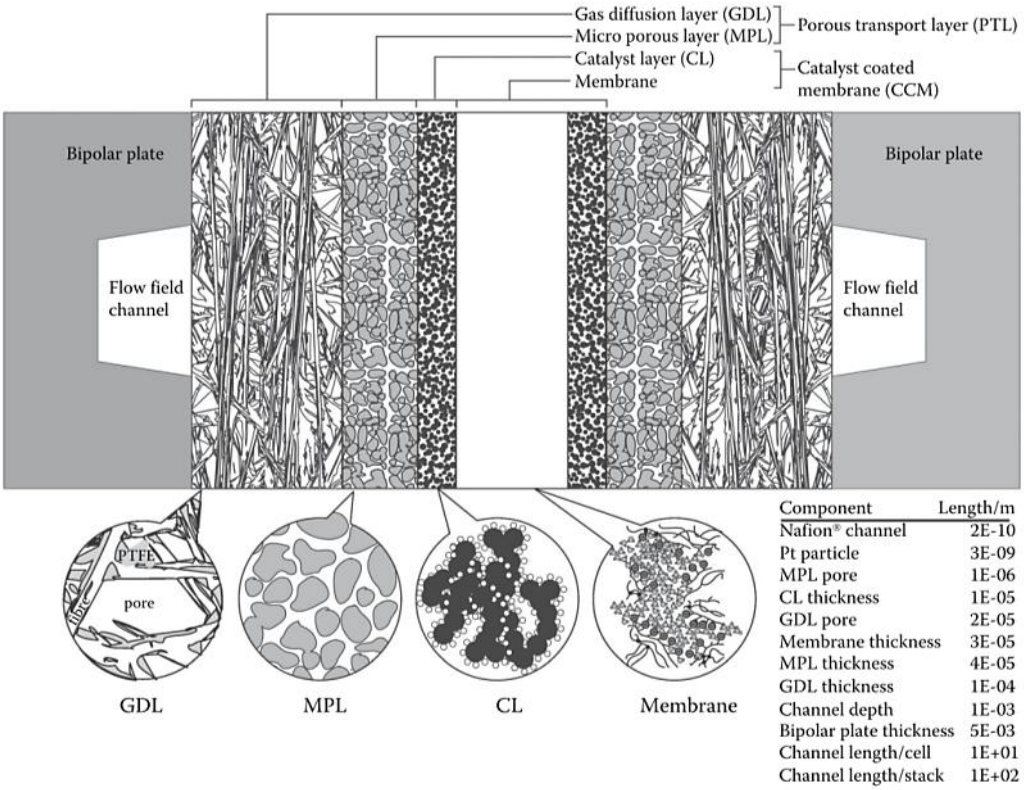

Figure 2-2. Different layers of a PEMFC [55].

2.2.1 The main details of membranes

The man purposes of a membrane in a PEMFC are conducting H^+ ions, preventing the mixing of hydrogen and oxygen and electrically separating anode and cathode [56]. One of the most famous membrane materials is Nafion. The chemical structure of Nafion is presented in Figure 2-3 [57].

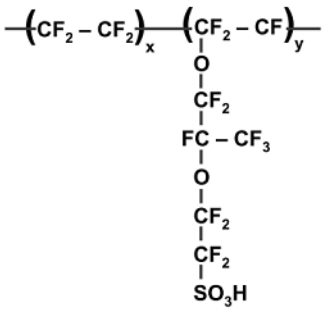

Figure 2-3. Structure of Nafion [57].

The backbone of Nafion is very hydrophobic. However, the end of the side chain (the SO_3H group) is very hydrophilic and Nafion is able to absorb up to 50 % Wt water. The SO_3^- ion and H^+ ion are ionically bonded in the SO_3H groups and protons can be conducted within well-hydrated regions of Nafion [57].

2.2.2 The main details of the catalyst layer

The thin (~ 5-15 µm [56]) catalyst layer is located between the membrane and MPL (Figure 2-2). There are three main components in the catalyst layer: an ionomer such as perflurousulfonate (PFSI), a catalyst and a hydrophobic material such as PTFE, as shown in Figure 2-4. Pt and Pt-alloys (with an area density of 0.3-0.4 mg/cm^2) are one of the most commonly used catalysts in PEMFCs. 4 nm or smaller particles of catalysts are used in order to enhance the surface area of the catalysts. These particles are dispersed on the surface of carbon particles (~ 40 nm) known as carbon support. The ionomer is also added to the catalyst particles and the carbon supports to provide a proton conduction path (Figure 2-4) [57].

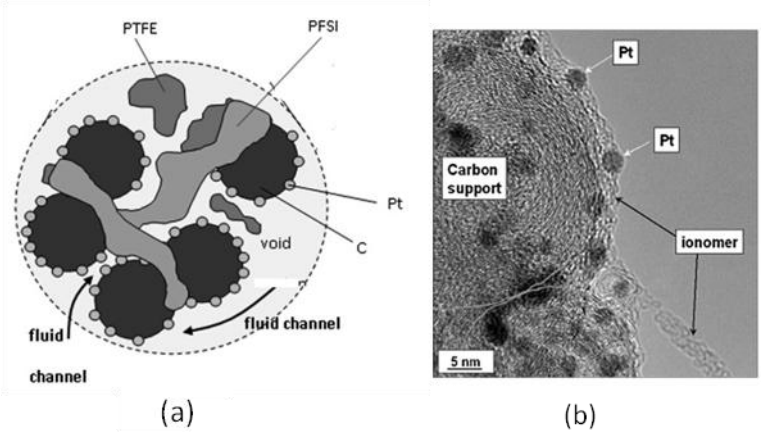

Figure 2-4. (a) Schematic of a catalyst layer, (b) TEM image of Pt particles on carbon support [58].

The electrochemical reactions of a PEMFC occur on the catalyst surface in the catalyst layer, where all species that are needed for these reactions (i.e. hydrogen or oxygen, H^+ ions and electrons) have access. These points are known as the three-phase boundary (boundary of solid, ionomer, and void phases) (see Figure 2-5) [56, 57].

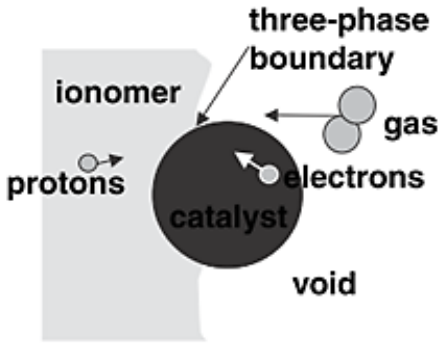

Figure 2-5. Three-phase boundary [57].

2.2.3 The main details of the GDL

Figure 2-6 shows the main function of GDL. GDL must be porous to provide the pathway for hydrogen and oxygen from the bipolar plate channels to the electrodes and for the generated water (vapor or liquid) in the cathode catalyst layer to the bipolar plate channels. The transport of the reactants and the generated water depends on the porosity and the hydrophobicity of GDL. Also, GDL must be electrically conductive to conduct electrons and thermally conductive to conduct generated heat from electrochemical reactions. In addition, GDL must be rigid enough to mechanically support MEA [57, 59].

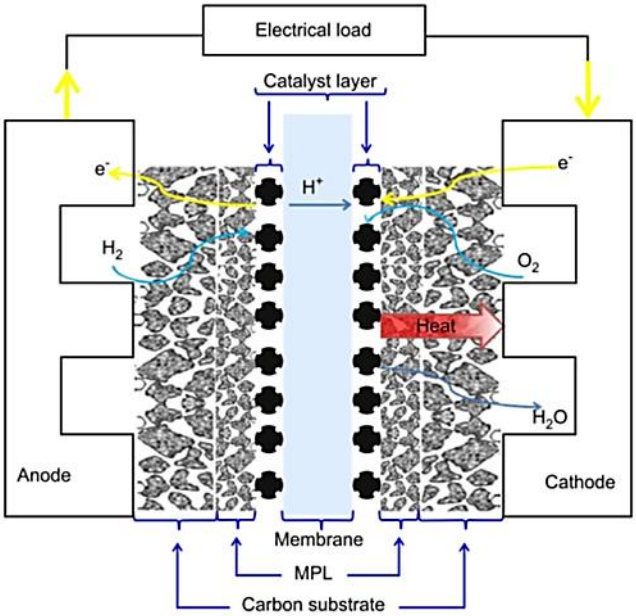

Figure 2-6. GDL (carbon substrate) main functions in a PEMFC [59].

To avoid the blockage of the GDL pores by water, they can be water-proofed by adding hydrophobic polytetrafluoroethylene (PTFE). Gas diffusion media (GDM) (GDL and MPL) are hydrophobic using 5% to 30% of PTFE loading. The thickness of GDLs produced by various companies is between 0.01 and 0.04 cm, their porosity is between 70% and 80% with pore size of 20 µm to 50 µm, and their density varies from between 0.21 to 0.73 g/cm^3. Figure 2-7 shows two types of GDLs i.e. carbon cloth and carbon fibre paper [57, 59].

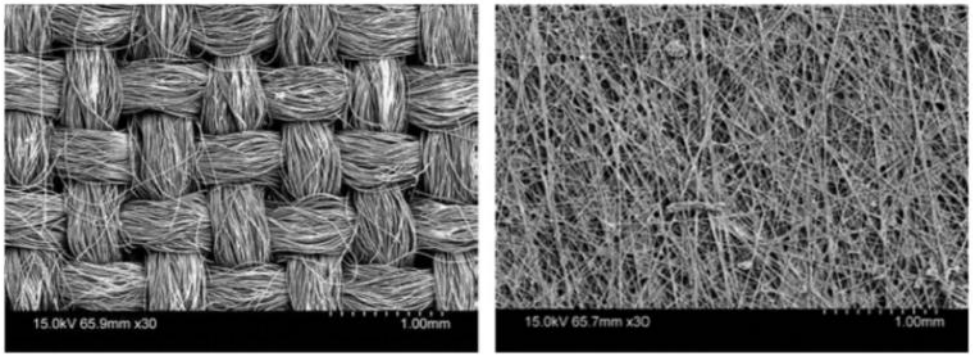

Figure 2-7. SEM image of a E-TEK carbon cloth (left) and a Toray carbon paper (right) [57].

2.2.4 The main details of the microporous layer

There is a hydrophobic MPL between the GDL and CL, which is a mixture of carbon particles and a PTFE binder. The hydrophobic agent (PTFE) varies from between 10 % and 45 % Wt. The pore sizes are between 0.1 µm and 0.5 µm. The main function of the MPL is to improve the wicking of generated water from the cathode CL into GDM [56, 57]. Properties of GDLs and MPLs from different well-known manufacturers and trademarks are summarized by El-kharouf et al. [59] and Barbir et al. [60].

There are randomly oriented cracks in the MPL as shown in Figure 2-8. These cracks have a considerable effect on water transport in MEAs [58, 61-70]. Hizie et al. [71] suggested that there is imperfect contact between the MPL and the CL (Figure 2-9). Water has a tendency to accumulate in the gaps between the CL and the MPL. These gaps are able to store significant (~ 6%-18%) amount of the entire water content in a PEM fuel cell. The size of the interfacial gaps in MPL/CL interfaces depends on the roughness and cracks of both the MPL and the CL (Figure 2-9) [71].

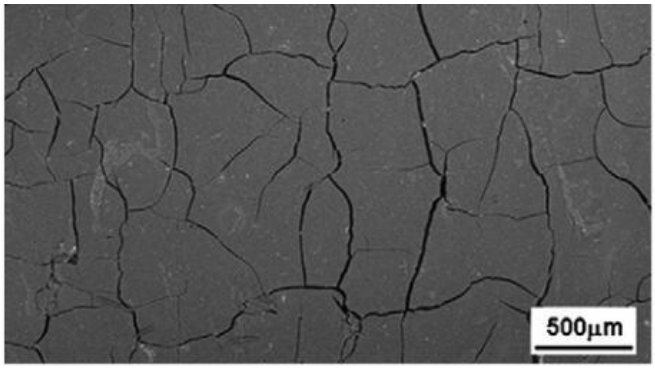

Figure 2-8. Plan view SEM image of MPL [61].

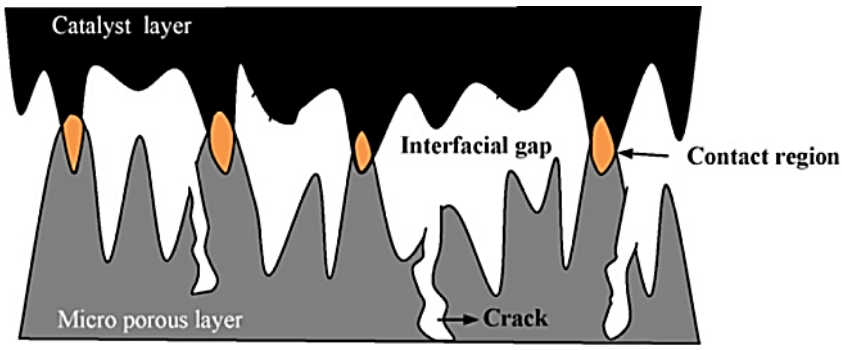

Figure 2-9. Schematic of the microporous layer/catalyst layer interfaces [71].

Defects in MPLs such as cracks and holes can be the main channels for transporting liquid water from the cathode CL to the interface between the MPL and GDL in the cathode [61-63, 67, 71, 72].

Distribution of liquid water in an operating PEMFC is shown in Figure 2-10. It can be seen that liquid water has a tendency to accumulate in the interface between the MPL and CL and then it mainly flows through the MPL cracks to the GDL [61].

Markötter et al.'s [62] in situ observation showed that liquid water presents in pores within the GDL, at channel walls and in MPL cracks as illustrated in Figure 2-11. They showed that there are liquid water transport paths through GDM starting from MPL cracks and ending at bipolar plate channels. When MPL cracks fill up with water, droplets arise in the GDL/MPL interface. These droplets form in the MPL cracks and detach from the GDL/MPL interface in a cyclic behaviour. The stream of air, hydrogen or other droplets carries away the detached droplets through the channel [62].

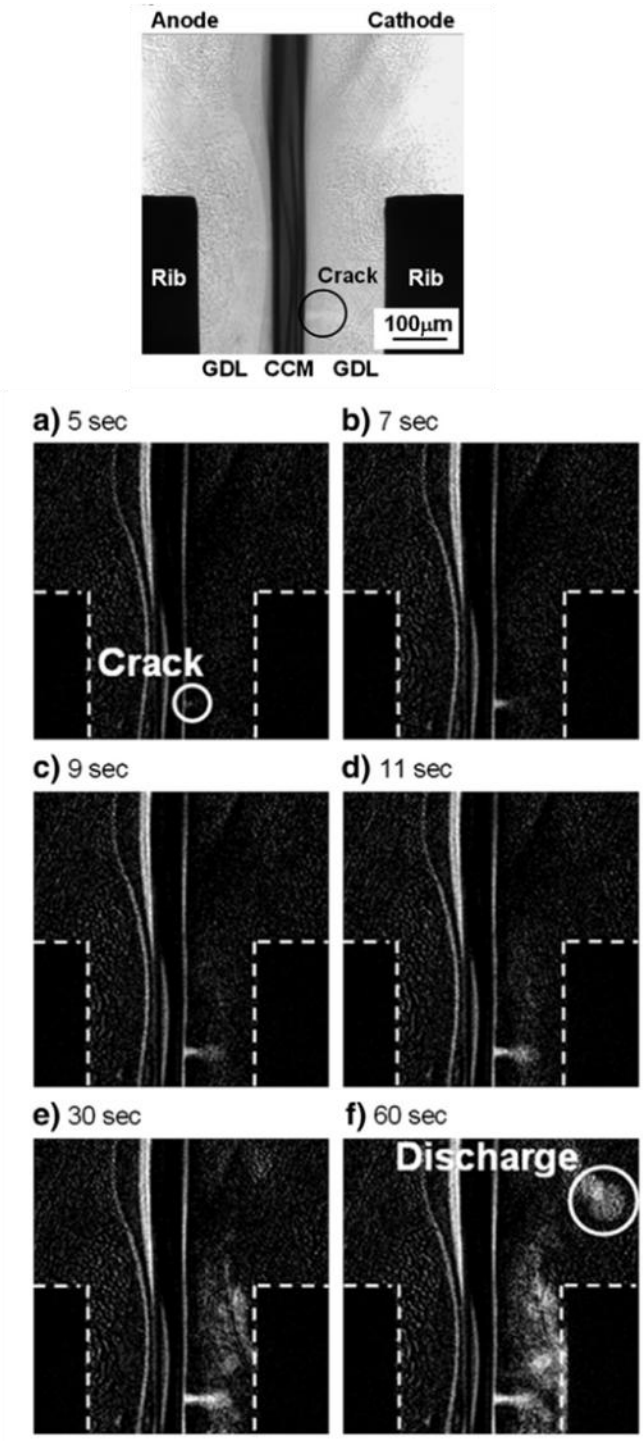

Figure 2-10. Distribution of liquid water in an operating PEM fuel cell. The image at the top shows the position of the anode side, the cathode side, the GDLs, the CCM (the membrane and the CL), a MPL crack, and the ribs. Liquid water is shown by the white colour in images (a) to (f) as a function of time. Liquid water accumulates in the MPL/CL interface and discharges through the MPL cracks to the GDL [61].

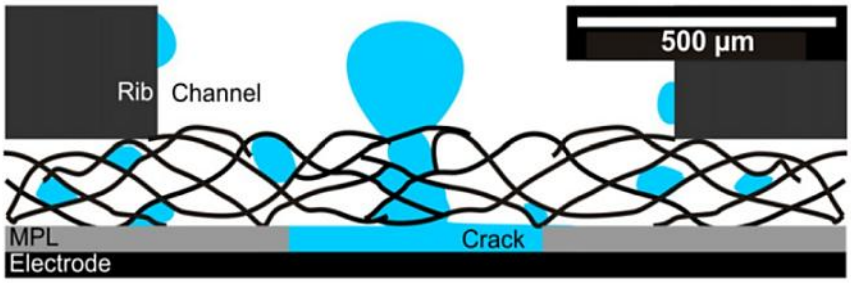

Figure 2-11. A droplet is formed in a crack in the MPL. Liquid water also presents in pores within the GDL and at channel walls. When MPL cracks fill up with water, droplets arise in the GDL/MPL interface [62].

2.3 Polarization behaviour of PEMFCs

Figure 2-12 shows a polarization curve of a PEM fuel cell and its different losses and regions.

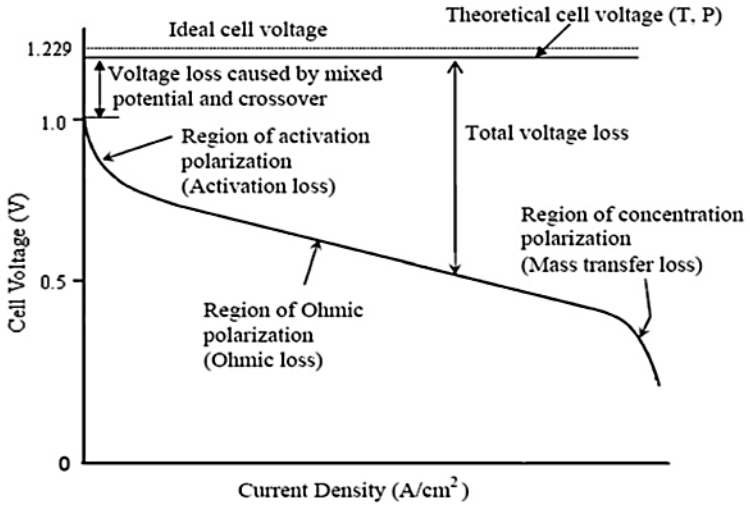

Figure 2-12. Characteristic polarization curve for a PEMFC [73].

If all available Gibbs free energy is used in the standard condition (i.e. 25 ºC, 1 atm) the ideal PEM fuel cell potential will be:

$$V_{cell}^{OCV}{}_{25\ °C,\ 1\ atm} = \frac{-\Delta G}{nF} = \frac{237{,}340}{2.96{,}485} = \frac{J\ mol^{-1}}{As mol^{-1}} = 1.229\ V \qquad (12)$$

The theoretical potential of anode, cathode and their difference (cell potential) are a function of partial pressure of products and reactants as well as temperature and for non-standard conditions can be calculated according to the Nernst equation. However, the measured cell potential for a PEM fuel cell is significantly lower than the potential that the Nernst equation suggests for a given temperature and pressure. The open circuit potential is typically 0.95-1.05 V which is about 20% less than the theory cell potential (1.23 V). This is because of different losses in the PEM fuel cells [73-75].

2.4 Voltage losses in PEM fuel cells

Figure 2-13 shows voltage losses as functions of the cell current. If the current generates, the cell potential decreases. The three losses are activation, ohmic (resistive) and concentration losses [76].

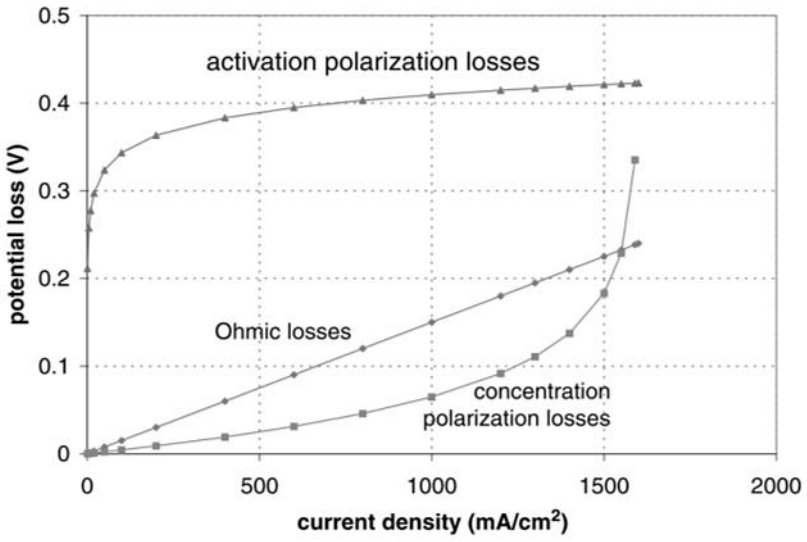

Figure 2-13. Voltage losses vs. cell current for a PEMFC [76].

2.4.1 Activation losses

The Butler-Volmer equation (Equation 8) shows that for generating current, some overvoltage is needed to overcome the activation energy of the reactions. The activation

losses occur in both anode and cathode and the Butler-Volmer equation can be used for both of them. At relatively high overpotentials, for anode, the reduction term (Equation 7) of the Butler-Volmer equation is negligible compared to the oxidation term (Equation 6), and for cathode the oxidation term is negligible compared to the reduction term [76, 77]. Among voltage losses in a PEM fuel cell, activation loss is the largest loss at any current density as shown in Figure 2-13 [76].

2.4.2 Ohmic (resistive) losses

There are resistances to the flow of ions and electrons through the fuel cell components which obey Ohm's law (V=IR). This causes losses which are known as Ohmic Losses. These resistances include ionic resistance in the membrane and electronic resistance in the bipolar plates, GDL, MPL, other electrically conductive components, and the interfacial contact resistance (ICR) at the GDL/bipolar plate interface. The most significant resistances are ionic resistance in the membrane and the ICR [76].

2.4.3 Concentration losses

Concentration losses are significant at high current densities. At high current densities, electrochemical reactions quickly consume reactants and these reactants cannot reach the catalyst surface quickly enough to satisfy the current's demand. Therefore, the concentration of oxygen or hydrogen on the catalyst surface decreases so that concentration gradients are established and the performance of the PEM fuel cells is limited by the reactant supply [76].

Figure 2-14 shows how activation, ohmic and concentration losses shape the actual polarization curve.

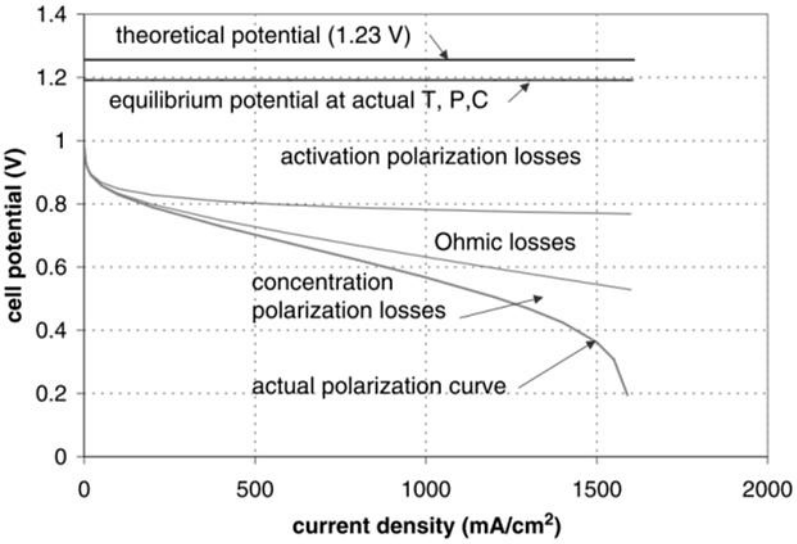

Figure 2-14. The polarization curve and different voltage losses [76].

2.5 Simulating the environment of PEMFCs for bipolar plate corrosion tests

The cell environment is wet, with both vapour and liquid water present. Any part of the bipolar plates which is in contact with aqueous phase could corrode. The environment pH is 3-6 [78] (there are also some reports of pH value 1–4 for the exhaust water [9, 79]) with the presence of F^-, SO_4^{-2}, and Cl^- ions [26, 78]. The reactions generate heat in the PEMFC; the PEMFC's operating temperature is usually 60 °C to 80 °C [1]. In addition, galvanic corrosion [25, 26, 80] and crevice corrosion [26] can happen between PEM fuel cell components. Such a wet, acidic environment at a temperature of about 80 °C with an air or hydrogen atmosphere is very corrosive for most of the commonly used metals [1, 3, 8, 54].

Contradictory results and conclusions have frequently been reported in previous works on the corrosion of bipolar plates. This could be because researchers have used very different solutions and test conditions [9, 78]. In the TSB project, the National Physical Laboratory (NPL) carried out several in situ measurements in PEMFC [27] to make sure that the correct

corrosion mechanism and environmental parameters were simulated in the ex situ corrosion tests which were designed and used in this PhD.

2.5.1 Solutions of ex situ corrosion experiments for bipolar plates

Different solution compositions have been used in the literature. Some of them are summarized in the tables that are available in the reviews of Antunes et al. [9] and Tawfik et al. [24, 52]. The cathode and anode environments have frequently been simulated with solution of 1m M to 1 M H_2SO_4 with the possible addition of 1m M to 0.01 M HCl, 0.01 M Na_2SO_4, or 2 to 15 ppm F^-. These solutions are bubbled by hydrogen to simulate the anode electrolyte and bubbled by air or oxygen to simulate the cathode electrolyte [9, 24, 52].

2.5.1.1 "Accelerated" and "simulated" solutions

There are two groups of solutions which are used in corrosion tests for bipolar plates: "accelerated" and "simulated" solutions. There are higher levels of anions and lower levels of pH values in "accelerated" solutions than those of the real stacks to accelerate corrosion in the ex situ tests. Examples of "accelerated" solutions are 0.5 M or 1 M sulphuric acid with 2 ppm F^-. However, for "simulated" solutions, the level of anions and pH are chosen close to those found in real PEMFC stacks [78] such as 1 mM H_2SO_4 , 1 mM H_2SO_4 + 10 mM HCL [26], 1×10^{-4} M F^- + 2×10^{-6} M Cl^- + 2×10^{-6} M SO_4^{2-} [78] and 1×10^{-5} M H_2SO_4 with 3×10^{-4} M F^- [53]. The source of F^- and SO_4^{2-} ions could be Nafion degradation. Cl^- ions could exist as pollution in the hydrogen and air [26].

Most researchers use "accelerated" solutions, however, "simulated" solutions are more realistic for the PEMFC environment. The corrosion of stainless steel depends on its passive film which can be affected by pH, solution composition, and applied potential during

polarization tests [78] (see Section 1.7). Therefore, corrosion tests in solutions with very low pH could change the passive layer in a manner that might never exist in a real PEMFC [81].

In a PEM fuel cell, there are the GDL and MPL between the bipolar plates and the Nafion membrane and therefore the bipolar plates are not in direct physical contact with the highly acidic Nafion membrane. However, it is very common to use solutions with about 1.0 - 0.5 M sulphuric acid and a few ppm fluoride ions to simulate the acidity of the Nafion membrane [27]. Recently, research groups tend to use more dilute and less acidic solutions based on exhaust water from stacks or single cells.

Hinds and Brightman [27] carried out in situ measurements of acidity at the surface of bipolar plates. Their results showed that pH for cathode and anode was in the range of 3-4 and 5-7, respectively.

2.5.1.2 The effect of adding ppm levels of fluoride ions to solutions

Yang et al. [53] reported that the corrosion current increases when 3×10^{-4} to 5×10^{-3} M F^- are added to 1×10^{-5} M H_2SO_4 in a simulated PEMFC anode environment. However, Laedre et al. [81] showed that adding 2 ppm F^- did not considerably affect corrosion rates. Mele et al. [26] reported that the effect of adding 15 ppm F^- to 1 mM H_2SO_4 on corrosion rates is negligible. In addition, F^- ions are less corrosive than Cl^- ions and F^- in the presence of Cl^- functions as an inhibitor [26]. In situ measurement of F^- showed that the concentration of this ion was lower than 2 ppm (the detection limit) in an operating PEMFC [27].

2.5.2 Temperature and time of ex situ corrosion experiments for bipolar plates

During PEMFC operation, the temperature increases to about 80 ºC and for the rest of the time the bipolar plates are at room temperature. These temperature cycles cause localized wet and dry cycles for droplets on the bipolar plates' surface. This may increase the

concentration of corrosive ions and acidity through evaporation [27]. The time of the corrosion test should be long enough to allow the passive layer of metal to fully develop and reach its steady state condition [79] (See section 1.11).

2.5.3 The estimate of the voltage range for bipolar plates in PEMFCs and first in situ measurements of corrosion potential for bipolar plates

Interfacial potential affects corrosion rates and thus the interfacial potentials between bipolar plates and their adjacent aqueous phase in PEMFCs should be considered when the PEMFC environment is simulated. It is assumed that the corrosion potential of flow field plates is approximately the potential of the nearest catalyst layer in an operating stack. However, in the TSB project, the first in situ measured corrosion potential for bipolar plates in PEMFC (measured by NPL) revealed that the corrosion potential of flow field plates is not significantly dependent on the potential of the nearest electrode [27]. This will be discussed in more detail in the following sections (also see Section 6.7.2).

2.5.3.1 The estimate of the voltage range over which bipolar plates operate in the anode and cathode environments of PEMFCs

Shores and Deluga [79] estimated that the potential of a flow field plate is mainly determined by the nearest electrode during current generation in fuel cells. The difference between the potential of bipolar plates and the potential of the nearest electrode is the Ohmic drop (IR) mainly because of contact resistance. In order to improve overall stack performance the contact resistances are low, as a result the potential of the bipolar plate and the nearest electrode are almost the same. When no current generates, the electrode do not

affect the bipolar plate potential and the local chemical environment determines the corrosion potential of the bipolar plate [79].

Potentials of both anode electrode and cathode electrode depend on cell current. It can be seen in Figure 2-15 that the potential of the cathode electrode decreases and the potential of the anode electrode increases when the cell generates a higher current [79, 82].

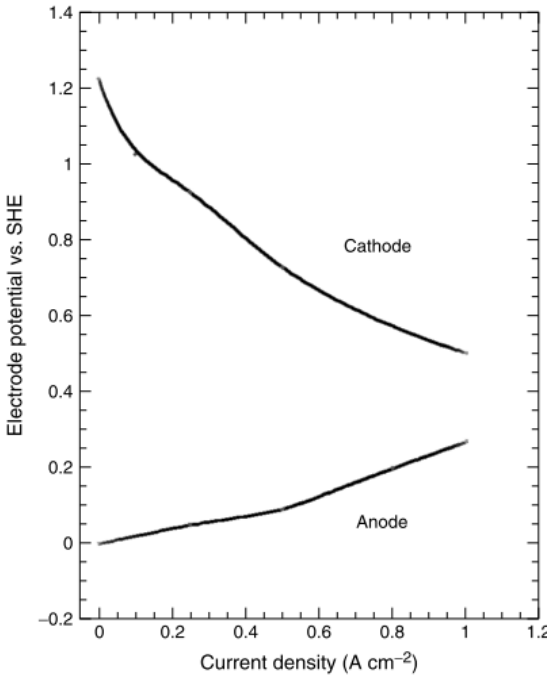

Figure 2-15. The potential of the anode electrode and the cathode electrode in a PEMFC plotted against the cell current density [79].

2.5.3.2 First in situ measurements of corrosion potential for bipolar plates in PEMFCs

NPL in situ results for 316L SS bipolar plates in operating PEMFCs are shown in Figure 2-16 to Figure 2-19.

Figure 2-16 and Figure 2-17 show the effect of altering cell current density and cell potential on the corrosion potential of bipolar plates in anode and cathode of PEM fuel cells, respectively [27].

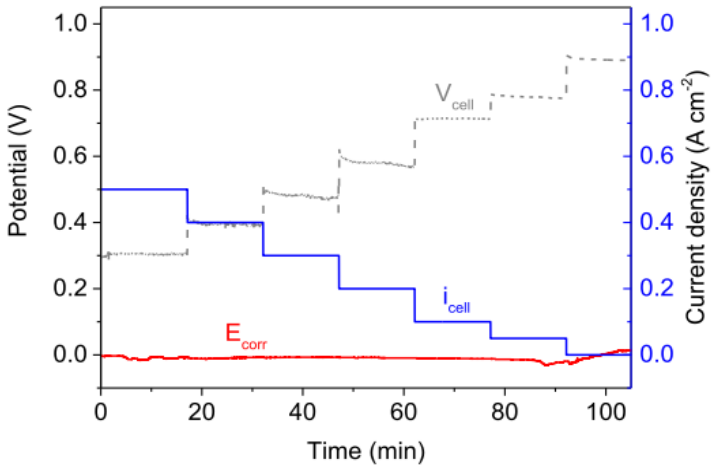

Figure 2-16. In situ measured corrosion potential (E_{corr}) (vs. RHE) for a 316L SS bipolar plate in anode of a PEMFC. The effect of changes in cell potential and cell current density [27].

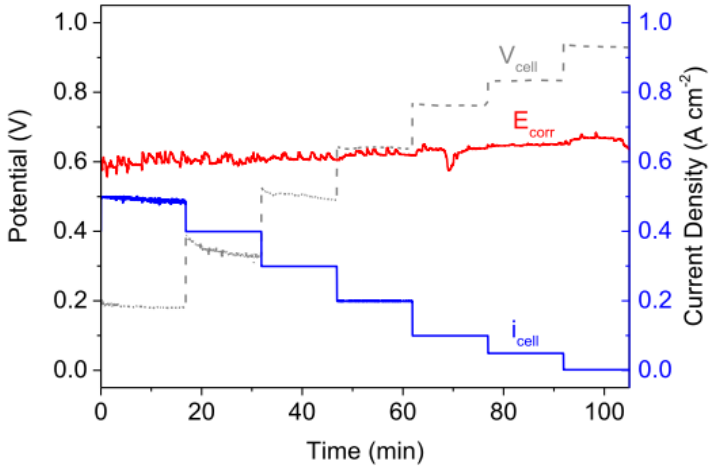

Figure 2-17. In situ measured corrosion potential (E_{corr}) (vs. RHE) for a 316L SS bipolar plate in cathode of a PEMFC. The effect of changes in cell potential and cell current density [27].

It can be seen in Figure 2-16 and Figure 2-17 that the cell current density was changed from 0.5 A.cm^{-2} to 0.0 A.cm^{-2} and the cell voltage was changed from 0.3 to 0.9 V vs. RHE. However, the in situ measured corrosion potential of the anode bipolar plate and that of the cathode bipolar plate were almost constant and about 0.0 V and 0.6 V vs. RHE, respectively.

Figure 2-18 and Figure 2-19 show the effect of the cell current density (and the cell voltage) cycling between 0.0 A.cm^{-2} and 0.5 A.cm^{-2} on in situ measured corrosion potential

of bipolar plates. It is obvious that these cycles and sudden changes in the potential and current of the cell do not show significant influence on the in situ measured corrosion potential of the bipolar plates.

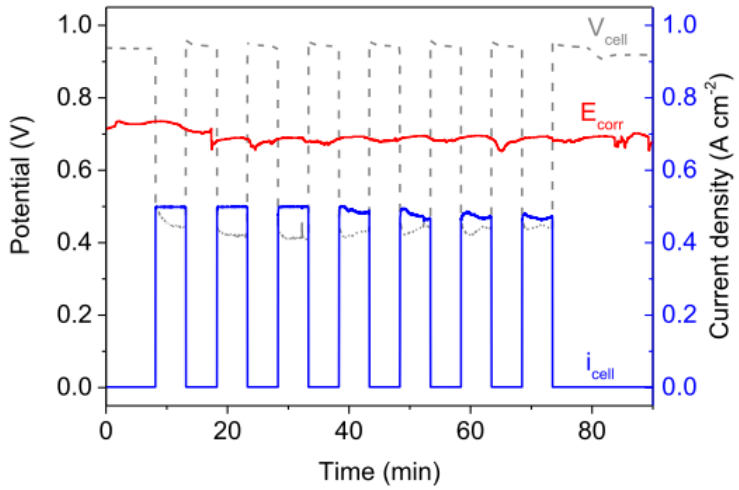

Figure 2-18. In situ measured corrosion potential (E_{corr}) (vs. RHE) for a 316L SS bipolar plate in cathode of a PEMFC. The effect of current (potential) cycling [27].

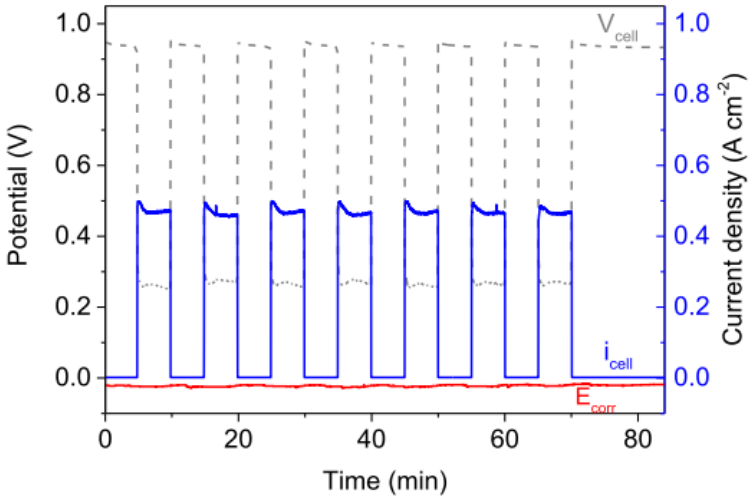

Figure 2-19. In situ measured corrosion potential (E_{corr}) (vs. RHE) for a 316L SS bipolar plate in anode of a PEMFC. The effect of current (potential) cycling [27].

Because the GDL and MPL are hydrophobic there is a very limited continuous aqueous phase between the bipolar plates and catalyst layers. Thus during operation of PEM fuel

cells, the low ionic conductivity between bipolar plates and CLs causes the corrosion potential of bipolar plates to be different from the potentials of the nearest CLs (see Section 6.7.2) [27].

2.5.4 Combined effects of crevice and galvanic corrosion in PEM fuel cells

The GDL is in electrical contact with the bipolar plate and there is enough wetting in the GDL/bipolar plate interface to consider that galvanic corrosion happens between the GDL and bipolar plate. The values of the in situ measured corrosion potential for bipolar plates confirmed that galvanic corrosion happens between the MEA and bipolar plates in PEMFCs [27]. The metallic bipolar plate acts as an anode and the MEA acts as a cathode in a galvanic cell. Carbon fibres provide a large surface area for the cathodic reaction and this high cathode surface-to-anode surface ratio can further increase corrosion rates see also Section 1.10).

MEAs are pressed to bipolar plates to decrease the interfacial contact resistance. This action can form a narrow crevice between MEAs and bipolar plates. Therefore, both galvanic corrosion and crevice corrosion may simultaneously occur in a PEM fuel cell between MEAs and bipolar plates (see also Sections 1.9.2).

2.6 Corrosion testing of bipolar plates

The PEMFC environment is too complicated to be exactly simulated in an out-of-stack corrosion test. Therefore, for validating the long-term durability of a bipolar plate in a stack, it is recommended that the bipolar plate is tested in the same stack for long times [79]. However, this is very expensive and time-consuming. Consequently, researchers have tried to use ex situ corrosion tests in the simulating environments to comparatively discriminate candidate materials [79, 83].

2.6.1 Weight change

In this method, a candidate bipolar plate is exposed to a simulated or real PEMFC environment and then the corrosion rate is assessed by measuring the weight change of the sample. However, this method has disadvantages: the weight changes can be negligible and additionally the process of cleaning the used bipolar plate may significantly affect the measured corrosion rate [79].

2.6.2 Use of potential-pH diagrams for predicting the corrosion behaviour of metallic bipolar plates in PEMFCs

Potential-pH diagrams have been used to predict corrosion behaviour and corrosion products for 6061 aluminium alloy, A36 steel, pure titanium [84], Fe and Au [85] in anode and cathode environment of PEM fuel cells.

Wang et al. [84] considered that pH was in the range 0-3.5 for both anode and cathode, and potential was -0.1 V vs. SCE for anode and 0.6 V vs. SCE for cathode. The predictions from potential-pH diagrams correlated well with both potentiostatic results and SEM images of samples after potentiostatic tests [84].

Kumar et al. [85] used a pH range of 3 to 5 and a voltage range of 0.0 to 1.2 V vs. RHE for predicting the corrosion behaviour of Au and Fe in PEM fuel cells. They predicted the stable forms of Fe would be Fe^{2+} and Fe_2O_3, and ICR would increase as a result of the formation of Fe_2O_3. However, Au would be mainly in the immunity region. These predictions were consistent with the polarization results.

2.6.3 Cyclic polarization

Figure 2-20 shows a cyclic polarization curve. This method is used by Mele et al. [86] to study the localised corrosion of bipolar plates. The direction of polarization is shown by the arrows on the curve. The intersection of the forward and backward scan is known as

protection potential (E_{prot}). At potentials lower than E_{prot} , stable pits do not initiate and existing pits are not able to grow. For potentials between E_{pit} and E_{prot} the existing pits can grow but stable pits can not initiate. At potentials higher than E_{pit} , stable pits can initiate and grow.

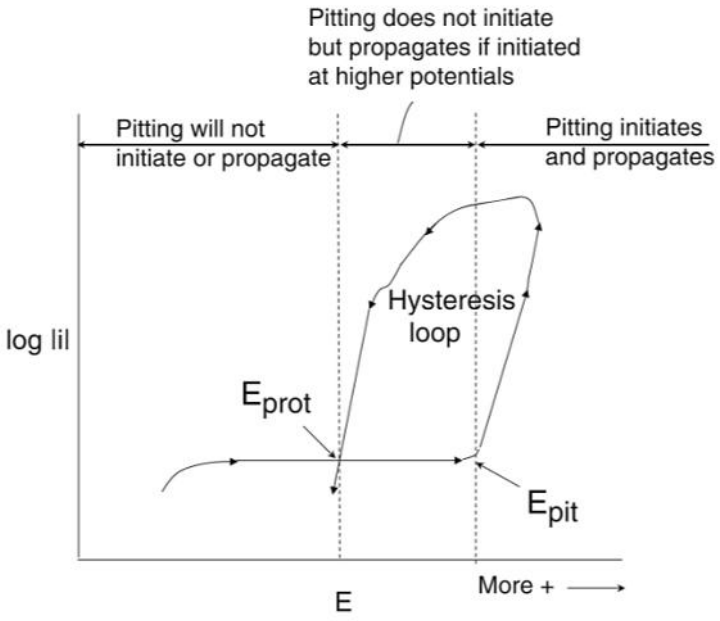

Figure 2-20. A cyclic polarization curve [30].

2.6.4 Polarization resistance

Polarization resistance is also used for evaluating bipolar plates [79, 87-89]. However this method is not used as frequently as potentiostatic and potentiodynamic measurements. Figure 2-21 (top) shows a plot of $\log|i|$ vs. E. If the same data is plotted for current density in linear scale vs. E, and the net cathodic current and the net anodic current are plotted as negative and positive current, respectively, then for a limited range (±10 mV [79]) the graph is almost linear, as shown in Figure 2-21 (bottom) [30].

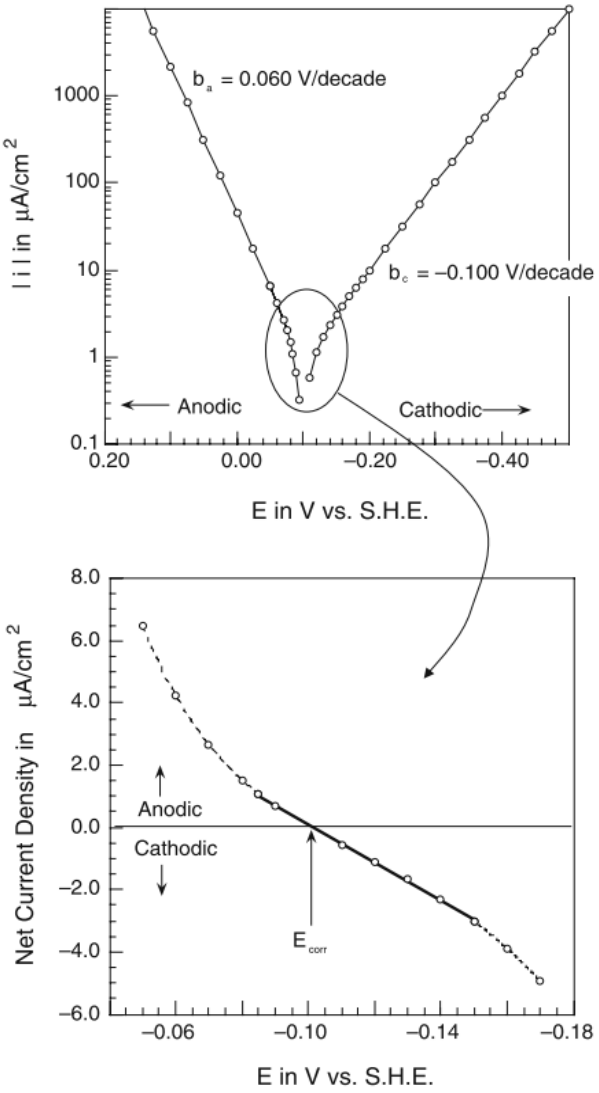

Figure 2-21. log|i| vs. E. (top). For the bottom image, the same data from the top is plotted in linear scale and the net cathodic current and the net anodic current are plotted negative and positive, respectively [30].

It can be shown that for a limited polarization from corrosion potential [30]:

$$R_p = \frac{\Delta\eta}{\Delta i} = \frac{\beta_a \beta_c}{2.3 i_{corr} (\beta_a + \beta_c)} \quad (13)$$

And i_{corr} is:

$$i_{corr} = \frac{\beta_a \beta_c}{2.3\, R_p (\beta_a + \beta_c)} \quad (14)$$

The slope of graph ($\frac{\Delta\eta}{\Delta i}$) is known as the polarization resistance (R_p) and this method is known as linear polarization. This method is easy to use and it measures the i_{corr} at the natural corrosion potential in the simulated environment [30, 31, 87-89].

2.6.5 Potentiodynamic and potentiostatic measurements

Potentiodynamic and potentiostatic measurements are frequently used to assess the corrosion resistance of bipolar plates. Some of these works have been summarised in the reviews of Antunes et al. [9] and Tawfik et al. [24, 52].

2.6.5.1 The link between the voltammetry and the voltage range over which a fuel cell operates

Figure 2-22 shows the relationship between a voltammetry curve for stainless steel in an acidic solution (left) and polarization curves for an anode electrode and a cathode electrode in a PEMFC (right) [55].

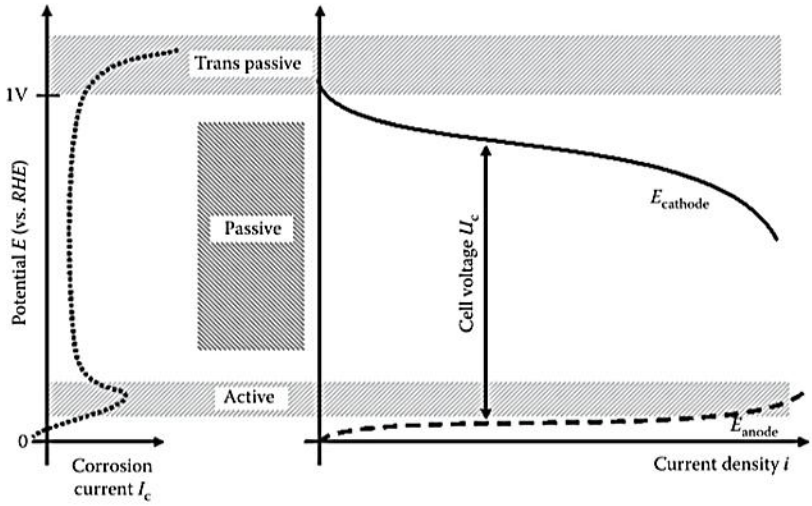

Figure 2-22. The link between a voltammetry measurement for stainless steel in an acidic solution (left) and polarization curves of an anode electrode and a cathode electrode (right) in a PEMFC [55].

Brett et al. [3] suggested the voltage ranges of 0.0 to 0.3 V and 0.5 to 1.1 V (vs. SHE) for anode and cathode electrodes in operating PEMFCs, respectively, as shown in Figure 2-23.

Assuming that the bipolar plates and the nearest electrode have almost the same interfacial potential, an ideal alloy or metal for bipolar plates should show passivation at the abovementioned voltage ranges. Thus the metal active/passive transition potential should be less than the open circuit potential of the anode electrode and its passive/transpassive transition potential should be higher than the open circuit potential of the cathode electrode [3, 79]. (See Sections 2.5.3.2 and 6.7.2).

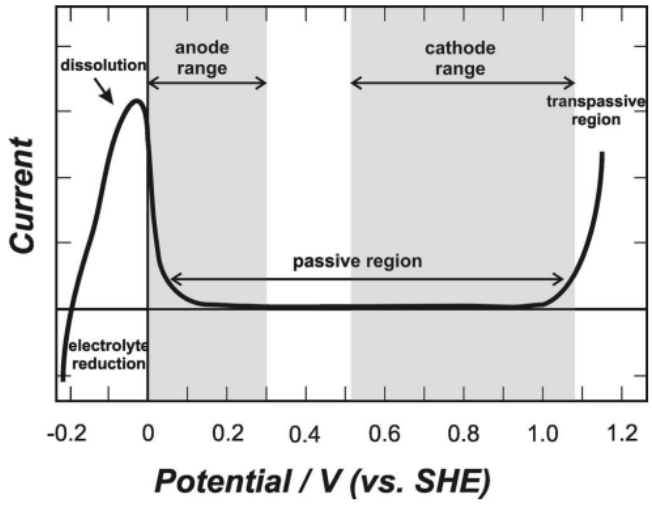

Figure 2-23. The potential range of the anode and the cathode during PEM fuel cell operation along with a potentiodynamic curve for stainless steel in an acidic solution [3].

2.6.5.2 Potentiodynamic and potentiostatic measurements for bipolar plates

For both potentiodynamic and potentiostatic measurements, a three-electrode set-up (see Section 1.6) in an environment which simulates fuel cell conditions (see Section 2.5) is used to measure the corrosion current density for applied potentials [90]. For potentiodynamic measurements, the applied potentials cover the potential range over which a fuel cell

operates (see Section 2.6.5.1). For potentiostatic voltammetry, a constant potential (0.1 vs SHE and 0.8 vs SHE for simulating anode potential and cathode potential, respectively) is applied [90].

Laboratory corrosion tests such as polarization resistance and potentiodynamic measurements are easier, faster and cheaper than running stacks or fuel cells. However, passive layers need some time to develop and reach their steady state condition and therefore the measured corrosion rates of a metallic sample using polarization resistance or potentiodynamic methods in a short period of time might not present realistic corrosion rates in PEMFCs [79, 91].

Therefore, potentiodynamic measurements alone can possibly be misleading for predicting the long-term performance of a bipolar plate in PEM fuel cells [14, 79, 91]. Potentiodynamic tests provide a quick preliminary assessment which should be confirmed with a long-term potentiostatic [90, 91] and in-stack tests [79]. Long-term measurements with enough time for the full development of the passive film provide a better prediction for bipolar plate behaviour in operating PEMFC conditions [79, 91].

2.6.6 Crevice corrosion and galvanic corrosion measurements for bipolar plates

The galvanic current between a 316L SS and a MEA in a solution with the composition of stack exhaust water at 60 °C has been measured using a Zero Resistance Ammeter (ZRA). The results revealed that galvanic corrosion rates are considerable in a PEM fuel cell [25].

Galvanic crevice corrosion between a porous carbon material (reticulated vitreous carbon (RCV)) and a 304 SS in 1 mM H_2SO_4 and 10 mM HCl solution has been investigated using potentiodynamic and potentiostatic measurements of the couple. The results showed a higher current density for the coupled RCV/304 SS than the uncoupled 304 SS [26].

The combination of galvanic corrosion and crevice corrosion in PEM fuel cells has also been studied using immersion tests. A 304 SS (as control) and a 304 SS/RCV couple were immersed in an aerated 0.5 M H_2SO_4 solution for 3 months. The control sample did not show any signs of localized corrosion. However, pitting was observed where the 304 SS was in contact with carbon-based material (i.e. the RCV). These pits were created by localised galvanic-crevice corrosion in the RCV/stainless steel contact areas [26].

These above mentioned studies and NPL's in situ measurements have shown that galvanic-crevice corrosion should be considered in simulating PEMFC environments for ex situ corrosion tests [25-27]. However, none of the published works have considered all the requirements for simulating corrosion conditions in PEMFCs. In this PhD, an electrochemical cell is designed which simulates all the requirements (see Section 6.7.1).

2.7 The mechanisms of degradation that can possibly be caused by the corrosion of metallic bipolar plates

One of the main disadvantages of metallic bipolar plates is that they corrode in a PEMFC environment and corrosion products affect the performance and durability of the bipolar plates and the other components [3].

The corrosion of bipolar plates may cause the formation of holes or cracks in bipolar plates. This leads to the mixing of hydrogen and oxygen which may result in an explosive condition or stack shutdown [79, 92]. In addition, corrosion may increase interfacial contact resistance (ICR) [12, 14-16] and the metallic ions which are released from corroding bipolar plates may contaminate the membrane or catalyst.

All of these corrosion effects lead to a deterioration in stack performance. In the stack water, the metallic ions may form oxide on the bipolar plates which may increase the ICR, or

they may be flushed out by the flow of fuel, coolant and air. However, they may also reach the membrane and catalyst layer and contaminate them. In order for metal ions to contaminate the membrane or catalyst, they must migrate from the corrosion location. This movement is facilitated by the presence of water [8]. The effect of the corrosion of bipolar plates on stack performance depends on how many of the metallic ions which are produced during the corrosion process will reach the membrane or catalyst layer. This is affected by the stack's design and water management [79, 92, 93].

2.7.1 Increase in interfacial contact resistance

ICR is one of the most important factors for evaluating the suitability of metallic bipolar plates for use in PEMFCs [3]. A new passive film may form (for polished samples) or the properties of an existing passive layer may change on the surface of metals when they are exposed to PEMFC environments. [3, 10-13, 16, 79, 94]. In addition, the local contact area between the bipolar plates and GDL may decrease as a result of changing the physical morphology of the bipolar plate surface through corrosion and corrosion products [3]. These may give rise to an increase in ICR.

Both the corrosion resistance and the ICR of a stainless steel alloy are related to its passive films. The properties of the passive film depend on both the chemical composition of the alloy and the environment to which the alloy is exposed [3, 12-15, 78, 94, 95].

The effect of cathode and anode environments on ICR has been investigated using in situ ICR measurements. The results showed an increase in ICR for the cathode side by increasing the operating time. However the in situ measured ICR showed no significant change for the anode side after more than 6000 h operation. Interchange of the anode and the cathode (i.e. the cathode bipolar plate was exposed to hydrogen and the anode bipolar plate was exposed to air) caused the ICR of the cathode bipolar plate (formerly acting as a cathode bipolar

plate) to drop to the ICR levels of the anode bipolar plate after about 50 h. This could be because the cathode passive layer was broken down in the anode environment. The anode bipolar plate (formerly acting as an anode bipolar plate) showed a slow increase in ICR in the oxygen atmosphere due to the formation of an oxide passive layer [96, 97].

Kim et al. [95] investigated the effect of alloying elements (Mo and Cr) on ICR. They found that ICR decreases linearly with the pitting resistance equivalent number (i.e. PREN = %Cr+ 3.3%Mo+ 16%N).

XPS and XPS depth profiles were used to study the chemical composition and thickness of passive films as well as the effect of environmental parameters such as pH on passive films [14, 78, 98]. Kumagai et al. [14] investigated the effect of pH on ICR and passive layers. The passive layers were formed on 310S SS surfaces in solutions with various pH (0.05 M $SO4^{2-}$ (pH 1.2-5.5) + 2 ppm F^-) during potentiostatic tests (8 h at 0.6 V vs. SCE). ICR increased when the pH of solutions increased from 1.2 to 5.5. The passive layers were enriched with chromium oxide for pH 1.2 to 3.3 and they were mainly iron oxide for pH 4.3 to 5.5. Furthermore, the passive films formed in pH 4.3 to 5.5 were thicker than those formed in pH 1.2 to 3.3.

2.7.1.1 Interfacial contact resistance (ICR) measurements

Bulk resistance and ICR are important properties of bipolar plates. ICR is much higher than bulk resistance for metallic bipolar plates [57]. The ICR of metallic bipolar plates is affected by corrosion in a PEM fuel cell environment. Therefore, the effect of corrosion on ICR is frequently studied [12, 14-16]. The ICR between GDLs and bipolar plates can be measured by compressing a bipolar plate between two GDLs or a GDL between two bipolar plates as shown in Figure 2-24 [3].

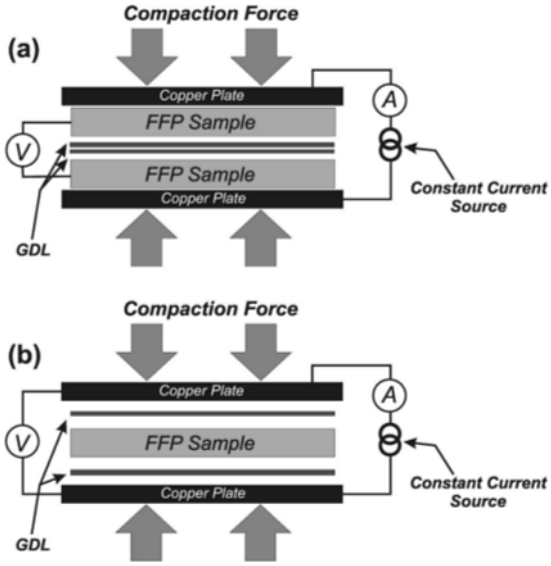

Figure 2-24. Measuring the ICR between bipolar plates and GDLs with (a) two bipolar plates and (b) a single bipolar plate [3].

A known current passes through the compressed bipolar plates and GDLs and the drop in voltage is measured. The total resistance can be calculated by Ohm's law (Figure 2-25 (a)). The calculated resistance (R_{mes}) is equal to total serial resistances (Figure 2-25 (b)):

$$R_{mes} = 2R_{Au\text{-}GDL} + 2R_{GDL} + 2\,R_{GDL\text{-}BP} + R_{BP} \quad (15)$$

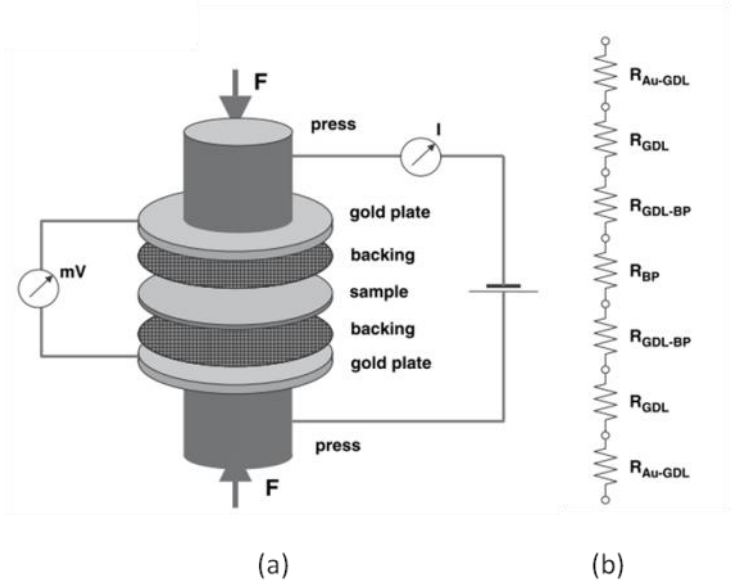

Figure 2-25. (a) Experiment for measuring total resistance. (b) The serial resistances for the "(a)" setup. $R_{Au\text{-}GDL}$ is the contact resistance between the Au contact plates and the GDL, R_{GDL} is the bulk resistance of the GDL, $R_{GDL\text{-}BP}$ is the contact resistance between the bipolar plate and the GDL, and R_{BP} is the bulk resistance of the bipolar plate [60].

R_{GDL} and R_{BP} are known from bulk electrical resistance measurements or from the supplier's specifications [60] (besides, they can be eliminated because they are not considerable compared to ICR [52]). $R_{Au\text{-}GDL}$ can be measured by a measurement that does not include the bipolar plate:

$$R_{mes2} = 2R_{Au\text{-}GDL} + R_{GDL}\,R_{BP} \quad (16)$$

The ICR between the GDL and bipolar plate is then:

$$R_{GDL\text{-}BP} = (R_{mes}\text{-}R_{mes2} - R_{BP} - R_{GDL}) / 2\,R_{BP} \quad (17)$$

The clamping pressure between the bipolar plate and GDL does not affect their bulk resistance. However it can be seen in Figure 2-26 that ICR is highly affected by clamping pressure [57]. The effect of altering clamping pressure on ICR can be as significant as or greater than the effect of changing the bipolar plate alloy [96]. This is because enhancing compression increases both the number of GDL fibre-bipolar plate contact points in bipolar plate/GDL interfaces and the number of fibre-fibre contact points within the GDL. Therefore, the total contact area increases when compression increases.

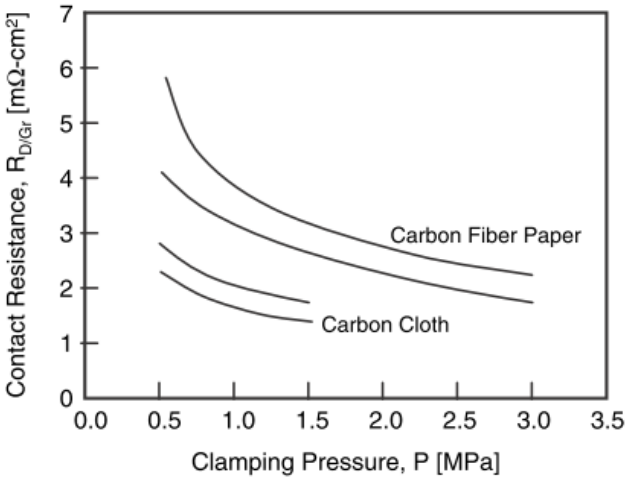

Figure 2-26. ICR is highly affected by clamping pressure [57].

The increase in compression force also decreases GDL porosity which is necessary for the GDL's proper performance. Therefore there is an optimum compression force for a GDL [3, 79].

2.7.2 Effect of metallic ions on membrane

2.7.2.1 Decrease of membrane ionic conductivity

Metallic ions from the corrosion of bipolar plates may be taken up by the membrane, leading to a decrease in membrane ionic conductivity [8, 44, 79, 91, 99, 100]. All metallic ions (except Li^+) show a higher affinity to the sulphonic acid groups of Nafion than protons do. Thus Nafion absorbs metallic cations which are released from the corrosion of bipolar plates. As a result, proton transport is reduced in contest with metallic ions [79, 99, 100].

Metallic ions with higher valence are more detrimental than monovalent metallic ions. This is because for each charge of multivalent metallic ions, one H^+ could be dislocated from sulphonic acid groups, and additionally multivalent metallic ions have a relatively stronger bind to sulphonic acid groups than monovalent metallic ions. As a result, their mobility is much lower. In general, the affinity of a metallic ion to the sulphonic acid groups of Nafion increases if the size and charge of the metallic cation increase [79, 99, 100]. When metallic ions are replaced with protons in Nafion, pH decreases in the environment [99] which may increase the corrosion of bipolar plates.

2.7.2.2 Membrane degradation

Metallic ions may accelerate membrane degradation by enhancing the production of H_2O_2 radicals in PEMFCs [8, 44-47, 100]. Metallic ions are damaging for the membrane in the order of $Fe^{2+} > Cu^{2+} > Ti^{2+} > Mg^{2+} > Na^{2+}$ [100].

LaConti et al. [100, 101] have suggested a mechanism for membrane degradation. According to this mechanism, low levels of oxygen molecules diffuse across the membrane from the cathode side to the anode side. Then, at the anode side these oxygen molecules react with hydrogen atoms, and hydrogen peroxide and hydroperoxide are generated (Stages 1-3, Reactions 18-20) (see Figure 2-27 [102]):

Stage 1: $H_2 \rightarrow 2H\bullet$ (at anode Pt catalyst) (18)

Stage 2: $H\bullet + O_2$ (oxygen crossover through membrane) $\rightarrow HO_2\bullet$ (19)

Stage 3: $HO_2\bullet + H\bullet \rightarrow H_2O_2$ (20)

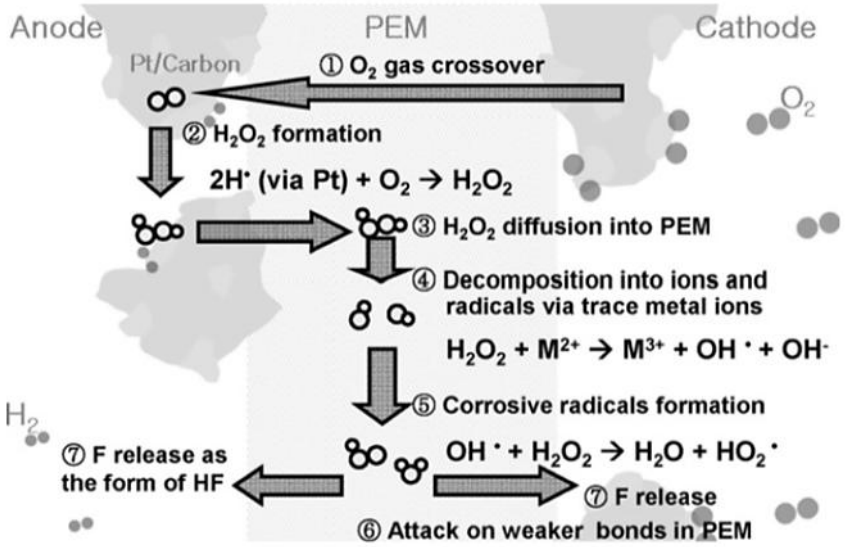

Figure 2-27. Effect of corrosion products (metallic ions) on the degradation of a PEM membrane [102].

If metallic ions are not added to a solution of 30% hydrogen peroxide at 80 ºC, this solution cannot affect membrane stability. However, H_2O_2 decomposes into hydroperoxy (•OOH) and hydroxyl (•OH) radical through metallic ions (Stages 4 and 5, Reactions 21 and 22). The produced radicals attack Nafion [101] (see Figure 2-27 [102]):

Stage 4: $H_2O_2 + M^{2+}$ (metallic ions: Fe^{2+} and Cu^{2+}) $\rightarrow M^{3+} + \bullet OH + OH^-$ (21)

Stage 5: $\bullet OH + H_2O_2 \rightarrow H_2O_2 + HO_2\bullet$ (H_2O_2 radicals attack the membrane) (22)

Membrane degradation releases the sulphonate groups and fluoride ions from the Nafion (membrane) which in turn increase the corrosion of the bipolar plates [8, 44-47]. Therefore, the release of corrosive ions from the membrane and the release of metallic ions from the metallic bipolar plates may accelerate each other similarly to an autocatalytic reaction.

2.7.3 Effect of metallic ions on catalyst

The efficiency of catalyst layers can be affected by metallic ions such as Fe^{3+} [20, 24, 79, 96]. Okada et al. [99, 103, 104] have reported a mode of degradation that happens because of the presence of metallic ions at the Pt catalyst/membrane interface. This mode of degradation significantly decreases the oxygen reduction reaction (ORR) rates [99, 103, 104]. This degradation mode may also cause detachment of the Pt catalyst/membrane contact. Low levels of metallic ions (~ 0.1% to 1%) are enough to considerably affect the performance of the cathode catalyst layer through this mode of degradation. The degradation is more significant for Ni^{2+} and Cu^{2+} than for Fe^{3+} [105].

2.7.4 Effect of corrosion products on the porosity of PEMFC components

Corrosion products may be transported by the flow of water, hydrogen, and air, and may be trapped in pores of PEMFC components. The pores may be blocked and subsequently water, air and hydrogen transport may be disrupted, which may decrease cell performance and efficiency [24, 92, 106].

2.8 Accelerated testing of fuel cells

Evaluating PEMFC components using normal operating conditions is too expensive and time-consuming. Consequently, accelerated stress test (AST) methods and protocols have been developed [18, 102, 107, 108]. Some of these ASTs are summarized in Yuan et al. [108] and Wu et al.'s [18] reviews. An AST protocol must activate the targeted degradation mode and eliminate the other degradation modes [102].

Makkus et al. [96, 97] used alternating load to evaluate different metallic bipolar plates. The frequencies of the alternating load were 30 minutes load (0.5 V) followed by 30 minutes OCV and in addition 55 minutes load (0.5 V) followed by 5 minutes OCV. This AST protocol provides more aggressive conditions than a constant load and simulates the real conditions in an automobile.

Pozio et al. [44] used alternating current for evaluating the end plate of PEMFCs. The temperature varied between 25 °C and 70 ºC and the current density changed between 9.4 mA/cm^2 and 141 mA/cm^2 as shown in Figure 2-28.

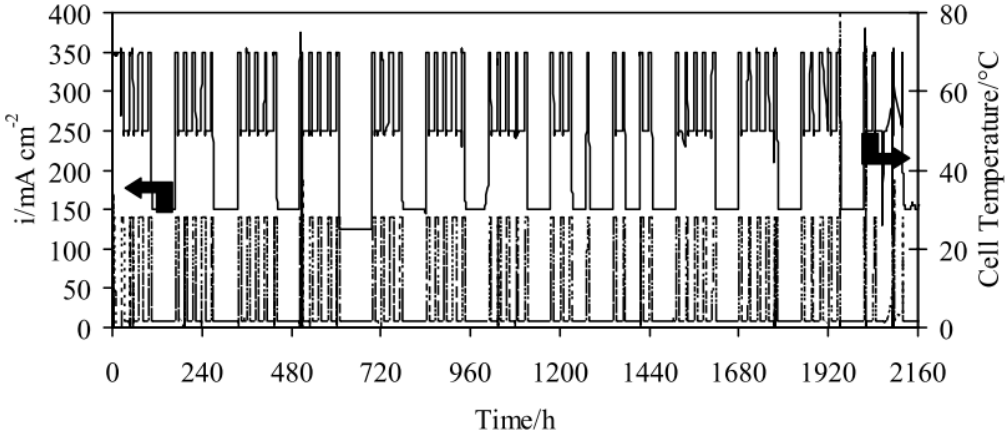

Figure 2-28. Alternating current for evaluating the metallic end plate of a PEMFC. The current density is shown by the dashed line and the cell temperature is shown by the solid line [44]

2.8.1 Start up/shut down

The hydrogen/air boundary which forms at anode may cause considerable degradation of PEMFC components [82, 109-113]. The hydrogen/air boundary may form during start-up and shut-down [111]. A PEMFC stack undergoes about 38,500 start-up/shut-down cycles over its life (5,500 h) in an automobile. These cycles cause the potential of the cathode electrode to reach 1.5 V vs. SHE in some regions [109].

Figure 2-29 shows an air/fuel boundary (dotted line) and four formed regions (A, B, C, and D) in a PEMFC. Regions B and A are at ~ 1.0 V and 0.0 V against the electrolyte potential (vs. SHE), respectively. Because the catalyst layers have high electrical conductivity, the absolute potentials of the catalyst layers are maintained uniform. However, the interfacial potential at the catalyst/electrolyte interface can be different in each region if the electrolyte potential changes. In region C, the interfacial potential at the catalyst/electrolyte interface should be about the equilibrium potential of oxygen, and the absolute potential of the electrode should be the same as region A. Consequently, the electrolyte potential should decrease on the left hand side of the hydrogen/air boundary (i.e. C and D). In region D of cathode, the interfacial potential of the catalyst/electrolyte will be the difference between the absolute potential of the catalyst layer in region B (i.e. ~ 1.0 V vs. SHE) and the (decreased) electrolyte potential in region C. Thus, the interfacial potential of the catalyst/electrolyte can be much higher than ~ 1.0 V vs. SHE for region D [109, 110, 112]. Hinds et al.'s [82] in situ measurement showed that this potential can reach to 1.4 V vs. SHE.

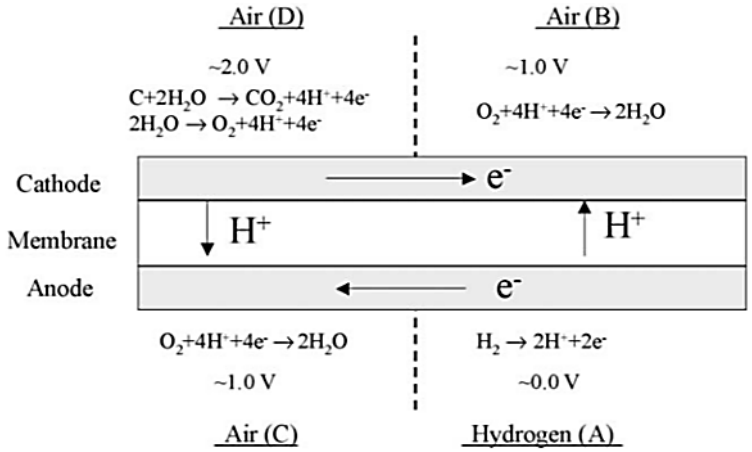

Figure 2-29. A fuel/air boundary (dotted line) forms four regions in a PEMFC [112].

In region D, the rates of water electrolysis (Reaction 23) and carbon oxidation (Reaction 24 and 25) are significant and the surface of Pt oxidizes (Reaction 26 and 27) [112]:

$$2H_2O \rightarrow O_2 + 4H^+ + 4e^- \quad (23)$$

$$C + 2H_2O \rightarrow CO_2 + 4H^+ + 4e^- \quad (24)$$

$$C + O_2 \rightarrow CO_2 \quad (25)$$

$$Pt + xH_2O \rightarrow PtO_x + 2xH^+ + 2xe^- \quad (26)$$

$$Pt + xO_2 \rightarrow PtO_{2x} \quad (27)$$

2.8.2 Pt dissolution

Pt dissolution is beyond the scope of this thesis. However, it is described briefly because of its importance in the degradation of PEM fuel cells. Pt in the catalyst layer dissolves both directly (Reaction 28) and from its oxide (Reactions 29 and 30):

$$Pt \rightarrow Pt^{2+} + 2e^- \quad (28)$$

$$Pt + H_2O \rightarrow PtO + 2H^+ + 2e^- \quad (29)$$

$$PtO + 2H^+ \rightarrow Pt^{2+} + H_2O \quad (30)[114]$$

Potential has a significant influence on the Pt dissolution process. If potential is increased from 0.65 to 1.1 V (vs. SHE), the dissolution of Pt increases. Owing to the formation of a

passive oxide film on the surface of Pt at potentials higher than 1.1 V (vs. SHE), the dissolution rate of Pt decreases [115]. Therefore, the potentials of accelerated stress test (AST) methods with an emphasis on Pt dissolution are normally chosen below 1.0 V (vs. SHE) [114, 116].

PEMFCs undergo potential cycling and start-up/shut-down in automobiles. Figure 2-30 shows the mechanism of Pt dissolution during potential cycling. Pt dissolves and also an oxide film may form on the surface of Pt during the potential increase of potential cycling. If the Pt which is protected with the Pt oxide film is maintained at high potentials, the Pt dissolution rates will be low. However, the oxide layer reduces to bare Pt during the potential decrease of potential cycling and Pt dissolution can continue rapidly when potential increases again. Consequently, rates of Pt dissolution significantly increase under potential cycling conditions compared to potentiostatic conditions. Therefore potential cycling is frequently used in AST methods to evaluate the durability of catalyst layers [114, 116].

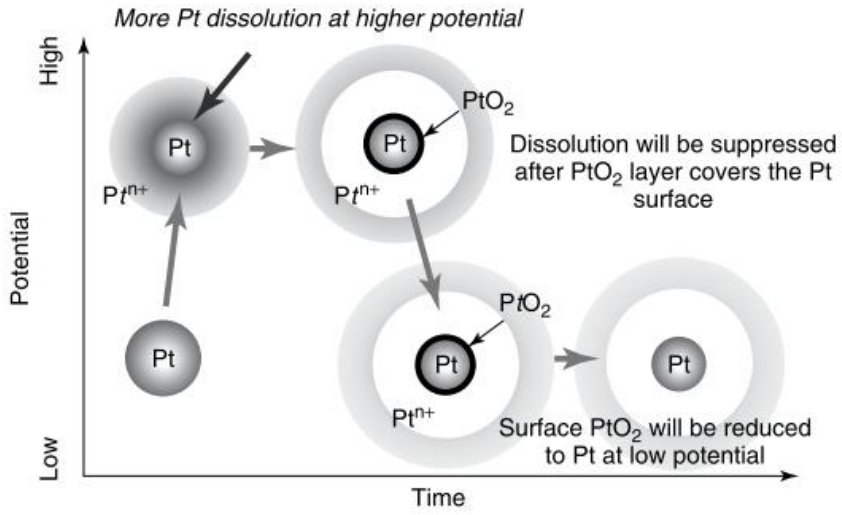

Figure 2-30. Pt dissolution during potential cycling [117].

2.9 Corrosion of stainless steel bipolar plates

Kumagai et al. [14] used 304 and 310S stainless steel as bipolar plates in single cells (1000 h/75 ºC). After durability tests, SEM images of rib surfaces barely showed corrosion on the anode sides of the bipolar plates, but there were considerable corrosion products on the cathode sides of the bipolar plates. There were higher levels of corrosion products on the cathode side of 304 SS bipolar plates than on the cathode side of 310S bipolar plates. The PEMFC with 304 SS bipolar plates showed a higher rate of degradation than the PEMFC with 310S SS bipolar plates, which may be due to higher corrosion rates of 304 SS bipolar plates than 310 SS bipolar plates in a PEMFC environment.

PH distribution has been investigated in a PEM fuel cell with 310S SS bipolar plates. For this, XPS results of the passive layers which were formed on 310S SS after polarization tests in solutions with various pHs were compared with XPS results of the passive layers which were formed on different regions of bipolar plates after a single cell test. The results showed that gas outlet regions of bipolar plates were exposed to an environment with lower pH than their centre and inlet regions. This pH gradient was supported with SEM images that showed more aggressive corrosion in the outlet regions than the centre and inlet regions [14].

Stainless steel bipolar plates have desirable properties as bipolar plates. However, because of corrosion and its effects, most untreated stainless steels are not suitable for use in PEM fuel cells and most of the literature suggested the use of coated or treated 316L SS or 904L SS [9, 52, 83].

One of the coatings that has been used for stainless steel bipolar plates is TiN. TiN coating provides a lower ICR between the bipolar plate and GDL, for instance TiN-coated 316L SS showed an ICR 30 $m\Omega\ cm^2$ lower than 316L SS at 150 $N\ cm^{-2}$ [118].

Generally, TiN coating on 316L SS shows a lower corrosion current compared to 316L SS [88, 91, 118-120]. Polarization measurements in a PEMFC simulated environment (0.05 M H_2SO_4 + 2 ppm F^-, 70 ºC, and purge with H_2 or air) showed a passive current density for this coating on 316L SS which was roughly ten times lower than that of 316L SS [118]. In addition, the corrosion current of TiN coating measured by linear polarization (0.1 M K_2SO_4, at pH =1, and at 80 ºC) was about 1/50 that of 316L SS [91]. Pitting was not observed for this coating after 4 hours potentiostatic measurements (0.05 M H_2SO_4 + 2 ppm F^- , 70 ºC, purge with air at 0.6 vs. SCE or purge with H_2 at -0.1 vs. SCE) [118].

However, the properties of TiN coating depend on its quality [88, 91]. It has been reported that for a poor quality TiN coating on 316L SS, the coating was mostly dissolved after about 1 hour potentiostatic measurement (0.1 M K_2SO_4 at pH =1, 80 ºC, air atmosphere and 0.6 V vs. Ag/AgCl) [91]. Additionally, for a TiN coating with pinholes, pitting corrosion was observed [88].

2.10 Theory of XRF

X-rays can be seen as electromagnetic radiation waves with short wavelengths (0.01 to 10 nm) or as beams of photons with associated energies (0.125 to 125 keV) (Figure 2-31). The binding energies of electrons in inner-shells are the same order of magnitude as the energies of these electromagnetic radiation waves.

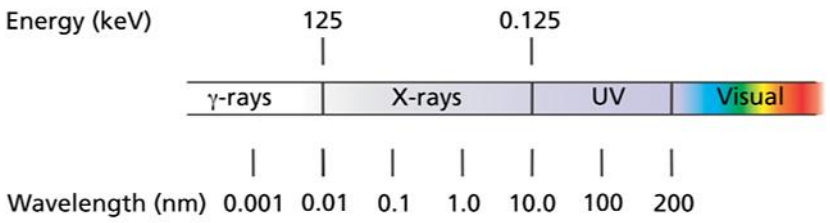

Figure 2-31. Electromagnetic radiation waves [121].

2.10.1 Interaction of X-ray with matter

The main interactions of X-rays with matter are fluorescence, scattering and absorption. It can be seen in Figure 2-32 that the intensity of the incident beam (I_0) decreases to the intensity I when it passes through matter with density of ρ because of absorption and scattering:

$$I = I_0 e^{-\mu\rho d} \quad (31)$$

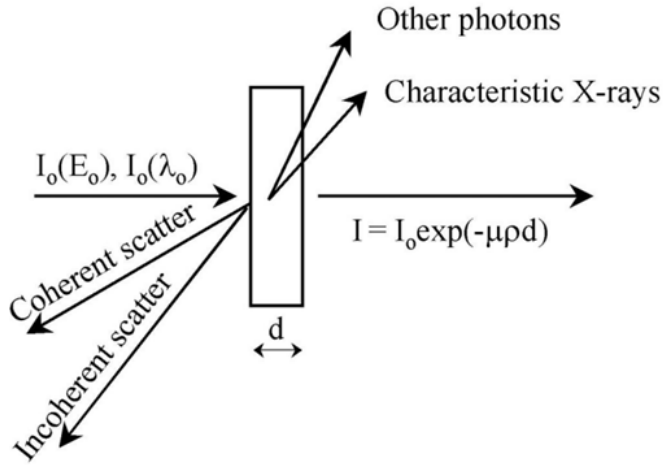

Figure 2-32. Interaction of incident X-ray with matter [122].

d is the distance that x-rays travel through matter and μ is known as the mass attenuation coefficient and the total cross section [121-123]. The mass attenuation coefficient of element *i* (μ_i) includes the mass absorption coefficient (τ_i) and the cross section for scattering (δ_i):

$$\mu_{i=} \tau_i + \delta_i \quad (32)$$

μ_i, τ_i and δ_i depend on energy (E) or wavelength (λ) and atomic number (Z). μ is roughly proportional to $Z^4 \lambda^3$ [122].

2.10.2 Photoelectric effect

Electrons can be ejected from their shells in atoms if they are struck by particles (electrons or X-ray photons) that have energies higher than the binding energies of the electrons in the atoms. Figure 2-33 (a) shows that a photon with sufficient energy is absorbed by an atom and an electron is ejected from its shell. This atom is not stable because there is a vacancy in the K-shell. This excited atom can become stable if an electron transfers from an outer shell to the vacancy. This transition can cause an X-ray photon to be emitted (Figure 2-33 (b)). The energy of this photon is proportional to the energy difference between the two states (shells) of the transferred electron. Because the shells of an element have specific energy levels, the emitted X-ray known as fluorescence is characteristic of the element [121-124].

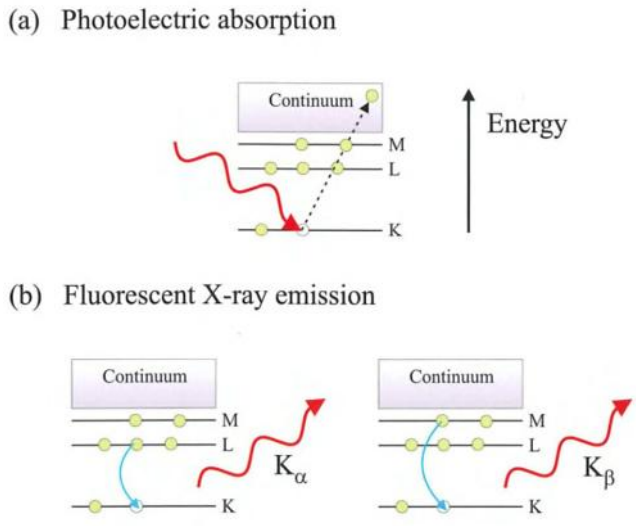

Figure 2-33. (a) Photoelectric absorption. (b) XRF emission [124].

2.10.3 Absorption edge

Figure 2-34 shows the variation of a photoelectric cross section (τ_{Mo}) vs. energy of the incident X-ray beam for Mo. It can be seen in Figure 2-34 that there are discontinuities at the binding energies of electrons in shells known as absorption edges. If the energy of the

incident beam is increased to just above these absorption edges, the X-ray fluorescence abruptly increases. In order to decrease the X-ray fluorescence of an element, the incident energy should be chosen just below the absorption edge because this energy is too low to eject electrons from the nearest shell, but it is too high to eject electrons from the lower energy shells [121, 122].

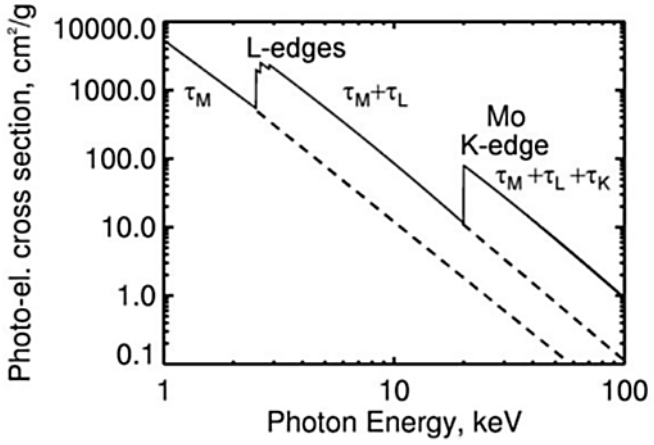

Figure 2-34. The variation of a photoelectric cross section (τ_{Mo}) with energy of the incident X-ray beam for Mo [122].

2.11 Measurement of bipolar plates corrosion products

The corrosion products of bipolar plates have been studied after single cell/stack durability tests or electrochemical tests to assess corrosion of different bipolar plates. Corrosion products from bipolar plates may be flushed out by the stack water, they may deposit on the surface of bipolar plate and affect ICR, and also they may contaminate MEAs. XRF [15, 20-24, 93, 125-127] and EDS [23, 96, 97, 128] have been used to measure MEA contamination. No contamination could be detected by EDS since the detection limit are part of thousands [128] but XRF, a more sensitive method, showed metallic contamination in the same samples [14, 17].

Inductively coupled plasma (ICP) [23, 78, 91, 96, 119, 129-134] and atomic absorption spectroscopy (AAS) [44, 96, 131, 135] have been used for studies of MEAs and exhaust water contamination of single cell/stack, or solution contamination after tests which were designed to simulate cell operation. Before using AAS and ICP methods, it is necessary to dissolve the MEA contaminants in a solution. As a result, the accuracy of these methods depends on how well MEA contamination is dissolved in the analyzed solution. Furthermore, it is difficult to use these methods to evaluate the distributions of contaminants. XRF is not destructive since it can measure contamination directly from MEA which makes this method simpler and more accurate than ASS and ICP.

2.11.1 Level of contamination in exhaust water of stack and MEAs

The levels of corrosion products which deposit on bipolar plates cannot practically be measured using weight change because most of the metallic candidate for bipolar plates are corrosion resistant and show insignificant weight change. Measuring levels of cations and anions in exhaust water from stack is not very informative for investigating corrosion of bipolar plates, since the reaction in the cathode and humidification may produce a considerable volume of water in which may decrease the concentration of cations and anions to below the detection limits. Also because of the stack design the exhaust water from the cathode may mix with the exhaust water of the anode and so comparing corrosion of anode side and cathode side will be impossible. The cations from corrosion of bipolar plates are absorbed by the MEA, therefore MEAs used in stacks can be chemically analyzed to investigate corrosion in PEM fuel cells [79].

Auvinen et al. [48, 131, 136] have investigated corrosion rates of electropolished, CrN and Au coated 430 SS, 316L SS and 904L SS after use in a “multisinglecell” an instrument

with 8 single cells operating simultaneously and identically- (for 618 h to 650 h at 80 ºC) from Fe levels found in MEAs, exhaust water and gas lines using AAS and ICP. MEA contamination levels were several times higher than exhaust gas contamination levels and Fe was mainly located in the MEA (membrane, catalysts and GDL). Despite significant corrosion rates of bipolar plates, exhaust water analysis was not able to reveal the difference between the corrosion resistances of different coatings because most of the measured contamination in exhaust water was below the detection limit of AAS and ICP. However, analysis of the MEA was able to show different contamination levels for each coating. For good quality coatings with high corrosion resistance, both MEAs and exhaust water showed similar low levels of contamination mainly close or below detection limits.

2.11.2 Investigation of MEA contamination using XRF

MEA contamination has been investigated using XRF [15, 20-24, 93, 106, 125-127]. XRF is sufficiently sensitive to detect metal ion contamination levels in MEAs [23]. It has been used to evaluate metallic bipolar plates with and without coatings: lower levels of MEA contamination indicate a higher corrosion resistance [15, 20-23].

It has been found that Fe and Ni are usually the main contaminant in used MEAs for stainless steel bipolar plates and Cr is close to the detection limits. Zawodzinski et al. [125] have evaluated the levels of Fe, Ni, Cr and Cu in a fresh MEA and in MEAs used in 2-4 cell stacks (time not specified / 80 ºC) and a single cell (2000 h/ 80 ºC), with 316 SS bipolar plates. The fresh MEA showed only Pt, whereas in all of the used MEAs, Fe and Ni levels were much higher than other contaminants. Cu was present in much lower than Fe and Ni and sometimes it was not detected; Cr and Mo were not detected for any of the MEAs (detection limit was 10 ppm). They refer to the same work later and they mentioned

observing trace of the Cr [23]. Kumagai et al. [15], used XRF to evaluate level of contamination in MEAs after use in a single cell (1000 h/75 °C) with 19Cr2Mo or 22Cr2Mo bipolar plates which contain Fe and Cr but not Ni and found significant levels of Fe; however, Cr levels was below the detection limits.

Traces of Cr have been reported by Toops et al. [21], who have measured levels of Fe, Ni, Cr and V (μg/cm^2) in MEA after single cell tests (more than 1000 h/80 ºC) with 904L SS bipolar plates. Used MEAs showed 1.1 μg/cm^2 Fe, 0.11 μg/cm^2 Ni, 0.18 μg/cm^2 Cr and V was below the detection limit (0.05 μg/cm^2) which was significantly higher than those of fresh MEAs (Fe was 0.5 μg/cm^2 and Ni, Cr and V were below the detection limits.).

2.11.3 Level of contamination in the cathode side vs. in the anode side

Corrosion rates depend on environmental conditions. The cathode side and the anode side of a PEM FC have different environmental parameters, for example the cathode atmosphere is air or oxygen, but the anode atmosphere is hydrogen. The pH could also be different in the anode side and the cathode side [137, 138]. A material or a coating may show a good corrosion resistance in both the cathode side and the anode side, only in the anode side or only in the cathode side. Kumagai et al. [15] carried out visual observation of 19Cr2Mo and 22Cr2Mo stainless steels after use in a single cell (1000 h/75 ºC) and saw no corrosion on either the cathode side or the anode side for 22Cr2Mo; however, there was significant corrosion product on the cathode side of 19Cr2Mo.

Because different coatings and metals may show different corrosion rates in the cathode side and in the anode side of fuel cells, they may show more corrosion product in the cathode side or in the anode side of MEAs [126]. Contamination levels of MEAs in the anode side and in the cathode side of single cells have been compared [48, 96, 97, 131, 136] and the

majority of the reports showed more corrosion products in the cathode side than in the anode side; however, a few tests showed more corrosion products in the anode side than in the cathode side [97, 136] this contradictory result could be because the coating quality was not identical for the anode test and the cathode test [136] or because of errors in the measurements [97].

Auvinen et al. [48, 131, 136] have compared corrosion on the cathode side and the anode side of PEM fuel cells. Coated and uncoated stainless steels bipolar plates were assembled in the cathode side or in the anode side where the other side bipolar plate was graphite in the multisinglecell (618 h to 650 h/ 80 ºC). Levels of contamination in MEAs were measured using AAS and ICP and showed a clear difference between the cathode side and the anode side. 904L SS and Au coated 904L and 403 SS coated by CrN showed much higher levels of contamination when they were assembled in the cathode than when they were assembled in the anode; the levels of contamination for the anode were very close to those of a fresh MEA. The optical and SEM images of the bipolar plates after use in the multisinglecell correlated with MEA contamination results. 316L SS coated by CrN showed higher values (hundreds of µg) of Fe when it was assembled in the anode side than when it was assembled in the cathode side, these levels (hundreds of µg) have not been reported anywhere else and did not correlate with SEM images which showed similar corrosion on the cathode side and on the anode side of the bipolar plates, therefore the author assumed the contamination did not originate from corrosion for this case.

Makkus et al. [96, 97] have run single cells (300 h/ 80 ºC) with stainless steel (not specified) bipolar plates. Similar to the work of Auvinen et al. [48, 131, 136], bipolar plates were used on one side (for example the cathode side) and a graphite bipolar plate was used on the other side (for example the anode side). The aging cycles for these single cells

provided more corrosive conditions in the anode side than the cathode side. They compared levels of MEAs (including GDL) contamination using AAS/ICP which showed the different between corrosion rates in the cathode side and in the anode side. The results showed higher contamination levels when one of stainless steels ("alloy A") was assembled in the cathode side than when "alloy A" was assembled in the anode side; however, the other stainless steel ("alloy B") showed the contradictory results. However, for "alloy B" they did not pay attention to repeatability of tests i.e. anode test-to-anode-test (repeating the anode side test) variation for "alloy B" was much higher than the variation between single cell with "alloy B" in the anode side and single cell with "alloy B" in the cathode side. They also did not take into account that the aging cycle provided a more corrosive situation in the anode side than in the cathode side.

2.11.4 Relationship between stack performance, contamination levels in MEA and interfacial contact resistance between bipolar plates and MEA

The correlation between single cell performance, contamination levels in MEAs and ICR between bipolar plates and MEA has been investigated [15, 21, 83].

There is a clear correlation between performance, ICR and contamination levels in MEAs, lower ICR and lower contamination levels in MEAs result in a better performance [15, 21, 83]. Wind et al. [83] used 316L SS and 316L SS with coatings as bipolar plates in single cells run 100 h-800 h at 80 ºC. They did not report the coatings (except for Au coating) and the method used for measuring MEA contaminations. The coating with the lowest contamination and the lowest ICR showed the best performance and the coating with the highest contamination and the highest ICR showed the worse performance.

ICR and MEA contamination are both important parameters and should be considered, because both of them may influence the performance of single cells [15, 21, 83]. A single

cell with significant levels of contamination in MEA may show a good performance because of a very low ICR [83]. The effect of MEA contamination on performance can also be significant, Kumagai et al. [15] evaluated 19Cr2Mo and 22Cr2Mo as bipolar plates in a single cells (1000 h/75 ºC). Both 19Cr2Mo and 22Cr2Mo showed a similar ICR; however, XRF analysis of used MEAs showed lower Fe contamination for 22Cr2Mo than for 19Cr2Mo. These XRF results correlated with performance of the single cells which shows a better performance for the single cell with 22Cr2Mo bipolar plates than the single cell with 19Cr2Mo bipolar plate.

Toops et al. [21] measured levels of contaminants in MEAs after use in a single cell (more than 1000 h and at 80 ºC) with stamped 904L SS bipolar plates, the levels of contaminants were acceptable; however, the high level of ICR for this metal significantly decreased its performance.

2.12 Summary

Some research has been carried out to measure levels of MEA contamination. Very little work has been done to assess the distribution of contamination in the MEA. However, because there are not uniform distributions of temperature, acidity, and water in the PEM fuel cell and because temperature, acidity, and amount of water affect corrosion rates, the distribution of contaminations can be not uniform in MEAs.

Galvanic and crevice corrosion between the MEA and bipolar plates are important corrosion mechanisms in PEMFCs; however, this galvanic-crevice corrosion mechanism has not been quantified in previous works. Based on the in situ measurements, the conditions for a more representative ex situ test for the corrosion of bipolar plates have been suggested

[27]. However, to our knowledge in previous works no electrochemical cell and testing protocols have been able to simulate these conditions.

In this PhD, an electrochemical cell (galvanic crevice cell) has been designed to simulate the galvanic crevice corrosion that takes place between the bipolar plate and the MEA. This electrochemical cell simulates conditions which have been suggested for more representative ex situ corrosion tests for bipolar plates in PEMFCs [27]. In addition, the distribution of metal ion contaminants in MEAs from fuel cells stacks that have operated for extended periods is evaluated with laboratory and synchrotron XRF.

3 Experimental Method

3.1 Materials

3.1.1 MEAs and bipolar plates for XRF experiments

Membrane electrode assemblies (MEAs) of the bonded catalyst substrate (BCS) and catalyst coated membrane (CCM) design were supplied by Johnson Matthey Fuel Cells (JMFC) to Intelligent Energy (IE), who ran them in five different PEM fuel cell stacks. JMFC also supplied unused MEAs for control measurements. Details of aging cycles, MEAs and bipolar plates are presented in Table 3-1. There were 20 cells in each stack. C1 is a TiN coating and C2 is a carbonaceous coating both are sub-micron in thickness, and deposited using a PVD process. Stacks are named using the following designation that comprises the following: plate (9 for 904L SS or 3 for 316L SS)-time (h)-temperature (°C).

All MEAs employed a nanoparticulate Pt catalyst on a high surface area carbon support in both the anode and cathode layers, combined with a 30 µm, mechanically and chemically stabilised perfluorosulfonic acid (PFSA) membrane. The initial BCS parts comprised equivalent anode and cathode layers with nominal Pt loadings of 0.4 mg_{Pt}/cm^2. As the project progressed, the Pt content of the MEAs was thrifted and the final CCMs provided were fabricated with a nominal 0.1 $mgPt/cm^2$ anode and 0.4 $mgPt/cm^2$ cathode. A common substrate/gas diffusion layer (GDL) i.e. SGL 35BC was employed in the testing of the BCS and CCM MEAs. In this thesis "MEA" includes membrane, catalyst layers and GDLs. Because of confidentiality further details of the samples can not be presented here.

Table 3-1. Stack operation time/temperature, bipolar plates, MEA and aging cycles.

Stack	Operating time and temperature	Bipolar plate	MEA	Aging cycles
9c1-2700-76	2700 h/76 °C	C1coated 904L SS	Bonded catalyst substrate (BCS)	IE's standard test (Section 3.1.2)
9-1000-78	1000 h/78 °C	Uncoated 904L SS	Bonded catalyst substrate (BCS)	Composite Accelerated Stress Testing (AST) (Section 3.1.2)
9-1941-69	1941 h/69 °C			
9-1360-65	1360 h/65 °C	Uncoated 904L SS	Catalyst coated membrane (CCM)	172000 voltage cycling AST (Section 3.1.2)
3c2-1515-67	1515 h/67 °C	C2 coated 316L SS		

The nominal composition of the 316L stainless steel and 904L stainless steel which was used to construct the bipolar plates for using in stacks is presented in Table 3-2.

Table 3-2. Nominal composition of 904L and 316L stainless steel, typical values wt% [139].

	C	Cr	Ni	Mo	Cu	Fe
904L SS	0.01	20	25	4.3	1.5	Balance
316L SS	0.02	17	11	2.6	-	Balance

3.1.2 Aging cycles

Stack 9c1-2700-76 ran IE's standard test protocol which consists of 10 h constant current followed by a set of 3 fluid tests and a polarization curve (~22hr cycle). Stacks 9-1941-69 and 9-1000-78 used a composite Accelerated Stress Test (AST) protocol that includes start-up/shutdown and voltage cycling, operation at constant current and a "driving cycle" that includes quick switching between start-up, idling running, partial load running

and full power acceleration. Stacks 3c2-1515-67 and 9-1360-65 used an AST that modulated the load between 0.7 $A.cm^{-2}$ and 0.005 $A.cm^{-2}$, corresponding to mean cell voltages of approximately 0.6 V and 0.95 V, respectively. Because of confidentiality further details of the aging cycles can not be presented here.

3.1.3 MEAs and metallic materials for electrochemical experiments

316L and 904L stainless steel and coated metallic samples were supplied by Intelligent Energy. C1 and C2 coating are a TiN coating and a carbonaceous coating respectively and C3, C4 and C5 are commercial coatings that are commercially sensitive. MEA (BCS type) and GDL (SGL 35BC) samples were supplied by Intelligent Energy and Johnson Matthey Fuel Cells.

3.2 Sample preparation

3.2.1 Sample preparation for laboratory-based XRF

Powder-free nitrile gloves were used for handling MEA samples to prevent contamination during sample preparation and experiment. Temperature is an important variable in the rate of corrosion and it is known that the temperature is not uniform in working fuel cells, therefore the distribution of corrosion product contamination was investigated in different regions of MEAs. "Cold" regions are closer to the coolant inlet, and "hot" regions are closer to the coolant outlet. The temperatures given in Table 3-1 (cell operating conditions) present the approximate temperature at the coolant outlet ("hot"). The temperatures of the cold regions were significantly lower than the temperatures of the hot regions.

3.2.2 Sample preparation for synchrotron-based XRF

Cross-sections of used and unused MEAs were mounted and polished by Johnson Matthey Fuel Cells. (See also Sections 3.4.1, 3.4.2 and 3.4.3.)

3.2.3 Preparation of metallic samples and MEA/GDL samples for electrochemical measurements

316L stainless steel and coated metallic samples were supplied by Intelligent Energy. MEA/GDL samples were supplied by Intelligent Energy and Johnson Matthey Fuel Cells and were cut into 4 cm x 2 cm pieces for use in the galvanic crevice cell.

For "polished" samples, the test area was abraded to 1200 grit about five minutes prior to the experiment, cleaned ultrasonically and washed with methanol and deionised water, and then dried using a hair dryer. "As received" and coated samples were washed with methanol and deionised water and then dried.

3.2.3.1 Connections of metallic and MEA/GDL samples

Crocodile clips were used for connecting wires to metallic and GDL/MEA samples in the early stages of developing testing protocols for the galvanic crevice cell (Section 3.5). However, corrosion was observed in contact areas between the crocodile clips and samples. For metallic sample/crocodile clip connections, crevice corrosion could possibly take place between crocodile clips and metallic samples in the contact areas. For MEA/crocodile clip connections, both galvanic corrosion and crevice corrosion could possibly occur between MEAs and metallic crocodile clips.

To solve this problem, a Ni wire with 99.98% purity and 0.5 mm diameter with a PEEK sheath was spot welded to the metallic samples, and the wire connections and all of the

sample surface except the test area (2 cm x 2 cm) were covered with 3M Scotch-Weld 9323 A/B epoxy as shown in Figure 3-1(a). To avoid galvanic corrosion where the wire contacted the MEA/GDL, a gold wire with 0.5 mm diameter was connected to the MEA using a plastic clip as shown in Figure 3-1 (b).

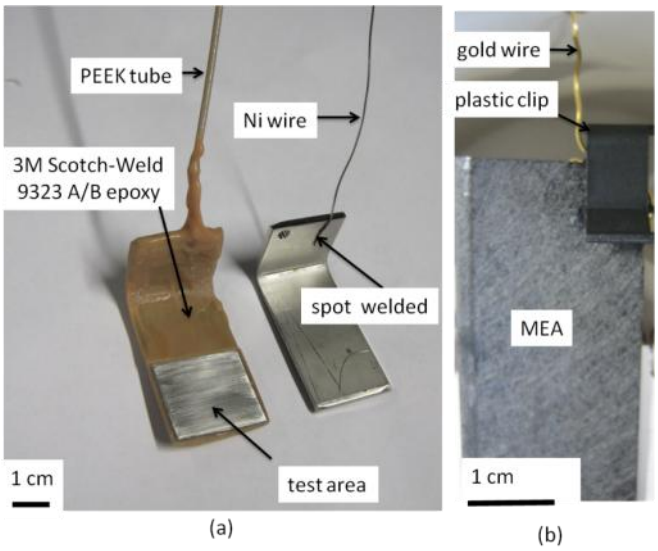

Figure 3-1. Preparation of metallic samples and MEA samples for electrochemical measurements. (a) Preparation of metallic samples and their connections. (b) Preparation of MEA samples and their connections.

3.3 Laboratory-based XRF

Laboratory XRF measurements were carried out on a Bruker S8 Tiger X-Ray Fluorescence Spectrometer, using a rhodium tube X-ray source operated at 3 kW with sample and mask diameters of 34 mm and 32 mm, respectively. The data collection time for all samples was 18 minutes. Possible contamination from the cut edges was avoided by ensuring that data only were collected from the centre of samples.

Both the cathode side and anode side of each MEA, (i.e. the side of the MEA facing the cathode and anode side of the bipolar plates respectively) were tested as illustrated in Figure 3-2.

Laboratory XRF data were analyzed with Bruker "Spectra Plus, Version 2" software supplied with the spectrometer. It was assumed that the matrix was carbon containing traces of metallic elements and it was assumed that across macro length scales, the density and the thickness of the MEAs are constant and homogeneous. The density and thickness of MEAs from different cells and stacks were determined to be 0.49±0.03 g/cm^3 and 640±10 µm respectively.

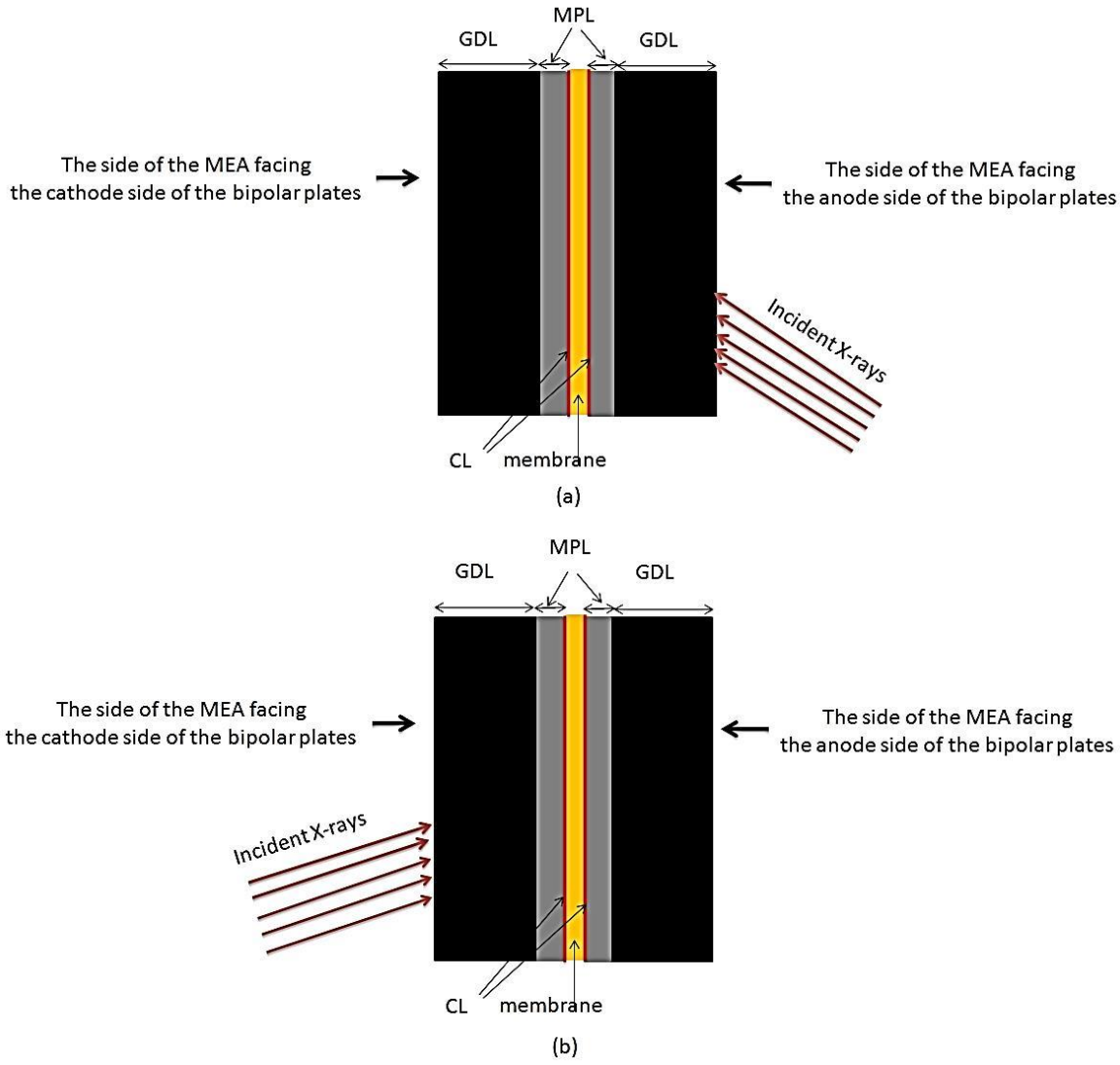

Figure 3-2. (a) Anode side test. (b) Cathode side test.

Because standard samples with known contamination were not available, a standard-less analysis package, "QuantEXPRESS", based on a fundamental parameters (FP) method for correlating intensity to amount of contamination was used. For a sample as thin as MEAs (640±10 µm) the FP method does not work as well as a quantitative calibrated method with proper standards hence ten percent of measured area density for each element is considered as a reasonable estimate of errors [140]. Two unused MEAs with known platinum loading were also used to estimate the accuracy of the measurements. The area density of platinum derived from XRF measurements was 0.80±0.08 mg/cm^2 which correlate well with platinum loading provided by the MEAs manufacturing company (Johnson Matthey fuel cells) 0.90 mg/cm^2.

Although there are some uncertainties in the estimate of absolute levels of the contaminations in MEAs because of the nature of the samples and the lack of proper calibration standards, there can be confidence in relative amounts of contaminants in different tests that show clear trends. Conclusions below are based upon consequence of relative levels of contamination in MEAs and are not based on absolute values.

This process was checked with Bruker and it was confirmed that the strategy is as good as possible with the resources available for this PhD [140]. The spectra of the XRF results cannot be presented because of confidentiality.

3.4 Synchrotron-based XRF

Synchrotron XRF experiments were performed at Diamond Light Source on the microfocus spectroscopy beamline I18 [141, 142] which uses a cryogenically-cooled Si (111) monochromator and a set of mechanically-bent Kirkpatrick-Baez mirrors which focus X-ray upon the sample. A 9-element Ge detector (Ortec) with XSPRESS2 processing was used. For each pixel, the exposure time was one second. During measurements, sample was

positioned at 45 degrees to the beam and to the detector (fluorescence mode). Table 3-3 summarizes the incident energies and beam sizes which were used in the experiments.

Table 3-3. The experiments, the year (beamtime), the incident energies and the beam size.

Experiment	Year	Energy (keV)	Beam size
Area survey scan	2010	10	60 µm x 60 µm
Plan view mapping	2010	11.52	60 µm x 60 µm
Plan view mapping	2011	11.54	60 µm x 60 µm and 6 µm x 6 µm
Line scans	2011	11.54	60 µm x 60 µm
Cross sections mapping	2012	11.51	60 µm x 60 µm and 6 µm x 6 µm

"Area survey scan" experiment includes five horizontal line scans on some of the samples which were used for the laboratory based tests as illustrated in Figure 3-3 (a). "Line scans" experiment includes "cold/hot" or "perpendicular" line scans on MEAs as shown in Figure 3-3 (b) (see Section 3.4.1). The beam sizes on the sample were 60 µm x 60 µm or 6 µm x 6 µm (see Table 3-3).

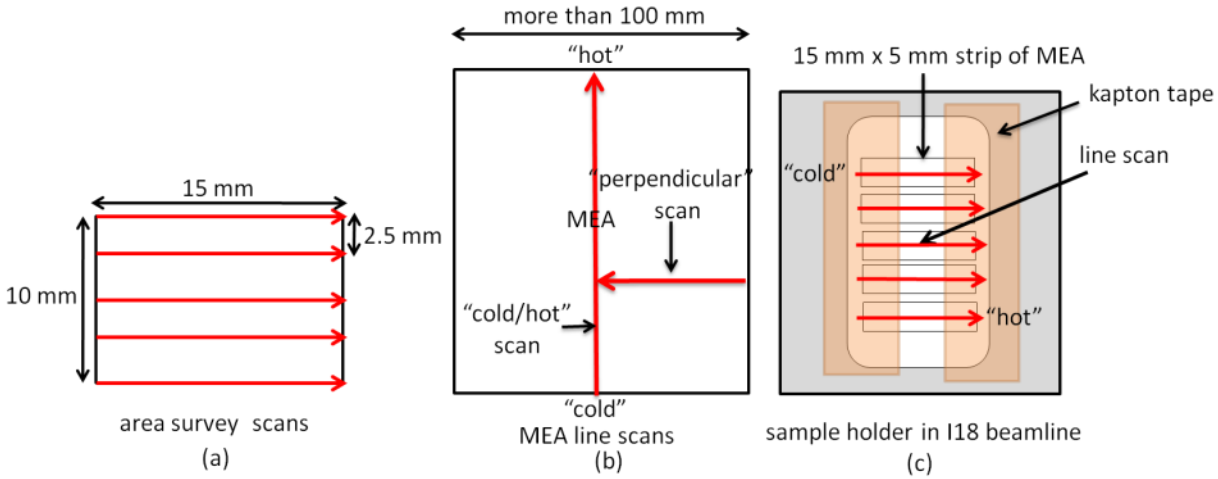

Figure 3-3. (a) Area survey scan; (b) "cold/hot" and "perpendicular" scan of MEA; (c) sample holder in I18 beamline with line scan sample. The red arrows show direction and position of line scans.

3.4.1 Problems and challenges for the line scan experiments

Because the movement of the sample holder was limited in I18 beamline (the maximum horizontal movement was 25 mm and the maximum vertical movement was 30 mm) and because the length and the width of MEAs were more than 100 mm, 15 mm x 5 mm strips were cut from MEAs and put on a sample holder as shown in Figure 3-3 (c) to scan a longer line (for example from “cold” to “hot” areas), as shown in Figure 3-3 (b) and (c).

3.4.2 Cross section experiments and their problems and challenges

A high resolution scan using a 6 µm x 6 µm beam size was much more time-consuming than a low resolution scan using a 60 µm x 60 µm beam size for scanning an area. However, it was necessary to use the high resolution scan (6 µm x 6 µm beam size) to study the membrane (~30 µm) and catalyst layers (~10 µm). Therefore, a two-step experimental protocol was designed as shown in Figure 3-4 to save time.

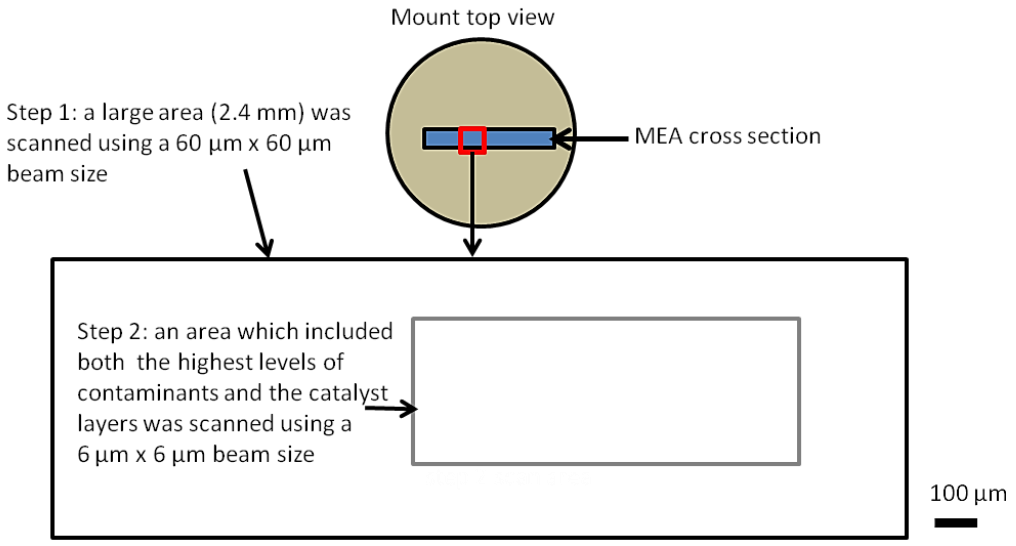

Figure 3-4. Two steps of synchrotron-based cross section experiments. Step 1: a large area was scanned using the low resolution scan. Step 2: an area which included both the area with the highest levels of contaminants in the low resolution map (step 1 map) and the catalyst layers was scanned with the high resolution scan.

First, a large area (2.4 mm of cross section) was scanned using the faster low resolution scan. After that, an area which included both the area with the highest levels of contaminants in the step 1 map (low resolution) and the catalyst layers was scanned using the high resolution scan.

Figure 3-5 (a) shows the cross section experiment which was designed for beamtime in 2010. It can be seen in Figure 3-5 (a) that each mount contains three cross sections which were positioned close to each other, and the scan direction of the X-ray beam was across the thickness of the MEAs for the first beamtime (2010). Because the incident X-ray beam penetrates to the inner parts through the cross sections, XRF data was from two or three samples and data analysis for a single specific sample was impossible as shown in Figure 3-5 (a).

This problem was recognised and solved for the 2012 beamtime. Figure 3-5 (b) shows the cross section mount and experiment for 2012 beamtime. It can be seen in Figure 3-5 (b) that only one cross section was in each mount and the scan direction was parallel to the length of the MEA samples for the 2012 beamtime. All synchrotron based XRF results of cross section in this thesis are from the type of the experiment which is described in Figure 3-5 (b).

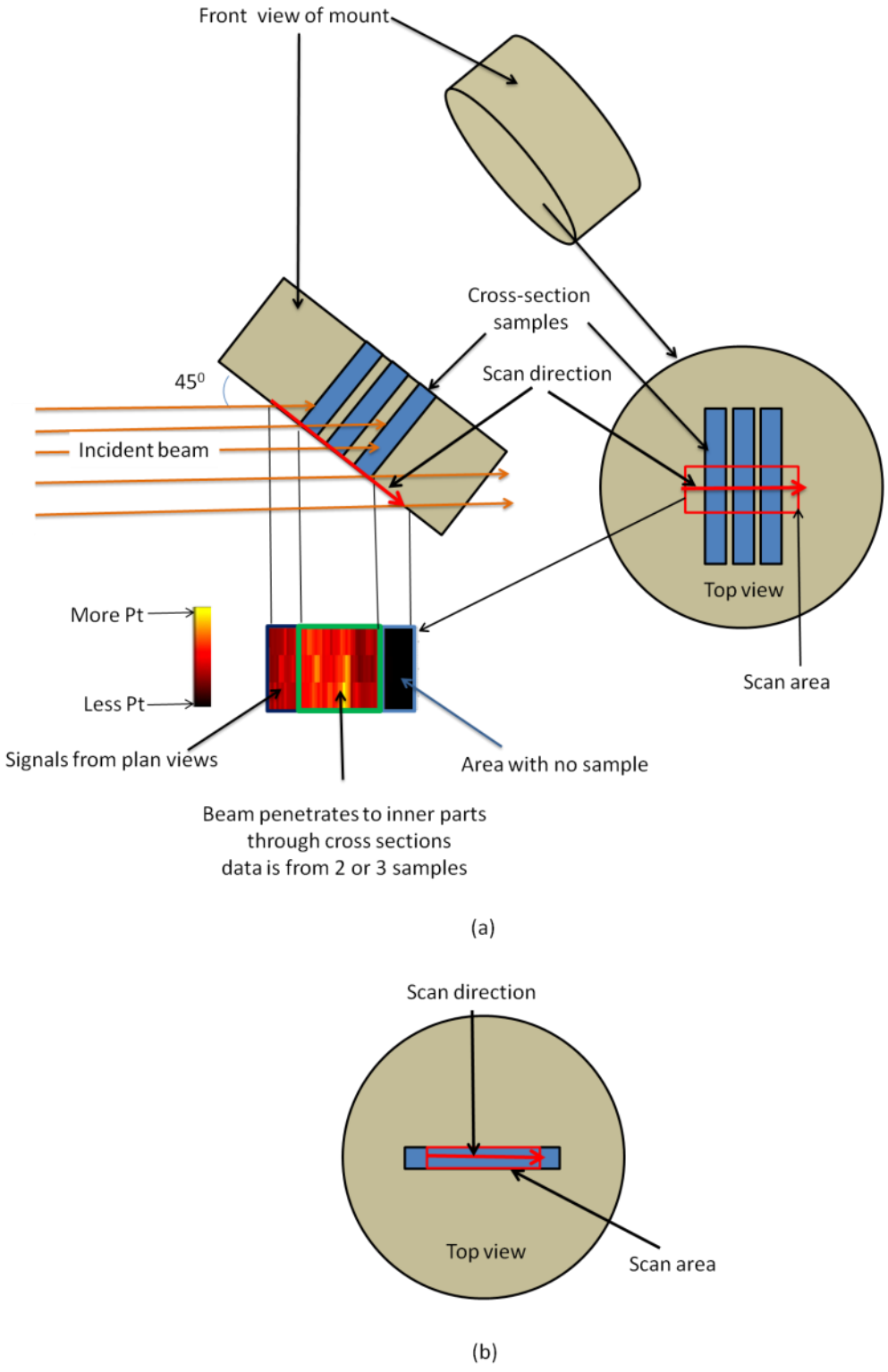

Figure 3-5. (a) Mounts which were prepared for 2010 beamtime contain three cross sections which were positioned close to each other. The X-ray beam penetrates to the inner part through cross sections and signals were from 2 or 3 samples, so data analysis for a single specific sample was impossible. (b) Modified sample and experiment for 2012 beamtime. Images are not to actual scale. The red arrows show scan direction.

3.4.3 Plan view XRF maps of the unused catalyst layer

Plan views of unused catalyst layers on the microporous layer (Figure 3-6) were analysed using SEM/EDS and synchrotron XRF. A 4 mm x 5 mm sample was tested using both SEM imaging at the University of Birmingham and also synchrotron-based micro XRF mapping at Diamond Light Source.

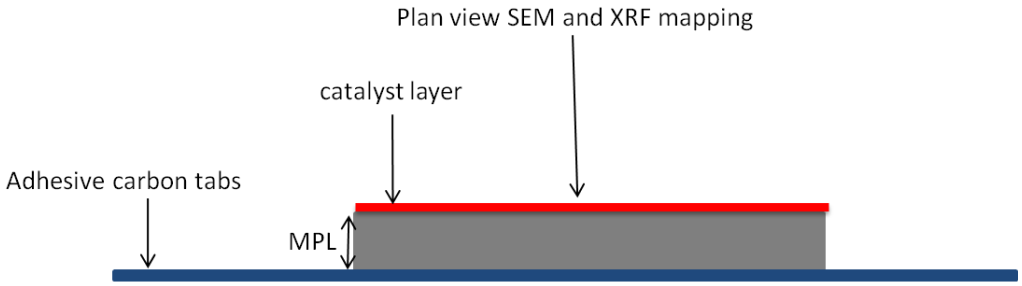

Figure 3-6. Cross section of the catalyst layer on the MPL.

For SEM/EDS measurements it was necessary to use adhesive carbon tabs as shown in Figure 3-6. The XRF results could be affected by the presence of Pt, Fe, Ni, Cu and Cr in the adhesive carbon tabs. Therefore a piece of adhesive carbon tab alone was tested using the same XRF set up. The adhesive carbon tab showed no signs of Pt, Fe, Ni, Cu or Cr.

3.4.4 Modifying the energy of the incident X-ray beam near the Pt edge

Photon counting detectors register the arrival of individual X-ray photons; however, each photon requires a period of time to process during which time no other photons can be recorded. As a consequence there is a maximum count rate associated with energy detector. Because the area density of Pt is many orders of magnitude larger than that of the corrosion products, when the energy of the X-rays is sufficient to excite fluorescence from Pt, the

signal from Pt overwhelms that from any corrosion products which may be present in the MEA. As a consequence, under these circumstances the fraction of signal on the detector arising from corrosion products is small and the signal/noise ratio in the XRF signals is small. Therefore the incident energy was chosen to be slightly below (50 eV) the Pt absorption edge (Pt L_3=11.56 keV) but within the low energy tail of the Pt absorption spectrum. As result the count rate from Pt was significantly reduced and the fraction of signal arising from corrosion products was greatly enhanced (the detector was moved close to the sample to get the total fluorescence to the maximum count rate) this procedure gave improved signal/noise ratio for corrosion products but did prevent quantitative analysis of the Pt concentration.

3.4.5 Analysing synchrotron-based data and fitting synchrotron-based spectra

Synchrotron-based data was recorded in both “rgb” and “mca” formats for 2010 and 2011 beamtime. The data was stored in a “nexus” format for 2012 beamtime.

There are two ways of analysing and visualizing synchrotron-based data. The data can be analyzed using “rgb” files which are created during experiments at Diamond Light Source (the first way). “Rgb” files contain the position of each pixel on a map or line scan and the counts (intensity) of elements. The second way is analysing spectra of pixels from “edf” files (“edf” files can be generated by converting “mca” files) and “nexus” files. These spectra can be analysed using PyMca software. PyMca can be used for mapping additional elements that were not in “rgb” files, peak fitting, resolving of overlapping peaks, background removal and semi-quantitative analysis [143, 144]. Both of these strategies were used during this study and they gave similar results and led to the same conclusions. Only the results of the more accurate strategy [145] (using “edf” and “nexus” files) are presented in this study.

The energy of the incident X-ray beam was chosen slightly below the Pt edge for some experiments (see Table 3-3 and Section 3.4.4). There were obvious Pt peaks in the spectra for these experiments. However, because the chosen energy was slightly below the Pt edge, PyMca software was not able to effectively fit the spectra, especially for Pt peaks. Consequently; for analysing data using PyMca, the incident energy was slightly increased (50 eV) to the Pt absorption energy.

3.4.6 Semi-quantitative analysis of synchrotron-based XRF data

A semi-quantitative approach was used to estimate relative quantities of metals in MEAs for the synchrotron-based data. PyMca software can be used for semi-quantitative analysis of synchrotron-based data. The details of semi-quantitative analysis using PyMca are described by Mosselmans and Geraki [143]. Briefly, a known concentration of an element in a reference sample or in the tested sample is used for calibration. After describing the sample and the experiment setup in PyMca software, the photon "flux" on the sample is adjusted in PyMca software for agreement between the known and measured concentrations. This calculated photon flux can then be used for calculating the relative quantities of the elements of interest.

Because the energy of incident X-ray beams was below the Pt edge (see Section 3.4.4), Pt was not as fully excited as the other metals, thus it was greatly underestimated. Therefore, the Pt loading provided by JM could not be used for the calibration. Consequently, laboratory-based results for Fe ($\mu g/cm^2$) (known values) were compared to synchrotron-based results to calculate a calibration factor ("flux").

In order to calculate the calibration factor ("flux"), the average of Fe counts was calculated for a synchrotron experiment. A pixel that had the same Fe count as the average

was found. The "flux" was adjusted in PyMca for agreement between the laboratory-based Fe value (known Fe ($\mu g/cm^2$)) and the calculated Fe value for the pixel with the average Fe count (for the adjustment several calculations using PyMca were necessary). When the incident energy changed, a new calibration was necessary; thus this calibration process was carried out three times for different experiments (see Table 3-3).

"Area survey scans" and "plan view mapping" (Table 3-3) were carried out on an area of laboratory-based samples and they were calibrated with the Fe ($\mu g/cm^2$) of these laboratory-based samples. "Line scans" were calibrated with the Fe values of the nearest laboratory-based sample as shown in Figure 3-7. The laboratory-based samples with the highest level of Fe were chosen for each calibration. It can be seen in Figure 3-7 that there was about 30 mm distance between the laboratory-based XRF sample and the synchrotron-based XRF sample. However, it will be shown in the results section that in the perpendicular direction (Figure 3-3 (b)) changes in the level of Fe, Ni, Cu and Cr are not significant (see Figure 4-11 (d)).Therefore, the area density of Fe for these two samples (Figure 3-7) can be assumed to be approximately the same. For cross section experiments, the matrix was too complicated for semi-quantitative analysis.

The calculated calibration factor was used for calculating an estimate of Ni, Cr and Cu for the calibration samples and Fe, Ni, Cr and Cu for the other samples. The semi-quantitative results which were calculated from synchrotron-based experiments were close to the laboratory-based XRF results.

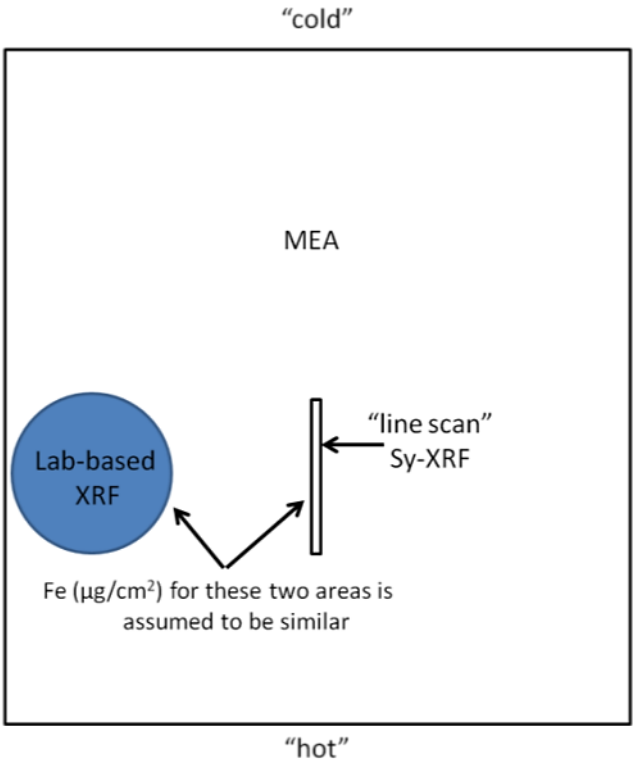

Figure 3-7. Semi-quantitative analysis of line scans. For calibration of line scans, the area density of Fe for laboratory-based XRF is assumed to be similar to the area density of Fe for synchrotron-based XRF in two adjacent areas of the MEA. Sy-XRF is Synchrotron-based XRF. Lab-based XRF is laboratory-based XRF.

3.4.7 Presenting synchrotron-based XRF results

All synchrotron data was analysed and visualized using Igor Pro software version 6.2.2.2 and "rgb" files for the first three years of this PhD. In this thesis, no data from "rgb" format files is presented. In the last year of this PhD, all synchrotron data was reanalysed and visualized using "edf" or "nexus" files and PyMca version 4.6.2. All synchrotron-based data that are presented in this thesis are from "edf" or "nexus" files which are analysed and visualized using PyMca.

Ideally, both synchrotron-based XRF measurements and laboratory-based XRF measurements should have been done over exactly the same area of MEA for the calibration process described in Section 3.4.6. However, the surface area of a laboratory XRF sample

was ~ 907 mm^2 and scanning this area using 60 µm x 60 µm beam size was too time-consuming for synchrotron-based XRF. Hence it was not practical to fully scan laboratory XRF samples using a 60 µm x 60 µm beam size and then to compare the results with the laboratory-based XRF results of the samples for the ideal calibration. Additionally, it was not possible to estimate how the calibration used (described in Section 3.4.6) affects the quantitative results. Therefore, quantitative results were not presented in this thesis.

Analysing and visualizing the semi-quantitative data, "edf" data, "nexus" data or "rgb" data all produced similar images and led to the same conclusions. In this thesis, all synchrotron data are shown as a peak area as determined by fitting and background subtraction of spectra (from "edf" files and "nexus" files) using PyMCa. All laboratory XRF data are presented as $\mu g/cm^2$. When the synchrotron data are presented, the relationship between the laboratory-based XRF data and synchrotron-based XRF data for the common samples is pointed out in the text so that an estimate of the contamination levels for the synchrotron data can be made. This protocol was checked with Diamond Light Source beamline staff and they confirmed that this is sensible [145].

3.5 Electrochemical measurements

3.5.1 Galvanic crevice corrosion tests

The galvanic crevice cell was designed in this study to quantify the galvanic-crevice corrosion in simulated PEMFC environments. The galvanic crevice cell simulates temperature, galvanic corrosion between MEAs and bipolar plates, pressure across the interfaces and the crevice geometry where the bipolar plate and the GDL are in contact. As illustrated in Figure 3-8, in order to make a direct measurement of the galvanic current, the bipolar plate and GDL/MEA were separated by a commercially available electrically

insulated Pall Nylaflo^{TM} Nylon membrane with 127 µm thickness and 0.2 µm porosity size. The Pall Nylaflo^{TM} Nylon membrane was saturated with electrolyte wicked up from a reservoir so that the galvanic current between the bipolar plate and GDL/MEA can be measured with a zero resistance ammeter (ZRA). The reference electrode (RE) was a Saturated Calomel Electrode (SCE) located outside the water bath at room temperature. A 50 cm PTFE Luggin Probe was used to connect the reference electrode through a continuous solution path to the galvanic crevice cell solution. The galvanic current (I) and potential (E) were measured using an ACM Instruments potentiostat and GILL AC serial No. 1408 software. The solution was 1 mM NaCl and 1 mM H_2SO_4 (see Sections 2.5.1). In order to simulate the pressure across the interface in a stack, 1 MPa pressure was applied to the metallic sample/separator/GDL interface. In addition, the compressed area simulates the approximate geometry of a bipolar plates flow field channel.

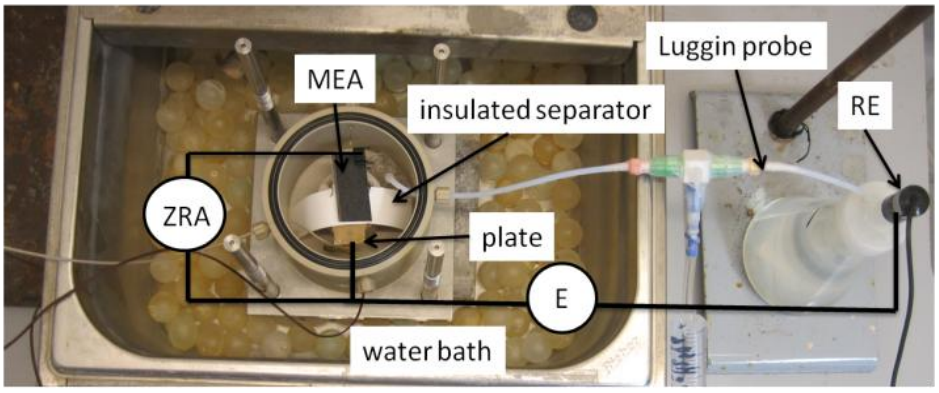

Figure 3-8. Galvanic crevice cell: in the galvanic crevice cell the metallic sample and GDL/MEA were separated by a porous insulated separator in order that the galvanic current between the two could be measured with a zero resistance ammeter (ZRA). Potential of the couple was monitored against SCE reference electrode (RE).

The galvanic crevice cell was heated using water bath. A thermocouple connected to an YCT YC-747UD data logger thermometer was used to measure temperature inside the

galvanic crevice cell for the duration of each test. The temperature was recorded with a PC using TEMP MONITOR_S2 software associated with the thermocouple. Tests involved room temperature and 80 °C cycles as presented in Figure 3-9 (also see Section 6.6 for an attempt at a shorter cycle). A thread was put inside the tubing that kept the reference electrode and the cell connected during tests (see Section 3.5.2). After each heating period, the temperature was rapidly decreased by pouring cold water in the water bath. For safety reasons, experiments were carried out in a fume cupboard. Experiments were carried out in an air atmosphere and simulated PEM fuel cells cathode.

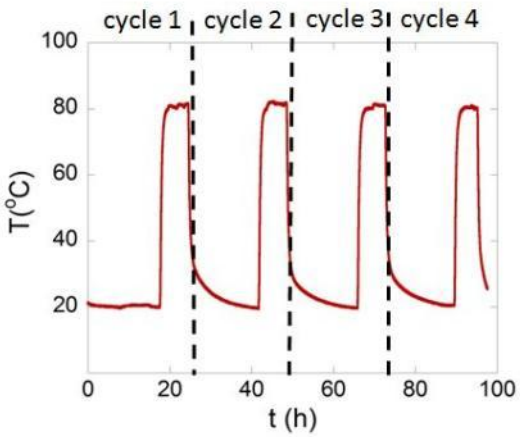

Figure 3-9. Room temperature and 80 °C cycles during galvanic crevice cell tests.

3.5.2 Problems and challenges with running the galvanic crevice cell at elevated temperatures

In the early stages of running the galvanic crevice cell at elevated temperatures, several measurements failed. This was due to the formation of bubbles in the reference electrode (RE) tubing during heating, which disconnected the cell and the reference electrode. An attempt to restore the connection was made by injecting solution into the tubing as shown in Figure 3-10; however injecting solution could possibly affect results (see potential variations

in Figure 3-10 when the solution was injected in the tubing). Later, this problem was solved, a thread was put inside the tubing, which kept the reference electrode and the cell connected during tests. All the electrochemical results that are presented in this thesis are measured with a thread inside the tubing.

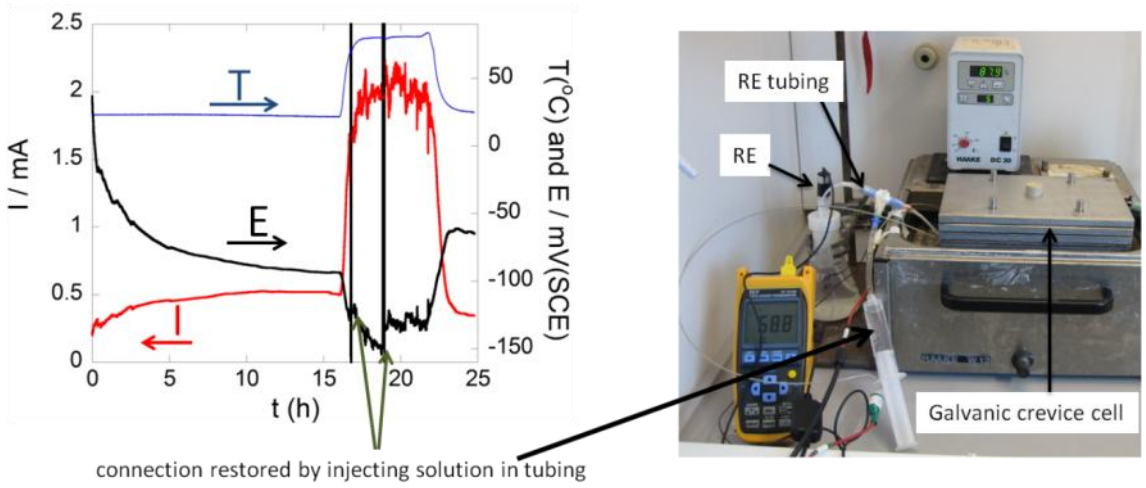

Figure 3-10. The problem of running the galvanic crevice cell at the elevated temperature. An attempt to restore the connection was made by injecting solution into the tubing.

3.5.3 Materials selection for the galvanic crevice cell parts

The cell parts are shown in Figure 3-11. Each part is labelled with a number. Part 1, 3, 8 and 9 are made of 304 stainless steel and the other parts are made of PEEK. Several factors were considered for the material selection. Because there was considerable pressure (1 MPa) on the samples at the elevated temperature, the mechanical properties of the cell materials should satisfy the required mechanical strength and creep resistance. Additionally, the materials should be easily machined. The price of the materials and their commercial availability in the required shapes were other factors that were considered for the material selection.

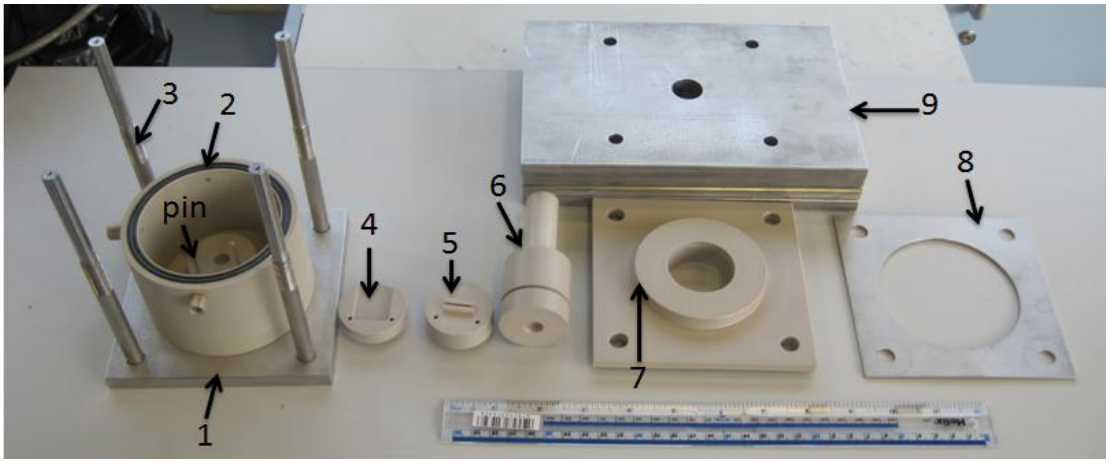

Figure 3-11. Cell components prior to assembly (component numbers are those referred to elsewhere in this thesis).

The materials of the parts which were in contact with the solution and samples should be inert and stable in the test condition (acidic solutions at 80 ºC) as well as electrically insulate. These parts were Parts 2, 4, 5, 6, 7 and the pin in Figure 3-11. No metallic material was in contact with the solution to prevent possible corrosion and releasing metallic contamination in the solution. Glass was one of the candidate materials. A corrosion cell which was made of glass was used to investigate the corrosion of bipolar plates by Tawfik et al. [52]. However, glass reacts with HF and there was a possibility of leaching fluoride ions from the membrane in the galvanic crevice cell. Therefore PEEK was chosen for parts which were in contact with solutions or samples. PEEK was not commercially available in the necessary shape and size for part 2 in the preliminary design and the cell design was adjusted (redesigned) to the commercially available rod sizes of the PEEK for this part.

The material for parts which were not in the contact with solution (i.e. Part 1, 3, 8 and 9 in Figure 3-11) should be also corrosion resistance because they were used in the oven or water bath which could be corrosive environment in the elevated temperature. Therefore these parts were made of a cheap stainless steel i.e. 304 SS. The deionized water was used in the water bath to eliminate the possible pitting corrosion of this metal in the water bath.

3.5.4 Cell design

A considerable amount of time (about a year) was spent on developing and designing the galvanic crevice cell in this PhD. Because no similar design was reported, the design required problem solving, innovation, and creativity.

The assembled cell and a cross section are presented in Figure 3-12. Details of the electrodes and contact region are shown in Figure 3-13. Numbers on figures are the part numbers shown in Figure 3-11. A downward pressure of 1 MPa is applied (by weight) with metal plates at the top of the cell. Within the cell is a solution reservoir for providing electrolyte to the separator.

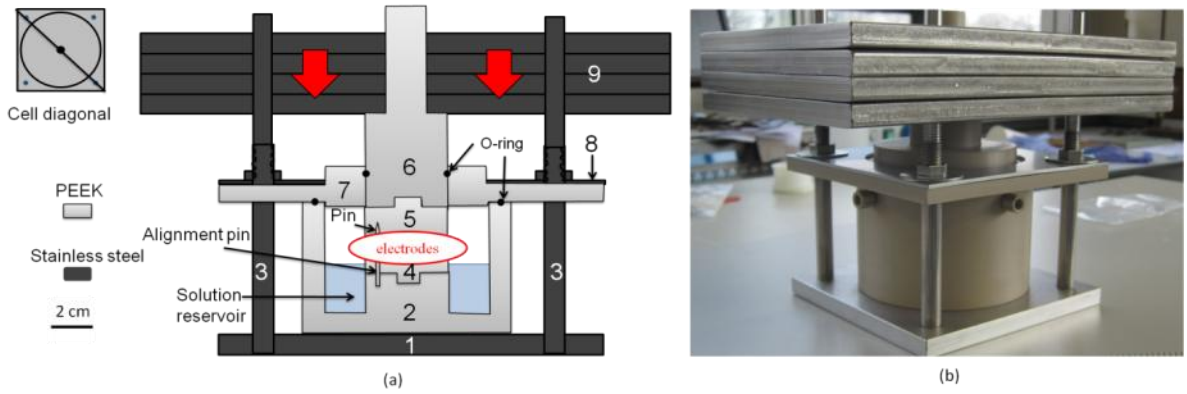

Figure 3-12. The assembled cell, (a) diagonal cross section and (b) photograph (numbers refer to part numbers in Figure 3-11).

3.5.5 Cell plan view, details of contact area and ports

Figure 3-13 shows sample holder (part 4), channel simulator (part 5), plan view and cross sections of the contact area and electrodes. The metallic sample sits in the sample holder (part 4) and overlaps with the GDL/MEA in the contact area (connections are made on opposite sides). An insulating separator material separates the two electrodes, and extends either side into the solution reservoir, wicking up electrolyte. Part 5 (see Figure 3-13) presses

on the GDL/MEA and its shape ensures that there are regions of high and low pressure contact to simulate the flow field channels in the GDL.

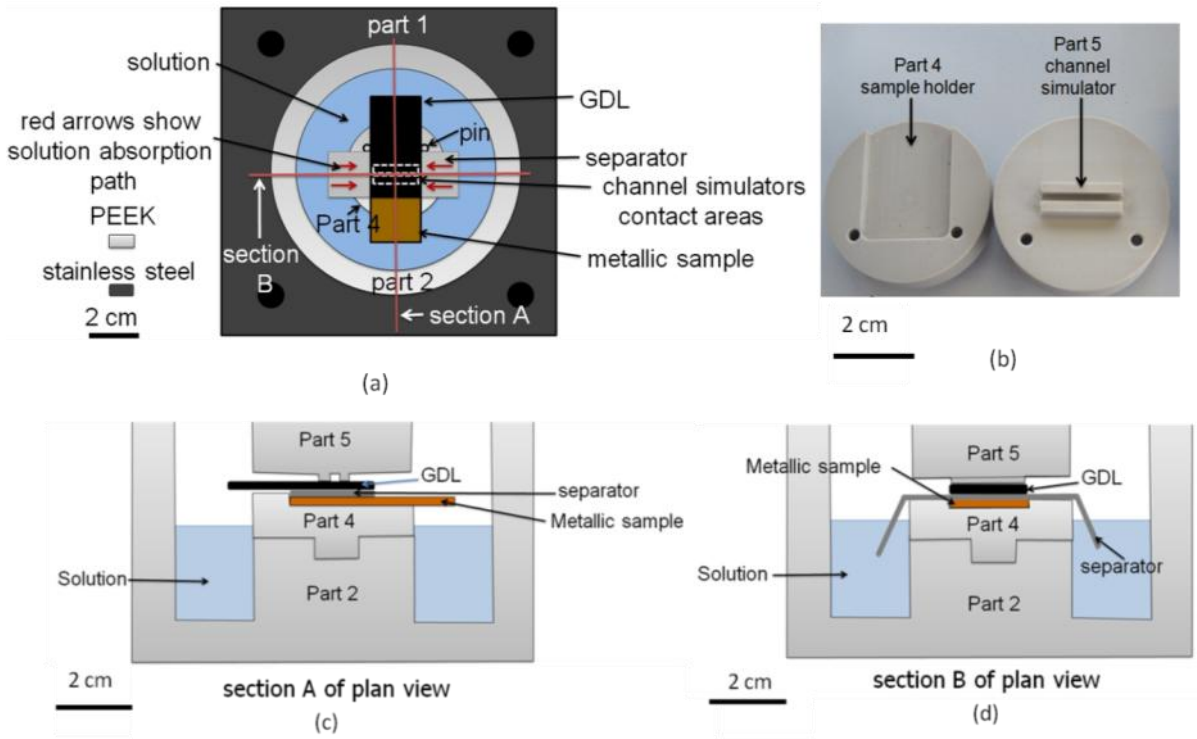

Figure 3-13. Contact area and electrodes in the cell: (a) plan view; (b) the sample holder (part 4) and the channel simulator (part 5), (c) vertical section A of plan view showing channel simulator pressing GDL/separator/metallic sample contact area (d) horizontal section B of plan view showing GDL/separator/metallic sample contact area and how separator wicks up electrolyte from a reservoir. Numbers refer to parts shown in Figure 3-11.

Figure 3-14 shows the port positions. The reference electrode sits outside the cell and is connected to the solution reservoir with a PTFE Luggin probe.

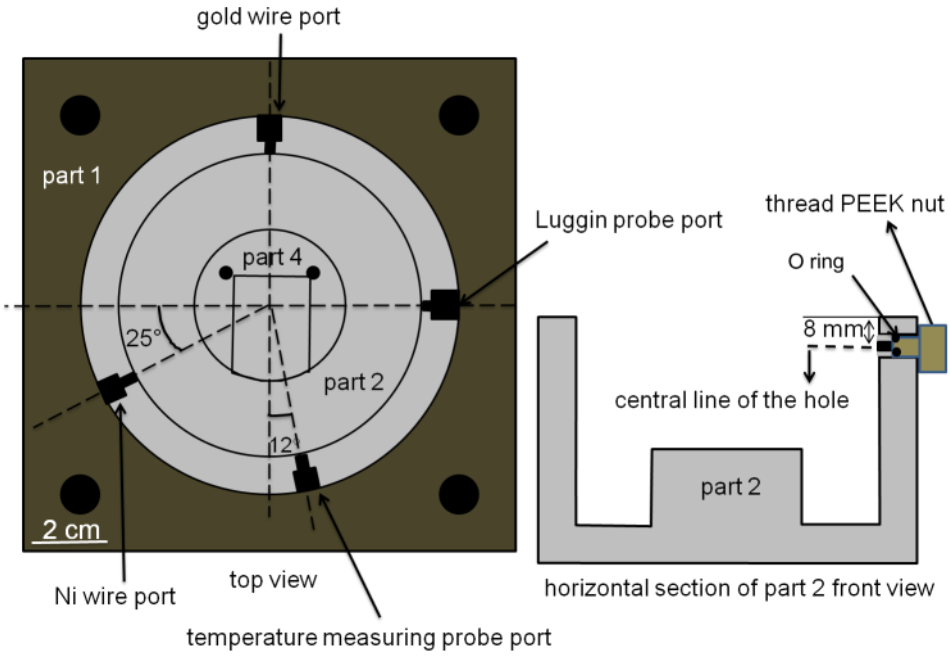

Figure 3-14. Plan view of cell showing positions of ports.

3.5.6 Considerations for the design of the galvanic crevice cell

The part 4 and part 2, as well as part 5 and part 6, are designed as separate pieces for the following reasons. The option of replacement for the parts which are under the risk of deformation is considered in the design. Parts 4 and 5 are under pressure and there is a possibility of deformation for these parts (Figure 3-13). Parts 4 and 5 can be replaced if they deform during long-term operation and this is much cheaper than making a new cell. In addition, Parts 4 and 5 can easily be redesigned and replaced for different sizes and shapes of test samples without the need to redesign the whole galvanic crevice cell. Additionally, the design considered easy assembly of the cell parts and easy use of the cell. The alignment pins help for easy assembly and also stop undesirable movement of Parts 4 and 5 (see Figure 3-11, Figure 3-12 and Figure 3-13).

The safety of using the galvanic crevice cell is also considered. The edges of Parts 1, 9 and 8 are curved to prevent possible hand cuts during assembly. In addition, the design is

modified to make the machining easy for the workshop. Moreover, overall dimensions of the galvanic crevice cell are designed to be suitable for use in the available oven or water bath in the laboratory.

The 3D and 2D drawings of the cell parts were drawn using CoCreate Modelng Personal Edition 3.0 software. The parts were machined at CNC Precision Limited, located in Redditch, Worcestershire.

In addition to the considerations presented here, there were other considerations for designing the cell and defining the testing protocol and they will be presented in Section 6.7.3.

3.5.7 Crevice separator

Pall Nylaflo^{TM} Nylon membrane with 127 µm thickness and 0.2 µm porosity size was used to separate the GDL or MEA and metallic sample. The Pall Nylaflo^{TM} Nylon membrane is hydrophilic, thin, porous, chemically inert and stable in the test solution and conditions, electrically insulate, it is able to absorb solution to keep the contact areas wet enough in order to continue electrochemical process between the GDL or MEA and metallic sample while they are insulated electrically [146]. The dimensions of the separators are shown in Figure 3-15, the width of the cut samples (more than 25 mm) were larger than the test area (20 x 20 mm) to make sure that the MEA and 316L stainless steel were not in direct electrical contact.

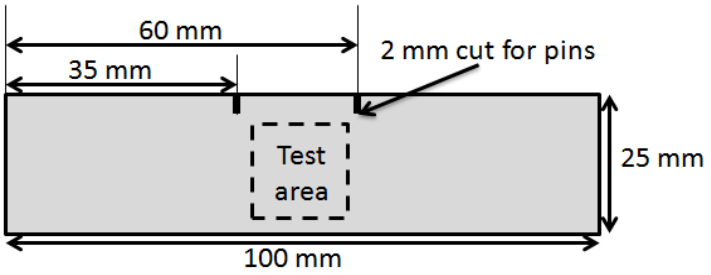

Figure 3-15. the dimensions of cut Pall Nylaflo™ Nylon used in the galvanic crevice cell.

3.6 SEM/EDS and optical microscopy

Optical images were taken using Zeiss AxioVision optical microscope at Diamond Light Source. A JEOL 6060 SEM equipped with Oxford Inca 300 EDS were used for SEM and (energy dispersive X-ray spectroscopy) EDS analysis of MEAs respectively. During EDS analysis accelerating voltage was 20 kV and working distance was 10 mm.

4 Macroscopic distribution of corrosion products in MEAs used in PEMFC stacks

4.1 Introduction

As explained in Section 2.11, measuring corrosion products in MEAs has been used to evaluate corrosion resistance of metallic bipolar plates. XRF is one of the methods that has been used to detect levels of corrosion products in MEAs [14, 15, 20-24, 125].

Corrosion of bipolar plates and the distribution of corrosion products in a MEA can be affected by factors such as water or temperature distribution in the cells during operation. The levels of corrosion and contamination can also be different on the cathode and anode sides of bipolar plates. However, to our knowledge, the distribution of contaminants in a MEA has not been previously investigated. In this chapter, the distribution of contamination in MEAs after long duration durability tests has been studied using laboratory-based and synchrotron based XRF. This chapter shows the results of 92 laboratory-based XRF and synchrotron-based XRF measurements. The focus of this chapter is on the macroscopic scale distribution of contamination in MEAs. The next chapter will focus on the microscopic scale distribution of contamination within MEAs.

4.2 Laboratory-based XRF results

Figure 4-1 to Figure 4-4 show the area density of Fe, Ni, Cu and Cr for stack 9-1000-78 and stack 9-1941-69, measured with laboratory-XRF (which samples a circle of diameter 34 mm). Stack 9-1000-78 was run for 1000 h at 78 °C and stack 9-1941-69 was run for 1941h at 69 °C. It can be seen that Fe and Ni are the predominant contaminants.

Figure 4-1 and Figure 4-2 show the area density of Fe and Ni in MEAs from stack 9-1000-78 and stack 9-1941-69. It can be seen that the levels of Ni and Fe in MEAs from these two stacks are higher than those in unused (control) MEAs.

Figure 4-1 and Figure 4-2 show that in all cases, the Ni levels and the Fe levels in the "hot" areas of the MEAs are significantly greater than those in the "cold" areas. It is also generally the case that higher Fe levels are found on the cathode side than the anode. However, in most cases, the levels of Ni on the anode and cathode sides of MEAs are the same within experimental error. The cell-to-cell variation in Ni levels and Fe levels within a stack is considerable, so it is not possible to identify any clear difference in contamination levels between the two stacks.

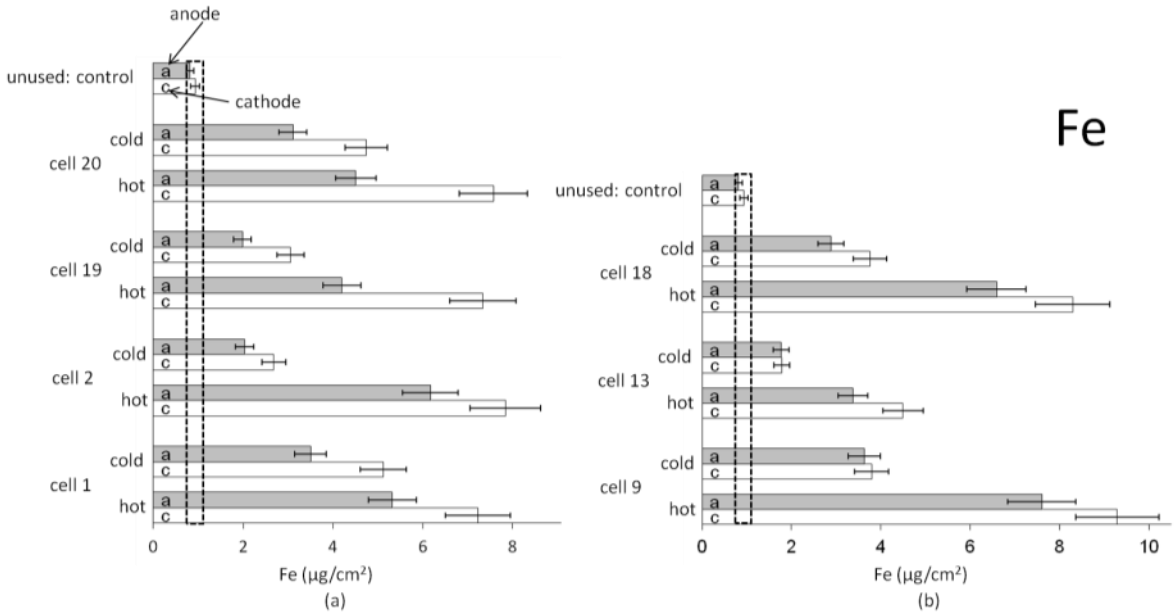

Figure 4-1. Laboratory XRF measurements of the area density of Fe (µg/cm^2) in MEAs operated in (a) stack 9-1000-78, 1000 h/78 °C, (b) stack 9-1941-69, 1941h/69 °C. Bipolar plates were uncoated 904L SS and the MEA was BCS type; the Fe level in an unused BCS MEA is shown for comparison. The broken lines show the range of Fe levels in the unused MEA. For each cell, MEA samples were chosen from "hot" and "cold" areas of MEAs; "a" is the anode side and "c" is the cathode side of each MEA. Ten percent of measured area density is considered as errors [140].

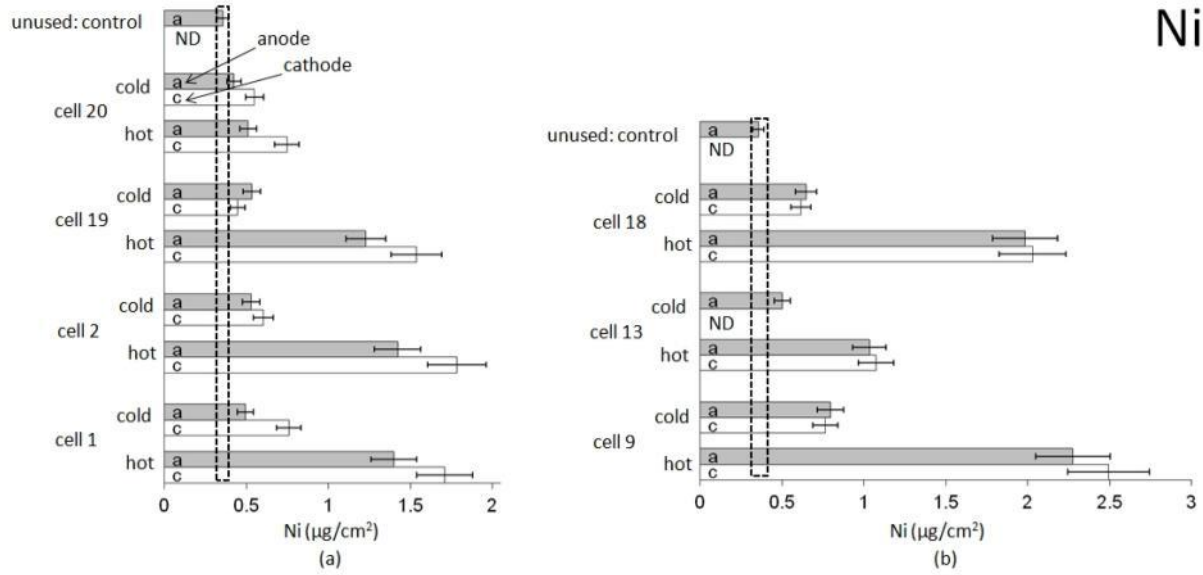

Figure 4-2. Laboratory XRF measurements, area density of Ni (µg/cm^2) in MEAs operated in (a) stack 9-1000-78, 1000 h/78 °C, (b) stack 9-1941-69, 1941h/69 °C. Bipolar plates were uncoated 904L SS and the MEA was BCS type; the Ni level in an unused BCS MEA is shown for comparison. The broken lines show range of Ni levels in the unused MEA. For each cell, MEA samples were chosen from "hot" and "cold" areas of MEAs; "a" is the anode side and "c" is the cathode side of each MEA. Ten percent of measured area density is considered as errors [140]. "ND" indicates that Ni was not detected, i.e. it was below the detection limit, which is estimated to be 0.2 µg/cm^2.

The area density of Cu in MEAs from stack 9-1000-78 and stack 9-1941-69 are shown in Figure 4-3. It can be seen that in Figure 4-3 (a), for stack 9-1000-78, the Cu levels in the MEAs are similar to the levels of Cu found in the unused MEA. For stack 9-1941-69, which ran for almost twice the length of time as stack 9-1000-78, the measurements show that the Cu levels appear to be slightly higher than the level of Cu in unused MEA, (Figure 4-3 (b)). Furthermore, the Cu levels in the "hot" area of the MEAs are not significantly different from the Cu levels in the "cold" area of the MEAs. The difference of Cu contamination in anode and cathode is not significant and the levels are similar to those in the unused sample.

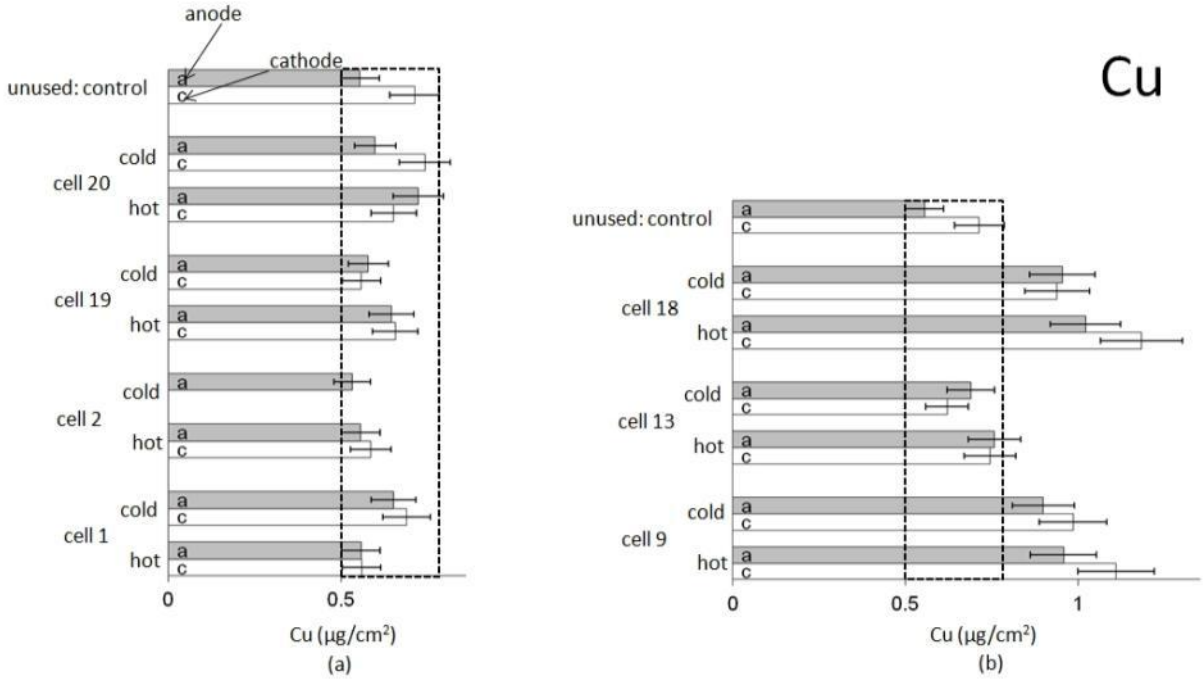

Figure 4-3. Laboratory XRF measurements, area density of Cu (µg/cm^2) in MEAs operated in (a) stack 9-1000-78, 1000 h/78 °C, (b) stack 9-1941-69, 1941h/69 °C. Bipolar plates were uncoated 904L SS and the MEA was BCS type; the Cu level in an unused BCS MEA is shown for comparison. The broken lines show range of Cu levels in the unused MEA. For each cell, MEA samples were chosen from "hot" and "cold" areas of MEAs; "a" is the anode side and "c" is the cathode side of each MEA. Ten percent of measured area density is considered as errors [140].

Cr contamination levels in MEAs from stack 9-1000-78 and stack 9-1941-69 are presented in Figure 4-4. The Cr levels are below the detection limit (0.2 µg/cm^2) for most of the measurements, including measurements carried out on the unused MEA. For both stacks, wherever Cr is detected, the values tend to show higher level of Cr in the cathode side than the anode side and in the "hot" area than the "cold" area.

The difference between used MEAs and unused MEA for Cr and Cu levels are not as large as the difference between used MEAs and unused MEAs for Fe and Ni levels. The cell to cell variations for Cu and Cr within a stack are as significant as the difference between two stacks. However, stack 9-1941-69 which was run for a longer time compared with stack 9-1000-78 tend to show higher levels of Cu or Cr (where Cr contamination is detected).

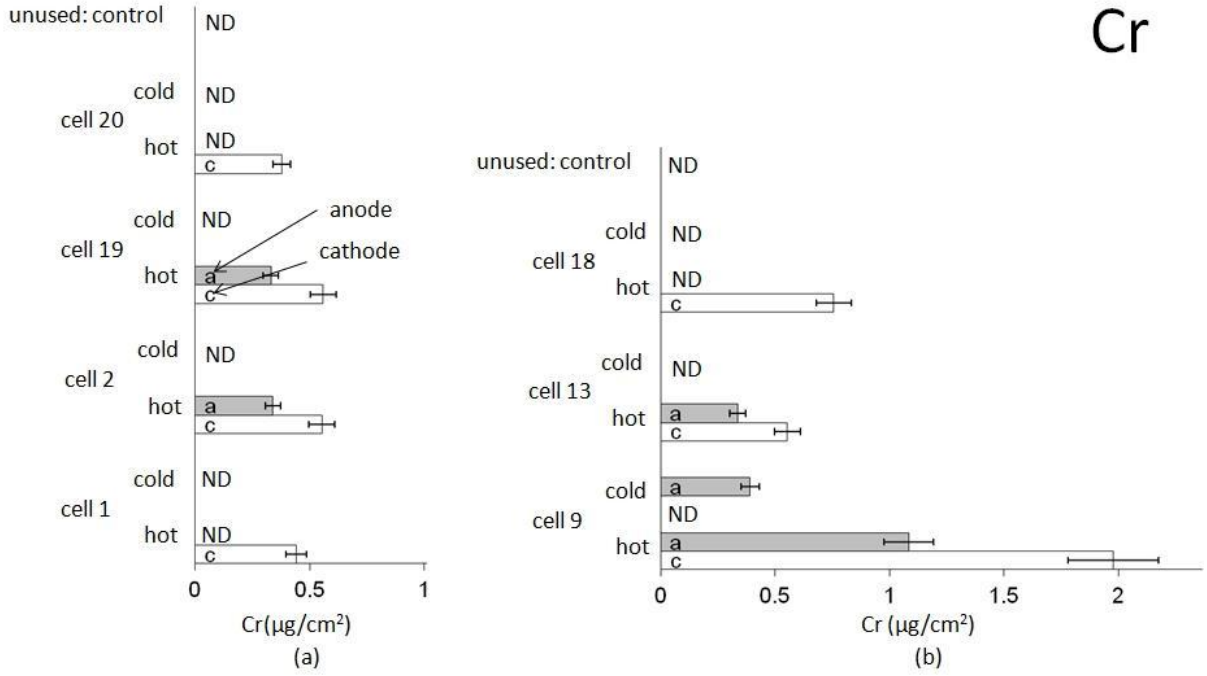

Figure 4-4. Laboratory XRF measurements, area density of Cr (µg/cm^2) in MEAs operated in (a) stack 9-1000-78, 1000 h/78 °C, (b) stack 9-1941-69, 1941h/69 °C. Bipolar plates were uncoated 904L SS and the MEA was BCS type; the Cr level in an unused BCS MEA is shown for comparison. For each cell, MEA samples were chosen from "hot" and "cold" areas of MEAs; "a" is the anode side and "c" is the cathode side of each MEA. Ten percent of measured area density is considered as errors [140]. "ND" indicates that Cr was not detected, i.e. it was below the detection limit, which is estimated to be 0.2 µg/cm^2.

Figure 4-5 shows the area densities of Fe, Ni, Cr and Cu in MEAs which were used in stack 9c1-2700-76. The description of the results for this stack is similar to the description of the results for stack 9-1000-78 and stack 9-1941-69 (Figure 4-1 to Figure 4-4) and the results for this stack are not described here in order to avoid unnecessary repetition.

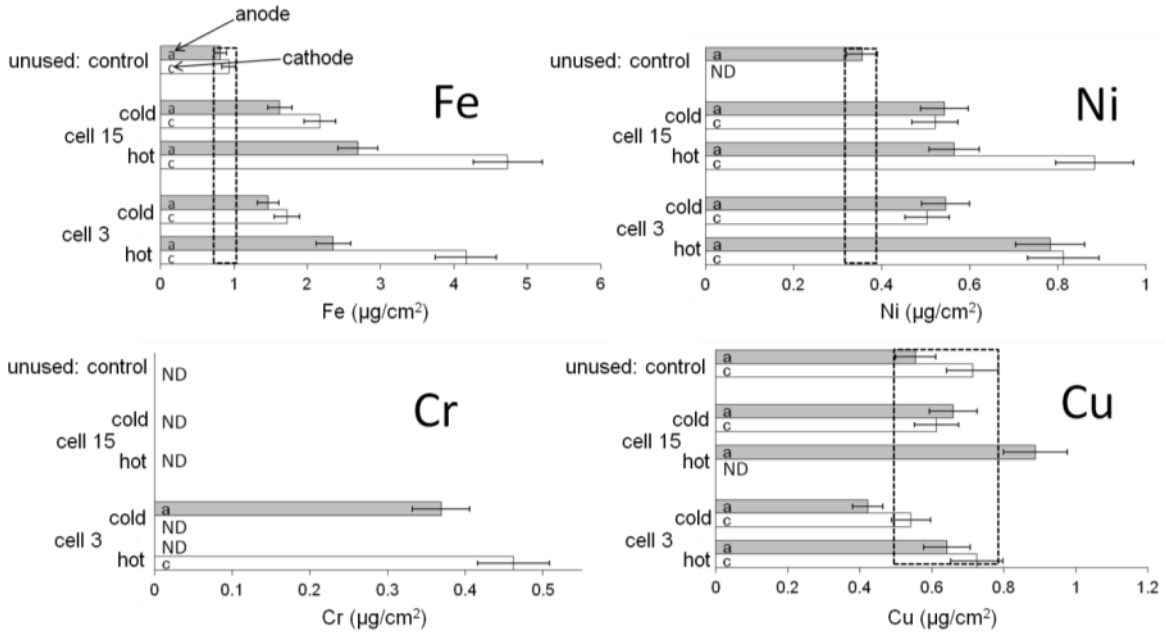

Figure 4-5. Laboratory XRF measurements, area density of Fe, Ni, Cr and Cu (µg/cm^2) in MEAs operated in stack 9c1-2700-76 for 2700 h/76 °C. Bipolar plates were C1 coated 904L SS and the MEA was BCS type; the Fe, Ni and Cu levels in an unused BCS MEA are shown for comparison. The broken lines show range of Ni levels in the unused MEA. For each cell, MEA samples were chosen from "hot" and "cold" areas of MEAs; "a" is the anode side and "c" is the cathode side of each MEA. Ten percent of measured area density is considered as errors [140]. "ND" indicates that Ni, Cr or Cu was not detected, i.e. it was below the detection limit, which is estimated to be 0.2 µg/cm^2.

Figure 4-6 shows the laboratory XRF results of MEAs from stack 9-1360-65 and stack 3c2-1515-67. For these two stacks control MEAs were not available. The trends which are observed for these two stacks, generally with few exceptions, are similar to the previously described stacks. The exceptions are that Ni for the majority of the measurements (though not for all of the measurements) shows higher levels in the hot areas than the cold areas and the difference of Fe contamination in anode and cathode is not as obvious as in previous stacks.

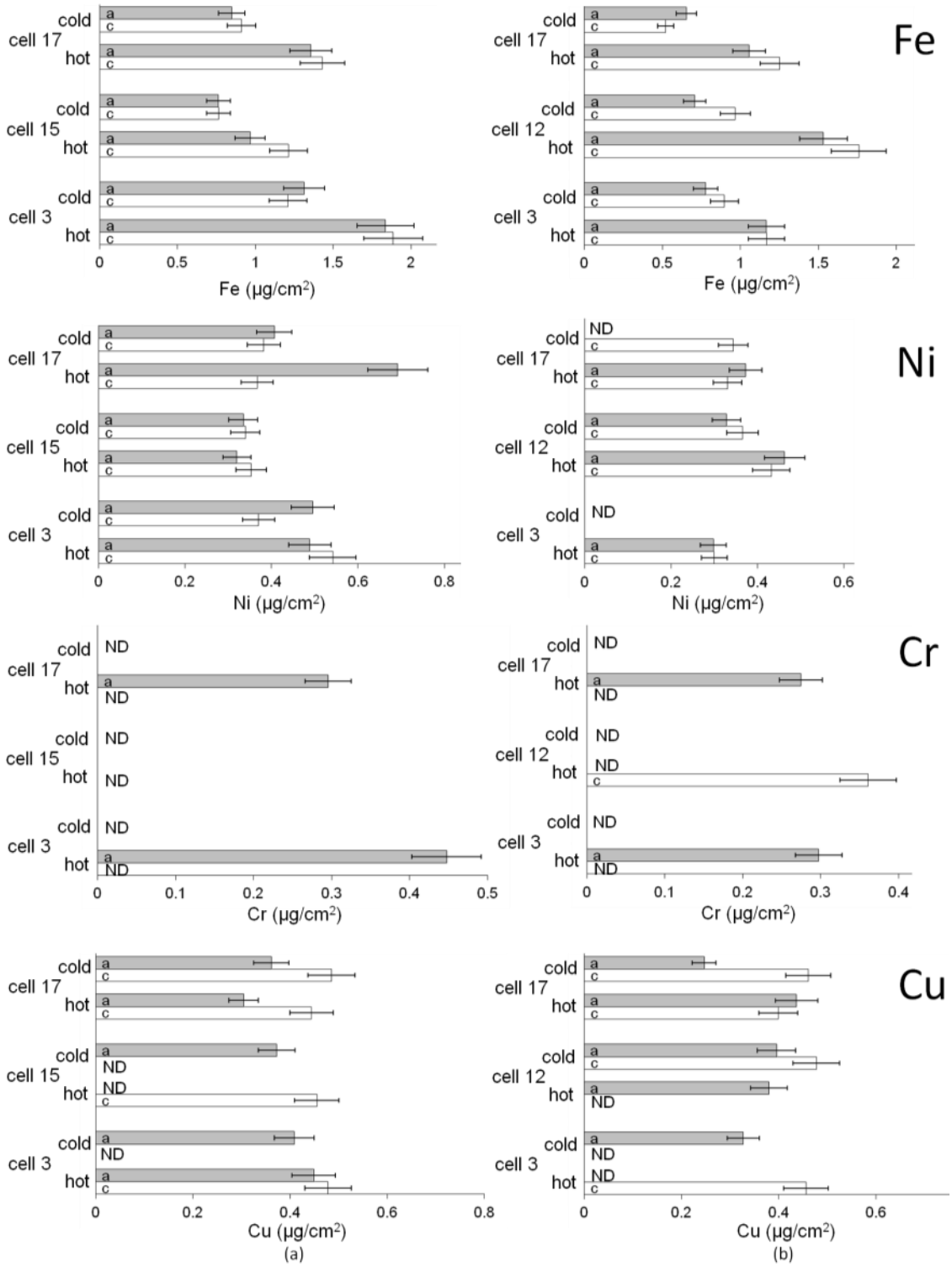

Figure 4-6. Laboratory XRF measurements, area density of Fe, Ni, Cr and Cu (µg/cm^2) in MEAs operated in (a) stack 9-1360-65 1360h/65 °C with uncoated 904L SS bipolar plate, (b) stack 3c2-1515-67 1515h/67°C with C2 coated 316L SS bipolar plate, MEA was CCM type (control was not available); For each cell, MEA samples were chosen from "hot" and "cold" areas of MEAs; "a" is the anode side and "c" is the cathode side of each MEA. Ten percent of measured area density is considered as errors [140]. "ND" indicates that Fe, Ni, Cr and Cu were not detected, i.e. it was below the detection limit, which is estimated to be 0.2 µg/cm^2.

4.3 Synchrotron XRF results

4.3.1 Area survey scan results

Synchrotron area survey scans were carried out upon a number of MEAs that had been previously studied by laboratory XRF as shown in Figure 3-3 (a) of the experimental method chapter. Figure 4-7 and Figure 4-8 present the results of the "area survey scan" experiment. Figure 4-7 shows the XRF counts measured for a series of line scans on an MEA from stack 9-1000-78 cell 20, for a "hot" area on the cathode side. The line scans used a 60 µm x 60 µm beam size and were 15 mm long and separated by 2.5 mm as shown in Figure 3-3 (a) of the experimental chapter and Figure 4-7. In Figure 4-7, the heights of the scans have been increased so that they are visible; however, the position of the scans within the scan area is to scale. The scan traversed a series of straight flow channels, and was designed to search for association between the channels and the contamination. It can be seen that the variation in contamination is considerable, but does not show any consistent pattern, and no correlation with channel location could observed. There is also no consistent correlation between the contamination levels for the different elements. Similar results (not shown) were obtained for cell 1.

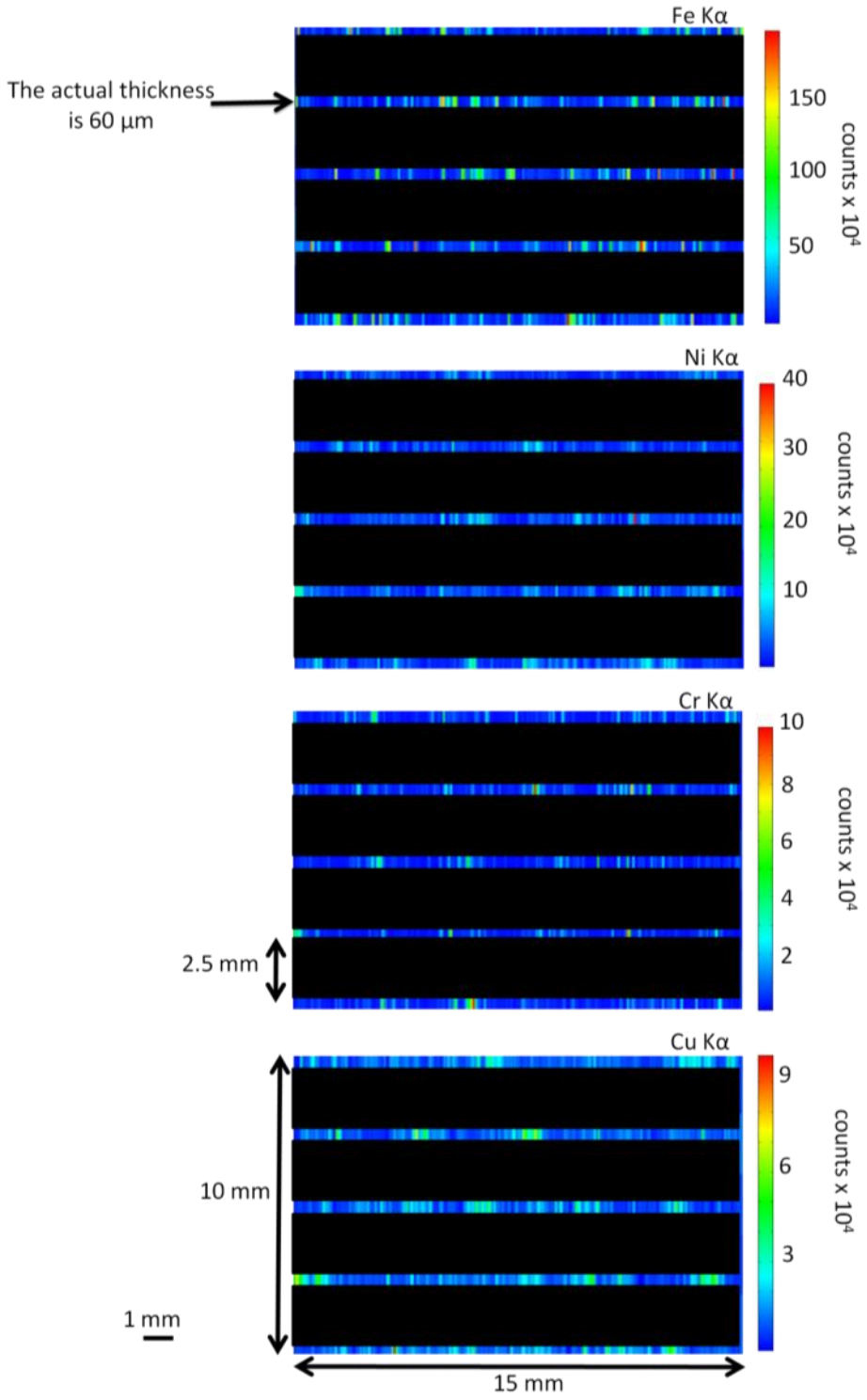

Figure 4-7. Synchrotron XRF, series of line scans ("area survey") for stack 9-1000-78 cell 20 "hot" area cathode side. The line scans were 15 mm long and were separated by 2.5 mm. The apparent heights of the scans in the figure have been increased so that they are visible; however, the position of the scans within the scan area is to scale. The scans traverse a series of straight flow channels of bipolar plate, and were designed to search for relationship between the channels and the distribution of contamination. The incident energy was 10 keV and beam size was 60 µm x 60 µm (see Figure 3-3).

Figure 4-8 shows the average number of counts per pixel for the “area survey scan” results of MEAs from cell 1 and cell 20 of stack 9-1000-78 together with laboratory XRF measurements of the same samples, (Figure 4-1 to Figure 4-4) shown for comparison. There is a good correlation between laboratory results and synchrotron results, and it is clear that the sensitivity of the synchrotron measurements is considerably higher than the laboratory measurements. This is particularly noticeable for Cr levels, which were mainly below the detection limit for the laboratory XRF.

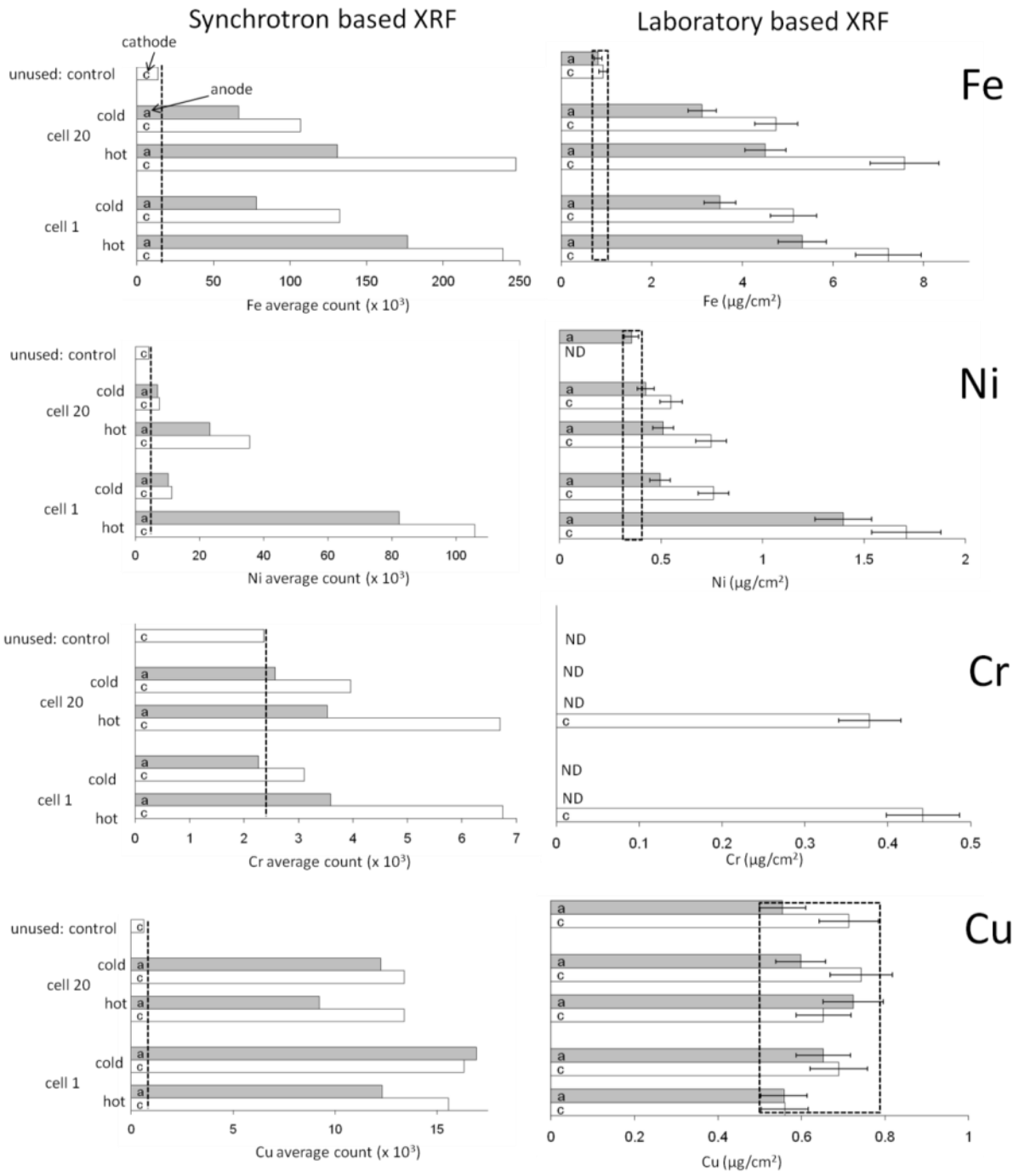

Figure 4-8. Synchrotron XRF average counts for area survey scan results for cell 1 and cell 20 of stack 9-1000-78 showing the average number of counts per pixel for Fe, Ni, Cr and Cu. The incident energy was 10 keV and beam size was 60 µm x 60 µm. Laboratory XRF measurements from the same samples are presented for comparison. The unused: control is the levels in an unused BCS MEA shown for comparison. For synchrotron experiments only the cathode side of unused MEA is measured. The broken lines show the range of contaminant levels in the unused MEA. For each cell, MEA samples were chosen from two areas of MEAs i.e. "hot" and "cold" areas, "a" is the anode side and "c" is the cathode side of MEA. ND is not detected.

4.3.2 Line scan results

Figure 4-9 to Figure 4-12 present the results of "line scan" experiments carried out using a 60 µm x 60 µm synchrotron X-ray beam. In most cases these were scans from "cold" towards "hot" areas of MEAs ("cold/hot" scan) and a scan was also performed in the perpendicular direction to the cold/hot scans, as illustrated in Figure 3-3 (b) and Figure 3-3 (c) of the experimental method chapter. A short scan was also carried out on an unused MEA for comparison.

Figure 4-9 (a) shows a cold/hot scan and Figure 4-9 (b) shows a scan that is perpendicular to the cold/hot scan at the ~50 mm position of the MEA from stack 9-1941-69 cell 18. Figure 4-9 (c) shows a line scan of the unused MEA for comparison. The top images are shown with a linear scale and the bottom images are shown with logarithmic scales to show the Cr, Ni and Cu scans more clearly. It is evident that the used MEA shows higher levels of contaminants than unused MEA. There are considerable variations in levels of contamination in both used and unused MEAs with measurements of up to 5 times the average value.

In the cold/hot scan (Figure 4-9 (a)), the cold area (0-30 mm) shows lower contamination than the hot area from about 80 mm onwards with a gradual transition between two. There is no significant variation in contamination across the unused MEA (Figure 4-9 (c)). The perpendicular scan (Figure 4-9 (b)) shows similar level of contamination throughout, and the contaminant levels are close to those of the cold/hot scan at ~50 mm (Figure 4-9 (a)) and much higher than those of unused MEA (Figure 4-9 (c)). Figure 4-10 shows regions of Figure 4-9 with expanded horizontal axes. It can be seen that in both the unused and used MEAs the local spots that give a high count rate are very small, sometimes even single points.

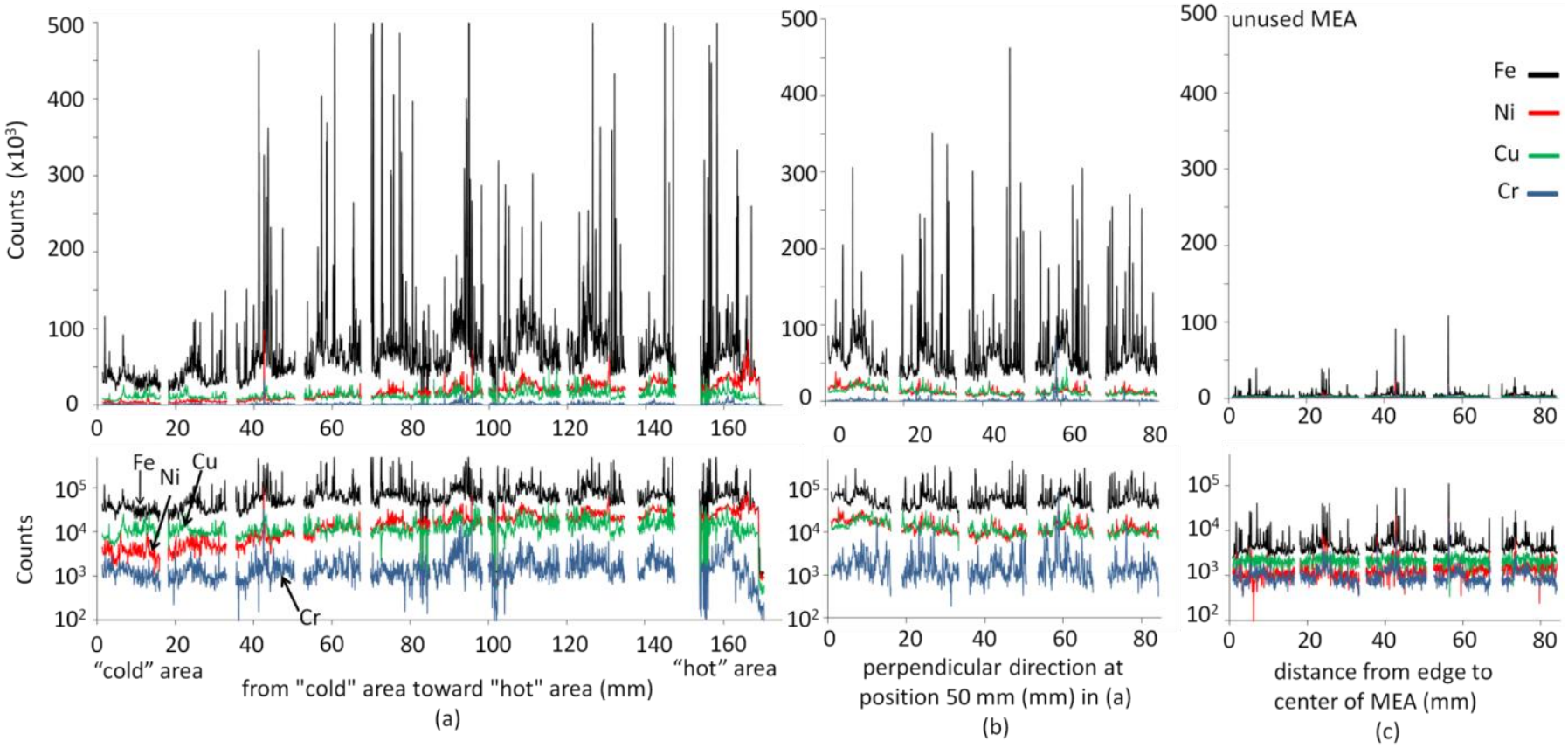

Figure 4-9. Synchrotron XRF line scans (a) "cold" area to "hot" area, (b) perpendicular to (a) at ~ 50 mm, for the MEA from stack 9-1941-69 cell 18; (c) line scan from an unused MEA. The cathode side of each MEA faced the incident beam. The incident energy was 11.54 keV and the beam size was 60 µm x 60 µm

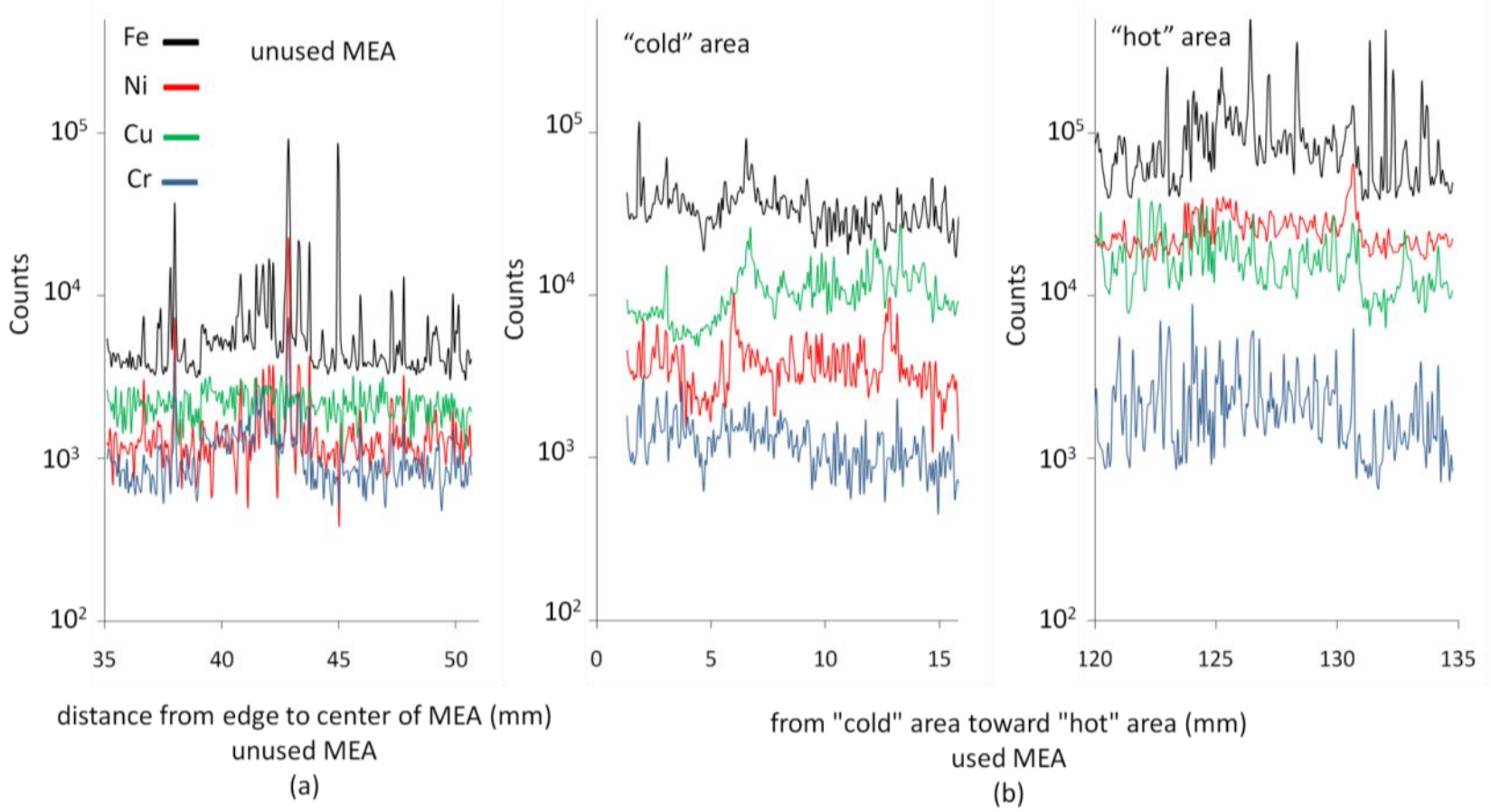

Figure 4-10. Synchrotron XRF. Regions from Figure 4-9 with extended horizontal axis. Line scan (a) 35-51 mm of unused MEA and (b) 0-16 mm of "cold" area and 120-136 mm of "hot" area for stack 9-1941-69 cell 18. The cathode side of each MEA faced the incident beam. The incident energy was 11.54 keV and the beam size was 60 µm x 60 µm.

Figure 4-11 and Figure 4-12 show the average counts from synchrotron XRF line scans of the type shown in Figure 4-9 and Figure 4-10. Figure 4-11 also compares the average counts from synchrotron XRF line scans with laboratory measurements.

Figure 4-11 shows stack 9-1941-69 and unused MEA. Figure 4-11 (h) shows location of laboratory based and synchrotron based measurements. Figure 4-11 (a), (b), (c) and (d) show average counts values (synchrotron XRF line scan measurements) for unused MEA (data from Figure 4-9 (c)), cell 9 (cold/hot), cell 18 (cold/hot, data from Figure 4-9 (a)), and perpendicular measurement at position ~50 mm for cell 18 (data from Figure 4-9 (b)), respectively.

Figure 4-11 (e), (f) and (g) show laboratory XRF data for unused MEA, cell 9 (cold/hot) and cell 18 (cold/hot), respectively. Figure 4-12 shows the average counts of synchrotron XRF line scan (cold/hot) for stack 9-1000-78 cell 1.

It is clear in Figure 4-9 to Figure 4-12 that the synchrotron-based XRF results (the counts) are consistent with laboratory based results in Section 4.2 and laboratory based results of MEAs presented in Figure 4-11 i.e. there are higher levels of contaminants in used MEAs than unused MEAs and “hot” areas show higher levels of contaminants than “cold” areas.

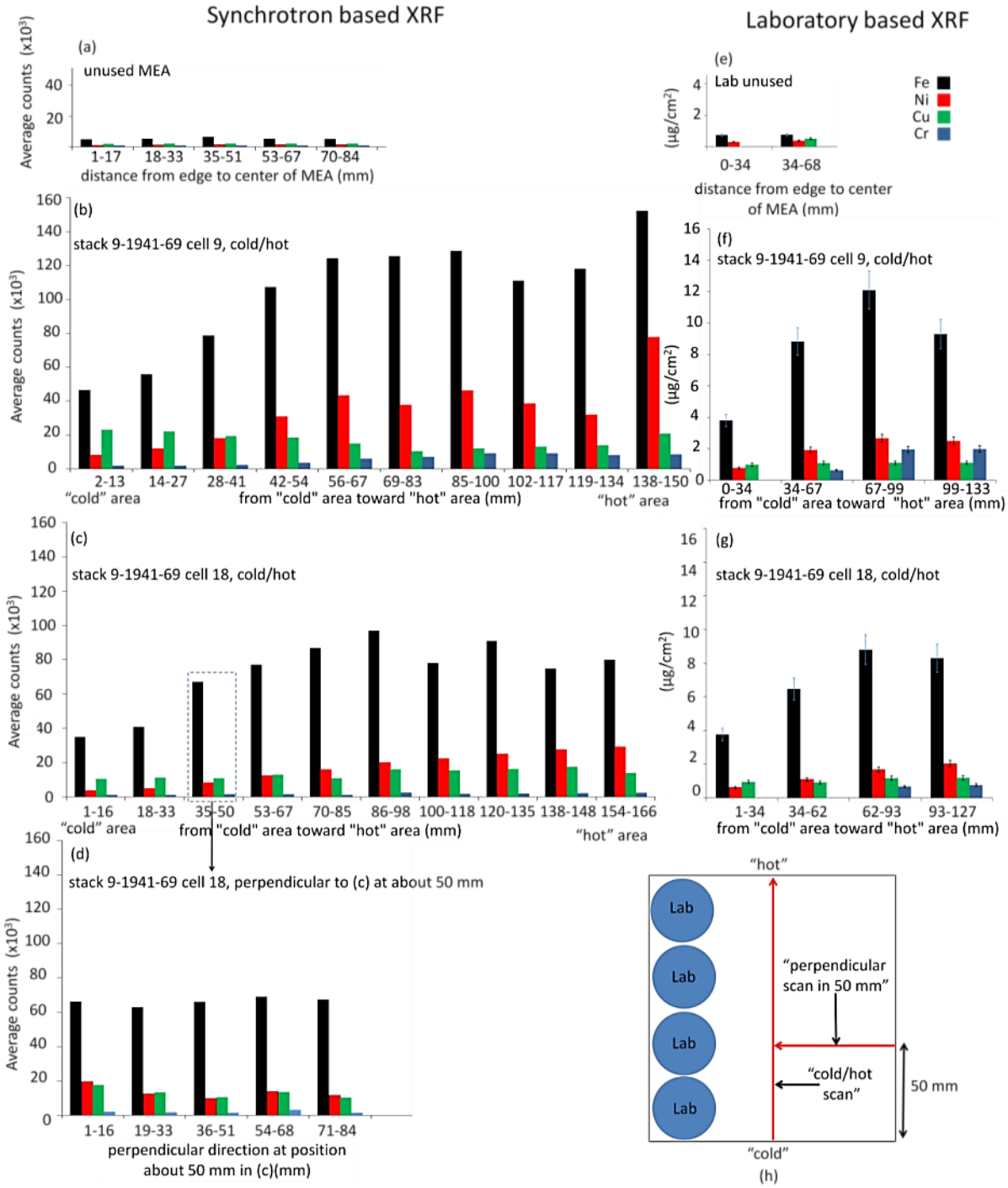

Figure 4-11. Average contamination levels of Fe, Ni, Cr and Cu for cell 9 and cell 18 of stack 9-1941-69 compared with an unused MEA. Synchrotron XRF line scan measurements of (a) unused MEA (data from Figure 4-9 (c)), (b) cell 9 (cold/hot), (c) cell 18 (cold/hot, data from Figure 4-9 (a)), (d) perpendicular measurement at position ~50 mm for cell 18 (data from Figure 4-9 (b)). Laboratory XRF data for (e) unused MEA, (f) cell 9 (cold/hot), (g) cell 18 (cold/hot) and (h) position and direction of line scans and laboratory XRF measurements. Each value is the average over a strip as shown in Figure 3-3 (c) of the experimental method chapter. In all cases, the cathode side of the MEA faced the incident beam, the incident energy was 11.54 keV and the beam size was 60 µm x 60 µm.

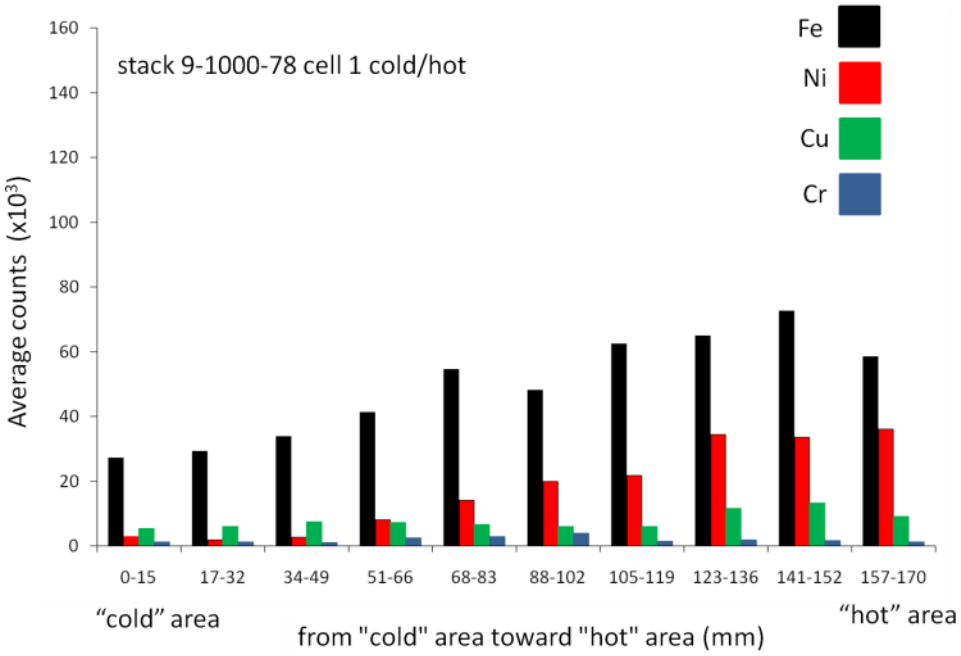

Figure 4-12. Synchrotron XRF line scan (cold/hot) for stack 9-1000-78 cell 1 cathode view. Each value is the average over a strip as shown in Figure 3-3 (c) of the experimental method chapter. The cathode side of the MEA faced the incident beam, the incident energy was 11.54 keV and the beam size was 60 µm x 60 µm.

Figure 4-9 to Figure 4-12 provide information about how levels of contamination changes from the "cold" area toward "hot" area. The change in contamination levels across the unused MEAs (Figure 4-9 to Figure 4-11) is not significant. Variations in contamination levels measured using laboratory XRF are consistent with synchrotron XRF results of MEAs from the same cell and stack (see Figure 4-11). This is described in more details for the used MEAs in the following.

It can be seen in Figure 4-9 to Figure 4-12 that across the "cold" area toward middle Fe, Ni, Cu and Cr gradually increase; the only exception is Cu in cell 9 of stack 9-1941-69 which shows a slight decrease from the "cold" area to the "hot" area. Across the "hot" area (from about the middle onwards) there are variations in levels of contamination but these variations are not as significant as change within the "cold" area toward middle, the only exception in this case is Cr in cell 1 of stack 9-1000-78

(see Figure 4-12) which after increase from “cold” area to middle then it decreases to “cold” area levels. These results are consistent with laboratory based results.

For the “perpendicular” scan (Figure 4-11 and Figure 4-9) changes in level of Fe, Ni, Cu and Cr are not as significant as changes in levels of Fe, Ni, Cu and Cr along “cold” to “hot” area direction. However; the level of contamination is much higher than in the unused MEA.

4.4 Discussion

4.4.1 Comparing used MEAs vs. unused MEA

Contamination levels investigated for different regions of MEAs which were used in 5 stacks running with different bipolar plates, aging cycles, operating time/temperature and MEA types (Table 3-1) using laboratory and synchrotron XRF.

In all cases, Fe and Ni (the main contaminants) in used MEAs consistently show higher levels than Fe and Ni in unused MEAs for both laboratory and synchrotron XRF studies. For synchrotron XRF measurements, Cr and Cu (generally with lower levels than Fe and Ni) in used MEAs show more elevated levels than those of unused MEAs. For laboratory XRF, Cu levels tend to be close to Cu levels in unused MEAs and for most of the measurements Cr are below the detection limit. These results suggest that XRF could be used effectively to evaluate corrosion products from bipolar plates in MEAs and synchrotron XRF is a more sensitive method than laboratory XRF for evaluating MEA contaminations.

As described in Section 2.11, XRF as previously has been used to detect corrosion products from bipolar plates in MEAs [15, 20-23, 93, 125, 128]. Zawodzinski et. al

[125] and Kumagai et al. [15] have reported similar results with laboratory XRF method, Zawodzinski et. al [125] have studied fresh MEA and MEAs after use in a 2-4 cell stacks and a single cell with 316 SS bipolar plates. Fresh MEA showed no contamination but in used MEAs, levels of Fe and Ni contaminations were much higher than Cu and Cr. Cu was not detected for some MEAs and Cr was not detected for any of MEAs. Kumagai et al. [15] used XRF to assess level of contamination in MEAs after use in single cells with Ni-free ferritic stainless steel bipolar plates (the chemical composition of stainless steels contains Fe and Cr but not Ni) and found significant levels of Fe; however, Cr was not detected. Because the aging cycles are very different in the literature [15, 20-23, 93, 125, 128] it is not possible to compare values found in this study with the other publications.

4.4.2 Trend between cells in stacks and comparing stacks

No trend was observed between cells within stacks. XRF results showed that generally the cell-to-cell variations in levels of contaminants within a stack are as significant as stack-to-stack variation; therefore, comparing stacks with each other is not sensible. Moreover, the ratio of elements for example Fe/Ni for stacks were calculated but again the cell-to-cell variations for these ratios within a stack were as significant as or higher than stack-to-stack variation.

4.4.3 Cathode vs. anode

Cathode side and anode side environment in PEMFC are different, for example in terms of hydrogen or oxygen atmosphere. Therefore different materials and coatings may show different corrosion behaviour in the cathode side or the anode side. For the

bipolar plates which are used in this thesis i.e. 904L SS, 904L SS coated by TiN and C2 coated 316L SS, both laboratory XRF results and synchrotron XRF results consistently show that there are more Fe (the main contaminant) on the cathode side of MEAs than on the anode side (possible reasons are presented in Sections 5.4.1 and 5.4.4). This is consistent with Auvinen et al. [48, 131, 136] where they reported AAS and ICP results of MEAs used in single cells with 904L SS and Au coated 904L SS and 403 SS coated by CrN bipolar plates. The visual observation of plates (because they are confidential, they are not presented here) also shows more corrosion product at cathodes than at anodes. More corrosion products are observed on the bipolar plate's surface [14, 15, 26, 136] or detected in MEAs using AAS, ICP and EDS [96, 97, 136] at the cathode side than the anode side after long duration stack or single cell operation. Makkus et al. [96, 97] also reported higher levels of contamination in anode than cathode for some of the AAS and ICP measurements of MEAs used in a single cell with unknown "alloy B" bipolar plate. However, they chose an aging cycle which was more corrosive on anode side than on the cathode side and they have not paid attention to repeatability and levels of errors in the tests as described in Section 2.11.3.

Because the MEA is mainly carbon and its thickness is about 640±10 μm, the incident beam can penetrate the full thickness of sample including both the cathode and anode. Therefore if more counts are measured on the cathode side than on the anode side, then it may be the case that the contamination detected on the anode side may in fact be contamination on the cathode side, so be higher than the true level of anode contamination. This will be discussed in more details in the microscopic distribution of contamination in MEA cross-sections in the next chapter where direct comparison of anode and cathode will be possible (Sections 5.3, 5.4.1 and 5.4.4).

4.4.4 "Cold" area vs. "hot" area

According to laboratory XRF results and synchrotron XRF results, more corrosion products are generally found at "hot" areas than at "cold" areas of the MEA. In addition, post mortem studies of plates showed more corrosion products at "hot" area than "cold" area (because they are confidential, they are not presented here). To our knowledge, this trend has not been reported for corrosion products of bipolar plates in MEAs. A number of possibilities come to mind as reasons for observing this trend: distribution of temperature, water, and pH in cells as well as the transport of corrosion products by the flow of reactants and coolant. They will be described as follows:

4.4.4.1 Temperature

For the stacks which are used in this study, coolant inlets were "cold" areas and coolant outlets were "hot" areas. The temperatures of the "cold" regions were significantly lower than the temperatures of the "hot" regions. Temperature may gradually increase from "cold" areas to "hot" areas. An increase in temperature significantly increases corrosion rates; this could be a reason for observing a gradual increase of corrosion products from "cold" areas to "hot" areas as shown in Figure 4-9, Figure 4-11 and Figure 4-12.

4.4.4.2 Distribution of water in cells

Previous work showed more corrosion products where water collected in cells. After extended periods of single cell operation, corrosion products were mainly observed where water tended to gather [14, 20, 26] such as outlets [14] (hot areas were coolant outlets). There is no information about the distribution of water in the cells which are studied here. However, if there were more water in "hot" areas than "cold"

areas, this may contribute in observing more corrosion products in “hot” areas than “cold” areas. More aggressive corrosion may happen where more wetness is available. Additionally, in order for metal ions to contaminate MEAs; they must be moved from the corrosion location i.e. bipolar plate surface. This transport is facilitated by the presence of water [8].

4.4.4.3 Distribution of pH in cells

The distribution of pH was not measured for the cells which are used in this study. However, the distribution of pH could be one of the reasons for observing higher corrosion products at hot areas (around coolant outlets) than cold areas (around coolant inlets). Kumagai et al. [14] showed that the environment around gas outlets can be more acidic than the environment around both gas inlets and centres of bipolar plates during operation of PEM fuel cells. This pH distribution may cause higher rates of corrosion around outlets than around inlets.

4.4.4.4 Transport of corrosion products by the flow of coolant

It has been reported that the corrosion products of bipolar plates were transported by the flow of reactants and water [24, 92]. The coolant flow could transport the liquid water and corrosion products (in the form of ions or solid particles) from other areas to hot areas (coolant outlets).

4.4.5 Comparing channel positions and synchrotron line scans

Synchrotron line scans show that contamination in both used and unused MEAs shows considerable fluctuation (Figure 4-9 and Figure 4-10), local high levels can be 5 times higher than average levels. This will be discussed more in the next chapter along

with plan view XRF maps (Section 5.2 and 5.4.1). Local regions with higher levels of contamination do not correlate with channels positions (Figure 4-7).

4.5 Conclusions

- Laboratory and synchrotron XRF can be used to detect corrosion products from bipolar plate corrosion in membrane electrode assemblies (MEAs) from PEMFCs.
- Laboratory XRF results are generally consistent with synchrotron XRF results.
- The order of contamination levels is Fe>Ni>Cu, Cr.
- The distribution of contamination in a MEA after use in a PEM fuel cell stack is not homogeneous and tends to gradually increase from the coolant inlet to the coolant outlet where temperature is higher.
- Higher levels of corrosion products were detected when the cathode sides of MEAs were exposed to incident X-ray compared with the anode sides of MEAs.
- There are considerable local variations in contamination levels and there are some spots which show contamination levels up to 5 times higher than average levels.
- The regions with higher levels of contamination on MEAs do not correlate with flow channels positions on bipolar plates.
- The cell-to-cell variation within stacks were greater than the stack-to-stack variation, therefore the comparison of stack contamination was not possible.

5 Microscopic distribution of corrosion products in MEAs used in PEMFC stacks

5.1 Introduction

As explained in Section 2.7, metal ions from the corrosion of stainless steel bipolar plates contaminate both the catalyst and membrane in PEM fuel cells [17-20]. A decrease in ionic conductivity [8, 17, 19, 23, 79] and membrane degradation [8, 44-47, 100] are consequences of metallic contamination. Corrosion of bipolar plates can be accelerated by membrane degradation owing to releasing corrosive anions from membrane [8, 44-47]. It also has been reported the catalyst efficiency deteriorates as a result of Fe contamination [20, 79, 96, 99, 103, 104].

Makkus et al. [96, 97] investigated the distribution of Fe in the MEA cross section using SEM and Energy Dispersive X-ray Spectroscopy (EXDS) mapping; their result showed that there was more Fe in cathode catalyst layer than in anode catalyst layer and in membrane.

XRF has been used for assessing levels of contamination in MEAs [15, 20-24]; EDS is not as sensitive and accurate as XRF for investigating trace of contaminants usually observed in MEAs as reported by Wilson et al. [20, 23].

In the previous chapter, the macroscopic levels of contamination of fuel cell MEAs were investigated with synchrotron and laboratory-based XRF. In this chapter high resolution synchrotron-based XRF is used for investigating the distribution of Fe, Ni, Cr and Cu in the cross section of MEAs and in the plan view of MEAs.

5.2 Plan view XRF maps of MEAs

In this thesis “MEA” includes membrane, catalyst layers and GDLs (gas diffusion layers). Figure 5-1 shows XRF maps of used and unused MEAs at low resolution (60 μm x 60 μm beam size) showing the distribution of Pt, Fe, Ni, Cr and Cu. XRF maps were made over an area 4 mm x 4 mm of unused MEA (left) and a used MEA from stack 9-1000-78 cell 20 “hot” area (right). During the measurement, the cathode side faced the incident beam. It can be seen that both the unused MEA and the used MEA show an inhomogeneous distribution of Pt. It also can be seen that the levels of Fe, Ni, Cr and Cu for the used MEA is more inhomogeneous than those of unused MEA and there are some areas of used MEA with high counts of Fe, Ni, Cr and Cu, particularly for Fe (the predominant contaminant based on the previous chapter). For the used MEA, the high levels of Fe usually correlate with the high levels of Pt.

Figure 5-2 (a) shows Pt, Fe, Ni, Cr and Cu plan view XRF maps with low resolution (60 μm x 60 μm beam size) over a 2 mm x 2 mm area of the “hot” area of an MEA used in stack 9-1941-69 cell 9. The XRF maps of this used MEA also shows inhomogeneous distribution of Pt, Fe, Ni, Cr and Cu and also usually a correlation between Fe and Pt. This is similar to XRF maps of the used MEA in Figure 5-1.

Figure 5-2 (b) shows XRF maps with higher resolution (6 μm x 6 μm beam size) of an area of 360 μm x 720 μm from the area shown by the black rectangle in Figure 5-2 (a). The regions of high Fe contamination appear to correlate approximately with regions of high Pt content, but not all regions with high levels of Pt show high levels of contamination.

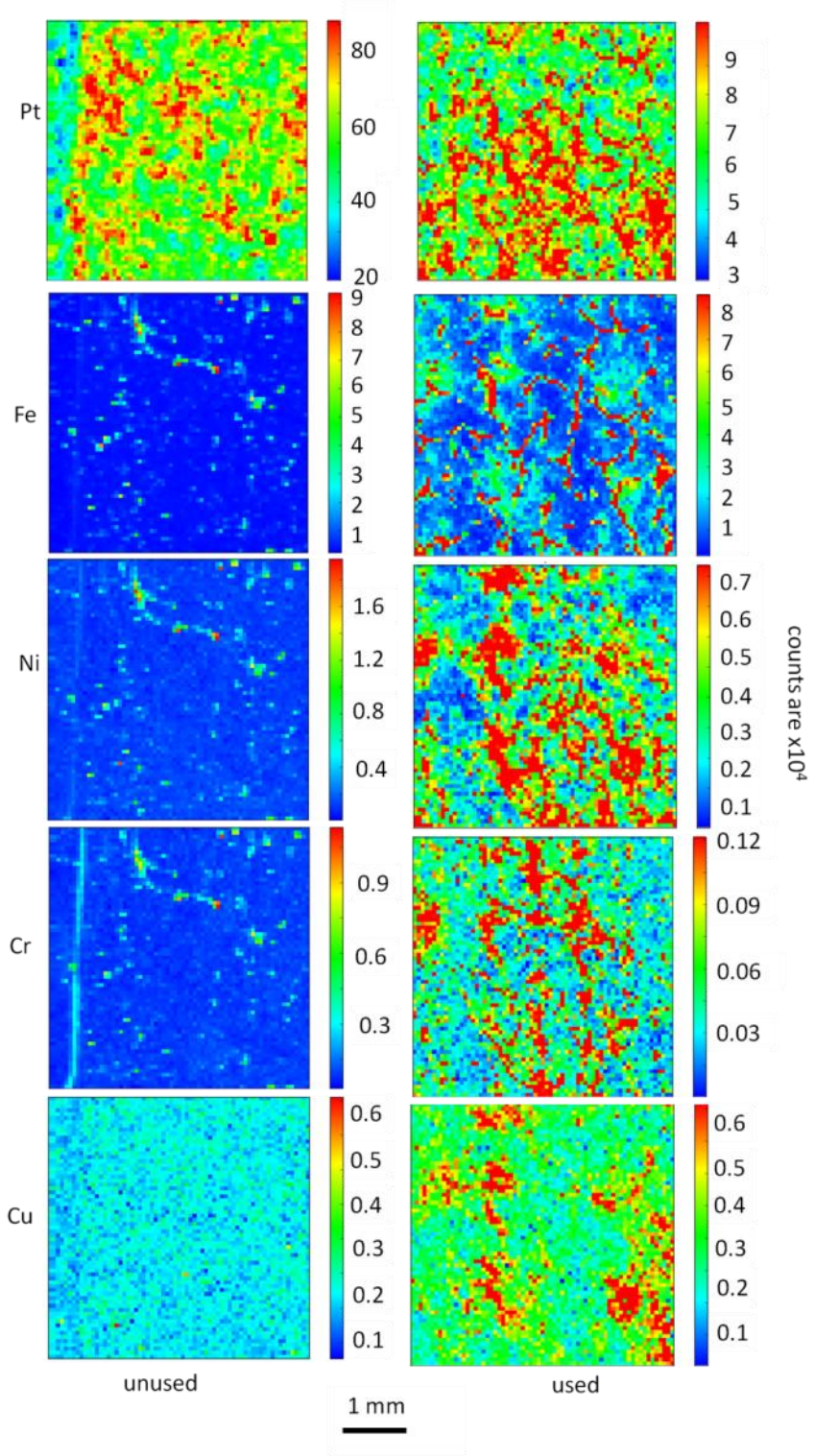

Figure 5-1. Plan view XRF maps. MEAs were from stack 9-1000-78 cell 20 "hot" area (used, right) and from unused MEA (left). The beam size was 60 µm x 60 µm. The cathode side faced the incident beam and the incident energy was 11.52 keV for the used MEA and 11.54 keV for unused MEA. Fe, Ni, Cr and Cu are shown with the same colour scale. The incident energy was slightly below the Pt edge (11.56 keV) and very small change in incident energy for used and unused MEA causes significant different for Pt counts.

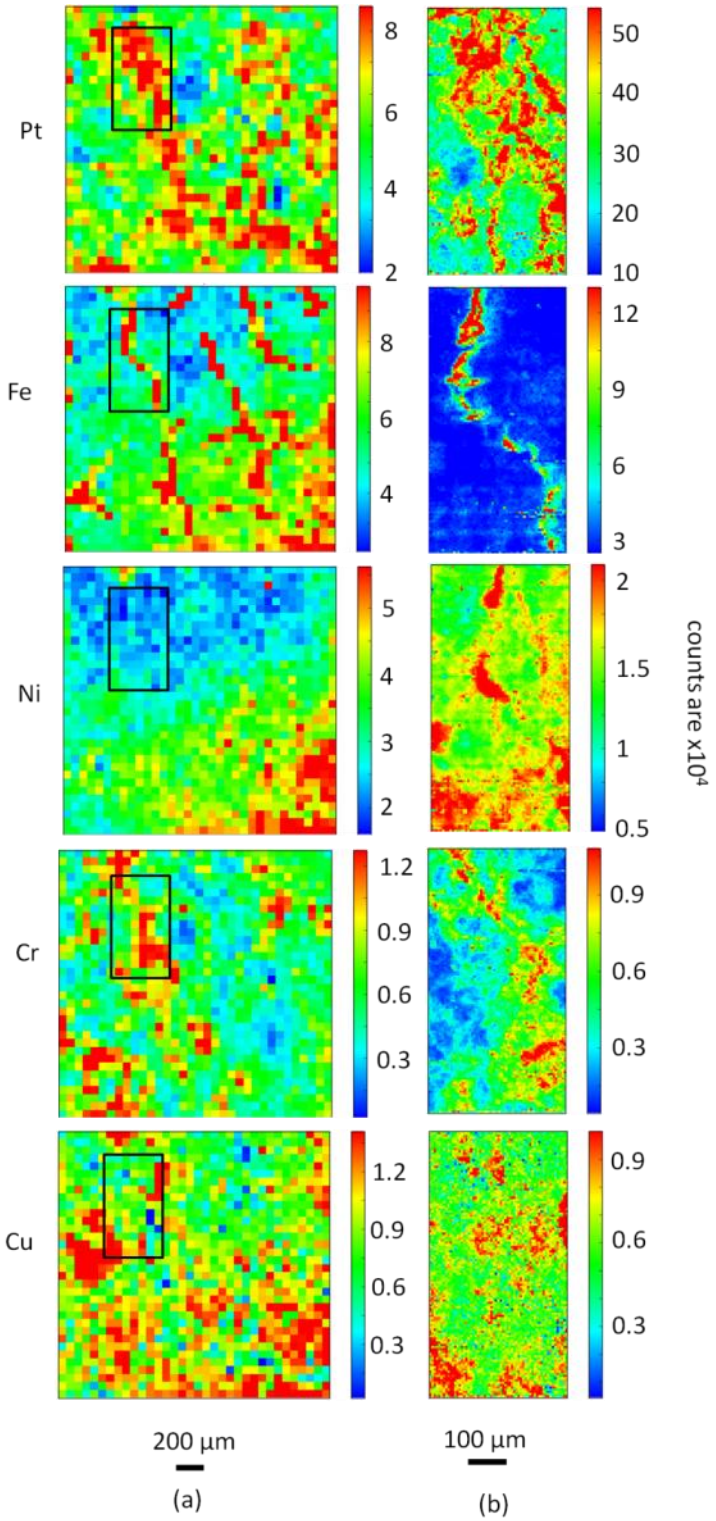

Figure 5-2. Plan view XRF maps. The MEA was from stack 9-1941-69 cell 9 "hot" area: (a) low resolution XRF maps with 60 µm x 60 µm beam size over an area 2 mm x 2 mm and (b) high resolution XRF maps with 6 µm x 6 µm beam size from the area shown by the black rectangle in "(a)" (360 µm x 720 µm). The cathode side faced incident beam. The incident energy was 11.54 keV.

SEM/EDS and XRF mapping analysis were done on plan view of used MEAs and plan view of unused cathode catalyst layer deposited on a microporous layer of carbon. Figure 5-3 shows SEM and EDS of a used sample from the same area of the used sample shown in Figure 5-1. The SEM image shows the GDL on the surface of the MEA. There is no sign of a pattern (similar to the Figure 5-1 pattern) in the Pt, Fe, Ni, Cr or Cu maps. The sampling volume of the EDS signal is ~1 µm, whereas the penetration depth of X-rays is much greater and the sensitivity of synchrotron XRF is higher. Thus the contaminants may be present at levels that are too low for EDS detection, or be found at greater depths than the GDL.

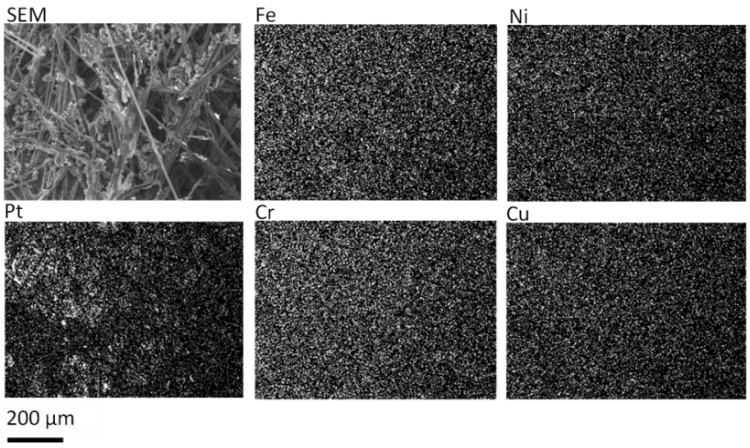

Figure 5-3. Plan view SEM and Fe, Ni, Pt, Cr and Cu EDS maps of used MEA from stack 9-1000-78 cell 20 "hot" area. The cathode side GDL faced the incident beam.

Figure 5-4 shows a plan view SEM image from an unused catalyst layer on the micro-porous layer which shows evidence of cracking (left) and an Fe XRF map from a used MEA (previously it was shown in Figure 5-1) (right). These cracks in catalyst layer are similar to distribution of high count areas observed in Fe XRF maps of the used MEA (Figure 5-1 and Figure 5-2).

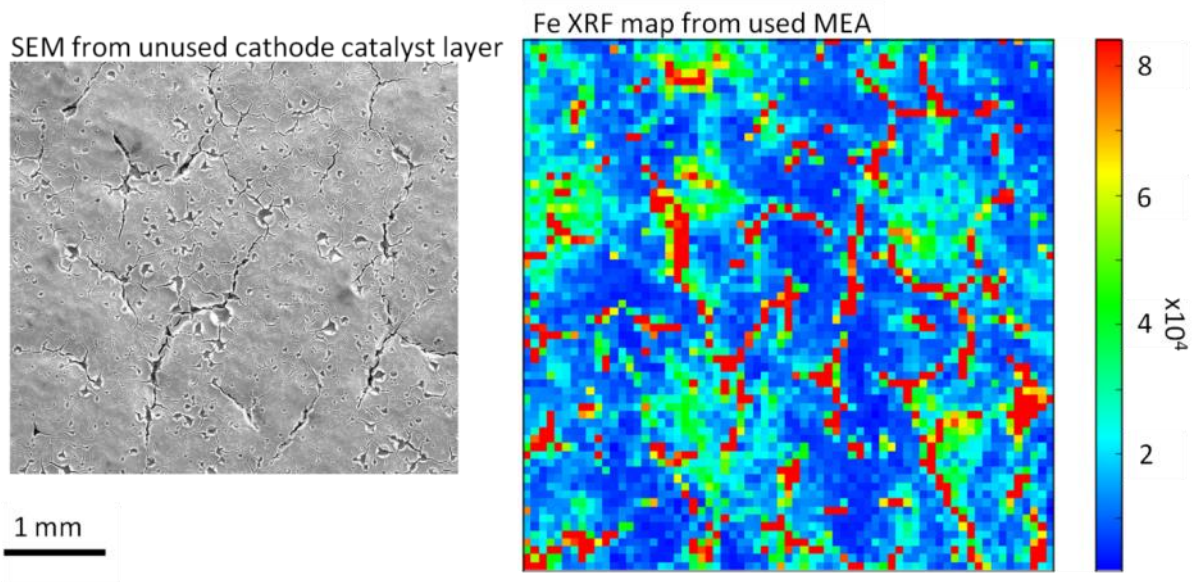

Figure 5-4. Plan view SEM of unused cathode catalyst layer on micro-porous layer (left) and Fe XRF maps of MEA from stack 9-1000-78 cell 20 "hot" area cathode side with 60 µm x 60 µm beam size (right). The incident energy was 11.52 keV. The size of the cracks in the catalyst layer could be changed for every batch products and the sample analysed by XRF and the sample analysed by SEM were from different batch.

Figure 5-5 shows a plan view SEM image and a Pt EDS map of a crack area in an unused catalyst layer. Higher levels of Pt can be seen along the edges of the cracks.

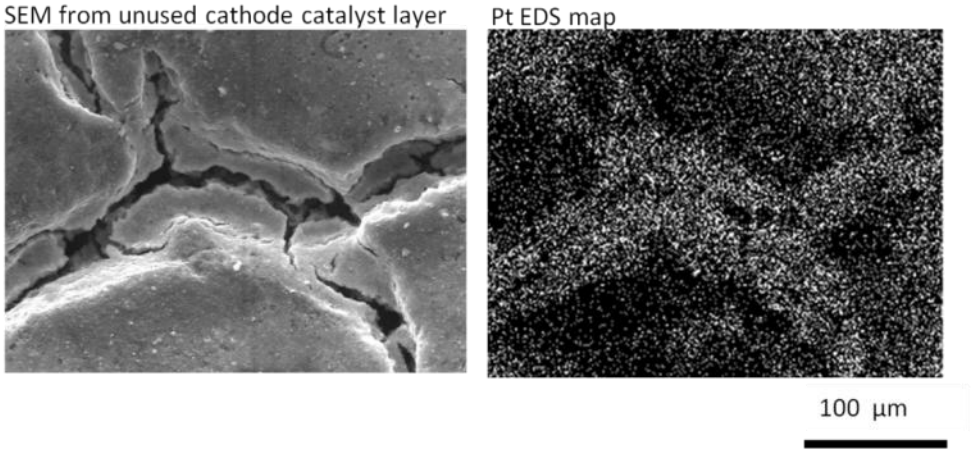

Figure 5-5. Plan view SEM image and Pt EDS map of an unused catalyst layer on micro-porous layer.

Figure 5-6 shows a plan view SEM image and Pt and Fe XRF maps of the exactly same area of an unused catalyst layer on a micro-porous layer (see Section 3.4.3 of the experimental method chapter). The black and white rectangles which show a selected

area are shown in a higher magnification in the bottom of the image. It is clear that there are high levels of Pt in/or adjacent of cracks areas in the unused catalyst layer; however, the distribution of Fe in this unused MEA is homogenous. Both Figure 5-5 and Figure 5-6 showed that there are high levels of Pt in/or adjacent some cracks in the catalyst layer.

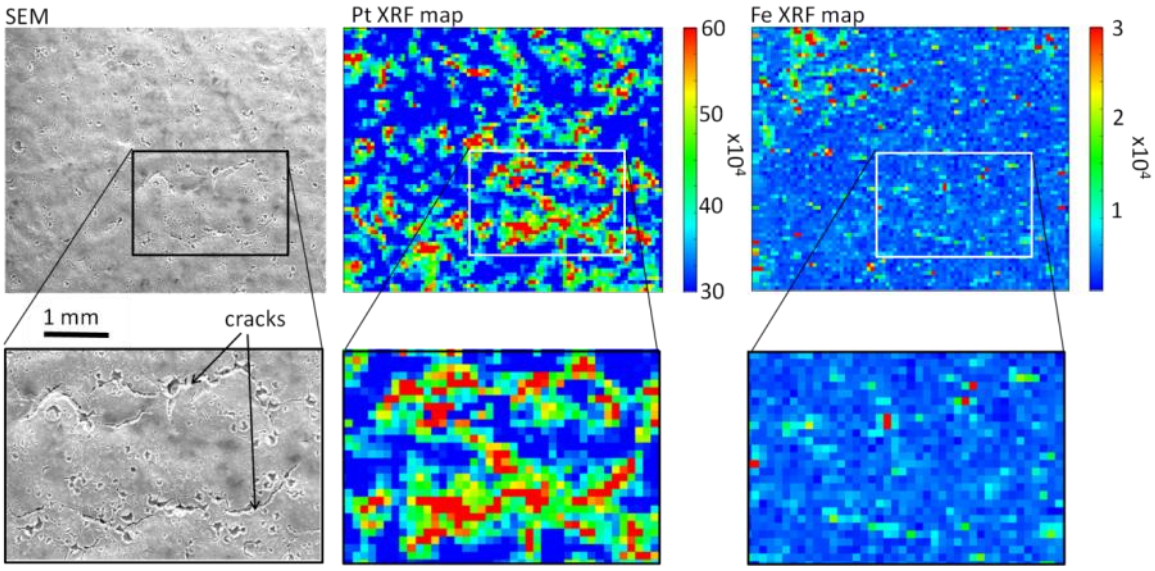

Figure 5-6. Plan view SEM image of an unused cathode catalyst layer and Pt and Fe XRF maps from the same area shown in the SEM image. The beam size was 60 µm x 60 µm and the incident energy was 11.54 keV. The rectangles show selected area of image which are presented in higher magnification in the bottom (See Section 3.4.3).

5.3 Cross section XRF maps

Synchrotron XRF maps of MEA cross-sections are presented in this section. MEA cross section maps provide two advantages compared to MEA plan view XRF experiments, firstly, MEA cross section maps can be used to investigate the distribution of contaminants in vulnerable components, i.e., membrane and catalyst layers and secondly, they can be used to directly compare and assess contamination levels in anode side and cathode side of MEAs.

Figure 5-7 shows a diagram of the cross section of the MEA samples used in the current work, the cathode side is defined as catalyst layer, microporous layer (MPL) and

GDL facing the cathode side of bipolar plate and the anode side is defined as catalyst layer, microporous layer and GDL facing the anode side of bipolar plate.

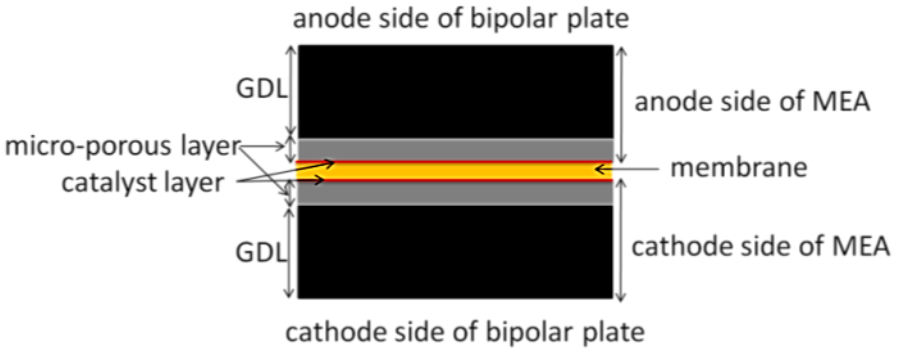

Figure 5-7. GDLs, micro-porous layers (MPL), catalyst layers, membrane, anode side and cathode side positions in a MEA cross-section.

Figure 5-8 shows XRF maps for Pt and Fe of the cross sections of the MEA from stack 9c1-2700-76 cell 3 in the "hot" area. The catalyst layers can be seen in the Pt map, enabling the location of the microporous layers (~100 μm) to be identified. The Fe map is shown both on a logarithmic scale and on a linear scale. From the linear scale map, it is clear that Fe is found predominantly in the microporous layer on the cathode side. The logarithmic map provides more information, it can also be seen that Fe contamination extends into the membrane and into the GDL on the cathode side, but is at much lower levels on the anode side.

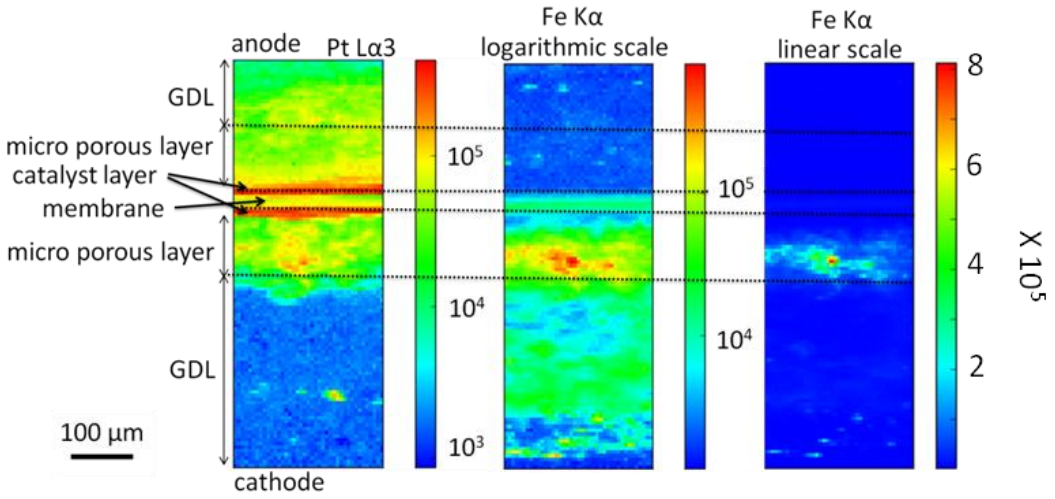

Figure 5-8. XRF maps for Pt and Fe of the cross section of the MEA from stack 9c1-2700-76 cell 3 in the "hot" area. The beam size was 6 µm x 6 µm and the incident energy was 11.51 keV. The dash lines show the position of the membrane, micro porous layers, GDL and catalyst layers based on the location of the highest levels of Pt (catalyst layers) and the thickness of the microporous layer, which is ~100 µm.

The low resolution XRF maps of cross sections (with 60 µm x 60 µm beam size) are presented in Section 5.3.1 and the high resolution XRF maps of cross sections (with 6 µm x 6 µm beam size) are presented in Section 5.3.2.

The focus of Section 5.3.1 is comparing used MEAs vs. unused MEA, "hot" area vs. "cold" area and anode side of MEA vs. cathode side of MEA; In this section the low resolution maps which cover both cathode side and anode side for a large area (2.4 mm of cross section) are used because they give a better view for comparing used MEAs vs. unused MEA, "hot" area vs. "cold" area and anode side vs. cathode side than high resolution maps which only cover a small area (240 µm of cross section).

The focus of Section 5.3.2 is on the distribution of Fe, Ni, Cr and Cu, and maps with both low and high resolution are used to analyze the distribution of these elements.

5.3.1 Comparing used and unused MEAs

In this section levels of Fe, Ni, Cr and Cu found in XRF maps of used MEA cross-sections are compared with those found in unused MEA cross-section, the levels of contamination in the cross section of unused MEA represent the contamination in unused MEA and also the possible contamination from preparation of cross-sections.

Figure 5-9 shows Pt XRF maps of MEA cross sections of an unused MEA and used MEAs from a number of different stacks. The levels of Pt in the used MEAs and the unused MEA are not significantly different; the only exception is stack 9-1000-78 cell 20 "hot" area which shows higher levels of Pt compared to other MEAs. This is explained in Section 5.4.6.

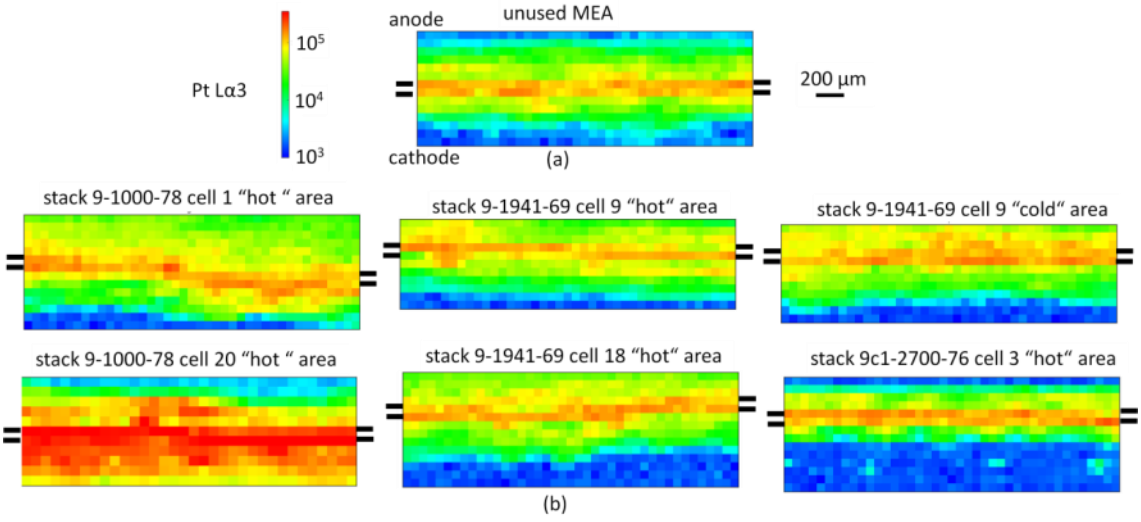

Figure 5-9. Pt XRF maps of MEA cross-sections. (a) The cross section of an unused MEA and (b) the cross-sections of the used MEAs from the stacks indicated. The beam size was 60 µm x 60 µm and incident energy was 11.51 keV, the X-ray counts scale is the same for all samples. The rough position of catalyst layers and membrane are marked with "=" based on the high levels of Pt are associated with catalyst layer.

The approximate position of the catalyst layers are marked with "=" based on the regions showing high levels of Pt. This marking is included in subsequent figures showing maps of the contaminant elements.

Figure 5-10 and Figure 5-11 show Fe and Ni XRF maps of MEA cross-sections, respectively. The levels of Fe and Ni found in used MEAs as shown in Figure 5-10 (b) and Figure 5-11 (b) are significantly higher than those found in unused MEA as can be seen in Figure 5-10 (a) and Figure 5-11 (a), respectively. These results are consistent with macroscopic distribution of contamination shown in the previous chapter.

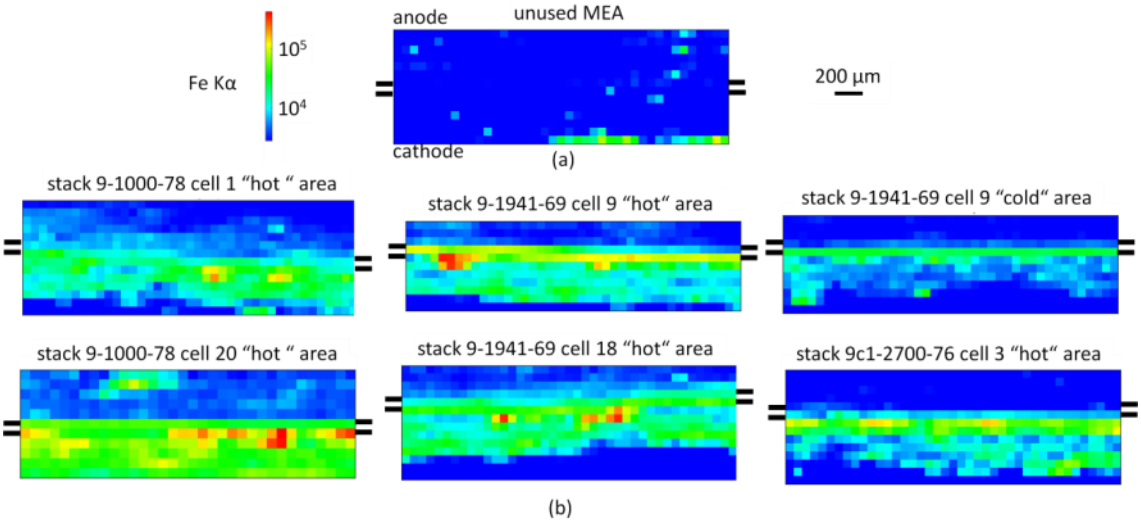

Figure 5-10. Fe XRF maps of MEA cross-sections. (a) The cross section of an unused MEA and (b) the cross-sections of the used MEAs from the stacks indicated. The beam size was 60 µm x 60 µm and incident energy was 11.51 keV, the X-ray counts scale is the same for all samples. The rough position of catalyst layers and membrane are marked with "=" based on the high levels of Pt are associated with catalyst layer.

Cr XRF maps of used MEA cross-sections and unused MEA cross section are shown in Figure 5-12. Levels of Cr found in stack 9c1-2700-76 cell 3 "hot" area MEA and unused MEA are not significantly different; however, all other samples show higher levels of Cr compared to unused MEA. Cr counts are much lower than Ni counts and Fe counts.

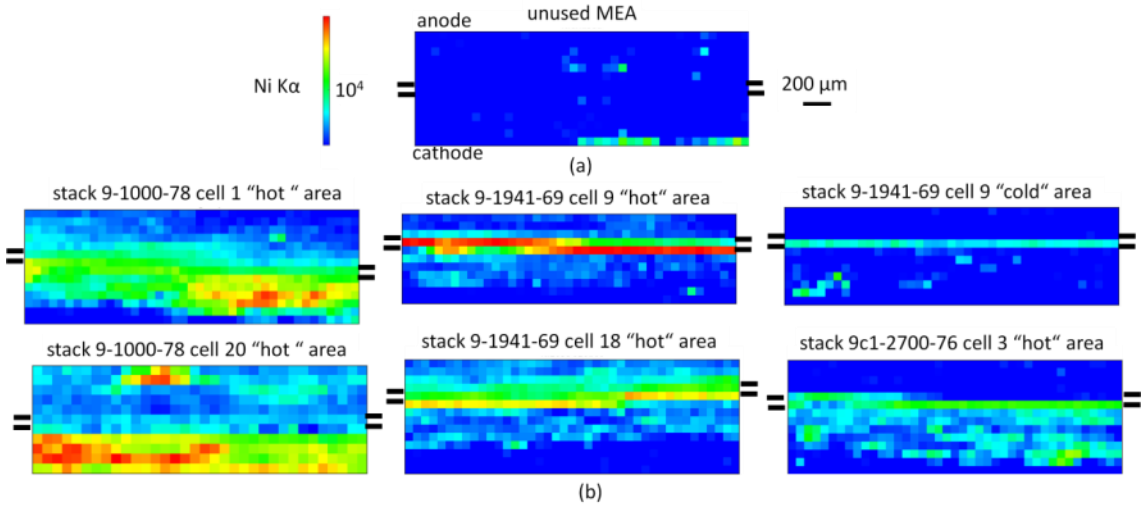

Figure 5-11. Ni XRF maps of MEA cross-sections. (a) The cross section of an unused MEA and (b) the cross-sections of the used MEAs from the stacks indicated. The beam size was 60 µm x 60 µm and incident energy was 11.51 keV, the X-ray counts scale is the same for all samples. The rough position of catalyst layers and membrane are marked with "=" based on the high levels of Pt are associated with catalyst layer.

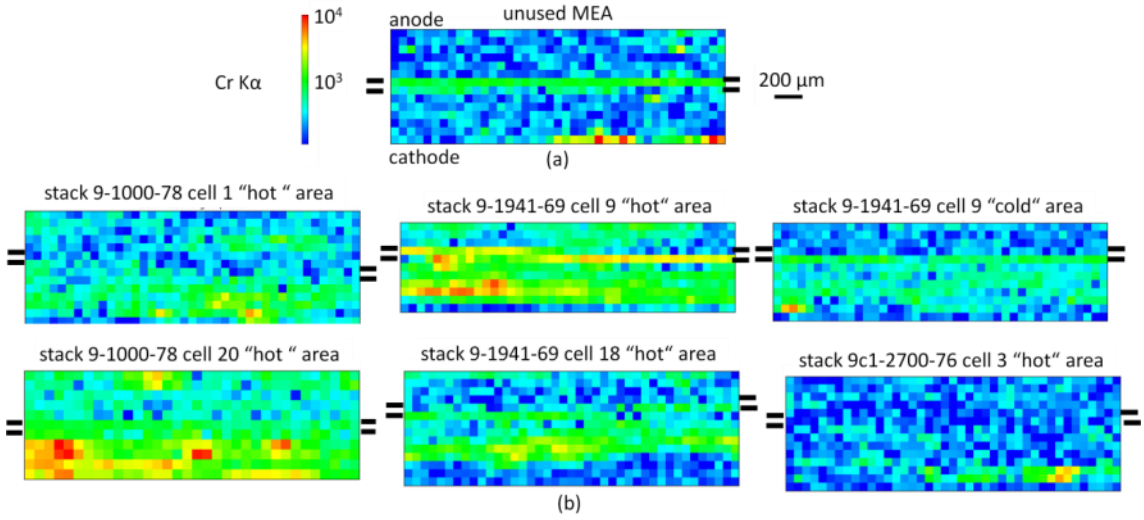

Figure 5-12. Cr XRF maps of MEA cross-sections. (a) The cross section of an unused MEA and (b) the cross-sections of the used MEAs from the stacks indicated. The beam size was 60 µm x 60 µm and incident energy was 11.51 keV, the X-ray counts scale is the same for all samples. The rough position of catalyst layers and membrane are marked with "=" based on the high levels of Pt are associated with catalyst layer.

XRF maps of Cu for cross-sections from used MEAs and the unused MEAs are presented in Figure 5-13. The levels of Cu in used MEAs are similar to the levels of Cu in unused MEAs and the difference between used and unused MEAs for Cu is not as

significant as the difference between used and unused MEAs for Ni and Fe; this is consistent with previous laboratory based results (Section 4.2); however, this is not consistent with previous synchrotron XRF results (Section 4.3). Cross-sections of used MEAs and unused MEA show different distribution of Cu; the area in which Cu is distributed is significantly larger for used MEAs than for unused MEA.

It can be seen in Figure 5-9 toFigure 5-13 that the cell-to-cell variation within a stack could be as significant as stack-to-stack variation; this is consistent with previous chapter.

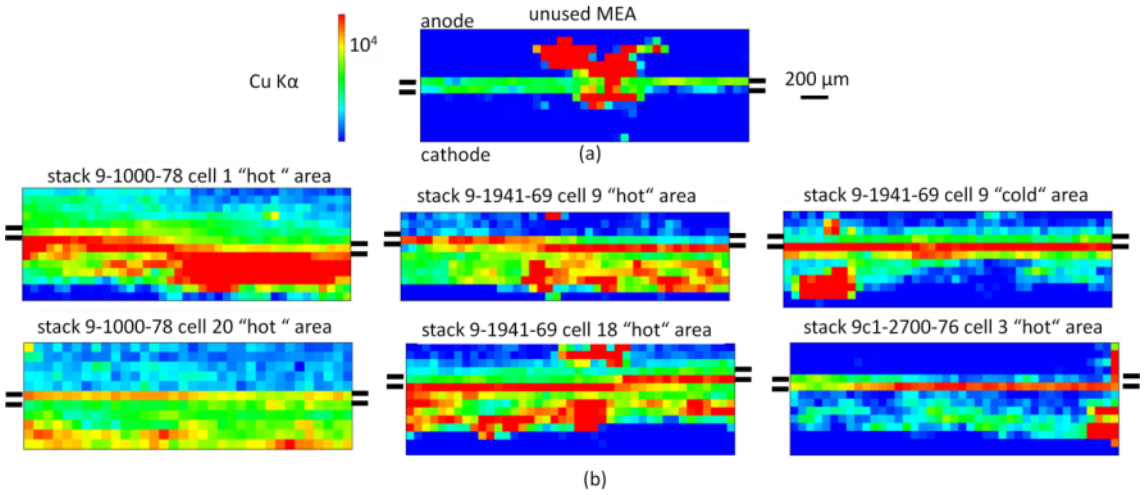

Figure 5-13. Cu XRF maps of MEA cross-sections. (a) The cross section of an unused MEA and (b) the cross-sections of the used MEAs from the stacks indicated. The beam size was 60 µm x 60 µm and incident energy was 11.51 keV, the X-ray counts scale is the same for all samples. The rough position of catalyst layers and membrane are marked with "=" based on the high levels of Pt are associated with catalyst layer.

5.3.1.1 Comparing anode side and cathode side of MEAs and "hot" and "cold" area

For cell 9 of stack 9-1941-69, the "hot" area of the MEA shows higher levels of Fe, Ni, Cu and Cr than the "cold" area of the MEA as depicted in Figure 5-9 toFigure 5-13. All used MEAs show higher levels of Fe, Cr, Ni and Cu in the cathode side than in the anode side as shown in Figure 5-9 to Figure 5-13. The only exception is Ni for stack 9-

1941-69 cell 18 “hot” area which shows the contradictory behaviour as shown in Figure 5-11 (b). This is consistent with laboratory based results and synchrotron based results presented in the previous chapter.

5.3.2 Distribution of Fe, Ni, Cr, and Cu in MEA cross-sections

In this section, the distribution of Fe, Ni, Cr, and Cu in cross-sections of MEAs is described. Figure 5-14 and Figure 5-15 show the high resolution XRF maps of the cross sections. In Figure 5-14 and Figure 5-15, it is considered that the thickness of microporous layer (MPL) is 100 µm and high levels of Pt are associated with catalyst layer and rough position of catalyst layers, membrane, microporous layer (MPL) and GDL are shown. Figure 5-14 shows XRF maps of Pt, Fe, Ni, Cu and Cr for cross-sections of an unused MEA (left) and the XRF map of the used MEA from stack 9-1000-78 cell 20 “hot” area (right). Low resolution maps are the same as those presented in Figure 5-9 and Figure 5-10. Pt and Fe are presented with both low resolution maps (60 µm x 60 µm beam size) and high resolution maps (6 µm x 6 µm beam size) from the area shown with the rectangles in low resolution maps. The optical images show a typical cross section area for a low resolution map and SEM images show a typical cross section for a high resolution map. It is clear that levels of Fe and Ni (the main contaminants according to the previous chapter) in the used MEA are significantly higher than the unused MEA.

Figure 5-15 show synchrotron XRF maps with high resolution (6 µm x 6 µm beam size). Each column shows an element. Figure 5-15 (a) shows stack 9c1-2700-76 cell 3 “hot” area, Figure 5-15 (b) shows stack 9-1941-69 cell 18 “hot” area, Figure 5-15 (c)

shows stack 9-1941-69 cell 9 “hot” area, Figure 5-15 (d) shows stack 9-1941-69 cell 9 “cold” area and Figure 5-15 (e) shows stack 9-1000-78 cell 1 “hot” area.

Maps with low resolution (with 60 µm x 60 µm beam size) (Figure 5-10 to Figure 5-13) cover a larger area (2.4 mm) of MEA cross sections comparing with high resolution maps which cover 240 µm of cross section. High resolution maps (Figure 5-14 and Figure 5-15) can be used to analyze levels of contaminant in catalyst layers and membrane. Therefore, for each element both high and low resolution maps were analysed to reach a correct and comprehensive description in Sections 5.3.2.1 to 5.3.2.4.

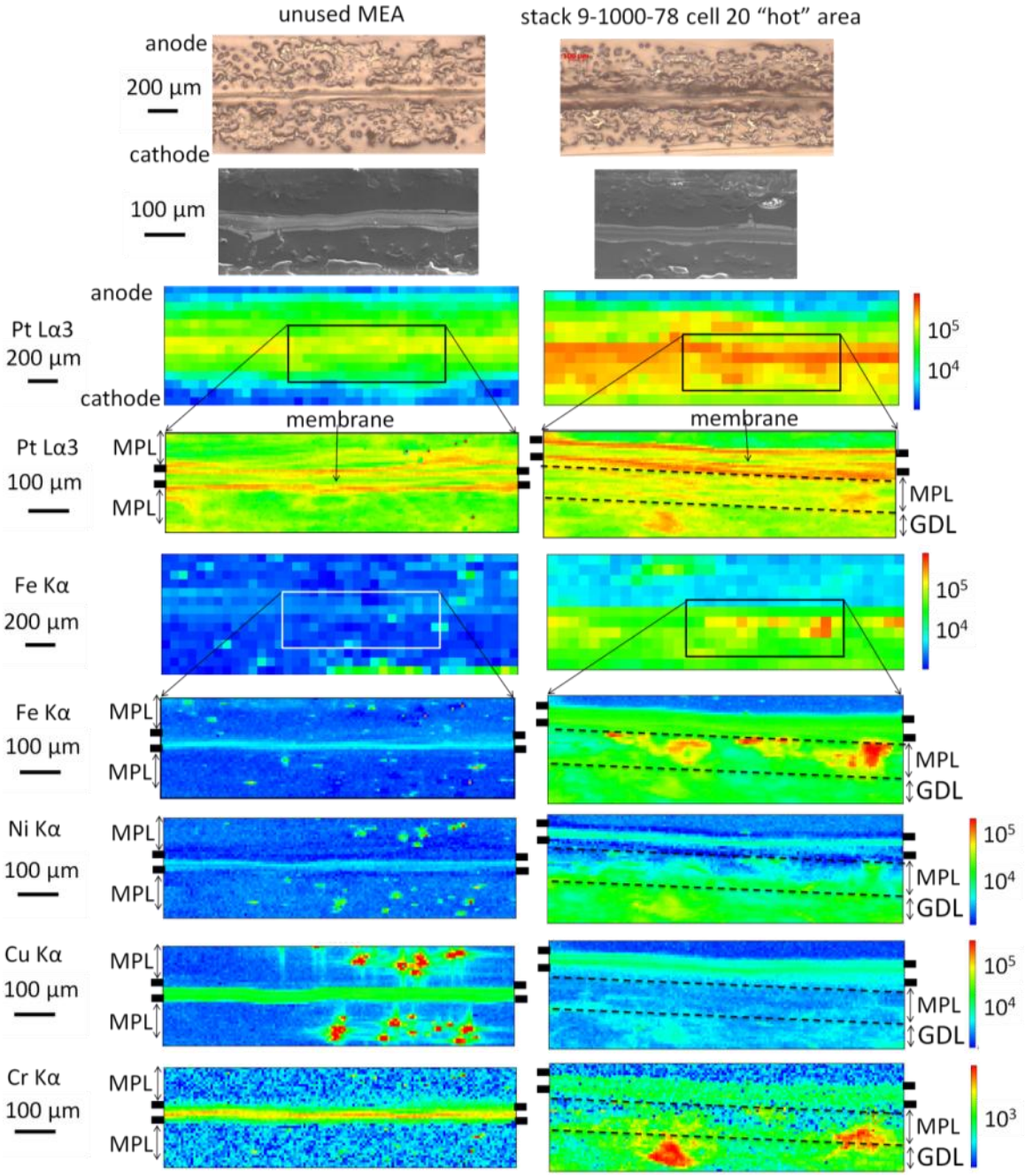

Figure 5-14. Pt, Fe, Ni, Cu and Cr XRF maps of MEA cross-sections with 60 µm x 60 µm or 6 µm x 6 µm beam size for the MEA from stack 9-1000-78 cell 20 "hot" area (right) and the unused MEA (left). The rough position of catalyst layers are marked with "=" and the dash lines show the position of micro porous layers (MPL) and GDL based on the location of the highest levels of Pt (catalyst layers) and the thickness of the microporous layer, which is ~100 µm. Pt and Fe are presented with both 60 µm x 60 µm beam size maps and 6 µm x 6 µm beam size maps from the area shown with the rectangles in 60 µm x 60 µm beam size maps. Ni, Cu and Cr are only presented with 6 µm x 6 µm beam size maps. The incident energy was 11.51 keV. The optical images show cross section image for maps with 60 µm x 60 µm beam size and the SEM images show cross section image for maps with 6 µm x 6 µm beam size, the images are not necessarily from the scan area.

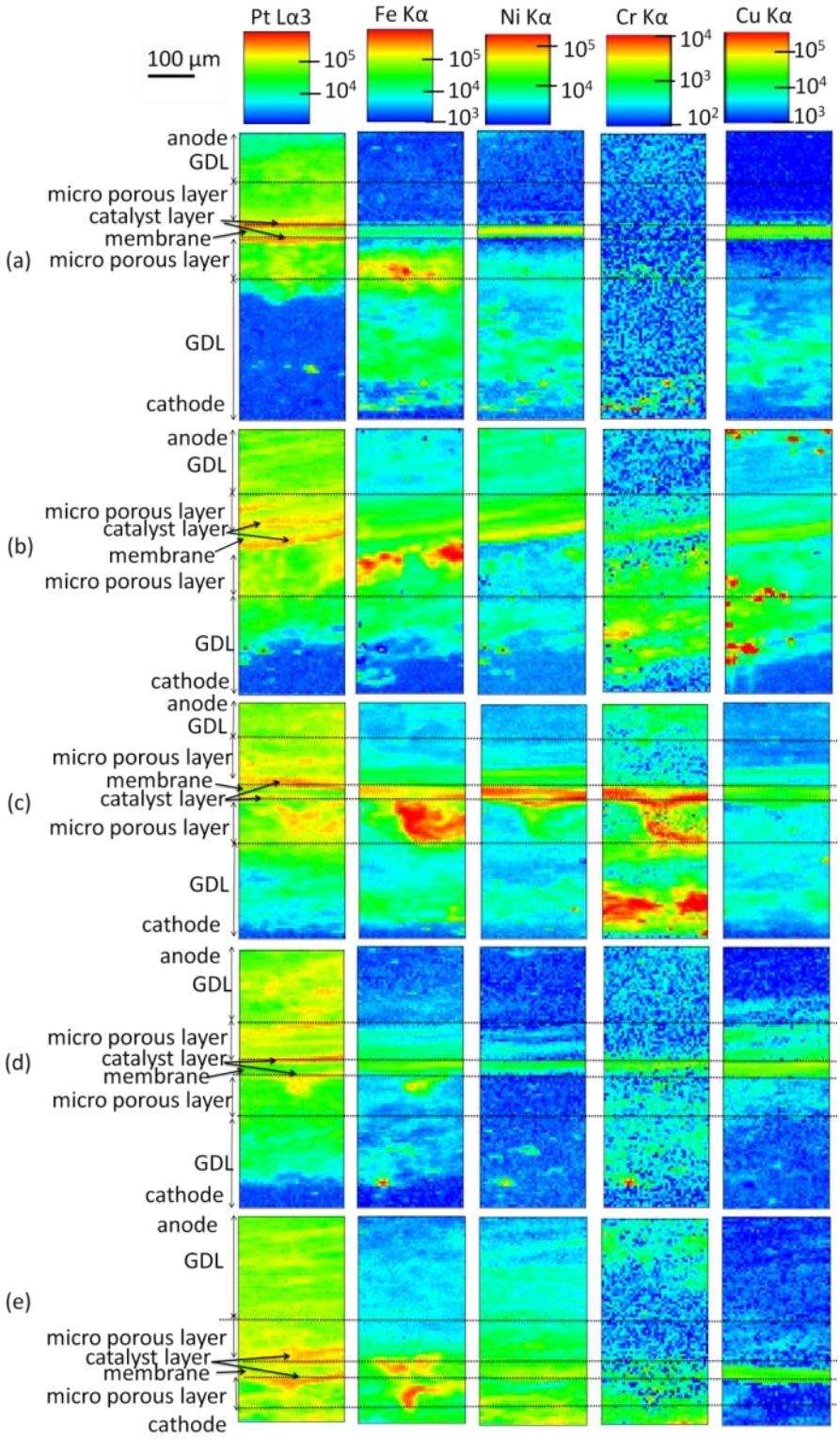

Figure 5-15. Pt, Fe, Ni, Cr, and Cu XRF maps of MEA cross-sections with 6 µm x 6 µm beam size. The incident energy was 11.51 keV. The dash lines show the position of the membrane, micro porous layers, GDL and catalyst layers based on the location of the highest levels of Pt (catalyst layers) and the thickness of the microporous layer, which is ~100 µm. (a) stack 9c1-2700-76 cell 3 "hot" area, (b) stack 9-1941-69 cell 18 "hot" area, (c) stack 9-1941-69 cell 9 "hot" area (d) stack 9-1941-69 cell 9 "cold" area and (e) stack 9-1000-78 cell 1 "hot" area.

According to both low resolution and high resolution maps, generally and without considering exceptions, anode side and catalyst layers mostly do not show significant level of any contaminant; however, contaminants generally tend to accumulate in the membrane and cathode side. Fe (the main contaminate) mostly is in the microporous layer of the cathode side. Ni, Cr and Cu are mainly in the membrane and/or the cathode side for most of the measurements. The distribution of these elements is fully described in the following.

5.3.2.1 Distribution of Fe

For used MEAs, Fe is mainly accumulated within the micro-porous layer (MPL) of the cathode side. It can be seen in Figure 5-14 and Figure 5-15 that the levels of Fe in this area is significantly higher than all other areas; lower levels of Fe than those found in micro-porous layer of cathode side are observed in membrane and in cathode GDL as can be seen in Figure 5-14 and Figure 5-15. For samples from stack 9-1941-69 levels of Fe also observed within micro-porous layer of anode side (Figure 5-15 (b), (c) and (d)). Fe levels in catalyst layers are not significant compared to the micro-porous layer of cathode side and membrane.

5.3.2.2 Distribution of Ni

For stack 9-1941-69 and stack 9c1-2700-76, the high levels of Ni are mainly found in the membrane as shown in Figure 5-11 and Figure 5-15. MEAs from stack 9-1000-78 shows the highest levels of Ni in the cathode side GDL (Figure 5-11) and lower levels than those mentioned are found in the membrane and the cathode micro-porous layer (Figure 5-11, Figure 5-14 and Figure 5-15 (e)). Figure 5-14 and Figure 5-15 show there are not significantly high levels of Ni in the catalyst layers compared to other areas.

5.3.2.3 Distribution of Cr

High levels of Cr are mainly found in cathode side and sometimes in the membrane as can be observed in Figure 5-12, Figure 5-14 and Figure 5-15.

5.3.2.4 Distribution of Cu

The overall levels of Cu found in used MEAs are not significantly different from those found in the unused MEA as described in Section 5.3.1; however, the distribution of Cu for used cross section MEAs is different from the distribution of Cu for the unused MEA. The highest levels of Cu are observed in membrane and also within the cathode side as can be seen in Figure 5-13 to Figure 5-15.

5.4 Discussion

5.4.1 Plan view XRF maps of MEAs

In the Pt XRF maps of used MEAs and unused MEAs, there are some regions of high Pt intensity (Figure 5-1 and Figure 5-2). These correlate with the appearance of crack-like regions in unused catalyst layers (e.g. Figure 5-6), which can be seen to have higher levels of Pt around the edges (Figure 5-5). Their origin is unknown.

For used MEAs, at regions with high levels of contaminants, particularly Fe, there are usually high levels of Pt (e.g. Figure 5-1 and Figure 5-2). To our knowledge, the increase in intensity of Pt and Fe in these crack-like areas has not been reported. More investigation is necessary to find the reason for this observation. However, a possible reason for observing the crack-like areas for high levels of Fe in XRF maps of used MEAs is described as follows:

Figure 5-16 shows a possible reason for observing the increase in intensity of Fe in the crack-like areas of XRF maps. The reaction that occurs in the cathode catalyst layer ($½\ O_2 + 2H^+ + 2e^- \rightarrow H_2O$) uses H^+ and generates water. Both using H^+ and generating water decrease the concentration of H^+ and increase the pH. It is described in Section 2.2.4 that the liquid water which is formed in the cathode catalyst layer mainly flows through MPL cracks to the GDL [61-63, 67, 71]. Consequently, pH may increase locally within the MPL cracks. If pH increases within MPL cracks such that FeOOH becomes the stable phase (see Pourbaix diagrams in Section 7.1.2), the iron ions from corrosion of the bipolar plates may form FeOOH in these MPL cracks. The iron ions which are in water droplets may transport from the surface of the bipolar plates to the MPL cracks by the flow of air, oxygen, and coolant in cells [62, 92], as shown in Figure 5-16.

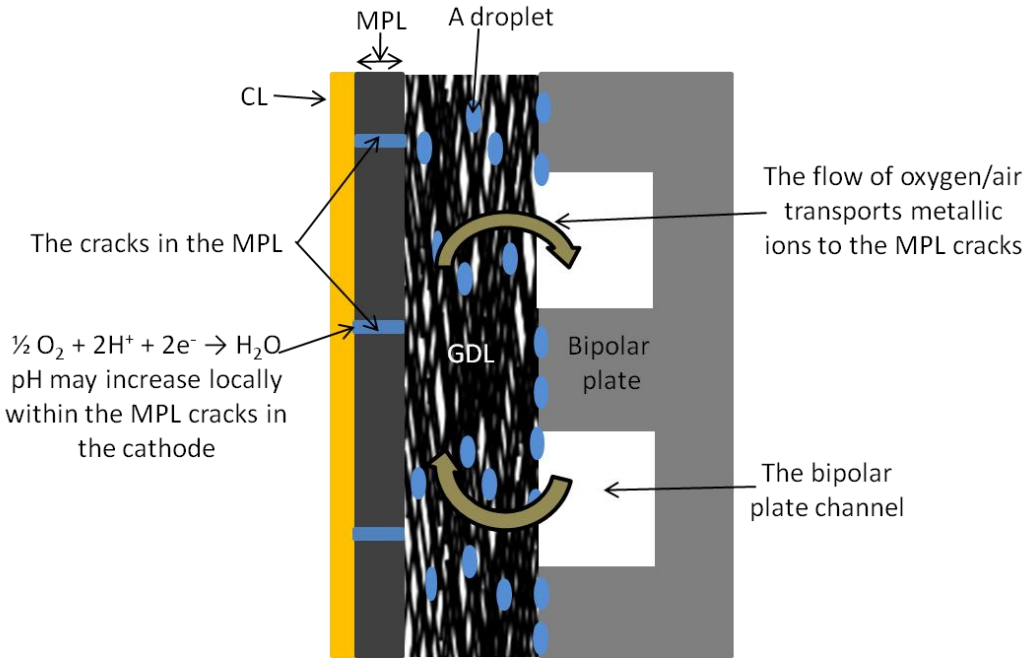

Figure 5-16. A possible reason for observing an increase in intensity of Fe in the crack-like areas of XRF maps (Figure 5-1 and Figure 5-2). pH is increased locally by the cathode reaction within the MPL cracks such that iron oxides become the stable phase. The iron ions from the corrosion of the bipolar plates which are transported to the MPL cracks by the flow of air/oxygen can form iron oxides in these MPL cracks. Therefore, the crack-like areas may be the cathode MPL cracks. MPL is the micro-porous layer and CL is the catalyst layer in the figure.

Therefore, the crack-like areas observed in Figure 5-1 and Figure 5-2 with the high intensity of Pt and Fe could be the cathode MPL cracks.

5.4.2 Cross section XRF maps: used vs. unused

The levels of Fe, Ni and in general Cr corrosion contaminants found in used MEA cross-sections were higher than those found in the unused MEA cross-section. This is generally consistent with laboratory and synchrotron-based XRF studies on plan view of MEA in the previous chapter. These plan view samples (in the previous chapter) were tested directly and without any preparation; this suggests that the cross section preparation method does not significantly add Fe, Ni and Cr contaminants to MEAs. The levels of Cu found in used MEAs were similar to or somewhat higher/lower than those found in the unused MEA; this is consistent with laboratory XRF measurements of plan view MEA but this is not in agreement with synchrotron-based XRF studies of plan view MEAs in previous chapter. Because there are very low levels of Cu (about 0.5-1 $\mu g/cm^2$ based on laboratory experiments) in MEAs used in the experiments low levels of Cu contaminant from cross section preparation method could possibly cause this contradictory for Cu levels measured by synchrotron XRF. In addition Fe, Ni, Cr and Cu maps of used MEAs show a different distribution compared with maps of the unused MEA. To avoid unnecessary repetition please refer to Section 4.4.1 where these results are compared with the literature.

5.4.3 Cross section XRF maps: distribution of elements

As described in Section 5.3.2, synchrotron-based XRF maps of used MEA cross sections showed the distribution of Fe, Ni, Cr and Cu in used MEAs is not random. The

main contaminant i.e. Fe is mainly found in microporous layers in the cathode side. A possible reason for this is described in Section 5.4.1 (see Figure 5-16).

The XRF maps reveal significant amounts of the Fe, Ni, Cu, and Cr contaminants tend to accumulate in one of the sensitive components, i.e. membrane. However, these contaminants do not show significant tendency to accumulate in the catalyst layers. The metallic ions release in the stack water may reach membrane [15] and these metallic ions may be absorb by the membrane [8, 17, 19, 23, 44, 79, 91].

These results for membrane and catalyst layer are not consistent with the EDS analysis of MEA cross-sections that showed more Fe in cathode catalyst layer than membrane [96, 97]. Makkus et al. [96, 97] investigated the distribution of Fe in the MEA cross section using SEM and Energy Dispersive X-ray Spectroscopy (EDS) mapping; their result showed that there was more Fe in cathode catalyst layer than in anode catalyst layer and in membrane. However, the EDS result of a control cross section from unused MEA was not presented; therefore Fe could have originated not only from corrosion of bipolar plates but also from the MEA production process or preparation of cross-sections. In addition, the reported EDS map only covered about 65 µm of the catalyst layers and the gas diffusion layer (GDL) was not included [96, 97]. The thickness of catalyst layers could vary and 65 µm of the catalyst layers could possibly not represent a cross section of the MEA. In addition, EDS results sample a thin layer of surface of about 1µm depth which could be easily contaminated during preparation of cross-sections such as polishing. X Ray Fluorescence (XRF) signals can emerge from deeper areas compared with EDS and it has been demonstrated as a more sensitive method than EDS for study contamination in MEAs [20, 23, 128].

5.4.4 Cross section XRF maps: direct comparison between the anode and cathode sides

Synchrotron-based XRF of MEA cross-sections made it possible to directly compare and evaluate contamination levels in the anode side and cathode side of MEAs, this was impossible for MEA plan view experiments since there was always XRF signals from both anode side and cathode side.

The levels of Fe, Ni, Cr and Cu found in the cathode sides were higher than those found in anode sides. This is consistent with visual observation of bipolar plates, previous AAS and ICP studies on MEAs from a "multisinglecell" (618 h to 650 h at 80 ^{o}C) with uncoated 904L SS bipolar plates (the bipolar plates which were used in this chapter were 904L SS) [136] and the results of the previous chapter. In order to avoid unnecessary repetition, please also see Section 4.4.3 where the presence of more contaminants on the cathode side than on the anode side is discussed.

It is discussed in Section 5.4.1 that the cathode reaction may increase local pH within the MPL cracks on the cathode side such that the iron oxides may become the stable phase within these MPL cracks. However, the anode reaction ($H_2 \rightarrow 2H^+ + 2e^-$) decreases pH and soluble species (Fe^{2+}) may be the stable form of iron on the anode side. The flow of hydrogen or coolant may move the water droplets which contain these iron ions out of stacks [62, 92]; this may be a possible reason for observing more Fe on the cathode side than on the anode side of used MEAs.

5.4.5 Cross section XRF maps: hot area vs. cold area

The cross section maps of the MEA from cell 9 of stack 9-1941-69 showed higher levels of Fe, Ni, Cu and Cr in the "hot" area than the "cold" area; this is consistent with

visual observation of bipolar plates as well as the laboratory and synchrotron XRF results which were presented in the previous chapter. In order to avoid unnecessary repetition, please see Section 4.4.4 for the detailed discussion.

5.4.6 Pt XRF map of the MEA from cell 20 of stack 9-1000-78

The Pt XRF map of the MEA from cell 20 of stack 9-1000-78 may give the wrong impression of Pt dissolution for this sample. However, the Pt level of this sample is significantly higher than that of the control and the other samples, as can be seen in Figure 5-9. Pt dissolution may cause Pt element loss [1-3]. However, it has not been reported that Pt dissolution causes an increase in Pt levels to levels higher than the Pt levels of the control. In addition, the MEA from the other cell of the same stack (cell 1 of stack 9-1000-78), which was aged under the same aging cycles and conditions, did not show a similar Pt XRF map (see Figure 5-9); this shows Pt dissolution was not responsible for the observation of more Pt in this MEA. It is possible the Pt loaded on the cathode side of this sample was higher than the Pt loaded on the other samples and the control.

5.5 Conclusions

- Microscopic distribution of contaminants was consistent with macroscopic distribution of contaminations in MEAs.
- Plan view XRF maps show an inhomogeneous distribution of Pt. The high levels of Fe correlate with the high levels of Pt and they present in cracks-like areas which can be cathode MPL cracks.
- The unused MEA cross section showed the lower levels of contaminants than the used MEA cross-sections.

- Used MEA cross-sections showed more contaminants in the cathode side than in the anode side.
- For most of the measurements Fe (the major contaminant) was found in the microporous layer of the cathode side. Ni, Cr and Cu were observed in the membrane and/or the cathode side.
- Significant levels of contaminants were observed in the membrane; however, the levels of contaminants in the catalyst layers were not significant compared to other areas of cross sections.
- The cross section from “hot” areas showed the higher levels of contaminants compared with the cross section from “cold” areas for stack 9-1941-69 cell 9.

6 Galvanic crevice corrosion in PEMFCs

6.1 Introduction

The corrosion susceptibility of bipolar plates in PEMFCs has been commonly tested using potentiodynamic and potentiostatic measurements. However, both galvanic effects and crevice effects that may found at the BP/GDL interface have not been simulated in these tests [9, 24].

Previous studies have investigated galvanic corrosion between bipolar plates and carbon-based materials [26] or catalyst layers [25]. These studies have showed the galvanic corrosion rates can be significant for bipolar plates in PEM fuel cells [25-27].

In this chapter, the results of 1150 hours of electrochemical measurements using the galvanic crevice cell are presented. According to in situ measurements in PEM fuel cells [27], the galvanic crevice cell simulates a more representative ex situ experiment for the corrosion of bipolar plates in PEM fuel cells, which includes simulating galvanic and crevice effects at the BP/GDL interface.

6.2 Corrosion behaviour of as received 316L SS coupled to GDL or MEA

Figure 6-1 shows the results of 200 hours of electrochemical measurements using the galvanic crevice cell for as received 316L SS coupled to an MEA (including GDL) or a GDL only. As described in Section 3.5.1, the temperature was cycled between room temperature and ~80 °C. It can be seen that changes in the current and potential coincide with the temperature cycles; for both experiments, the galvanic current is significantly higher at 80 °C than at room temperature, and the potential at 80 °C is significantly lower than that at room temperature. In addition, Cycle 1 is very different with the other cycles in terms of change in current and potential; however, Cycles 2, 3 and 4 are similar. As received 316L SS coupled to an MEA (left side of the figure) shows a significantly higher current and potential than as received 316L SS coupled to a GDL (right).

It can be concluded that in a PEM fuel cell, the presence of the MEA including both the GDL and the carbon-supported Pt catalyst will lead to an increased potential at the bipolar plate surface, therefore for the rest of the experiments metallic samples were coupled to an MEA (including the GDL).

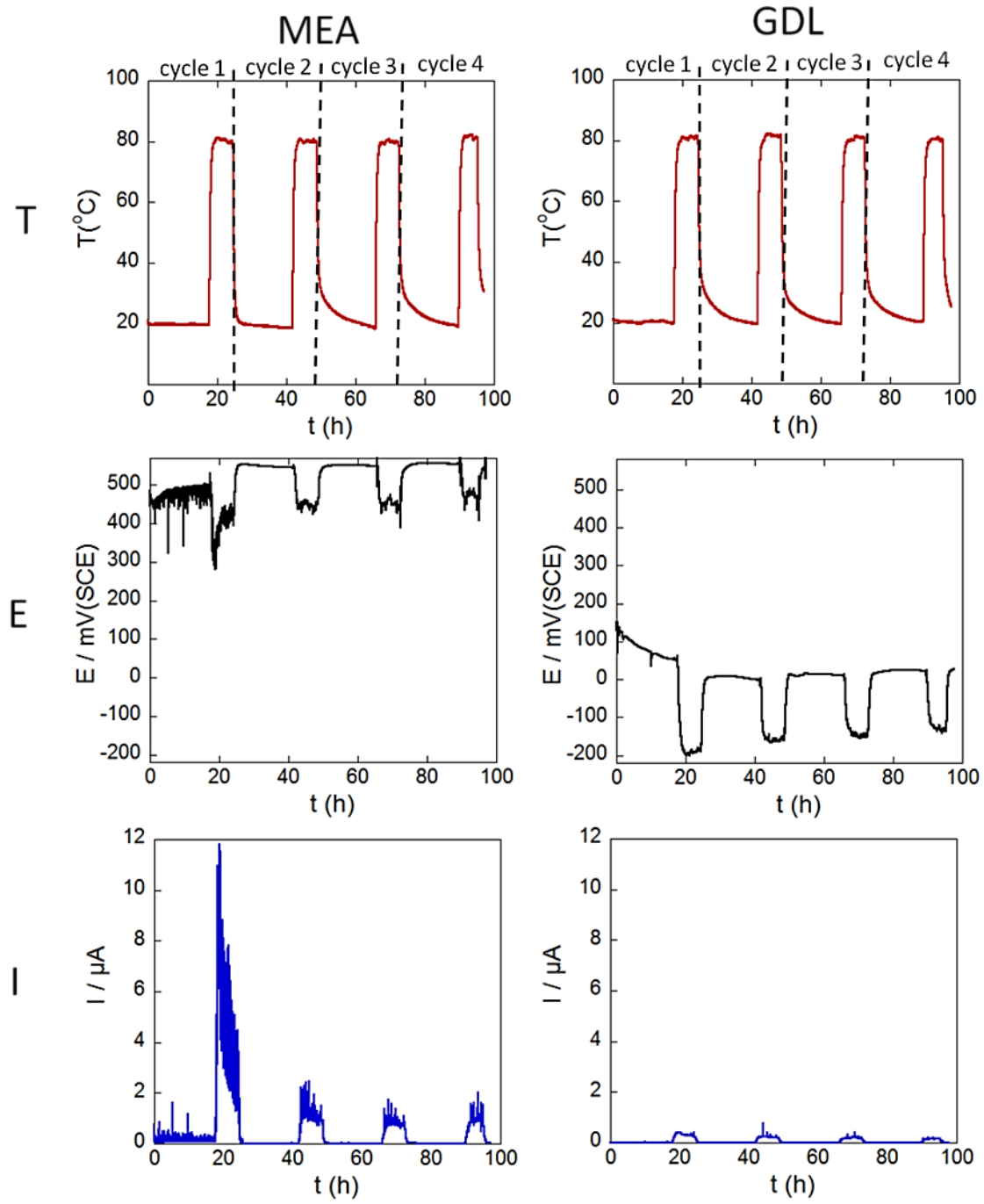

Figure 6-1. Galvanic current and potential measurements (200 hours measurement), cycling between room temperature and ~ 80 °C for as received 316L stainless steel coupled to a MEA (including GDL), left, or a GDL alone, right, with a Pall Nylaflo™ Nylon membrane separator, in a solution of 1 mM NaCl + 1 mM H_2SO_4. 1 MPa pressure was applied to the electrodes. T is the cell temperature, E is the potential (vs. SCE) and I is the galvanic current.

6.3 Corrosion behaviour of uncoated 316L SS and uncoated 904L SS

Figure 6-2 shows the results of 300 hours of electrochemical measurements using the galvanic crevice cell for as received 316L SS (Figure 6-2 (a), (b) and (c)), polished 316L SS (Figure 6-2 (d) and (e)) and as received 904L SS (Figure 6-2 (f)) (Figure 6-2 (a) is the same data from Figure 6-1 for MEA). The current and potential changes in Figure 6-2 (a), (d) and (f) coincide with the temperature cycles. When the temperature was 80 °C it is marked with red lines in the top of the images, for the rest of the measurement time, samples were at room temperature (see temperature cycle in Figure 6-1 of this chapter or Figure 3-9).

Figure 6-2 (a), (b), and (c) show results for as received 316L SS, this stainless steel shows initially significant noise at room temperature, this is shown in greater detail in Figure 6-2 (b) where current peaks coincide with sudden fall in potential which is characteristic of metastable pits, an example of theses peaks is shown in Figure 6-2 (c).

Figure 6-2 (d) shows freshly polished 316L SS results. In the Cycle 1, at room temperature, the potential is significantly lower than Figure 6-2 (a) as the passive film has been removed and is re-growing. The current decrease and potential increase show growth of passive film but there is not any sign of metastable pitting as can be seen in Figure 6-2 (e).

Figure 6-2 (f) shows results for as received 904L SS. No metastable pits are observed at room temperature during the Cycle 1. It can be seen that in Cycle 1, 904L SS shows less increase in current than 316L SS with increasing temperature. As received 904L SS shows lower current than 316L SS as shown in Figure 6-2 (a), (d) and (f).

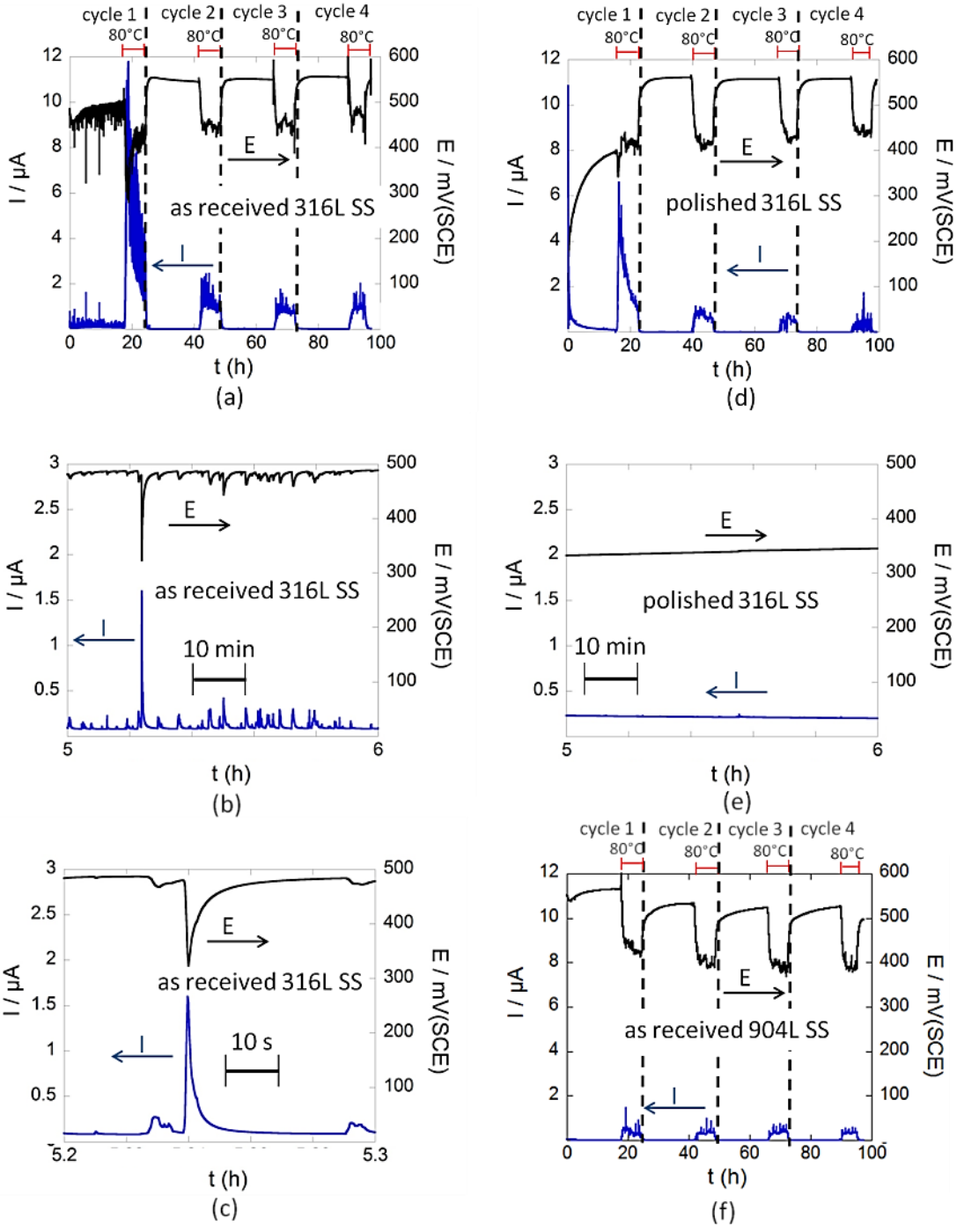

Figure 6-2. galvanic current and potential measurements (300 hours measurement), cycling between room temperature and ~80°C (marked with red lines), for (a), (b) and (c) as received 316L SS, (d) and (e) polished 316L SS and (f) as received 904L SS coupled to MEA with a Pall Nylaflo™ Nylon membrane separator, in a solution of 1 mM NaCl + 1 mM H_2SO_4. (b) and (c) show parts of (a) with different axis limits. (e) shows (d) with a different axis limit. 1 MPa pressure was applied to the electrodes. E is the potential (vs. SCE) and I is the galvanic current. (b), (c) and (e) are measured in the room temperature.

Cycles 2, 3 and 4 are slightly different with each other; however, Cycle 1 is different with the other cycles. During Cycle 1, potential and current change more significantly than those in Cycle 2, 3, and 4 as shown in Figure 6-2 (a), (d) and (f).

All stainless steels show similar behaviour in Cycles 2, 3 and 4; however, they are different in Cycle 1, for polished 316 SS the changes in potential and current are sharper than as received 316 SS and as received 904L SS in the beginning of the tests (between 0 h to 15 h) at room temperature (see Figure 6-2 (a), (d) and (f)).

Figure 6-2 (b), (c) and (e) which show parts of the Cycle 1 for Figure 6-2 (a) and (d) present the other difference between polished and as received 316 SS. As received uncoated 316L SS shows many peaks (fluctuation in current and potential) as can be seen in Figure 6-2 (b) and (c); Figure 6-2 (c) shows one of these peaks which usually starts with a very fast increase in current (decrease in potential) and followed by a slow decrease in current (increase in potential); however, as received 904L SS and polished 316 SS (Figure 6-2 (d), (e) and (f)) show a smooth diagram without any peaks. After Cycle 1, no peak for as received 316L SS are observed in the room temperature as shown in Figure 6-2 (a).

6.4 Corrosion behaviour of coated 316L SS

Figure 6-3 shows the results of 600 hours of electrochemical measurements using the galvanic crevice cell for as received 316L SS and 316L SS with different coatings.

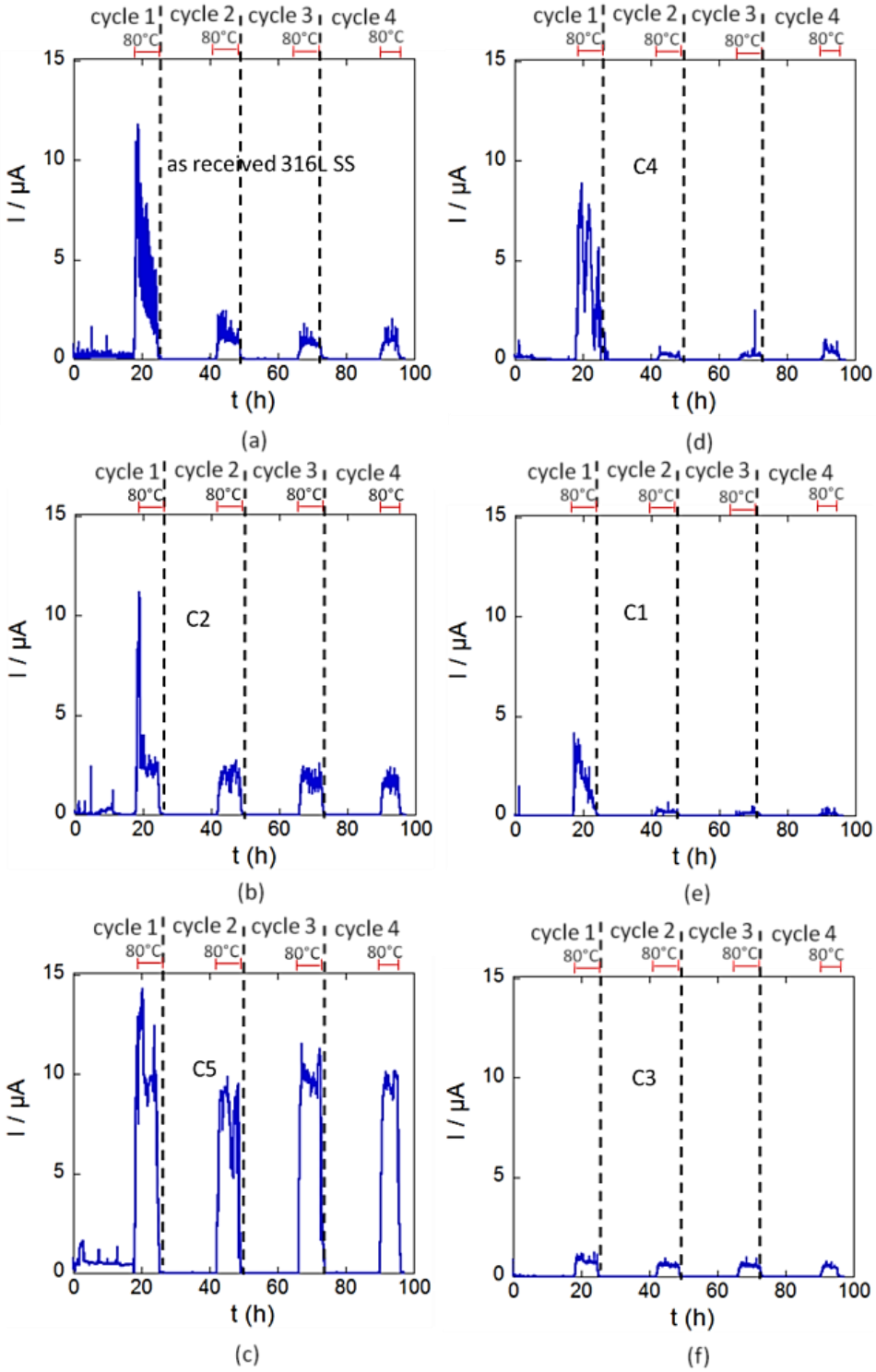

Figure 6-3. Galvanic current measurement results for coatings (600 hours), cycling between room temperature and ~80°C (marked with red lines) for coatings and as received 316L SS for comparison, (a) as received 316L SS (b) C2 (c) C5 (d) C4, (e) C1 and (f) C3 coupled to MEA with a Pall Nylaflo™ Nylon membrane separator, in a solution of 1 mM NaCl + 1 mM H_2SO_4. 1 MPa pressure was applied to the electrodes. E is the potential (vs. SCE) and I is the galvanic current.

The current changes in Figure 6-3 correlate with the temperature cycles as shown in Figure 3-9 of the experimental chapter. Current increases with increasing temperature and Cycle 1 is different from Cycle 2, 3 and 4 in terms of change in current, the only exception is coating C3 which shows similar behaviour in all cycles. This is consistent with the previous results for uncoated samples.

6.5 The steady state corrosion currents at ~80°C

Cycle 1 shows a higher current and higher rate of current decrease (except for coating C3) compared to Cycle 2, 3 and 4. This could be because in early stage of corrosion (Cycle 1), the properties of the existed passive layer (or re-growing passive layer on the polished sample) changed and modified according to the environmental conditions inside the galvanic crevice cell [9, 14] and then in Cycle 2, 3 and 4, the passive layer gradually reach its steady state conditions. Cycle 3 and 4 were very similar and so their average currents were considered to represent a steady state corrosion current.

Figure 6-4 shows the average currents for Cycles 3 and 4 at ~80°C for electrochemical measurements using the galvanic crevice cell (900 hours). According to these results, coatings C1, C4 and C3 show lower galvanic current than as received 316L SS whereas coatings C2 and C5 show higher galvanic current than as received 316L SS. As received 904L SS shows better corrosion resistance than as received 316L SS.

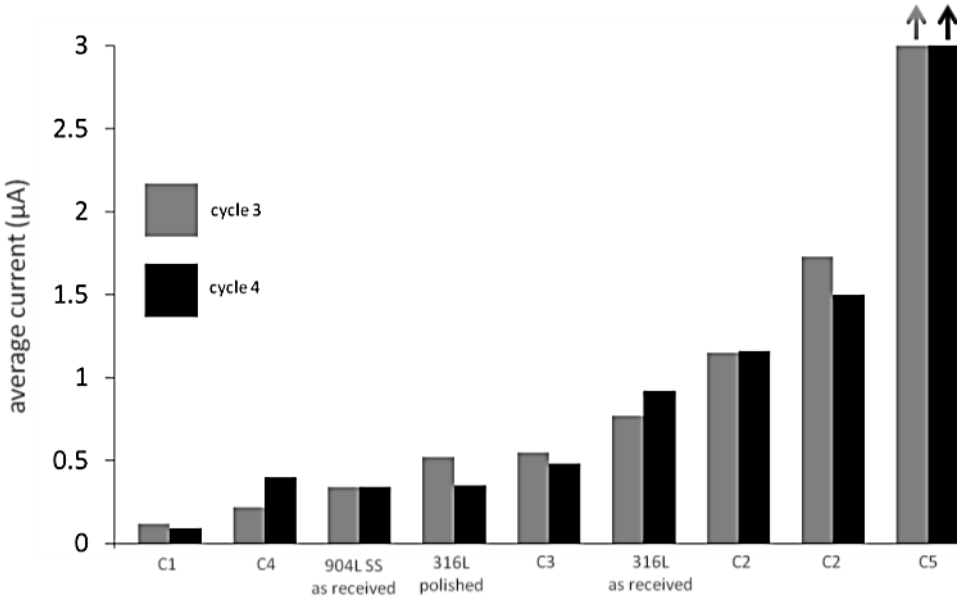

Figure 6-4. The results of 900 hours of measurements using a galvanic crevice cell, average of currents in Cycle 3 and Cycle 4 at T ≈ 80 °C for coatings (C1, C4, C3, C2, repeat of C2 and C5), polished 316L SS, as received 316L SS and as received 904L SS coupled to MEA with a Pall Nylaflo™ Nylon membrane separator, in a solution of 1 mM NaCl + 1 mM H_2SO_4. 1 MPa pressure was applied to the electrodes. E is the potential (vs. SCE) and I is the galvanic current.

6.6 Attempt at a shorter electrochemical measurement

The testing protocol was 100 hours to make sure that the passive films on the bipolar plates reached their steady state conditions. However, such a long testing protocol has disadvantages. A very long time (thousands of hours) was needed to evaluate several coatings. Additionally, if a test failed before it ended then a long time was wasted. As a result, a shorter protocol that could give similar results to the 100 hours protocol could be very useful. Therefore, a shorter protocol (Figure 6-5 (a)) was attempted and its results were compared with the results of the long tests (100 hours).

Figure 6-5 shows the result of 150 hours of electrochemical measurement using a 30-hour testing protocol (short test). It can be seen in Figure 6-5 that the current at 80 °C tends to decrease from the first cycle to the third cycle. This could be because of the development of passive layers on the bipolar plates.

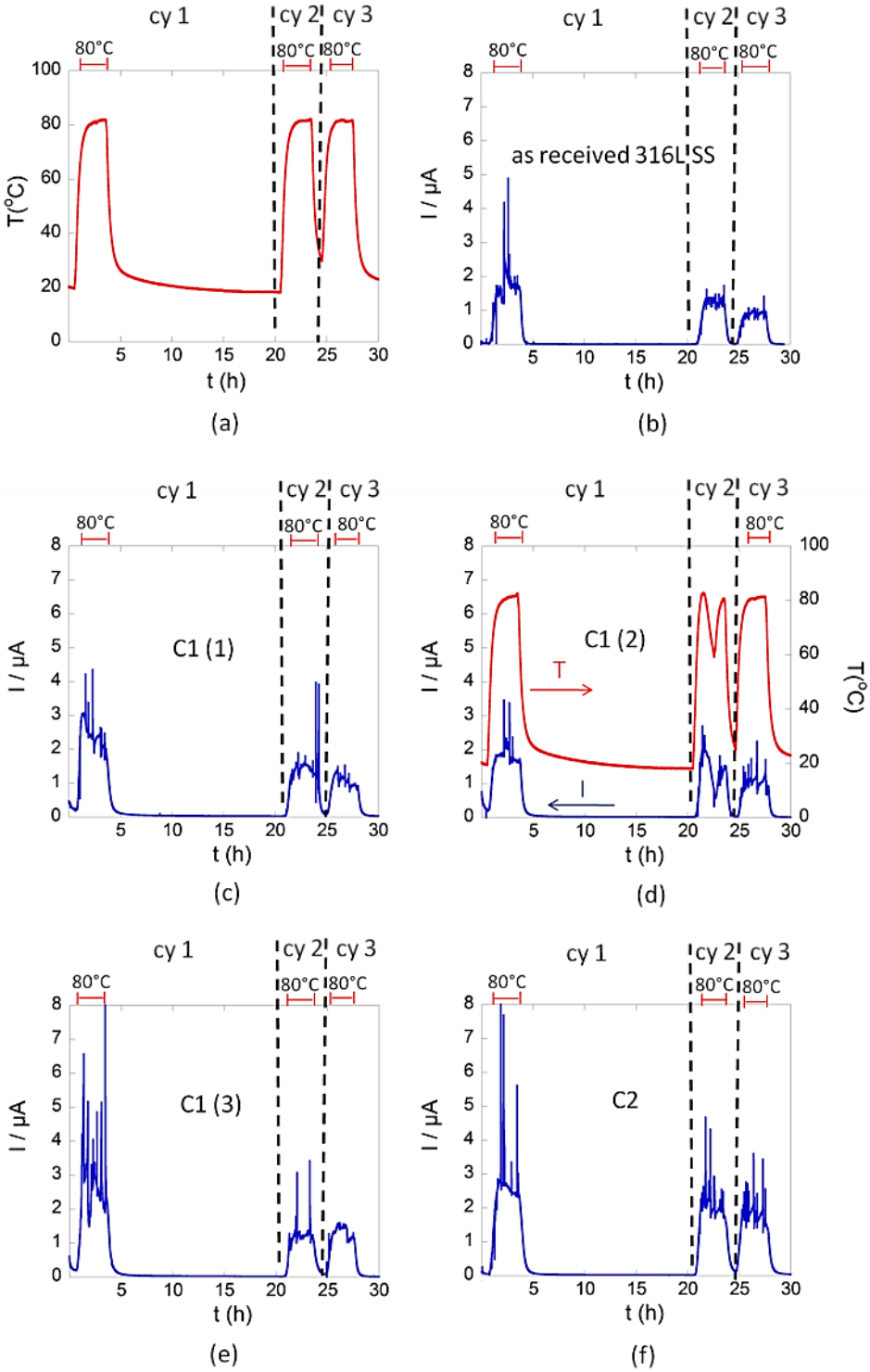

Figure 6-5. 150 hours of electrochemical measurements using the short protocol (30 hours). (a) temperature cycles for the short test (b) as received 316L SS (c), (d) and (e) C1 coated 316L SS and (f) C2 coated 316 SS coupled to an MEA with a Pall Nylaflo™ Nylon membrane separator, in a solution of 1 mM NaCl + 1 mM H_2SO_4. 1 MPa pressure was applied to the electrodes. E is the potential (vs. SCE) and I is the galvanic current. Temperature cycles between room temperature and ~80°C (marked with red lines) for coatings and as received 316L SS. Cy is cycle. For (d), the heating system stopped working due to an electricity shutdown in the middle of Cycle 2.

Figure 6-6 compares the long test (100 hours) and the short test (30 hour) for 316L SS (Figure 6-6 (a)) and for C1 coating (Figure 6-6 (b)). It can be seen in Figure 6-6 that the currents at the end of the short test (between ~25 h to ~30 h) are significantly higher than the currents at the end of Cycle 3 of the long test ((between~ 65 h to ~70 h)). This shows that the long test is required to reach the steady state condition of passive films.

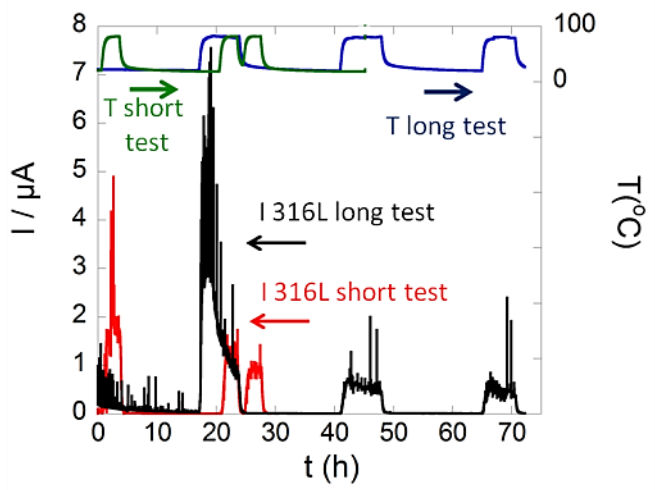

Figure 6-6. Comparing the long test and the short test for (a) as received 316L SS and (b) C1 coated 316L SS coupled to an MEA with a Pall Nylaflo™ Nylon membrane separator in a solution of 1 mM NaCl + 1 mM H_2SO_4. 1 MPa pressure was applied to the electrodes. E is the potential (vs. SCE), T is temperature and I is the galvanic current. Temperature cycles between room temperature and ~80°C for C1 and as received 316L SS.

6.7 Discussion

6.7.1 Comparing the galvanic crevice cell with previous work

In situ measurements of corrosion potential for bipolar plates in PEM fuel cells have been presented in a recently published paper by NPL [27]. The results have revealed that cell current density and cell potential do not have a significant influence on the corrosion potential of bipolar plates and the galvanic crevice corrosion mechanism can be the most important corrosion mechanism for bipolar plates in PEM fuel cells [27].

Andre et al. [25] studied the galvanic current between a homemade MEA (Pt loading of the MEA was not reported) and surface-modified 316L SS in a bulk solution with the composition of stack exhaust water at 60 °C using zero resistance ammeter (ZRA) measurements. After 5 hours, the measured galvanic current was 0.14 $\mu A/cm^2$ and the measured potential for the couple was 880 mV vs. RHE. For comparison of their results with the galvanic crevice cell results, the measured currents were about 0.2 $\mu A/cm^2$ and 0.1 $\mu A/cm^2$ and the measured potentials were 710 mV and 690 mV vs. RHE for as received and polished 316L SS, respectively. However, Andre et al. [25] did not take into account the crevice geometry between MEAs and bipolar plates and pressure across the interface of the stack.

Mele and Bozzini [26] studied galvanic crevice corrosion between reticulated vitreous carbon (RVC) and 304 SS (1 mM H_2SO_4 and 10 mM HCl, room temperature) using the potentiodynamic and potentiostatic measurements of the couple. Although the crevice geometry and stack pressure were simulated, the samples were under potential control and they were in contact, so the galvanic corrosion current between the two

components was not measured. They also did not simulate the typical temperature in an operating PEM fuel cell [9, 50, 53].

The galvanic crevice cell and the testing protocol (as described in Section 3.5) simulate galvanic corrosion, crevice corrosion, temperature cycles and uniaxial pressure in PEM fuel cells. The galvanic crevice cell was successfully used to discriminate different coatings for bipolar plates. To our knowledge, no similar design or testing protocol has been reported.

6.7.2 The interfacial potentials between bipolar plates and their adjacent aqueous phase

Corrosion of a metal is controlled by the interfacial potential between the metal and its adjacent aqueous phase. Figure 6-7 (a) shows a schematic diagram of a cross section of bipolar plates and MEAs in PEMFCs and Figure 6-7 (b) illustrates a schematic diagram of the electrical and ionic conductivity between bipolar plates and catalyst layers through the GDL and MPL in PEMFCs. It can be seen in Figure 6-7 (b) that the SBP and SCL are two points in the aqueous phase which are located just outside of the bipolar plate and the catalyst layer, respectively; and the MBP and MCl are two points in the bipolar plate and the catalyst layer, respectively. The interfacial potential between the bipolar plate and its adjacent aqueous phase ($E_{MBP/SBP}$) is:

$$E_{MBP/SBP} = E_{MBP} - E_{SBP} \quad (33)$$

E_{MBP} is the potential of the point MBP in the bipolar plate and E_{SBP} is the potential in the point SBP. There is a low IR drop between the point MBP and the point MCL because bipolar plates and catalyst layers are in electrical contact through the GDL and MPL and the electrical resistance between bipolar plates and catalyst layers (including

ICR) are usually low to improve overall stack performance [79]. Therefore, E_{MBP} is close to the potential of the nearest catalyst layer (E_{MCL}) (Figure 6-7 (b)).

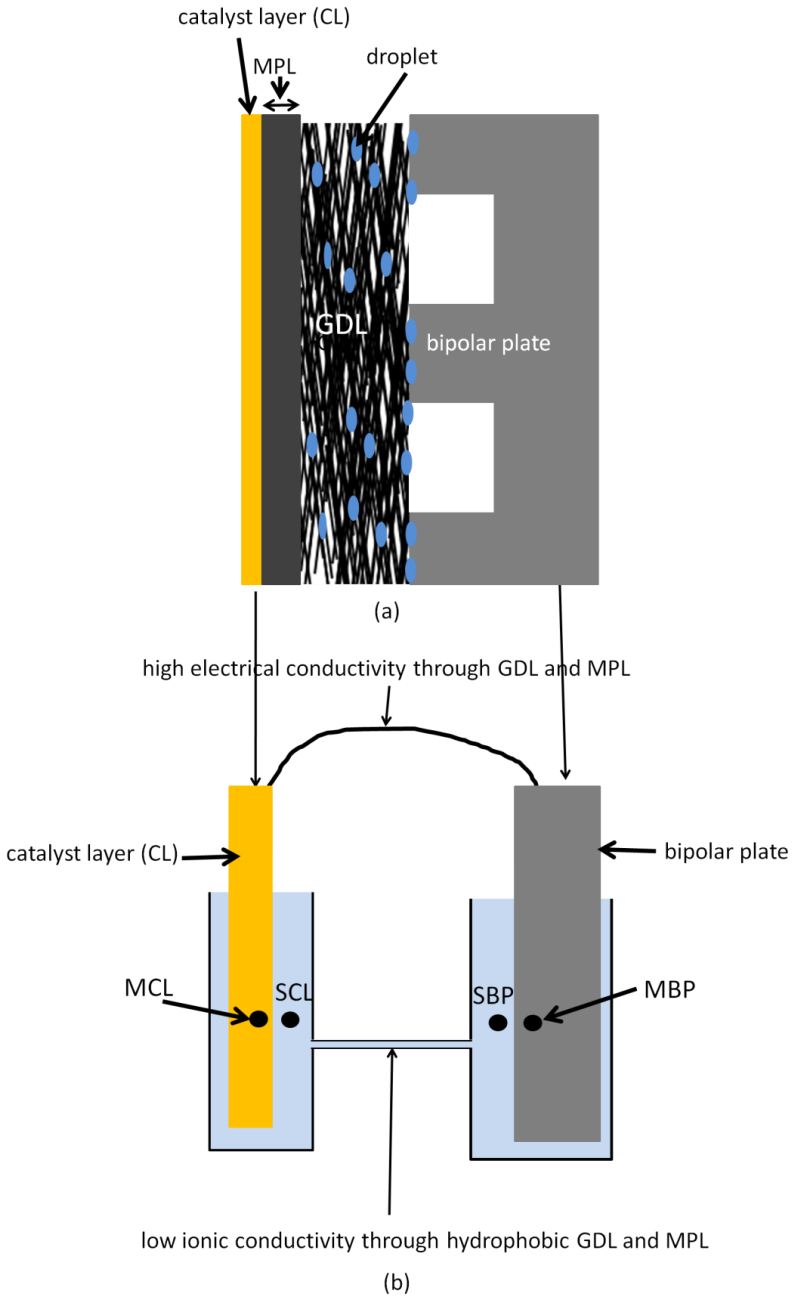

Figure 6-7. The interfacial potential between the bipolar plate and its adjacent aqueous phase. (a) Illustrates a schematic diagram of a cross section of bipolar plates and MEAs in PEMFCs. (b) Illustrates a schematic diagram of the electrical and ionic conductivity between bipolar plates and catalyst layers through the GDL and MPL in PEMFCs. Because of high ionic resistance between the point SCL and the point SBP, the interfacial potential between the bipolar plate and its adjacent aqueous phase are significantly different from the interfacial potential between the catalyst layer and its adjacent aqueous phase.

However, because the GDL and MPL are hydrophobic and there is a flow of reactants and coolant which moves isolated droplets through the GDL, there is a very limited continuous aqueous phase and a high ionic resistance (a high IR drop) between the point SBP and the point SCL (Figure 6-7 (b)). Therefore, E_{SBP} is significantly different from E_{SCL} and as a result the interfacial potential between the bipolar plate and its adjacent aqueous phase ($E_{MBP/SBP} = E_{MBP} - E_{SBP}$) is different from the interfacial potential between the catalyst layer and its adjacent aqueous phase ($E_{MCL/SCL} = E_{MCL} - E_{SCl}$). This is consistent with the results of the in situ measurements of corrosion potentials on the surface of bipolar plates in operating PEM fuel cells (see Section 2.5.3.2) [27].

6.7.3 Considering the requirements of corrosion tests for bipolar plates in the design of the galvanic crevice cell

Based on in situ measurements, the requirements of a more representative ex situ test for the corrosion of bipolar plates have been suggested [27]. The galvanic crevice cell and testing protocols which are designed in this PhD fulfill all these requirements. This is described in Sections 6.7.3.1 to 6.7.3.4.

6.7.3.1 Temperature cycling and time of tests

The temperature cycles are considered in the tests to simulate both operating temperature (~ 80 ºC) and room temperature for when PEM fuel cells operate and do not operate, respectively as shown in Figure 3-9.

The time of the corrosion tests was 100 hours to allow the passive layers to fully develop and reach their steady state conditions. Furthermore, a shorter test (30 hours) was designed and tested but it was not long enough for the passive layers to reach steady state conditions.

6.7.3.2 Simulating corrosion potentials of bipolar plates in PEM fuel cells

There is a very weak communication between corrosion potentials of bipolar plates and potentials of the nearest catalyst layers. However, bipolar plates are polarized due to galvanic coupling with a nobler MEA [27] (Sections 2.5.3.2 and 2.5.4).

The samples were polarized because of galvanic coupling to MEAs in the galvanic crevice cell. The values of the measured corrosion potentials using the galvanic crevice cell correlate well with the values of the in situ measured corrosion potentials for bipolar plates in PEM fuel cells [27] (See Section 6.7.8). Therefore, external potentials (for example 0.8 vs. SHE for simulating cathode potential) were not applied to samples in the galvanic crevice cell.

6.7.3.3 Simulating both crevice corrosion and galvanic corrosion

In addition to galvanic coupling with MEAs, a crevice geometry forms between MEAs and bipolar plates which may enhance corrosion rates (see Figure 6-8 (b)) [27].

The bipolar plates and GDL/MEAs are separated by a hydrophilic, thin, and porous membrane in the galvanic crevice cell so that the galvanic current between the bipolar plates and GDL/MEAs can be measured with a ZRA. In addition, the galvanic crevice cell simulates pressure across the interfaces (1 Mpa) and the crevice geometry in a PEMFC (see Figure 6-8 (c) and (d)).

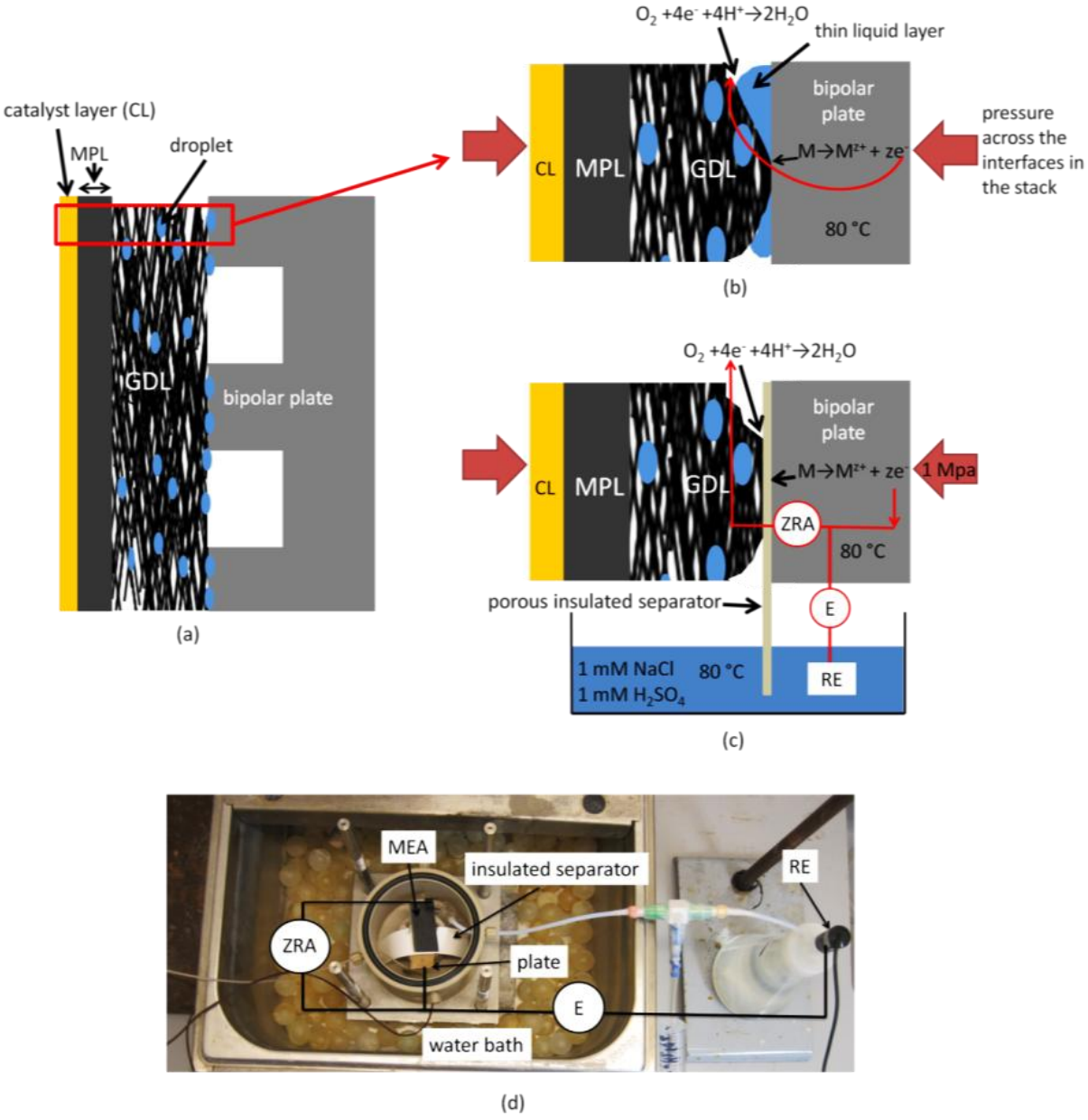

Figure 6-8. Corrosion mechanism of bipolar plates in PEMFCs and simulating/quantifying this mechanism using the galvanic crevice cell. (a) Because of the high ionic resistance of the aqueous phase in hydrophobic MPLs and GDLs, the potentials of the nearest catalyst layers do not have a significant influence on the corrosion potentials of bipolar plates [27], (b) shows an area of (a) with higher magnification, galvanic corrosion and crevice corrosion can occur in the bipolar plate/MEA interface, (c) simulating galvanic corrosion and crevice corrosion in the galvanic crevice cell and measuring potential of the couple (E) vs. SCE RE and the galvanic current. Samples and MEAs were separated by an insulated separator so that the galvanic current could be measured with a ZRA, (d) image of top view of the galvanic crevice cell.

6.7.3.4 Solution

A "simulating" solution including SO_4^{2-} and Cl^- ions was chosen for this study (i. e. 1 mM H_2SO_4 + 1 mM NaCl). The solution was chosen based on a chemical analysis of exhaust water from PEMFC stacks reported in the literature [25, 26, 147]. In situ measurement of F^- concentration showed that the concentration of this ion was lower than 2 ppm in PEMFCs [27] and it has been reported that adding 2 ppm F^- does not considerably affect corrosion rates. Moreover, F^- ions function as an inhibitor in the presence of Cl^- [26, 81]. Therefore, fluoride ions were not added to the solution. This is described in more detail in Section 2.5.1.

6.7.4 Effect of temperature

Increasing temperature causes an increase in the rate of the electrochemical reactions which increases the corrosion rate (corrosion current) [51]. This is consistent with galvanic crevice cell results where changes of current coincide with the temperature cycles.

6.7.5 Coupling to MEA vs. coupling to GDL

A higher current and potential was observed for as received 316L SS coupled to an MEA compared with as received 316L SS coupled to a GDL (Figure 6-1). The difference between GDL alone and MEA including the GDL is the presence of the Pt-based catalyst layers. Pt is nobler than carbon and can thus promote galvanic corrosion of coupled stainless steel.

6.7.6 Growth of passive layer on polished 316L SS

In Figure 6-2 (d), it can be seen that polished 316L SS shows a sharper increase in potential and decrease in current than as received 316L SS at room temperature between 0 h to 15 h (Figure 6-2 (a)). This may be because polished 316L SS had a thinner passive layer at the start of the test and the passive layer re-grew during Cycle 1 while as received 316L SS was covered with a passive layer made in air before the test (see Figure 6-2 (a) and (d)).

6.7.7 Metastable pitting of 316L SS

The other difference of as received 316L SS and polished 316L SS in Cycle 1 is shown in Figure 6-2 (b), (c) and (e). The oscillation of current and potential i.e. increase in current and decrease in potential in Figure 6-2 (b), (c) could be because of creation and death of metastable pits. In Figure 6-2 (c), the increase in current (decrease in potential) from background levels could be because of initiation and sharp growth of a metastable pit followed by the decrease of current (increase of potential) because of repassivation [34, 36, 39]. Gorse and Baroux [34] showed that this type of the metastable pit which starts with fast increase in current and then followed by slow decrease in current as can be seen in Figure 6-2 (c), could initiate on the metal matrix and the existence of MnS inclusion is not necessary. Baroux et. al. [36] have reported that very quick increase in current is because of a local breakdown of passive film which causes fast dissolution of unprotected stainless steel followed by slow decrease in current because of passive film recovery which is slower than the first step (see Figure 6-2 (c)).

In Cycle 1, more metastable pits observed for as received stainless steel as presented in Figure 6-2 (b) compared with polished one as depicted in Figure 6-2 (e), this is consistent with previous reports, Isaacs et al. [42] have showed a thicker passive layer on 304 stainless steel can increase the number of active pits compared with polished samples. Their results showed stainless steels with passive layers present worse pitting resistance than electropolished or abraded stainless steel.

6.7.8 Correlation between potentials measured by the galvanic crevice cell and in situ measured potentials in PEMFCs

After reaching steady state condition at Cycle 4, the averages of potentials between 92 to 95 hours at 80 °C were about 0.71V and 0.69 V vs. RHE (470 mV and 450 mV vs. SCE) for as received and polished 316L SS respectively. These measured potentials correlate well with in situ measured potential (i.e. about 0.6-0.7 V vs. RHE) for the cathode 316L stainless steel bipolar plates in operating PEM fuel cells at 80 °C (see Section 2.5.3.2 for the in situ results) [27, 148, 149].

6.7.9 Comparing corrosion rates of 904L SS and 316L SS

As received 904L SS shows a lower current than 316L SS as can be seen in Figure 6-4 and Figure 6-2. Wang et al. [150] also have reported a better corrosion resistant for 904L SS than 316L SS measured using anodic polarization in 1 M H_2SO_4 and 2 ppm F^- bubbled with hydrogen or air at 70 °C. This could be because of different chemical composition of these alloys, 904L SS contains more Ni, Cr, Cu and Mo than 316L SS which affects its passivity and passive layer in PEMFC corrosive environments [151].

6.7.10 Relationship between corrosion rates of bipolar plates measured using the galvanic crevice cell and performance of stacks

The galvanic crevice cell measures the galvanic current; however, it is not clear whether the current forms soluble species that may be flushed out by water flow, dissolve away possibly contaminating the MEAs, or whether they form solid products that may lead to increase in interfacial contact resistance (ICR) between GDL and bipolar plate. Corrosion of bipolar plates may cause increase in interfacial contact resistance and contamination of MEA, both of these cause degradation in performance of PEM fuel cell stacks. A coating may show low galvanic current (i.e. low release of metallic ions in the solution which can cause contamination of MEAs); however, increase in interfacial contact resistance can be significantly decreases the performance of the stack [15, 83].

Corrosion rates measured using galvanic crevice cell are in the order of C1 < C4 < 904L SS < C3 < 316L SS < C2 < C5 (Figure 6-4) and the interfacial contact resistance (ICR) measured by IE is in the order of C5 < C2 < C3 < C4 < C1 < 316L SS (the values of ICRs are confidential). Durability tests carried out by IE showed that coatings C5, C2 and C3 have all demonstrated good performance in stack testing. Coating C1, which showed the lowest corrosion rate in Figure 6-4, showed slightly poorer performance than C5, C2 and C3 which could be because of its high ICR. It can be seen that C5, C2 and C3 showed the worse corrosion resistance among coatings tested in the present work; however, because they showed the low ICR, their performance in the stack was good.

6.8 Conclusions

- An electrochemical cell (galvanic crevice cell) was designed and testing protocols were defined to simulate galvanic crevice corrosion in PEM fuel cells. The galvanic crevice cell was successfully used to discriminate between different coatings on stainless steel bipolar plates. The results showed better corrosion resistance for 904L SS compared to 316L SS.
- Stainless steel coupled to an MEA (with a GDL) shows much higher currents and potentials compared with stainless steel coupled to a GDL alone, indicating that it is necessary to use an MEA for a realistic galvanic corrosion tests.
- The potential measurements using the galvanic crevice cell correlate well with in situ work measuring the potential of bipolar plates in operating fuel cells [27].
- No clear correlation between electrochemical results and the performance of the stacks was observed and the possible reasons for this were discussed.

7 General discussion and future work

7.1 General discussion

7.1.1 Distribution of contaminants in a MEA after use in a PEM fuel cell

Synchrotron and laboratory XRF measurements showed consistent results for MEAs selected from five stacks with different bipolar plates, aging cycles and MEA type. There were significantly higher levels of contaminants in used MEAs compared with unused MEAs and Fe was the main contaminant for the bipolar plates which were used in this study.

The distribution of contamination in a MEA which was used in a PEM fuel cell stack was not uniform. More contaminants were observed in hot areas (near to the coolant outlet) than cold areas (near to the coolant inlets). Levels of corrosion products observed in the cathode side were higher than in the anode side. Fe was mainly found in the microporous layer of the cathode side and Ni, Cr and Cu were mainly found in the membrane and/or the cathode side. The level of contaminants in the catalyst layers were not significant compared to the cathode side and the membrane.

Local regions with high levels of contamination in the plan view of MEAs did not correlate with the channel positions of bipolar plates and plan view mapping of MEAs using synchrotron XRF showed that these local high levels of contaminants have a pattern which can possibly be cathode MPL cracks.

This study suggests that XRF measurements of used MEAs can be used effectively to evaluate levels of contaminants in MEAs. Because the levels of contaminants in MEAs depend on the location in the cell, the findings of this study suggest that when

comparing levels of contamination between two cells, the location of XRF measurements on MEAs should be kept the same.

7.1.2 Predicting both bipolar plate corrosion and corrosion products in anode and cathode of PEMFCs using Pourbaix diagrams

Hinds et al. [27] carried out in situ measurements of acidity and corrosion potential for 316L SS bipolar plates in PEM single cells. The current density of the single cells varied between 0.0 and 0.5 A/cm^2 (the cell potential varied between 0.2 V and 0.9 V vs. RHE). For the cathode, the potential of 316L SS bipolar plates changed between 0.6 V and 0.7 V vs. RHE and the pH was between 3.4 and 4.0. For the anode, the corrosion potential of 316L SS bipolar plates was about 0.0 V vs. RHE and the pH was between 5.0 and 7.0.

Figure 7-1 to Figure 7-4 show Pourbaix diagrams of Fe, Ni, Cr, and Cu. Because Pourbaix diagrams were not available at PEM fuel cell operating temperature (~ 80 ºC), they were presented at room temperature. The range of in situ measured potentials for 316L SS bipolar plates and the range of in situ measured pH in PEM fuel cells [27] are shown by blue and red areas for anodes and cathodes, respectively.

7.1.2.1 Iron

It can be seen in Figure 7-1 that for the 316L SS bipolar plates, Fe was in the passivity area and the thermodynamically stable form of Fe was Fe_2O_3 for the cathode conditions. Both corrosion with the release of Fe^{2+} (for 5.0 < pH < ~ 6.5) and passivation with the formation of Fe_2O_3 (for ~ 6.5 < pH < 7.0) were possible, depending on pH values for the anode conditions. When the thermodynamically stable state of Fe is Fe_2O_3, if there is no chloride in the solution, it is expected that Fe does not corrode. However, if there is some chloride in the solution, localized corrosion may happen. Chloride ions were detected in exhaust water from PEMFC stacks [25, 26, 147]. If there is localized corrosion and the pH in the environment is high enough, FeOOH will form.

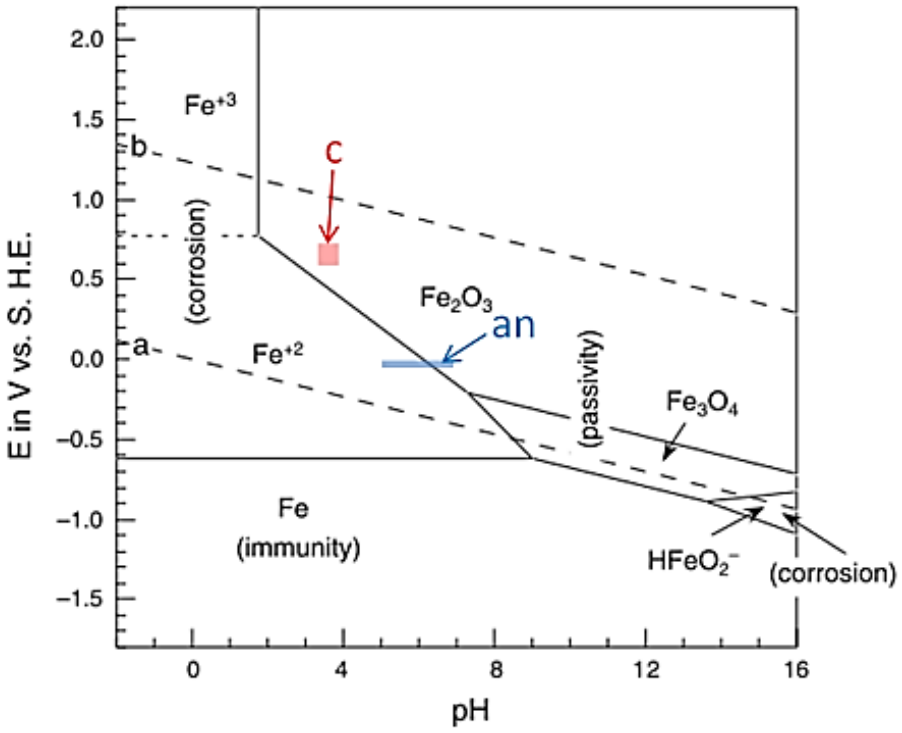

Figure 7-1. Pourbaix diagram for Fe-water system at 25 ºC (not the temperature of the experimental measurements) [30]. The range of potentials and pHs are shown by the blue area for anode (labelled "an") and the red area for cathode (labelled "C") for 316L SS bipolar plates. These ranges of potentials and pH are reported from Hinds et al. [27].

7.1.2.2 Nickel

Figure 7-2 shows the Pourbaix diagram for Ni. For both the anodic and the cathodic conditions Ni was always in the corrosion region and its stable form was Ni^{2+} ion for the 316L SS bipolar plates.

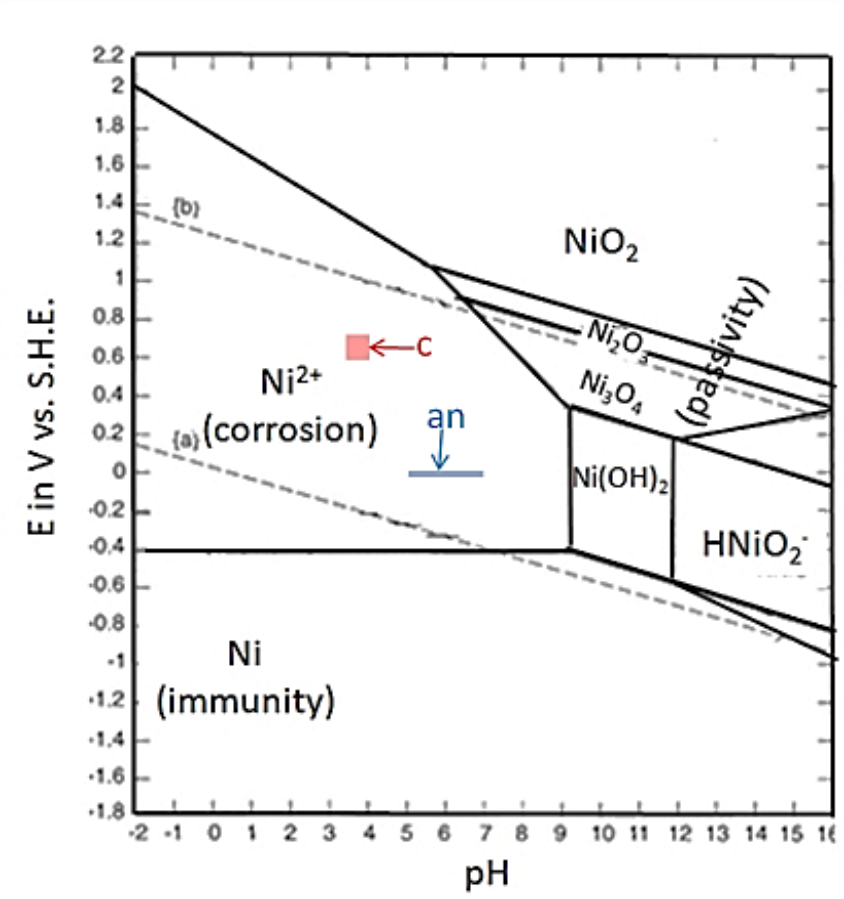

Figure 7-2. Pourbaix diagram for Ni-water system at 25 ºC (not the temperature of the experimental measurements) [152]. The range of potentials and pHs are shown by the blue area for anode (labelled "an") and the red area for cathode (labelled "C") for 316L SS bipolar plates. These ranges of potentials and pH are reported from Hinds et al. [27].

7.1.2.3 Chromium

It can be seen in Figure 7-3 that for the 316L SS bipolar plates, Cr was in the corrosion zone for the cathode conditions and the passivity zone for the anode conditions. The thermodynamically stable form of Cr was Cr^{3+} and Cr_2O_3 for the cathode and anode conditions, respectively.

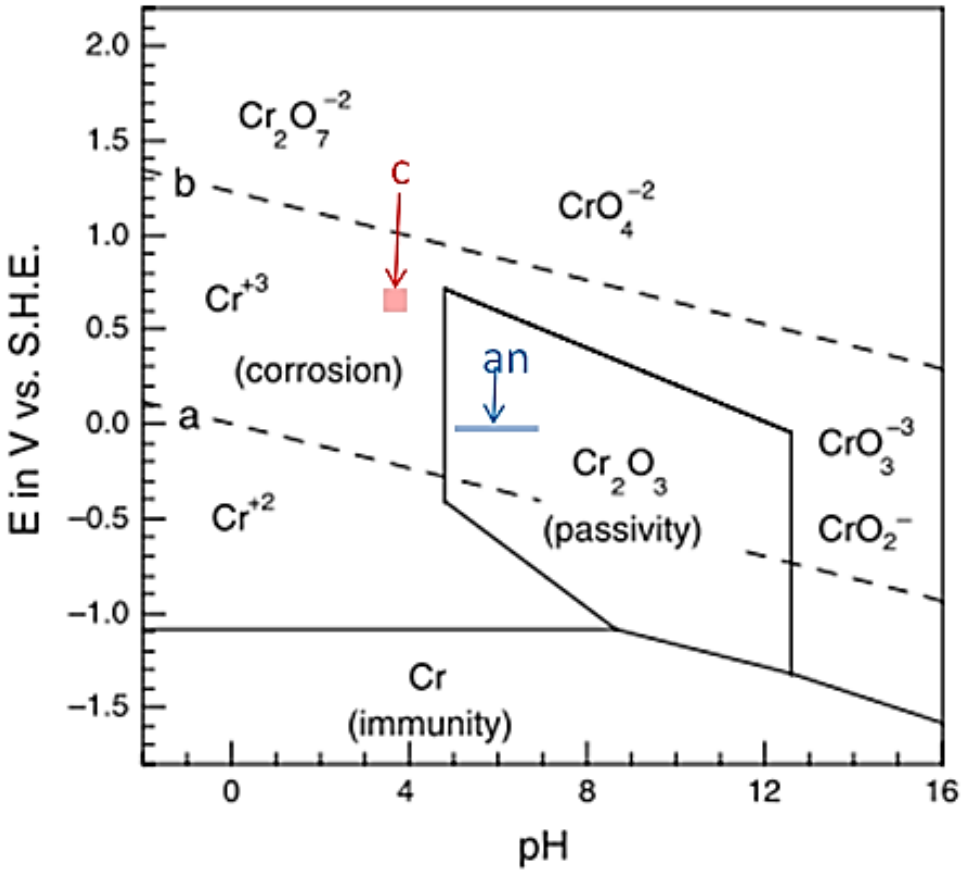

Figure 7-3. Pourbaix diagram for Cr-water system at 25 ºC (not the temperature of the experimental measurements) [30]. The range of potentials and pHs are shown by the blue area for anode (labelled "an") and the red area for cathode (labelled "C") for 316L SS bipolar plates. These ranges of potentials and pH are reported from Hinds et al. [27].

7.1.2.4 Copper

For the 316L SS bipolar plates, it can be seen in Figure 7-4 that Cu^{2+} was the stable form of Cu and this metal would corrode in the cathode. Cu was in the immunity region in anode as shown in Figure 7-4.

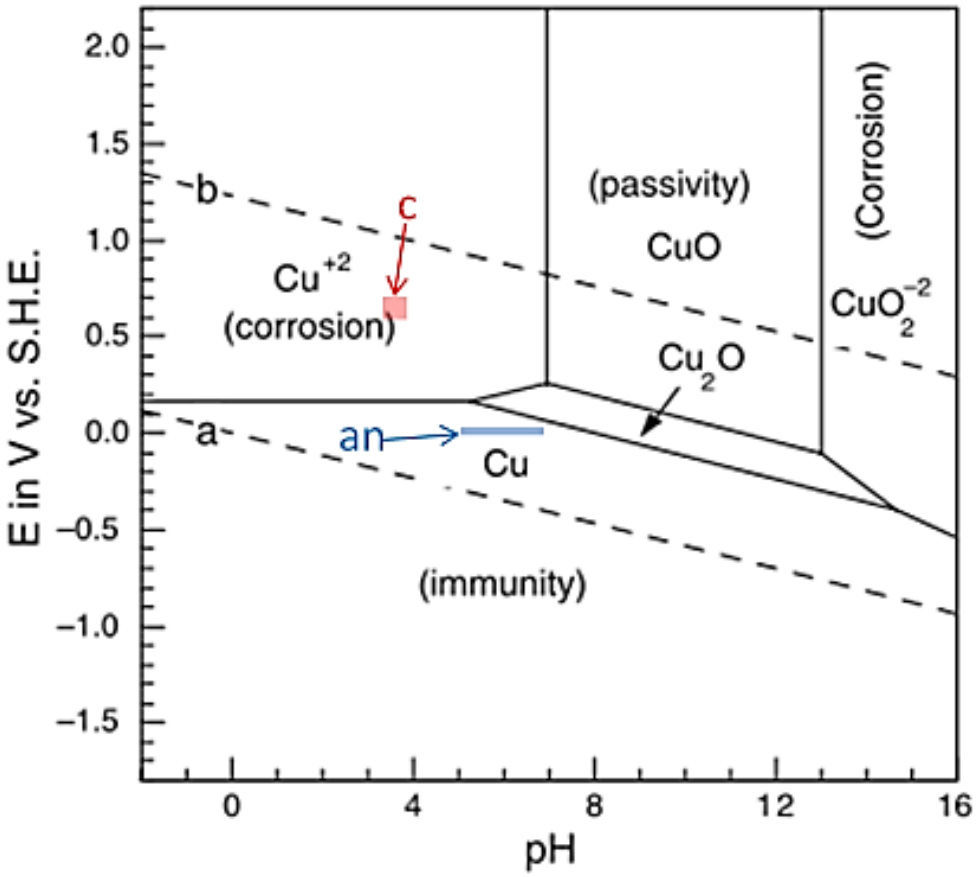

Figure 7-4. Pourbaix diagram for Cu-water system at 25 ºC (not the temperature of the experimental measurements) [30]. The range of potentials and pHs are shown by the blue area for anode (labelled "an") and the red area for cathode (labelled "C") for 316L SS bipolar plates. These ranges of potentials and pH are reported from Hinds et al. [27].

7.1.3 Comparing XRF results and predictions from Pourbaix diagrams

In situ measurements of pH and corrosion potential were made for 316L SS bipolar plates in PEM single cells [27] but the MEAs which were studied by XRF were from PEM fuel cell with 904L SS bipolar plates. The pH was measured at the base of the gas channel in the bipolar plate for single cells operating at 70 ºC and 100 % relative humidity [27]. There is no information about pH within the MEAs used in this thesis. Additionally, Pourbaix diagrams do not provide any information about quantities of corrosion products. However, comparing XRF results with information from Pourbaix diagram was attempted.

7.1.3.1 Iron

Laboratory and synchrotron XRF results for Fe correlate well with the Fe Pourbaix diagram. It can be seen in Figure 7-1 that Fe was in the Fe_2O_3 area for the cathode conditions. It is discussed in Section 5.4.1 that the cathode reaction may increase local pH within the MPL cracks on the cathode side. Increase of pH maintained Fe in the Fe_2O_3 area (Figure 7-1) and therefore Fe_2O_3 was the stable phase within MPL cracks. This is consistent with cross section and plan view XRF maps (synchrotron based XRF, Chapter 5) for Fe (i.e. observing Fe in the MPL cracks of cathode sides).

Both corrosion with the release of Fe^{2+} and the formation of Fe_2O_3 were possible, depending on pH values for the anode conditions. The anode reaction decreases pH and Fe^{2+} may become the stable form of iron within MEAs in anode sides (Figure 7-1) and the flow of hydrogen may move Fe^{2+} ions out of stacks. This is consistent with XRF results that showed lower level of contaminants for the anode sides than the cathode sides (chapters 4 and 5).

7.1.3.2 Nickel

Laboratory and synchrotron XRF results for Ni can be explained using the Ni Pourbaix diagram. Figure 7-2 shows the stable form of Ni was Ni^{2+} ion for both the anodic and the cathodic conditions. The high levels of Ni were mainly found in membranes (synchrotron based XRF, Chapter 5). For most laboratory XRF measurements, the levels of Ni in the anode and cathode side of MEAs were the same within experimental errors (Chapter 4). This could be because Ni^{2+} ions may be taken up by the membrane. Because the membrane was located in the middle of the MEA, the levels of Ni for the anode and cathode tests (see Figure 3-2 (Chapter 3)) of MEAs were the same within experimental errors (laboratory based XRF, Chapter 4).

7.1.3.3 Chromium and Copper

It can be seen in Figure 7-3 and Figure 7-4 that Cr and Cu would not corrode in the anode. However, they would corrode in the cathode. Cu levels in used MEAs were mainly similar to the levels of Cu found in the controls and Cr levels were mainly below the detection limit (Chapter 4). This could be because of low corrosion rates of Cr and Cu in PEMFCs. However, Pourbaix diagrams do not provide any information about corrosion rates.

7.1.4 Electrochemical measurements using galvanic crevice cell

An electrochemical cell was designed in this study to simulate galvanic corrosion, crevice corrosion and temperature cycles in a PEMFC. This cell was used successfully to discriminate between different coatings. A metallic sample coupled to an MEA (including a GDL) showed a higher potential and galvanic current than a metallic

sample coupled to a GDL only. The galvanic crevice cell results correlate with in situ measurements obtained from operating PEMFC.

The performance of four coatings (C1, C2, C3 and C5) were tested and all performed well in the IE stacks but the one (C1) that performed slightly less well than the others was the one that gave the lowest current in the galvanic crevice cell; however, in tests carried out by IE, it showed the highest ICR.

The technical suggestion of this part of the study is that the galvanic crevice cell can be used for preliminary discrimination of coatings and it is much cheaper than running single cells or stacks. However, ICR values should be measured because ICR may have an important influence on performance.

7.1.5 Effect of corrosion of bipolar plates on MEA contamination

Stack 9-1360-65 (1360h/65 °C) with 904L SS bipolar plate and stack 3c2-1515-67 (1515h/67 °C) with C2 coated 316L SS were run with a similar aging cycle and MEA type (Table 3-1). It is possible that the main difference between these two stacks lies in different bipolar plates. These two bipolar plates showed significantly different corrosion rates in the galvanic crevice cell. Therefore, they are suitable for study effect of the bipolar plate corrosion on the levels of MEA contamination.

C2 coated 316L SS showed corrosion current about 3-4 times higher than uncoated 904L SS according to the galvanic crevice cell results (Figure 6-4). The corrosion of bipolar plates may cause an increase in ICR or MEA contamination. As a result, it may be expected to see significantly higher corrosion products in MEAs from the stack with C2 coated 316L SS than the stack with 904L SS. However, the highest contamination levels (Fe) were 1.9 ± 0.2 $\mu g/cm^2$ and 1.8 ± 0.2 $\mu g/cm^2$ for stack with uncoated 904L SS

and C2 coated 316L SS bipolar plates, respectively, showing no significant difference in contamination levels.

There were significant cell-to-cell variations within stacks which were greater than stack-to-stack variations and a comparison between the stacks was impossible.

Corrosion of bipolar plates could be a slow process. Part of the metallic ions released from bipolar plates may be transported by water to MEAs and may contaminate the MEA, therefore the contamination process by metallic ions could be much slower than the corrosion rate or the release rate of the metallic ions and the operation time may be too brief to cause significant contamination levels in MEAs.

7.2 Future work

7.2.1 Simulating anode conditions using the galvanic crevice cell

Because post-mortem study of bipolar plates showed more corrosion products in the cathode side than the anode side, the cathode conditions in the PEM fuel cells is simulated in the galvanic crevice cell using an air atmosphere. However, the galvanic crevice cell designed here could also be used with a hydrogen atmosphere to simulate anode conditions.

7.2.2 Measuring ICR and passive layer properties

Because this study showed that the effect of ICR on the stack performance can be significant, it may be a good idea to measure the ICR after galvanic crevice cell tests and since ICR are affected by passive film properties, the passive film properties should be related to the values of ICR. X-ray photoelectron spectroscopic (XPS) analysis have

been used to evaluate passive films and corrosion products on the bipolar plates surfaces [14, 98, 134, 153, 154], and this can be done using XPS.

7.2.3 In situ measurement of pH distribution in the cell

Kumagai et al. [14] suggested a gradient of pH on cathode side of bipolar plates (a more acidic environment around the outlets than from inlet to centre) during operation which correlates with MEAs contamination results i.e. higher levels of contamination around outlets than from inlet to centre (Chapter 4 and Chapter 5). Therefore, it will be a good idea to do in situ measurement of pH in at least these three positions: around inlet, around centre, and around outlet.

7.2.4 Synchrotron-based absorption-edge tomography for 3D images of the GDL with chemical analysis

Synchrotron-based tomography is a 3D visualisation technique which can offer high resolution (> 1µm) images in a short time (seconds to minutes). Synchrotron facilities provide tenable monochromatic X-ray beams in which the energy of these beams can be adjusted to be above and below the absorption edge of the elements of interest. Since the absorption coefficient of an element increases substantially as the X-ray energy is changed from below to above an absorption edge, the difference between these images can be used to highlight the 3D distribution of the element of choice. This method is known as synchrotron-based absorption-edge tomography [155].

Synchrotron-based absorption-edge tomography can be used for 3D imaging of Fe, Ni, Cr, and Cu in MPL/GDLs. However, this could be time-consuming because a number of measurements may be required for each sample.

If the concentration of elements is too low for synchrotron-based absorption-edge tomography to be viable for 3D imaging of MPL/GDLs, fluorescence tomography can be used. However, fluorescence tomography will be also a time-consuming procedure since the concentration of elements is low [155-157].

8 Conclusions

- Laboratory and synchrotron XRF can be used to evaluate the level of corrosion products from bipolar plate corrosion in MEAs used in PEMFCs. The unused MEA showed lower levels of contaminants than the used MEA and the order of contamination levels was Fe>Ni>Cu, Cr.
- Synchrotron XRF results were generally consistent with laboratory XRF results and the microscopic distribution of contaminants was consistent with the macroscopic distribution of contaminants.
- MEAs from PEM fuel cell stacks showed a heterogeneous distribution of contaminants. Contamination levels increased from the coolant inlet to the coolant outlet.
- After use in PEM fuel cell stacks, the cathode sides of MEAs showed higher levels of contaminants than the anode sides. Fe, the predominant contaminant, was mainly located in the microporous layer of the cathode side and some lower levels of it were also observed in the membrane. Ni, Cr and Cu were mostly accumulated in the membrane and/or the cathode side. The catalyst layers did not show significant levels of contaminants compared to the cathode side or membrane.
- Plan view XRF maps showed that high levels of Fe are associated with high levels of Pt in a distribution pattern which can possibly be cathode MPL cracks.

- The cell-to-cell variations in MEA contamination within stacks were greater than the stack-to-stack variations; therefore the comparison of stack contamination was not possible.
- A galvanic crevice cell that simulates galvanic crevice corrosion in PEM fuel cells was designed and successfully was used to discriminate between different coatings on stainless steel bipolar plates. The results of this galvanic crevice cell correlates with in situ corrosion potential measurements of PEM fuel cells.
- An MEA (including catalyst layers and GDL) coupled to stainless steel showed much higher galvanic current and potential than a GDL alone coupled to stainless steel.
- No clear correlation between XRF measurements of MEAs with electrochemical results was observed for two stacks which were run under similar conditions.

9 List of references

1. Barbir, F., *PEM Fuel Cells: Theory and Practice*. 2005: Elsevier Academic Press.
2. Borup, R., J. Meyers, B. Pivovar, Y.S. Kim, R. Mukundan, N. Garland, D. Myers, M. Wilson, F. Garzon, D. Wood, P. Zelenay, K. More, K. Stroh, T. Zawodzinski, J. Boncella, J.E. McGrath, M. Inaba, K. Miyatake, M. Hori, K. Ota, Z. Ogumi, S. Miyata, A. Nishikata, Z. Siroma, Y. Uchimoto, K. Yasuda, K.I. Kimijima, and N. Iwashita, *Scientific aspects of polymer electrolyte fuel cell durability and degradation.* Chemical Reviews, 2007. **107**(10): p. 3904-3951.
3. Brett, D.J.L. and N.P. Brandon, *Review of materials and characterization methods for polymer electrolyte fuel cell flow-field plates.* Journal of Fuel Cell Science and Technology, 2007. **4**(1): p. 29-44.
4. *Hydrogen, fuel cells and technologies program. In: Multi-year research, development and demonstration plan 1.0 Introduction*. 2013; Available from: http://energy.gov/sites/prod/files/2014/03/f12/introduction.pdf.
5. Barbir, F., *Chapter 1 - 1. Introduction*, in *PEM Fuel Cells*, F. Barbir, Editor. 2005, Academic Press: Burlington. p. 1-16.
6. *Hydrogen, fuel cells and technologies program. In: Multi-year research, development and demonstration plan 3.4 Fuel cells*. 2014; 29]. Available from: http://energy.gov/sites/prod/files/2014/12/f19/fcto_myrdd_fuel_cells.pdf.
7. Wang, H., H. Li, and X. Yuan, *1. Introduction*, in *PEM Fuel Cell Failure Mode Analysis*. 2011, CRC Press. p. 1-2.
8. Buchi, F.N., M. Inaba, and T.J. Schmidt, *Polymer Electrolyte Fuel Cell Durability*. 2009: Springer.
9. Antunes, R.A., M.C.L. Oliveira, G. Ett, and V. Ett, *Corrosion of metal bipolar plates for PEM fuel cells: A review.* International Journal of Hydrogen Energy, 2010. **35**(8): p. 3632-3647.
10. de Bruijn, F.A., V.A.T. Dam, and G.J.M. Janssen, *Durability and degradation issues of PEM fuel cell components.* Fuel Cells, 2008. **8**(1): p. 3-22.
11. Schmittinger, W. and A. Vahidi, *A review of the main parameters influencing long-term performance and durability of PEM fuel cells.* Journal of Power Sources, 2008. **180**(1): p. 1-14.
12. Davies, D.P., P.L. Adcock, M. Turpin, and S.J. Rowen, *Bipolar plate materials for solid polymer fuel cells.* Journal of Applied Electrochemistry, 2000. **30**(1): p. 101-105.
13. Davies, D.P., P.L. Adcock, M. Turpin, and S.J. Rowen, *Stainless steel as a bipolar plate material for solid polymer fuel cells.* Journal of Power Sources, 2000. **86**(1-2): p. 237-242.
14. Kumagai, M., S.T. Myung, S. Kuwata, R. Asaishi, and H. Yashiro, *Corrosion behavior of austenitic stainless steels as a function of pH for use as bipolar plates in polymer electrolyte membrane fuel cells.* Electrochimica Acta, 2008. **53**(12): p. 4205-4212.
15. Kumagai, M., S.T. Myung, T. Ichikawa, and H. Yashiro, *Applicability of extra low interstitials ferritic stainless steels for bipolar plates of proton exchange membrane fuel cells.* Journal of Power Sources, 2010. **195**(21): p. 7181-7186.
16. Andre, J., L. Antoni, J.P. Petit, E. De Vito, and A. Montani, *Electrical contact resistance between stainless steel bipolar plate and carbon felt in PEFC: A comprehensive study.* International Journal of Hydrogen Energy, 2009. **34**(7): p. 3125-3133.
17. Kelly, M.J., G. Fafilek, J.O. Besenhard, H. Kronberger, and G.E. Nauer, *Contaminant absorption and conductivity in polymer electrolyte membranes.* Journal of Power Sources, 2005. **145**(2): p. 249-252.

18. Wu, J.F., X.Z. Yuan, J.J. Martin, H.J. Wang, J.J. Zhang, J. Shen, S.H. Wu, and W. Merida, *A review of PEM fuel cell durability: Degradation mechanisms and mitigation strategies.* Journal of Power Sources, 2008. **184**(1): p. 104-119.
19. Kelly, M.J., B. Egger, G. Fafilek, J.O. Besenhard, H. Kronberger, and G.E. Nauer, *Conductivity of polymer electrolyte membranes by impedance spectroscopy with microelectrodes.* Solid State Ionics, 2005. **176**(25-28): p. 2111-2114.
20. Wilson, M.S., C. Zawodzinski, S. Moller-Holst, D.N. Busick, F.A. Uribe, and T.A. Zawodzinski, *PEMFC stacks for power generation.* Proceedings of the 1999 U.S DOE Hydrogen Program Review 1999: p. 1-14.
21. Toops, T.J., M.P. Brady, P.F. Tortorelli, J.A. Pihl, F. Estevez, D. Connors, F. Garzon, T. Rockward, D. Gervasio, W. Mylan, and S.H. Kosaraju, *Pre-oxidized and nitrided stainless steel alloy foil for proton exchange membrane fuel cell bipolar plates. Part 2: Single-cell fuel cell evaluation of stamped plates.* Journal of Power Sources, 2010. **195**(17): p. 5619-5627.
22. Brady, M.P., K. Weisbrod, I. Paulauskas, R.A. Buchanan, K.L. More, H. Wang, M. Wilson, F. Garzon, and L.R. Walker, *Preferential thermal nitridation to form pin-hole free Cr-nitrides to protect proton exchange membrane fuel cell metallic bipolar plates.* Scripta Materialia, 2004. **50**(7): p. 1017-1022.
23. Wilson, M.S., C. Zawodzinski, and S. Gottesfeld, *Corrosion testing of stainless steel fuel cell hardware.* 1998 Fuel Cell Seminar Palm Springs, CA, 1998.
24. Tawfik, H., Y. Hung, and D. Mahajan, *Metal bipolar plates for PEM fuel cell - A review.* Journal of Power Sources, 2007. **163**(2): p. 755-767.
25. Andre, J., L. Antoni, and J.P. Petit, *Corrosion resistance of stainless steel bipolar plates in a PEFC environment: A comprehensive study.* International Journal of Hydrogen Energy, 2010. **35**(8): p. 3684-3697.
26. Mele, C. and B. Bozzini, *Localised corrosion processes of austenitic stainless steel bipolar plates for polymer electrolyte membrane fuel cells.* Journal of Power Sources, 2010. **195**(11): p. 3590-3596.
27. Hinds, G. and E. Brightman, *Towards more representative test methods for corrosion resistance of PEMFC metallic bipolar plates.* International Journal of Hydrogen Energy, 2015. **40**(6): p. 2785-2791.
28. Fontana, M.G., *Corrosion Engineering* 1987, McGraw-Hill Book Company: New York.
29. Kelly, R.G., J.R. Scully, D.W. Shoesmith, and R.G. Buchheit, *Electrochemical Techniques in Corrosion Science and Engineering*. 2003, Marcel Dekker, Inc.: New York.
30. McCafferty, E., *Introduction to corrosion science*. 2010, Springer: New York.
31. Trethewey, K.R. and J. Chamberlain, *Corrosion for Science and Engineering*. 1995, Longman Group Limited.
32. Davis, J.R., ed. *Corrosion understand the basics*. 2000, ASM International: Ohio
33. Hinds, G., ed. *The electrochemistry of corrosion.* 2008, NPL: London.
34. Gorse, D. and B. Baroux. *Investigating pitting corrosion of stainless steels by single processing techniques*. in *Passivity of metals and semicondoctors: Proceedings of the Eighth International Symposium* 1999: ECS Proceedings.
35. Frankel, G.S., *Pitting corrosion of metals. A review of the critical factors (vol 145, pg 2186, 1998).* Journal of the Electrochemical Society, 1998. **145**(8): p. 2970-2970.
36. Baroux, B., *Corrosion mechanisms in theory and Practice*, P. Marcus and J. Oudar, Editors. 1995, Marcel Dekker Inc.: NY.
37. Pistorius, P.C. and G.T. Burstein, *METASTABLE PITTING CORROSION OF STAINLESS-STEEL AND THE TRANSITION TO STABILITY.* Philosophical Transactions of the Royal Society of London Series a-Mathematical Physical and Engineering Sciences, 1992. **341**(1662): p. 531-559.
38. Revie, R.W., *Uhlig's Corrosion Handbook (2nd Edition)*. 2000, John Wiley & Sons.

39. Frankel, G.S., L. Stockert, F. Hunkeler, and H. Boehni, *METASTABLE PITTING OF STAINLESS-STEEL.* Corrosion, 1987. **43**(7): p. 429-436.
40. Isaacs, H.S. and G. Kissel, *Surface preparation and pit propagation in stainless steels.* Journal of the Electrochemical Society, 1972. **119**(12): p. 1628-&.
41. Isaacs, H.S., *THE LOCALIZED BREAKDOWN AND REPAIR OF PASSIVE SURFACES DURING PITTING.* Corrosion Science, 1989. **29**(2-3): p. 313-323.
42. Isaacs, H.S. and G. Kissel, *SURFACE PREPARATION AND PIT PROPAGATION IN STAINLESS-STEELS.* Journal of the Electrochemical Society, 1972. **119**(12): p. 1628-&.
43. Isaacs, H.S., *A STOCHASTIC-ANALYSIS OF POTENTIAL FLUCTUATIONS DURING PASSIVE FILM BREAKDOWN AND REPAIR OF IRON.* Corrosion Science, 1993. **34**(3): p. 525-528.
44. Pozio, A., R.F. Silva, M. De Francesco, and L. Giorgi, *Nafion degradation in PEFCs from end plate iron contamination.* Electrochimica Acta, 2003. **48**(11): p. 1543-1549.
45. Kinumoto, T., M. Inaba, Y. Nakayama, K. Ogata, R. Umebayashi, A. Tasaka, Y. Iriyama, T. Abe, and Z. Ogumi, *Durability of perfluorinated ionomer membrane against hydrogen peroxide.* Journal of Power Sources, 2006. **158**(2): p. 1222-1228.
46. Inaba, M., T. Kinumoto, M. Kiriake, R. Umebayashi, A. Tasaka, and Z. Ogumi, *Gas crossover and membrane degradation in polymer electrolyte fuel cells.* Electrochimica Acta, 2006. **51**(26): p. 5746-5753.
47. Li, H., K. Tsay, H.J. Wang, J. Shen, S.H. Wu, J.J. Zhang, N.Y. Jia, S. Wessel, R. Abouatallah, N. Joos, and J. Schrooten, *Durability of PEM fuel cell cathode in the presence of Fe3+ and Al3+*. Journal of Power Sources, 2010. **195**(24): p. 8089-8093.
48. Auvinen, S., T. Tingelof, J.K. Ihonen, and J. Siivinen, *Stainless Steel in-situ Corrosion Testing in a PEFC Multisinglecell.* ECS Meeting Abstracts, 2009. **902**(10): p. 1108.
49. Schütze, M., *Corrosion Books: Handbook of Corrosion Engineering. By Pierre R. Roberge - Materials and Corrosion 4/2002.* Materials and Corrosion, 2002. **53**(4): p. 284-284.
50. Revie, R.W., *Uhlig's Corrosion Handbook (2nd Edition)*. 2000, John Wiley & Sons.
51. Roberge, P.R., *handbook of corrosion engineering*. 2000, McGraw-Hill.
52. Tawfik, H., Y. Hung, and D. Mahajan, *Chapter 5 - Bipolar Plate Durability and Challenges*, in *Polymer Electrolyte Fuel Cell Degradation*, M. Matthew, et al., Editors. 2012, Academic Press: Boston. p. 249-291.
53. Yang, Y., L.J. Guo, and H.T. Liu, *The effect of temperature on corrosion behavior of SS316L in the cathode environment of proton exchange membrane fuel cells.* Journal of Power Sources, 2011. **196**(13): p. 5503-5510.
54. Wind, J., A. LaCroix, S. Braeuninger, C. Hedrich, c. Heller, and S. M., *Handbook of Fuel Cells-Fundamentals, Technology and Applications,* , ed. W. Vielstich, H. Gasteiger, and A. Lamm. Vol. 3: Fuel Cell Technology and Applications. 2003, New York: John Wiley & Sons. 289-292.
55. Kühnemann, L., T. Derieth, P. Beckhaus, and A. Heinzel, *PEM Fuel Cell Failure Mode Analysis*, in *PEM Fuel Cell Failure Mode Analysis*. 2011, CRC Press. p. 139-186.
56. de Bruijn, F.A., R.C. Makkus, R.K.A.M. Mallant, and G.J.M. Janssen, *Chapter Five Materials for State-of-the-Art PEM Fuel Cells, and Their Suitability for Operation Above 100°C*, in *Advances in Fuel Cells*, K.D.K. T.S. Zhao and N. Trung Van, Editors. 2007, Elsevier Science. p. 235-336.
57. Barbir, F., *Chapter Four - Main Cell Components, Material Properties, and Processes*, in *PEM Fuel Cells (Second Edition)*, F. Barbir, Editor. 2013, Academic Press: Boston. p. 73-117.
58. Ous, T. and C. Arcoumanis, *Degradation aspects of water formation and transport in Proton Exchange Membrane Fuel Cell: A review.* Journal of Power Sources, 2013. **240**: p. 558-582.

59. El-kharouf, A. and B.G. Pollet, *Chapter 4 - Gas Diffusion Media and their Degradation*, in *Polymer Electrolyte Fuel Cell Degradation*, M.M.M.C.K.N. Veziroglu, Editor. 2012, Academic Press: Boston. p. 215-247.
60. Barbir, F., *Chapter 4 - 4. Main Cell Components, Materials Properties and Processes*, in *PEM Fuel Cells*, F. Barbir, Editor. 2005, Academic Press: Burlington. p. 73-113.
61. Sasabe, T., P. Deevanhxay, S. Tsushima, and S. Hirai, *Soft X-ray visualization of the liquid water transport within the cracks of micro porous layer in PEMFC.* Electrochemistry Communications, 2011. **13**(6): p. 638-641.
62. Markötter, H., J. Haußmann, R. Alink, C. Tötzke, T. Arlt, M. Klages, H. Riesemeier, J. Scholta, D. Gerteisen, J. Banhart, and I. Manke, *Influence of cracks in the microporous layer on the water distribution in a PEM fuel cell investigated by synchrotron radiography.* Electrochemistry Communications, 2013. **34**: p. 22-24.
63. Deevanhxay, P., T. Sasabe, S. Tsushima, and S. Hirai, *Observation of dynamic liquid water transport in the microporous layer and gas diffusion layer of an operating PEM fuel cell by high-resolution soft X-ray radiography.* Journal of Power Sources, 2013. **230**: p. 38-43.
64. Haußmann, J., H. Markötter, R. Alink, A. Bauder, K. Dittmann, I. Manke, and J. Scholta, *Synchrotron radiography and tomography of water transport in perforated gas diffusion media.* Journal of Power Sources, 2013. **239**: p. 611-622.
65. Karst, N., V. Faucheux, A. Martinent, P. Bouillon, and J.-P. Simonato, *Improvement of water management in polymer electrolyte membrane fuel cell thanks to cathode cracks.* Journal of Power Sources, 2010. **195**(16): p. 5228-5234.
66. Kim, S.G. and S.J. Lee, *A review on experimental evaluation of water management in a polymer electrolyte fuel cell using X-ray imaging technique.* Journal of Power Sources, 2013. **230**: p. 101-108.
67. Mukaide, T., S. Mogi, J. Yamamoto, A. Morita, S. Koji, K. Takada, K. Uesugi, K. Kajiwara, and T. Noma, *In situ observation of water distribution and behaviour in a polymer electrolyte fuel cell by synchrotron X-ray imaging.* Journal of Synchrotron Radiation, 2008. **15**: p. 329-334.
68. Tsushima, S. and S. Hirai, *In situ diagnostics for water transport in proton exchange membrane fuel cells.* Progress in Energy and Combustion Science, 2011. **37**(2): p. 204-220.
69. Tsushima, S. and S. Hirai, *An overview of cracks and interfacial voids in membrane electrode assemblies in polymer electrolyte fuel cells.* Journal of Thermal Science and Technology, 2015. **10**(1): p. JTST0002-JTST0002.
70. Wu, R., X. Zhu, Q. Liao, R. Chen, and G.M. Cui, *Liquid and oxygen transport in defective bilayer gas diffusion material of proton exchange membrane fuel cell.* International Journal of Hydrogen Energy, 2013. **38**(10): p. 4067-4078.
71. Hizir, F.E., S.O. Ural, E.C. Kumbur, and M.M. Mench, *Characterization of interfacial morphology in polymer electrolyte fuel cells: Micro-porous layer and catalyst layer surfaces.* Journal of Power Sources, 2010. **195**(11): p. 3463-3471.
72. Deevanhxay, P., T. Sasabe, S. Tsushima, and S. Hirai, *In situ diagnostic of liquid water distribution in cathode catalyst layer in an operating PEMFC by high-resolution soft X-ray radiography*. Electrochemistry Communications, 2012. **22**(0): p. 33-36.
73. Zhang, J., H. Zhang, J. Wu, and J. Zhang, *Chapter 1 - PEM Fuel Cell Fundamentals*, in *Pem Fuel Cell Testing and Diagnosis*, J. Zhang, et al., Editors. 2013, Elsevier: Amsterdam. p. 1-42.
74. Barbir, F., *Chapter 2 - 2. Fuel Cell Basic Chemistry and Thermodynamics*, in *PEM Fuel Cells*, F. Barbir, Editor. 2005, Academic Press: Burlington. p. 17-32.
75. Zhang, J., H. Zhang, J. Wu, and J. Zhang, *Chapter 7 - Fuel Cell Open Circuit Voltage*, in *Pem Fuel Cell Testing and Diagnosis*, J. Zhang, et al., Editors. 2013, Elsevier: Amsterdam. p. 187-200.

76. Barbir, F., *Chapter Three - Fuel Cell Electrochemistry*, in *PEM Fuel Cells (Second Edition)*, F. Barbir, Editor. 2013, Academic Press: Boston. p. 33-72.
77. Barbir, F., *Chapter 3 - 3. Fuel Cell Electrochemistry*, in *PEM Fuel Cells*, F. Barbir, Editor. 2005, Academic Press: Burlington. p. 33-72.
78. Feng, K., G. Wu, Z. Li, X. Cai, and P.K. Chu, *Corrosion behavior of SS316L in simulated and accelerated PEMFC environments.* International Journal of Hydrogen Energy, 2011. **36**(20): p. 13032-13042.
79. Shores, D.A. and G.A. Deluga, *Basic materials corrosion issues*, in *Handbook of Fuel Cells-Fundamentals, Technology and Applications*, , W. Vielstich, H. Gasteiger, and A. Lamm, Editors. 2003, John Wiley & Sons: New York. p. 273-285.
80. Bozzini, B., A. Gianoncelli, B. Kaulich, M. Kiskinova, M. Prasciolu, and I. Sgura, *Metallic Plate Corrosion and Uptake of Corrosion Products by Nafion in Polymer Electrolyte Membrane Fuel Cells.* Chemsuschem, 2010. **3**(7): p. 846-850.
81. Laedre, S., O.E. Kongstein, A. Oedegaard, F. Seland, and H. Karoliussen, *The effect of pH and halides on the corrosion process of stainless steel bipolar plates for proton exchange membrane fuel cells.* International Journal of Hydrogen Energy, 2012. **37**(23): p. 18537-18546.
82. Hinds, G. and E. Brightman, *In situ mapping of electrode potential in a PEM fuel cell.* Electrochemistry Communications, 2012. **17**(0): p. 26-29.
83. Wind, J., R. Spah, W. Kaiser, and G. Bohm, *Metallic bipolar plates for PEM fuel cells.* Journal of Power Sources, 2002. **105**(2): p. 256-260.
84. Wang, Y. and D.O. Northwood, *an investigation of metallic bipolar plate corrosion in simulated anode and cathode environments of pem fuel cells using potential-pH diagrams.* International Journal of Electrochemical Scince 2006. **1**: p. 447-455.
85. Kumar, A., M. Ricketts, and S. Hirano, *Ex situ evaluation of nanometer range gold coating on stainless steel substrate for automotive polymer electrolyte membrane fuel cell bipolar plate.* Journal of Power Sources, 2010. **195**(5): p. 1401-1407.
86. Mele, C., *Corrosion Performance of Austenitic Stainless Steel Bipolar Plates for Nafion- and Room-Temperature Ionic-Liquid-Based PEMFCs.*
87. Wang, Y. and D.O. Northwood, *An investigation into polypyrrole-coated 316L stainless steel as a bipolar plate material for PEM fuel cells.* Journal of Power Sources, 2006. **163**(1): p. 500-508.
88. Wang, Y. and D.O. Northwood, *An investigation into TiN-coated 316L stainless steel as a bipolar plate material for PEM fuel cells.* Journal of Power Sources, 2007. **165**(1): p. 293-298.
89. Wang, Y. and D.O. Northwood, *An investigation of the electrochemical properties of PVD TiN-coated SS410 in simulated PEM fuel cell environments.* International Journal of Hydrogen Energy, 2007. **32**(7): p. 895-902.
90. Kühnemann, L., T. Derieth, P. Beckhaus, and A. Heinzel, *Degradation of Bipolar Plates and Its Effect on PEM Fuel Cells*, in *PEM Fuel Cell Failure Mode Analysis*. 2011, CRC Press
p. 139-186.
91. Ma, L., S. Warthesen, and D.A. Shores, *Evaluation of materials for bipolar plates in PEMFCs.* Journal of New Materials for Electrochemical Systems, 2000. **3**(3): p. 221-228.
92. Kimble, C., S. Woodman, and B. Anderson. *Characterization of Corrosion-Protective Methods for Electrically Conductive Coatings on Aluminum*. in *AESF SUR/FIN '99 Proceedings*. June 21-24 1999: American Electroplaters and Surface Finishers Society.
93. Ahn, S.Y., S.J. Shin, H.Y. Ha, S.A. Hong, Y.C. Lee, T.W. Lim, and I.H. Oh, *Performance and lifetime analysis of the kW-class PEMFC stack.* Journal of Power Sources, 2002. **106**(1-2): p. 295-303.

94. Kumagai, M., S.T. Myung, H. Yashiro, and Y. Katada, *Direct observation of the passive layer on high nitrogen stainless steel used as bipolar plates for proton exchange membrane fuel cells.* Journal of Power Sources, 2012. **210**: p. 92-95.
95. Kim, J.S., W.H.A. Peelen, K. Hemmes, and R.C. Makkus, *Effect of alloying elements on the contact resistance and the passivation behavior of stainless steels.* Corrosion Science, 2002. **44**(4): p. 635-655.
96. Makkus, R.C., A.H.H. Janssen, F.A. de Bruijn, and R. Mallant, *Use of stainless steel for cost competitive bipolar plates in the SPFC.* Journal of Power Sources, 2000. **86**(1-2): p. 274-282.
97. Makkus, R.C., A.H.H. Janssen, F.A. de Bruijn, and R. Mallant, *Stainless steel for cost-competitive bipolar plates in PEMFCs.* fc bull, 2000. **3**: p. 5-9.
98. Wang, H.L. and J.A. Turner, *Ferritic stainless steels as bipolar plate material for polymer electrolyte membrane fuel cells.* Journal of Power Sources, 2004. **128**(2): p. 193-200.
99. Okada, T., *Effect of ionic contaminants*, in *Handbook of Fuel Cells – Fundamentals, Technology and Applications*, W. Vielstich, H.A. Gasteiger, and A. Lamm, Editors. 2002, Wiley: New York. p. 627- 646.
100. LaConti, A.B., M. Hamdan, and R.C. McDonald, *Mechanisms of Membrane Degradation*, in *Handbook of Fuel Cells – Fundamentals, Technology and Applications*, W. Vielstich, H.A. Gasteiger, and A. Lamm, Editors. 2002, Wiley: New York. p. 647–662.
101. Inaba, M., *Chemical Degradation of Perfluorinated Sulfonic Acid Membranes*, in *Polymer Electrolyte Fuel Cell Durability*, F.N. Buchi, T.J. Schmidt, and M. Inaba, Editors. 2009, Springer: New York. p. 57-70.
102. Zhang, J., H. Zhang, J. Wu, and J. Zhang, *Chapter 11 - Fuel Cell Degradation and Failure Analysis*, in *Pem Fuel Cell Testing and Diagnosis*, J. Zhang, et al., Editors. 2013, Elsevier: Amsterdam. p. 283-335.
103. Okada, T., Y. Ayato, H. Satou, M. Yuasa, and I. Sekine, *The effect of impurity cations on the oxygen reduction kinetics at platinum electrodes covered with perfluorinated ionomer.* Journal of Physical Chemistry B, 2001. **105**(29): p. 6980-6986.
104. Okada, T., J. Dale, Y. Ayato, O.A. Asbjornsen, M. Yuasa, and I. Sekine, *Unprecedented effect of impurity cations on the oxygen reduction kinetics at platinum electrodes covered with perfluorinated ionomer.* Langmuir, 1999. **15**(24): p. 8490-8496.
105. Okada, T., Y. Ayato, J. Dale, M. Yuasa, I. Sekine, and O.A. Asbjornsen, *Oxygen reduction kinetics at platinum electrodes covered with perfluorinated ionomer in the presence of impurity cations Fe3+, Ni2+ and Cu2+*. Physical Chemistry Chemical Physics, 2000. **2**(14): p. 3255-3261.
106. Kumagai, M., S.-T. Myung, T. Ichikawa, and H. Yashiro, *Evaluation of polymer electrolyte membrane fuel cells by electrochemical impedance spectroscopy under different operation conditions and corrosion.* Journal of Power Sources, 2010. **195**(17): p. 5501-5507.
107. Perry, M.L., *Chapter Eleven - Durability of Polymer Electrolyte Fuel Cells*, in *PEM Fuel Cells (Second Edition)*, F. Barbir, Editor. 2013, Academic Press: Boston. p. 435-467.
108. Yuan, X.-Z., H. Li, S. Zhang, J. Martin, and H. Wang, *A review of polymer electrolyte membrane fuel cell durability test protocols.* Journal of Power Sources, 2011. **196**(22): p. 9107-9116.
109. Yu, P., W. Gu, J.J. Zhang, R. Makharia, N. Wagner, and H. Gasteiger, *Carbon-Support Requirements for Highly Durable Fuel Cell Operation*, in *Polymer Electrolyte Fuel Cell Durability*, Buchi FN, Inaba M, and S. TJ., Editors. 2009, Springer. p. 29-43.
110. Reiser, C.A., L. Bregoli, T.W. Patterson, J.S. Yi, J.D.L. Yang, M.L. Perry, and T.D. Jarvi, *A reverse-current decay mechanism for fuel cells.* Electrochemical and Solid State Letters, 2005. **8**(6): p. A273-A276.

111. Baumgartner, W.R., P. Parz, S.D. Fraser, E. Wallnöfer, and V. Hacker, *Polarization study of a PEMFC with four reference electrodes at hydrogen starvation conditions*. Journal of Power Sources, 2008. **182**(2): p. 413-421.
112. Tang, H., Z.G. Qi, M. Ramani, and J.F. Elter, *PEM fuel cell cathode carbon corrosion due to the formation of air/fuel boundary at the anode.* Journal of Power Sources, 2006. **158**(2): p. 1306-1312.
113. Brightman, E. and G. Hinds, *In situ mapping of potential transients during start-up and shut-down of a polymer electrolyte membrane fuel cell.* Journal of Power Sources, 2014. **267**(0): p. 160-170.
114. Sasaki, K., M. Shao, and R. Adzic, *Dissolution and Stabilization of Pt in oxygen cathodes*, in *Polymer Electrolyte Fuel Cell Durability*, F.N. Buchi, M. Inaba, and T.J. Schmidt, Editors. 2009, Springer. p. 7-24.
115. Wang, X.P., R. Kumar, and D.J. Myers, *Effect of voltage on platinum dissolution relevance to polymer electrolyte fuel cells.* Electrochemical and Solid State Letters, 2006. **9**(5): p. A225-A227.
116. Zhang, S.S., X. Yuan, and H. Wang, *Catalyst Degradation*, in *PEM Fuel Cell Failure Mode Analysis*, K. Lars, et al., Editors. 2011, CRC Press. p. 3-26.
117. Iiyama, A., K. Shinohara, S. Iguchi, and A. Daimaru, *Membranes and catalyst performance targets for automotive fuel cells*, in *Handbook of Fuel Cells*. 2010, John Wiley & Sons, Ltd. p. 3227.
118. Tian, R.J. and J.C. Sun, *Corrosion resistance and interfacial contact resistance of TiN coated 316L bipolar plates for proton exchange membrane fuel cell.* International Journal of Hydrogen Energy, 2011. **36**(11): p. 6788-6794.
119. Wang, Y. and D.O. Northwood, *Effect of substrate material on the corrosion of TiN-coated stainless steels in simulated anode and cathode environments of proton exchange membrane fuel cells.* Journal of Power Sources, 2009. **191**(2): p. 483-488.
120. Li, M.C., S.Z. Luo, C.L. Zeng, J.N. Shen, H.C. Lin, and C.N. Cao, *Corrosion behavior of TiN coated type 316 stainless steel in simulated PEMFC environments.* Corrosion Science, 2004. **46**(6): p. 1369-1380.
121. Brouwer, P., ed. *Theory of XRF*. 3 ed. 2010, PANalytical B. V.: Almelo. 62.
122. Janssens, K., *X-ray Fluorescence Analysis*, in *Handbook of Spectroscopy*, G. Gauglitz and T. Vo-Dinh, Editors. 2003, Wiley-VCH. p. 365-420.
123. Jenkins, R., *X-ray fluorescence spectrometry*. 1999, John Wiley & sons: New York.
124. Als-Nielsen, J. and D. Mcmorrow, *Elements of modern x-ray physics*. 2001: John Wily and Sons Ltd.
125. Zawodzinski, C., M. Wilson, and S. Gottesfeld. *Metal Screen and Foil Hardware for Polymer Electrolyte Fuel Cells*. in *in Proton Conducting Membrane Fuel Cells II*. 1998.
126. Park, Y.-C., S.-H. Lee, S.-K. Kim, S. Lim, D.-H. Jung, S.-Y. Choi, J.-H. Kim, and D.-H. Peck, *Effects of CrN/Cr coating layer on durability of metal bipolar plates under a fuel recirculation system of direct methanol fuel cells.* International Journal of Hydrogen Energy, (0).
127. Brady, M.P., H. Wang, B. Yang, J.A. Turner, M. Bordignon, R. Molins, M. Abd Elhamid, L. Lipp, and L.R. Walker, *Growth of Cr-Nitrides on commercial Ni-Cr and Fe-Cr base alloys to protect PEMFC bipolar plates.* International Journal of Hydrogen Energy, 2007. **32**(16): p. 3778-3788.
128. Zawodzinski, C., M.S. Wilson, and S. Gottesfeld, *Stainless steel wire mesh flow-fields for polymer electrolyte fuel cells*. 1996. Medium: ED; Size: 5 p.
129. Caqué, N., M. Paris, M. Chatenet, E. Rossinot, R. Bousquet, and E. Claude, *Characterization of Uncoated Stainless Steel as Proton Exchange Membrane Fuel Cell Bipolar Plates Material.* Fuel Cells, 2012. **12**(2): p. 248-255.

130. Wei, G.Q., Y.X. Wang, C.D. Huang, Q.J. Gao, Z.T. Wang, and L. Xu, *The stability of MEA in SPE water electrolysis for hydrogen production.* International Journal of Hydrogen Energy, 2010. **35**(9): p. 3951-3957.
131. Auvinen, S., T. Tingelof, J.K. Ihonen, J. Siivinen, and M. Johansson, *Stainless Steel In-situ Corrosion Testing in a PEFC Multisinglecell.* ECS Transactions, 2009. **25**(1): p. 1811-1821.
132. Wang, H.L., J.A. Turner, X.N. Li, and G. Teeter, *Process modification for coating SnO2 : F on stainless steels for PEM fuel cell bipolar plates.* Journal of Power Sources, 2008. **178**(1): p. 238-247.
133. Lee, G.Y., M.K. Jung, S.N. Ryoo, M.S. Park, S.C. Ha, and S. Kim, *Development of cost innovative BPs for a PEMFC stack for a 1 kW-class residential power generator (RPG) system.* International Journal of Hydrogen Energy, 2010. **35**(23): p. 13131-13136.
134. Feng, K., Z.G. Li, X. Cai, and P.K. Chu, *Corrosion behavior and electrical conductivity of niobium implanted 316L stainless steel used as bipolar plates in polymer electrolyte membrane fuel cells.* Surface & Coatings Technology, 2010. **205**(1): p. 85-91.
135. Yoon, W., X.Y. Huang, P. Fazzino, K.L. Reifsnider, and M.A. Akkaoui, *Evaluation of coated metallic bipolar plates for polymer electrolyte membrane fuel cells.* Journal of Power Sources, 2008. **179**(1): p. 265-273.
136. Auvinen, S., T. Tingelof, J.K. Ihonen, J. Siivinen, and M. Johansson, *Cost Effective In-Situ Characterization of Coatings for PEFC Bipolar Plates Demonstrated with PVD Deposited CrN.* Journal of the Electrochemical Society, 2011. **158**(5): p. B550-B556.
137. Abdullah, A.M., T. Okajima, F. Kitamura, and T. Ohsaka, *Effect of Operating Conditions on the Acidity of H2/Air PEM Fuel Cells' Water.* ECS Transactions, 2008. **16**(2): p. 543-550.
138. Abdullah, A.M., A.M. Mohammad, T. Okajima, F. Kitamura, and T. Ohsaka, *Effect of load, temperature and humidity on the pH of the water drained out from H-2/air polymer electrolyte membrane fuel cells.* Journal of Power Sources, 2009. **190**(2): p. 264-270.
139. *Outokumpu Stainless,* *http://www.outokumpu.com/applications/upload/pubs_4272642.pdf*. 2011.
140. Slater, C., *private communication with Bruker UK limited*. 2014.
141. Davenport, A.J., A.J. Dent, M. Monir, J.A. Hammons, S.M. Ghahari, P.D. Quinn, and T. Rayment, *XANES Study of the Chemistry of Molybdenum in Artificial Corrosion Pits in 316L Stainless Steel.* Journal of the Electrochemical Society, 2011. **158**(5): p. C111-C117.
142. Mosselmans, J.F.W., P.D. Quinn, A.J. Dent, S.A. Cavill, S.D. Moreno, A. Peach, P.J. Leicester, S.J. Keylock, S.R. Gregory, K.D. Atkinson, and J.R. Rosell, *I18-the microfocus spectroscopy beamline at the Diamond Light Source.* Journal of Synchrotron Radiation, 2009. **16**: p. 818-824.
143. Mosselmans, F. and T. Geraki. *Pymca: Full Analysis and Quantification*. 2015; Available from: http://confluence.diamond.ac.uk/display/I18Tech/Pymca%3A+Full+Analysis+and+Quantification.
144. Solé, V.A., E. Papillon, M. Cotte, P. Walter, and J. Susini, *A multiplatform code for the analysis of energy-dispersive X-ray fluorescence spectra.* Spectrochimica Acta Part B: Atomic Spectroscopy, 2007. **62**(1): p. 63-68.
145. Geraki, T., *private communication with Diamond Light Source* 2013.
146. Sucheta, S., *private communication with technical product support team, VWR International Europe*. 2011.
147. Dhanasekaran, B., *A new water source: can fuel cells provide safe potable water sources?* . 2007, Thesis submitted at Arizona State University.
148. Hinds, G., *private communication with National Physical Laboratory*. 2013.

149. Kelly, R.G. and R.G. Scully, *Electrochemical Techniques in Corrosion Science and Engineering*, P.E. Schweitzer, Editor. 2003, Marcel Dekker, Inc.: New York.
150. Wang, H.L., M.A. Sweikart, and J.A. Turner, *Stainless steel as bipolar plate material for polymer electrolyte membrane fuel cells.* Journal of Power Sources, 2003. **115**(2): p. 243-251.
151. Iversen, A.K., *Stainless steels in bipolar plates--Surface resistive properties of corrosion resistant steel grades during current loads.* Corrosion Science, 2006. **48**(5): p. 1036-1058.
152. Walker, R., *Principles and prevention of corrosion: Denny A. Jones Macmillan, 1992, ISBN 0-02-361215-0, £16.95.* Materials & Design, 1993. **14**(3): p. 207.
153. Shao, Y.Y., R. Kou, J. Wang, V.V. Viswanathan, J.H. Kwak, J. Liu, Y. Wang, and Y.H. Lin, *The influence of the electrochemical stressing (potential step and potential-static holding) on the degradation of polymer electrolyte membrane fuel cell electrocatalysts.* Journal of Power Sources, 2008. **185**(1): p. 280-286.
154. Wang, H., M.P. Brady, K.L. More, H.M. Meyer, and J.A. Turner, *Thermally nitrided stainless steels for polymer electrolyte membrane fuel cell bipolar plates - Part 2: Beneficial modification of passive layer on AISI446.* Journal of Power Sources, 2004. **138**(1-2): p. 79-85.
155. Banhart, J., ed. *Advanced Tomographic Methods in Materials Research and Engineering*. 2008, Oxford University Press: New York.
156. Yuasa, T. and T. Takeda, eds. *Fluorescent X-Ray Computed Tomography Using Synchrotron Radiation Towards Molecular Imaging, Molecular Imaging*. ed. B. Schaller. 2012.
157. Bourassa, D., S.-C. Gleber, S. Vogt, H. Yi, F. Will, H. Richter, C.H. Shin, and C.J. Fahrni, *3D imaging of transition metals in the zebrafish embryo by X-ray fluorescence microtomography.* Metallomics, 2014. **6**(9): p. 1648-1655.